N°d'ordre NNT : 2023ISAL0049

THESE de DOCTORAT DE L'INSA LYON, membre de l'Université de Lyon

Ecole Doctorale N° 162
Mécanique, Énergétique, Génie civil, Acoustique (MEGA)

Spécialité/discipline de doctorat :
Génie Mécanique

Soutenue publiquement le 28/08/2023, par :
Georges Amine

High sliding EHL contacts: thermal effects of DLC coatings

Devant le jury composé de :

Larsson, Roland	Professeur des Universités/ Luleå University of Technology	Rapporteur
Habchi, Wassim	Professeur des Universités/ Lebanese American University	Rapporteur
Minfray, Clotilde	Professeur des Universités/ École Centrale de Lyon	Examinatrice
Fillot, Nicolas	Professeur des Universités/ INSA Lyon	Directeur de thèse
Dufils, Johnny	Docteur/ HEF groupe	Invité
Philippon, David	Maître de Conférences/ INSA Lyon	Invité

Département FEDORA – INSA Lyon - Ecoles Doctorales

SIGLE	ECOLE DOCTORALE	NOM ET COORDONNEES DU RESPONSABLE
CHIMIE	**CHIMIE DE LYON** **https://www.edchimie-lyon.fr** Sec. : Renée EL MELHEM Bât. Blaise PASCAL, 3e étage secretariat@edchimie-lyon.fr	**M. Stéphane DANIELE** C2P2-CPE LYON-UMR 5265 Bâtiment F308, BP 2077 43 Boulevard du 11 novembre 1918 69616 Villeurbanne **directeur@edchimie-lyon.fr**
E.E.A.	**ÉLECTRONIQUE, ÉLECTROTECHNIQUE, AUTOMATIQUE** **https://edeea.universite-lyon.fr** Sec. : Stéphanie CAUVIN Bâtiment Direction INSA Lyon Tél : 04.72.43.71.70 secretariat.edeea@insa-lyon.fr	**M. Philippe DELACHARTRE** INSA LYON Laboratoire CREATIS Bâtiment Blaise Pascal, 7 avenue Jean Capelle 69621 Villeurbanne CEDEX Tél : 04.72.43.88.63 **philippe.delachartre@insa-lyon.fr**
E2M2	**ÉVOLUTION, ÉCOSYSTÈME, MICROBIOLOGIE, MODÉLISATION** **http://e2m2.universite-lyon.fr** Sec. : Bénédicte LANZA Bât. Atrium, UCB Lyon 1 Tél : 04.72.44.83.62 secretariat.e2m2@univ-lyon1.fr	**Mme Sandrine CHARLES** Université Claude Bernard Lyon 1 UFR Biosciences Bâtiment Mendel 43, boulevard du 11 Novembre 1918 69622 Villeurbanne CEDEX **sandrine.charles@univ-lyon1.fr**
EDISS	**INTERDISCIPLINAIRE SCIENCES-SANTÉ** **http://ediss.universite-lyon.fr** Sec. : Bénédicte LANZA Bât. Atrium, UCB Lyon 1 Tél : 04.72.44.83.62 secretariat.ediss@univ-lyon1.fr	**Mme Sylvie RICARD-BLUM** Institut de Chimie et Biochimie Moléculaires et Supramoléculaires (ICBMS) - UMR 5246 CNRS - Université Lyon 1 Bâtiment Raulin - 2ème étage Nord 43 Boulevard du 11 novembre 1918 69622 Villeurbanne Cedex Tél : +33(0)4 72 44 82 32 **sylvie.ricard-blum@univ-lyon1.fr**
INFOMATHS	**INFORMATIQUE ET MATHÉMATIQUES** **http://edinfomaths.universite-lyon.fr** Sec. : Renée EL MELHEM Bât. Blaise PASCAL, 3e étage Tél : 04.72.43.80.46 infomaths@univ-lyon1.fr	**M. Hamamache KHEDDOUCI** Université Claude Bernard Lyon 1 Bât. Nautibus 43, Boulevard du 11 novembre 1918 69 622 Villeurbanne Cedex France Tél : 04.72.44.83.69 **hamamache.kheddouci@univ-lyon1.fr**
Matériaux	**MATÉRIAUX DE LYON** **http://ed34.universite-lyon.fr** Sec. : Yann DE ORDENANA Tél : 04.72.18.62.44 yann.de-ordenana@ec-lyon.fr	**M. Stéphane BENAYOUN** Ecole Centrale de Lyon Laboratoire LTDS 36 avenue Guy de Collongue 69134 Ecully CEDEX Tél : 04.72.18.64.37 **stephane.benayoun@ec-lyon.fr**
MEGA	**MÉCANIQUE, ÉNERGÉTIQUE, GÉNIE CIVIL, ACOUSTIQUE** **http://edmega.universite-lyon.fr** Sec. : Stéphanie CAUVIN Tél : 04.72.43.71.70 Bâtiment Direction INSA Lyon mega@insa-lyon.fr	**M. Jocelyn BONJOUR** INSA Lyon Laboratoire CETHIL Bâtiment Sadi-Carnot 9, rue de la Physique 69621 Villeurbanne CEDEX **jocelyn.bonjour@insa-lyon.fr**
ScSo	**ScSo*** **https://edsciencessociales.universite-lyon.fr** Sec. : Mélina FAVETON INSA : J.Y. TOUSSAINT Tél : 04.78.69.77.79 melina.faveton@univ-lyon2.fr	**M. Bruno MILLY** Université Lumière Lyon 2 86 Rue Pasteur 69365 Lyon CEDEX 07 **bruno.milly@univ-lyon2.fr**

*ScSo : Histoire, Géographie, Aménagement, Urbanisme, Archéologie, Science politique, Sociologie, Anthropologie

Résumé

Cette thèse explore l'influence des revêtements Diamond-Like Carbon (DLC) sur à la fois le frottement et l'épaisseur du film dans les contacts thermo-élastohydrodynamiques (TEHL) pour une large gamme de conditions de glissement. Des études précédentes ont principalement examiné la réduction du frottement due aux revêtements DLC sous des conditions de roulement-glissement et ont trouvé une influence négligeable sur l'épaisseur du film. Cependant, les surfaces thermiquement isolantes sont suspectées de réduire l'effet bénéfique du « viscosity wedge » à haut cisaillement. Cette thèse étudie une large gamme de conditions de glissement, telles que le glissement opposé trouvé dans divers composants mécaniques tels que le contact came-linguet. Une double approche expérimentale et numérique est utilisée. D'une part, des expériences sont menées sur un tribomètre tonneau-sur-disque et sur un banc d'essai came-linguet-poussoir. D'autre part, une approche EHL quantitative est proposée sur la base d'une caractérisation rhéologique indépendante d'un lubrifiant commercial et réalisée à l'aide d'un solveur éléments finis. Les résultats démontrent la capacité du modèle numérique à reproduire à la fois les mesures de frottement et d'épaisseur du film, en particulier dans des conditions de glissement opposé. Sur une large gamme de conditions de fonctionnement examinées dans cette étude, le modèle numérique montre que l'utilisation des revêtements DLC conduit non seulement à une diminution du frottement (d'environ 30 % dans certains cas), mais également à une diminution de l'épaisseur de film (jusqu'à 10 %). De plus, les résultats numériques et expérimentaux indiquent tous deux que l'application d'un revêtement DLC au contact came-linguet est bénéfique en termes de réduction du frottement. En outre, cette étude vise à quantifier la diminution de l'épaisseur du film lors du glissement à haute vitesse, ce qui est essentiel pour anticiper le risque de contact entre aspérités.

Mots-clés : Lubrification TEHL, Fort glissement, Effet thermique, Revêtement DLC, Came-linguet.

Abstract

This thesis explores the influence of thermally insulating Diamond-Like Carbon (DLC) coatings on both friction and film thickness in thermal-elastohydrodynamic (TEHL) contacts across a wide range of sliding conditions. Previous studies have primarily examined friction reduction due to DLC coatings under rolling-sliding conditions and found a negligible influence on film thickness. However, thermally insulating surfaces are suspected to reduce the beneficial viscosity wedge effect at high shear. This thesis investigates a large range of sliding conditions, such as the opposite sliding found in various mechanical components like the cam-finger follower contact. A dual experimental-numerical approach is employed. On one hand, experiments are carried out on a barrel-on-disk tribometer and a cam-follower-valve test rig. On the other hand, a quantitative EHL approach is proposed based on an independent rheological characterization of a commercial lubricant and realized using a finite element solver. The findings demonstrate the ability of the numerical model to reproduce both friction and film thickness measurements, particularly under opposite sliding conditions. Across a wide range of operating conditions examined in this study, the numerical model shows that the use of DLC coatings leads not only to a decrease in friction (about 30 % in some cases) but also in film thickness (up to 10 %). Furthermore, both numerical and experimental results indicate that applying a DLC coating to the cam-follower contact is beneficial in terms of friction reduction. Moreover, this study aims to quantify the decrease in film thickness at high sliding which is essential to anticipate the risk of asperity contact.

Keywords: TEHL lubrication, High sliding, Thermal effect, DLC coating, Cam-follower.

Acknowledgments

I would like to express my deepest gratitude and appreciation to all those who have contributed to the completion of this doctoral thesis. This work would not have been possible without the support, guidance, and encouragement of numerous individuals. I would like to extend my heartfelt thanks to the following:

First and foremost, I am profoundly grateful to my academic supervisor, Nicolas Fillot, and industrial supervisors Etienne Macron and Johnny Dufils for their unwavering support, invaluable guidance, and continuous motivation throughout this research journey. Their expertise, insightful feedback, and constructive criticism have been instrumental in shaping the direction and quality of this thesis. I am indebted to them for their patience, mentorship, and for pushing me to achieve my best.

I extend my sincere appreciation to the members of my thesis jury members: Roland Larsson, Wassim Habchi, and Clotilde Minfray, for their valuable input, and meticulous examination of my manuscript. I am grateful for their time, thoughtful comments, and insightful suggestions.

I am grateful to LaMCoS (INSA Lyon) and IREIS (HEF group) for providing a conducive research environment and access to resources, facilities, and support. Their commitment to excellence and dedication to fostering an atmosphere of intellectual growth have played an integral role in shaping my doctoral journey. I am especially thankful to David Philippon, Nathalie Bouscharain, Nicolas Devaux, and Lionel Lafarge for their help in the experimental part of my work.

I wish to express my heartfelt gratitude to my colleagues who have provided support, encouragement, and stimulating discussions throughout my thesis.

Finally, I would like to express my deepest gratitude to my close and distant family. Their love, encouragement, and belief in my abilities have been my source of strength throughout this journey. I am grateful for my friends with whom I shared unforgettable moments: Simona, Joey, Ramona, Sarah, Khawla, Marwa, Sana, Ahmad, Hadi, Koko.

To all those mentioned above and to anyone else who has contributed in any way, whether big or small, I offer my heartfelt thanks. This thesis is the culmination of years of hard work and collaboration, and it is a testament to the support and encouragement I have received along the way.

To my family, to Yorgo and Roy.

Table of Contents

Nomenclature

Abbreviations:

BDC	Bottom dead center
BL	Boundary lubrication
CCW, CW	Counter-clockwise and Clockwise
CFD	Computational fluid dynamics
CVD	Chemical vapor deposition
DCI	Differential colorimetric interferometry
DLC	Diamond-like carbon
DOF	Degree of freedom
ECWR	Electron cyclotron wave resonance
EHL	Elastohydrodynamic lubrication
EVC	Exhaust valve close
EVO	Exhaust valve opens
FCVA	Filtered cathodic vacuum arc
FEM	Finite element method
FSI	Fluid-Structure Interaction
GNP	Gross national product
GRG	Generalized reduced gradient
HL	Hydrodynamic lubrication
ICE	Internal combustion engine
IS	Ignition starts
IVC	Inlet valve close
IVO	Inlet valve opens
LSS	Limiting shear stress
ML	Mixed lubrication
PACVD	Plasma-assisted chemical vapor deposition
PECVD	Plasma-enhenced chemical vapor deposition
PVD	Physical vapor deposition
RF	Radio frequency
RGB	Red-green-blue
RMS	Root mean squared
SRR	Slide-to-roll ratio
SThM	Scanning thermal microscopy
TDC	Top dead center
TEHL	Thermal-elastohydrodynamic lubrication
WLF	Williams–Landel–Ferry
ZEV	Zero entrainment velocity

Roman alphabet:

a^{1D}	Half-width of the line contact
a^{2D}	Semi-minor axis length of the elliptical contact
a_{CY}	Parameter of modified Carreau-Yasuda model
a_{ref}	Semi-minor axis length of the elliptical contact at the reference time
a_v	Parameter of Tait density model
$A_1,\ A_2$	Parameters of WLF viscosity model
A_c	Contact area
b^{2D}	Semi-major axis length of the elliptical contact
b_{ref}	Semi-major axis length of the elliptical contact at the reference time
$B_1,\ B_2$	Parameters of WLF viscosity model
c_H	Hydrogen content
$\boldsymbol{C}$	Stiffness tensor
$C_1,\ C_2$	Parameters of WLF viscosity model
C_f	Friction coefficient
Cp	Heat capacity
D	Ratio of radii of curvature in the x and y directions
E	Young's modulus of elasticity
E_{eq}	Equivalent Young's modulus of elasticity
E'	Reduced Young's modulus of elasticity
F_2	Elliptical integral used to calculate b^{2D}
F_f	Friction force
F_T , F_T^{1D}, F_T^{2D}	Tangential friction force
G	Dimensionless load parameter
G_{CY}	Parameter of modified Carreau-Yasuda model
h	Lubricant film thickness
h_0	Rigid body displacement
h_m, h_c, $h_{m,c}$, h_a	Minimum, central, minimum on central line, and average lubricant film thickness respectively
h_{coat}	Coating thickness
$\bar{h}_{coat}$	Dimensionless coating thickness
H	Dimensionless thickness
H_m, H_c	Minimum, central and minimum on central line dimensionless lubricant film thickness respectively
k	Thermal conductivity
k_e	Elliptical integral used to calculate a^{2D} and b^{2D}
$\bar{k}$	Dimensionless thermal conductivity
K_{00}	Parameter of Tait density model
K'_0	Parameter of Tait density model
L_x^{1D}, L_x^{2D}, L_y^{2D}	Reynolds domain dimensions
M_c	Instantaneous cam torque
n_{CY}	Parameter of modified Carreau-Yasuda model

$\vec{n}$	Outwards-pointing vector normal to a geometric boundary
O_c	Location of the axis of rotation of the cam
O_f	Location of the axis of rotation of the follower
p	Pressure
$p_{Hz}, p_{Hz}^{1D}, p_{Hz}^{2D}$	Maximum Hertzian pressures
P_{atm}	Atmospheric pressure
P_f	Friction power loss
q_i	Heat flow from the contact to a given zone/component
q_{tot}	Total heat flow generated in the contact
q_{tot}^*	Overall total heat flow generated in the contact
Q_c, Q_s	Compressive and shear heat sources respectively
R, R^{1D}, R^{2D}	Reduced radii of curvature
R^2	Coefficient of determination
R_{CY}	Parameter of modified Carreau-Yasuda model
R_{eq}	Equivalent radius of curvature
$R_{q,i}$	Root mean squared roughness of a surface
R_q	Composite roughness of two contacting surfaces
R_x, R_y	Radii of curvature in the x and y directions respectively
t	Time
t_{SRR}	Time elapsed in a given sliding condition
T	Temperature
T_0	Ambient contact temperature
T_{ext}	Temperature of the lubricant in the external bath
T_g	Glass transition temperature
T_{in}, T_{out}	Temperature of the lubricant at the inlet and outlet of the test chamber respectively
T_r	Reference temperature
T_{room}	Ambient room temperature
u	Displacement in the x-direction
u_1, u_2	Surface velocities of solids 1 and 2
u_e	Entrainment velocity
$\overrightarrow{u_f}$	Fluid velocity vector
U	Dimensionless velocity parameter
v	Displacement in the y-direction
w	Displacement in the z-direction
w_{1D}, w_{2D}, w_N	Normal loads
W_{1D}, W_{2D}	Dimensionless load parameters
W_f	Friction work
x, y, z	Spatial dimensions
$\bar{x}, \bar{y}, \bar{z}$	Dimensionless spatial dimensions

Greek alphabet:

α, α^*	Viscosity-pressure coefficient at atmospheric pressure
β_k	Parameter of Tait density model
$\dot{\gamma}$	Shear rate
Γ	Weissenberg number
δ	Sum of displacement of the two surfaces in the z-direction
$\Delta\theta$	Temperature rise
Δt	Duration of a camshaft rotation cycle
∂	Designates a geometric boundary
$\boldsymbol{\epsilon}$	Strain tensor
η	Dynamic viscosity of the lubricant
$\frac{1}{\eta_e}, \frac{1}{\eta'_e}$	Integral terms used in the generalized Reynolds equation
θ_c	Camshaft angle
λ	Film thickness parameter
μ	Newtonian viscosity
μ_0	Viscosity of the lubricant at atmospheric pressure
μ_g	Glass transition viscosity
μ_r	Reference viscosity
ν	Poisson's ratio
ν_{eq}	Equivalent Poisson's ratio
ρ	Density
ρ_0	Density of the lubricant at atmospheric pressure
$\rho_e, \rho'_e, \rho''_e$	Integral terms used in the generalized Reynolds equation
ρ_r	Reference density
$\boldsymbol{\sigma}$	Stress tensor
$\tau, \tau_{zx}, \tau_{zy}$	Shear stress
φ	Film thickness correction factor
ψ	Friction coefficient correction factor
ω	Camshaft rotation speed
Ω	Designates a geometric domain

Résumé étendu

1 Introduction

Avec le resserrement des objectifs environnementaux dans differents pays [1-3], les chercheurs s'efforcent de trouver des technologies plus efficaces dans tous les secteurs, en particulier dans celui des transports. Une partie non négligeable de l'énergie du carburant est perdue par frottement à l'intérieur d'un moteur à combustion interne. Holmberg et al [6] estiment que ces pertes s'élèvent à 11,5 % de l'énergie chimique totale du carburant. Le développement de techniques de réduction des frottements dans les systèmes tribologiques constitue une étape essentielle vers la mobilité durable. L'une de ces techniques consiste à recouvrir les composants mécaniques de couches minces de carbone amorphe (Diamond-Like Carbon, DLC) afin de réduire le frottement et d'augmenter la durée de vie de ces composants. Cette thèse explore l'influence des revêtements Diamond-Like Carbon (DLC) sur à la fois le frottement et l'épaisseur de film dans les contacts thermo-élastohydrodynamiques (TEHL) pour une large gamme de conditions de glissement.

Le système d'intérêt dans ce travail est le mécanisme came-linguet-soupape illustré dans la Figure 1. Ce mécanisme fait partie du système de distribution qui contrôle l'ouverture et la fermeture des soupapes d'admission et d'échappement dans un moteur thermique. On s'intéresse particulièrement au contact entre la came et la face supérieure du linguet.

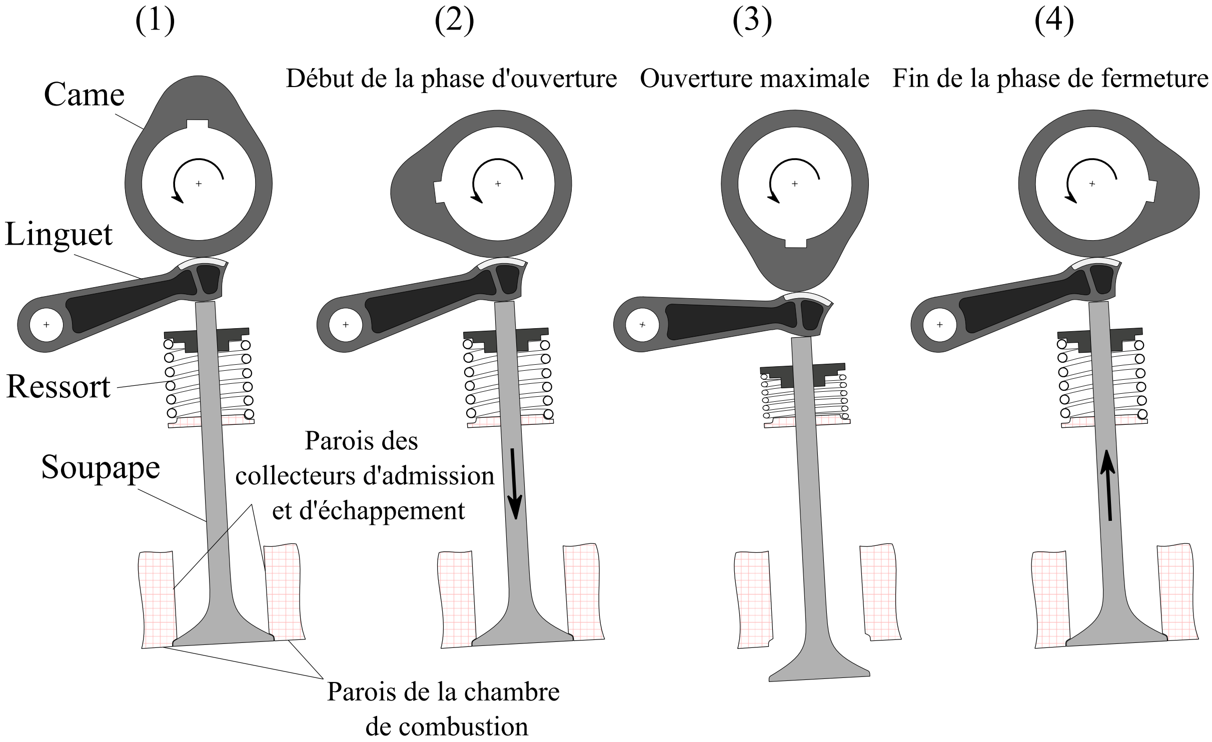

Figure 1: Dessins schématiques du mécanisme came-linguet-soupape. Chacun des dessins (1) à (4) correspond à une position pendant le cycle de rotation de la came.

Ce contact est caractérisé par le fait que les vitesses des surfaces, la charge normale et les rayons de courbure des corps en contact changent rapidement au cours de chaque cycle de came. u_1 et u_2 sont les vitesses de la surface de la came et de la surface du linguet. La vitesse d'entrainement est définie par $u_e = \frac{u_1+u_2}{2}$. Durant la majorité du cycle, les surfaces se déplacent en direction opposée avec un taux de glissement $SRR = \frac{u_1-u_2}{u_e} > 2$ qui atteint un maximum de 10. D'où l'importance d'approfondir la connaissance dans le domaine de la lubrification à glissement élevé où le profil d'épaisseur de film lubrifiant se distingue de celui à faible glissement par la présence (possible) d'un « dimple » dans la zone de haute pression. Ceci a été observé expérimentalement à glissement infinie par Cameron [36] qui a inventé le terme « viscosity wedge » désignant la capacité du lubrifiant à porter la charge même à entrainement nul. Ces observations ont montrées que la théorie EHL classique est insuffisante pour expliquer le comportement d'un contact lubrifié à fort glissement. Cependant, avec l'avancement des méthodes numériques et la dérivation du l'équation Reynolds généralisée [34] il est maintenant possible de modéliser le contact EHL à fort glissement tout en prenant en compte les effets thermiques et la rhéologie non-Newtonienne des lubrifiants.

L'application des revêtements DLC au composant de système de distribution montre une réduction de frottement dans des contact en régime mixte et limite [95, 96]. En outre, des études précédentes ont examiné la réduction du frottement due aux revêtements DLC sous des conditions de roulement-glissement en régime elastohydrodynamiques avec des géométries simples (contact circulaire) [120-122]. En utilisant des modèles numériques, une réduction de frottement et une influence négligeable sur l'épaisseur de film ont été montrées. La diminution de frottement est attribuée au fait que le DLC joue le rôle d'isolant thermique qui empêche la chaleur produite dans le lubrifiant de s'échapper facilement vers les surfaces solides. Par conséquence, la température du lubrifiant augmente et sa viscosité diminue, ce qui diminue le frottement. Cependant, les surfaces thermiquement isolantes sont suspectées de réduire l'effet bénéfique du « viscosity wedge » à haut cisaillement.

Cette thèse étudie une large gamme de conditions de glissement, telles que le glissement opposé trouvé dans divers composants mécaniques comme le contact came-linguet. Elle se concentre sur les effets des revêtements DLC à la fois sur le frottement et sur l'épaisseur de film. Une double approche expérimentale et numérique, décrite dans les sections ci-après, est utilisée.

2 Approche Expérimentale

Tribomètre tonneau-sur-disque

Des expériences sont menées sur un tribomètre tonneau-sur-disque développé au LaMCoS (INSA Lyon) par Molimard et al. [72] pour mesurer l'épaisseur de film et le frottement dans les contacts EHL. La mesure de l'épaisseur est réalisée par interférométrie colorimétrique différentielle (Differential Colorimetric Interferometry, DCI) tandis que les mesures de la force de frottement tangentielle et la force normale dans la zone de contact sont réalisées par un capteur à jauge multiaxiale. L'installation est représentée schématiquement dans la Figure 2a et est similaire à celle de Meziane et al. [44].

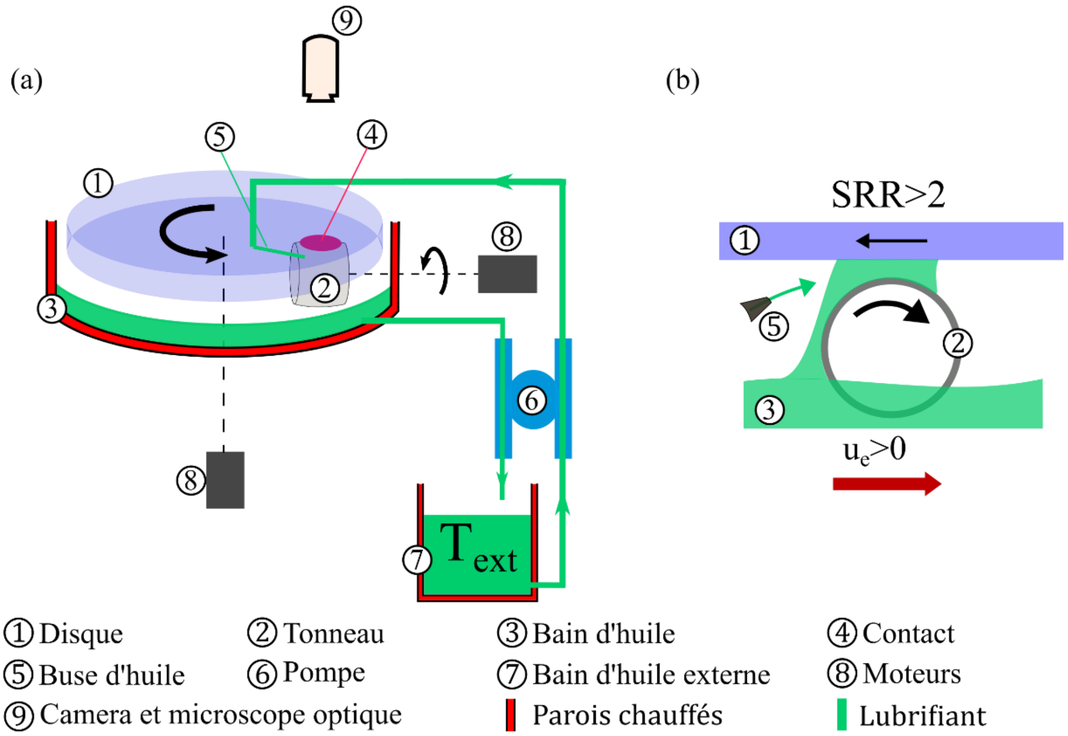

Figure 2: (a) Représentation schématique de l'installation du tribomètre inspirée de [44]. (b) Vue latérale illustrant les voies de lubrifaction du contact.

Le disque et le tonneau sont montés respectivement sur des axes verticaux et horizontaux. Les rotations du disque et du tonneau sont contrôlées par deux moteurs indépendants capables de tourner dans les deux sens. Il s'agit d'une caractéristique obligatoire pour cette étude où une large gamme de SRR est étudiée. La position de l'axe horizontal sur lequel le tonneau est monté est contrôlée par un bras de levier, un ressort et une plaque de manière à ce que le tonneau puisse être poussé vers le haut en direction du disque. De cette manière, la charge normale est ajustée avec précision.

La mesure d'épaisseur nécessite l'utilisation de disques transparents. Dans les expériences réalisées durant ce travail un disque en saphir chromé et un disque en verre (N-BK8) revêtu DLC semi-transparent sont utilisés. De plus, deux tonneaux sont utilisés dont un est revêtu DLC. La conductivité thermique du DLC est 10 fois plus faible que celle de l'acier, d'où l'importance d'étudier son effet thermique sur le contact. La géométrie des tonneaux produit un contact elliptique large.

Le lubrifiant est amené directement au contact par une buse et par l'entraînement du lubrifiant qui submerge partiellement la partie inférieure du tonneau, comme le montre la Figure 2b. Un thermocouple placé à une position fixe à l'intérieur du bain d'huile externe enregistre la température T_{ext} tout au long de l'expérience. Cependant, la température T_0 est difficile à connaître avec suffisamment de précision.

Banc d'essai Monocam

Un banc d'essai came-linguet-poussoir est utilisé pour étudier le frottement dans un contact came-linguet pour différentes configurations de surface (acier non revêtu ou acier revêtu DLC). Une partie du mécanisme est illustrée dans la Figure 3 où le lubrifient est projeté vers le point de contact entre la came et le linguet à travers un orifice dans le linguet. La température du lubrifient est contrôlé à l'entrée de culasse.

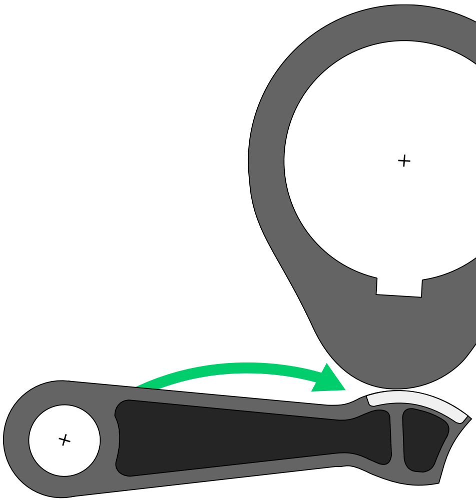

Figure 3: Illustration du mécanisme came-linguet avec la projection du lubrifiant vers le point du contact.

Au cours d'un cycle de rotation de la came, la variation des vitesses des surfaces par rapport au point du contact, la variation des rayons de courbure, et la variation de la charge normale sont calculées théoriquement. Ces grandeurs sont ensuite utilisées comme entrées pour le modèle numérique transitoire.

Une gamme de vitesses de rotation entre 350 tr/min et 2030 tr/min sont testées pour chaque configuration de surface. Trois configurations sont testées : came en acier/ linguet en acier, came en acier/ linguet en acier revêtu DLC, et came en acier revêtu DLC/ linguet en acier revêtu DLC.

Un système de mesure de couple est monté sur l'arbre à cames. Ce qui permet de mesurer le couple instantané dynamique durant un cycle de rotation. Ce couple est converti en force et coefficient de frottement par une approche d'analyse dynamique simplifiée du mécanisme (voir Annexe B).

3 Caractérisation du Lubrifiant

De manière à suivre une approche quantitative, une caractérisation rhéologique indépendante du lubrifiant en dehors du contact EHL est nécessaire. Le lubrifiant utilisé dans cette étude est une huile de moteur commerciale. La caractérisation rhéologique du lubrifiant a été réalisée au LaMCoS par Bouscharain [131]. La dépendance de la densité du lubrifiant de sa pression et sa température est exprimée par l'équation d'état de Tait [132]. La viscosité a été mesurée à l'aide de trois rhéomètres différents : viscosimètre basse pression, viscosimètre haute pression, et rhéomètre de Couette à haute pression. D'une part, un model WLF modifié est utilisé pour décrire la viscosité Newtonienne en termes de pression et température. D'autre part, le modèle Carreau-Yasuda modifié est utilisé pour décrire le comportement non-Newtonien du lubrifiant sous cisaillement. Les paramètres des modèles de viscosité ont été ajustés à la viscosité mesurée sur les instruments rhéologiques, indépendamment de tout test tribologique. Ces paramètres sont utilisés pour définir le lubrifiant dans les simulations numériques réalisées dans ce travail.

4 Approche Numérique

Il est rarement facile d'instrumenter les bancs d'essai expérimentaux pour recueillir des données et des connaissances sur les phénomènes physiques pertinents. Dans ce cas, les modèles numériques s'avèrent utiles. Les modèles numériques utilisés dans cette étude sont des modèles Eléments Finis basés sur l'approche du système complet, proposée pour la première fois par Habchi [30]. Wheeler [31] a ajouté la possibilité de simuler des contacts non circulaires. Raisin et al. ont inclus un solveur transitoire [32] et la possibilité de simuler des surfaces revêtues [33].

Géométries et équations

Un contact TEHL est décrit par un ensemble d'équations : l'équation de Reynolds (classique ou généralisée), l'équation de déformation élastique, l'équation d'équilibre des charges et l'équation d'énergie. Dans cette thèse, deux modèles numériques sont utilisés : l'un pour le contact elliptique (2D) et l'autre pour le contact linéique (1D). Chaque modèle est construit sur deux géométries illustrées dans la Figure 4. La géométrie 1 est utilisée pour résoudre la pression du lubrifiant, la déformation élastique du solide et l'équation d'équilibre de la charge. La géométrie 2 est utilisée pour résoudre l'équation d'énergie et calculer les variables d'intérêt à travers l'épaisseur du lubrifiant.

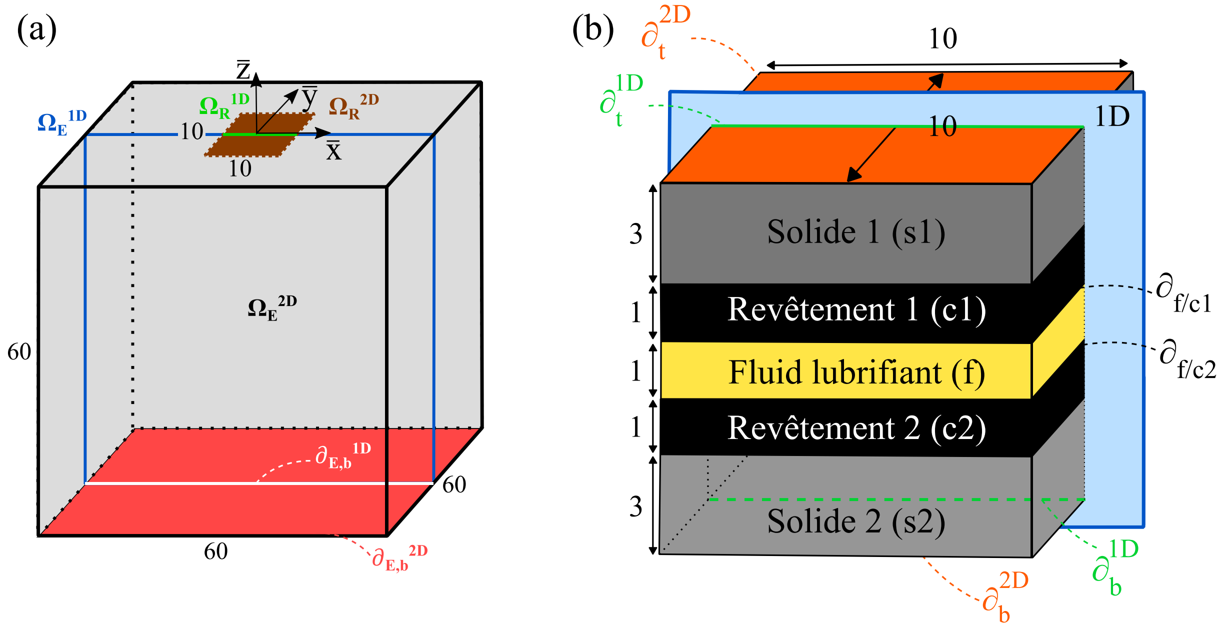

Figure 4: (a) Géométrie 1 permettant la résolution des équations d'élasticité et de Reynolds généralisée. La géométrie 1D est obtenue en coupant la géométrie 2D en $\bar{y} = 0$. Les différents domaines sont désignés par la lettre grecque Ω avec les indices "R" et "E" correspondant respectivement aux domaines de Reynolds et aux domaines élastiques. En outre, les exposants "1D" et "2D" sont utilisés pour distinguer les domaines appartenant aux contacts 1D et 2D respectivement. Les limites des domaines élastiques sont indiquées par le symbole "∂". (b) Géométrie 2 permettant la résolution de l'équation d'énergie. La géométrie 1D est obtenue en coupant la géométrie 2D en $\bar{y} = 0$.

L'équation de Reynolds généralisée permet la variation de la viscosité et de la densité à travers l'épaisseur de film. Ainsi, les fluides non-Newtoniens et les effets thermiques peuvent être modélisés. Elle a été dérivée pour la première fois dans [34] et peut être écrite sous la forme de l'équation (1) en se basant sur la forme donnée dans [139]. Elle est résolue sur le domaine Ω_R^{2D}

et Ω_R^{1D} respectivement, dans les modèles 2D et 1D. Les termes correspondant à la direction y sont supprimés de cette équation dans le modèle 1D.

$$\frac{\partial}{\partial x}\left[\left(\frac{\rho}{\eta}\right)_e \frac{\partial p(x,y,t)}{\partial x}\right] + \frac{\partial}{\partial y}\left[\left(\frac{\rho}{\eta}\right)_e \frac{\partial p(x,y,t)}{\partial y}\right] - \frac{\partial}{\partial x}(\rho_x^*) - \frac{\partial}{\partial y}(\rho_y^*) - \frac{\partial}{\partial t}(\rho_e) = 0 \qquad (1)$$

Pour la forme détaillée des diffèrents termes le lecteur est invité à voir les équations (2.19) et (2.20) du Chapitre 2.

Une pression nulle est imposée aux limites de Ω_R^{1D} et Ω_R^{2D}. À la sortie du contact, une pression négative peut se produire. La méthode de pénalité présentée pour la première fois par Wu [140] est utilisée pour résoudre ce problème.

L'équation de déformation élastique (2) est résolue dans un domaine déformable désigné respectivement par Ω_E^{1D} et Ω_E^{2D} pour les modèles 1D et 2D de la Figure 4. Un module de Young et un ratio de Poisson équivalents sont affectées aux domaines déformables.

$$\nabla \cdot \boldsymbol{\sigma} = 0 \qquad (2)$$

avec $\boldsymbol{\sigma} = \boldsymbol{C}\boldsymbol{\epsilon}(u,v,w)$ étant le tenseur des contraintes exprimé en fonction du tenseur de rigidité $\boldsymbol{C}$ et du tenseur de déformation $\boldsymbol{\epsilon}$. Ce dernier est une fonction des déplacements u, v et w dans les directions x, y et z respectivement.

Le domaine élastique a une contrainte fixe à la limite inférieure $\partial_{E,b}^{1D}$ ou $\partial_{E,b}^{2D}$ dans les modèles 1D et 2D respectivement. Toutes les autres frontières sont libres. De plus, la pression p calculée par l'équation de Reynolds généralisée est appliquée à la frontière supérieure du domaine élastique. La résolution de (2) avec ces conditions aux limites donne le déplacement du domaine solide équivalent, $\delta(x,y,z=0,t) = w(x,y,z=0,t)$. δ représente la somme des déplacements des deux surfaces réelles.

En plus de l'équation de Reynolds et de l'équation de déformation élastique, **l'équation d'équilibre de la charge** (3) assure l'équilibre entre la pression hydrodynamique générée p et la charge normale w_n.

1D
$$\int_{\Omega_R^{1D}} p(x,t)dx = w_{1D}(t)$$

2D
$$\iint_{\Omega_R^{2D}} p(x,y,t)dxdy = w_{2D}(t) \qquad (3)$$

L'épaisseur de film de lubrifiant h peut être exprimée comme dans l'équation (4) où h_0 est le déplacement du corps rigide, δ est calculé par l'équation d'élasticité et les termes centraux représentent la géométrie équivalente de film lubrifiant.

1D
$$h(x,t) = h_0(t) + \underbrace{\frac{x^2}{2R_{eq}^{1D}}} + \delta(x,t)$$

Géométrie équivalente de film lubrifiant (4)

2D
$$h(x,y,t) = h_0(t) + \overbrace{\frac{x^2}{2R_{eq,x}^{2D}} + \frac{y^2}{2R_{eq,y}^{2D}}} + \delta(x,y,t)$$

L'équation d'énergie est résolue sur la géométrie 2 illustrée dans la Figure 4b. L'équation d'énergie peut être écrite sous une forme générale (5).

$$\rho_i Cp_i \left(\underbrace{\overrightarrow{u_i}\nabla T}_{advection} + \frac{\partial T}{\underbrace{\partial t}_{transitoire}} \right) - \underbrace{\nabla(k_i \nabla T)}_{conduction} = \underbrace{Q_i}_{source\ de\ chaleur} \tag{5}$$

Dans l'équation ci-dessus, l'indice "i" est remplacé par "s1", "s2", "c1", "c2" ou "f" pour représenter les propriétés ou les variables dans chaque sous-domaine de la Figure 4b. Cette forme d'équation est utilisée dans le modèle 2D. Elle peut être utilisée dans le modèle 1D en supprimant les composantes y des différents termes.

D'une part, pour le domaine fluide ($i = f$), l'advection dans l'équation (5) dans la direction z est négligée. En revanche, l'advection domine la conduction de la chaleur dans les directions x et y. Par conséquent, seule la composante z du terme de conduction est utilisée dans l'équation (5). En outre, le terme source Q_i devient la somme de Q_s et Q_c qui représentent les sources de chaleur de cisaillement et de compression respectivement. D'autre part, pour les domaines solides, l'advection dans la direction z est négligée par rapport à l'advection dans le plan xy. Dans le cas des solides, la conduction peut se produire dans toutes les directions. Par conséquent, toutes les composantes du terme de conduction sont utilisées dans l'équation (5). En outre, le terme source Q_i est fixé à zéro étant donné qu'aucune chaleur n'est générée dans les domaines solides. Les propriétés des matériaux ρ_i, k_i et Cp_i dans chaque domaine sont remplacées par les propriétés du lubrifiant et des différents types de solides et de revêtements respectivement. Si aucun revêtement n'est utilisé, les propriétés thermiques des solides 1 et 2 sont appliquées aux revêtements 1 et 2 respectivement.

La température ambiante T_0 est imposée aux frontières ∂_t^{2D} et ∂_b^{2D} dans le modèle 2D et aux frontières ∂_t^{1D} et ∂_b^{1D} dans le modèle 1D. En outre, la même température T_0 est imposée aux frontières latérales, désignées par ∂_i, si le matériau (solide ou fluide) se déplace vers le centre de contact. En pratique, ces conditions aux limites reflètent l'idée que le matériau entrant dans le contact est à la température ambiante T_0. En revanche, la température du lubrifiant ou des solides sortant du contact est dictée par ce que le matériau subit au cours de sa traversée du contact. Par ailleurs, le flux de chaleur par conduction est conservé dans la direction z à travers les interfaces fluide/revêtement et revêtement/solide

Effets transitoires : Le temps caractéristique associé à un phénomène indique quand ce phénomène atteint un état stable après une fluctuation. Les auteurs de [32] ont constaté que les temps caractéristiques associés à l'écoulement hydrodynamique du fluide et aux effets thermiques sont beaucoup plus longs que les temps caractéristiques associés à d'autres phénomènes tels que l'élasticité des solides. C'est pourquoi les effets transitoires sont pris en compte dans l'équation de Reynold généralisée et l'équation de l'énergie, mais pas dans l'équation d'élasticité.

Calcul du coefficient de frottement : On suppose qu'il n'y a pas de glissement aux interfaces fluide/revêtement, que les surfaces sont lisses et que la séparation des films est totale. Il n'y a donc pas de régime de lubrification mixte ou limite. Le coefficient de frottement numérique est calculé par les équations (6) et (7) dans les modèles 1D et 2D respectivement.

1D

$$C_f = \frac{\int_{\partial_{f/c1}^{1D}} \tau_{zx}\, dx + \int_{\partial_{f/c2}^{1D}} \tau_{zx}\, dx}{2 \times w_{1D}} \tag{6}$$

2D

$$\begin{gathered} C_{f,x} = \frac{\iint_{\partial_{f/c1}^{2D}} \tau_{zx}\, dxdy + \iint_{\partial_{f/c2}^{2D}} \tau_{zx}\, dxdy}{2 \times w_{2D}} \\ C_{f,y} = \frac{\iint_{\partial_{f/c1}^{2D}} \tau_{zy}\, dxdy + \iint_{\partial_{f/c2}^{2D}} \tau_{zy}\, dxdy}{2 \times w_{2D}} \end{gathered} \tag{7}$$

avec τ_{zx} et τ_{zy} les contraintes de cisaillement calculées dans le domaine du fluide au niveau des frontières $\partial_{f/c1}$ et $\partial_{f/c2}$. L'intégration de ces grandeurs permet d'obtenir la force de frottement aux limites supérieure et inférieure du domaine fluide. Enfin, la force de frottement moyenne est divisée par la charge normale pour obtenir le coefficient de frottement.

Mise en œuvre du modèle numérique

Les équations sont mises en œuvre sous leur forme adimensionnelle dans COMSOL 5.5 [141], un logiciel commercial multi-physique d'analyse par éléments finis. Ces équations (couplées et non-linéaires) sont ensuite résolues par une méthode de Newton-Raphson jusqu'à ce que la convergence soit atteinte. Le même modèle peut être utilisé pour des simulations paramétriques stationnaires où les différentes conditions d'essai (SRR, charge normale, etc.) sont fournies comme paramètres à balayer ou pour des simulations transitoires lorsque les conditions de contact changent au fil du temps (par exemple, pour la simulation d'un contact came-linguet). Dans ce cas, l'évolution de différentes variables dans le temps peut être étudiée.

La résolution numérique d'un problème TEHL non newtonien permet d'obtenir un grand nombre de résultats : le profil d'épaisseur de film et les distributions de pression de lubrifiant sur les domaines de Reynolds Ω_R^{1D} et Ω_R^{2D}, le coefficient de frottement, le transfert de chaleur et la distribution de la température dans les différentes parties du système sont aussi accessibles en résolvant l'équation de l'énergie. De plus, les variables telles que la vitesse, la viscosité, la contrainte de cisaillement et le taux de cisaillement sont obtenues en tout point des domaines fluides 2D ou 3D (Figure 4b).

5 Contact TEHL : du roulement pur au glissement opposé

La capacité de la modélisation quantitative TEHL (impliquant une caractérisation rhéologique indépendante d'un lubrifiant commercial) à prédire simultanément l'épaisseur de film et le coefficient de frottement est évaluée dans chapitre 3. Une double approche expérimentale et numérique est utilisée, dans laquelle les mesures et les prédictions sont comparées sur une gamme relativement large de conditions de glissement, allant du roulement pur au glissement opposé. En outre, l'approche numérique est utilisée pour étudier les effets simultanés de conditions de fonctionnement variables sur l'épaisseur de film et le coefficient de frottement dans un contact TEHL. Enfin, une expression semi-analytique impliquant le taux de glissement SRR est proposée pour estimer l'épaisseur minimale de film dans un contact linéique TEHL.

Une double approche expérimentale et numérique : surfaces thermo-conductrices

D'une part, des expériences sont menées sur le tribomètre tonneau-sur-disque à glissement variable (SRR entre 0 et 4). Les autres conditions opératoires sont fixes. Le disque en saphir et le tonneau en acier sont utilisés pour représentés des surface thermo-conductrices. D'autre part, des simulations correspondantes aux même conditions sont réalisées avec le modèle numérique du contact linéique (1D) en respectant une équivalence entre la géométrie réelle du contact elliptique (2D) et la géométrie approximé (1D). Pour plus de détails voire l'Annexe C.

Comme indiqué précédemment, il est difficile de connaître la température d'entrée du lubrifiant T_0 avec suffisamment de précision. Cette valeur est estimée en comparant la mesure de l'épaisseur de film et l'estimation de cette dernière au début de l'essai par une expression classique (pour plus de détails voire l'Annexe D). De cette manière, T_0 est estimé à 39°C au début des expériences. Cette valeur est utilisée comme température d'entrée dans les simulations numériques correspondantes.

Les résultats simultanés de l'épaisseur minimale sur la ligne centrale $h_{m,c}$ et du coefficient de frottement sont présentés respectivement dans la Figure 5a et la Figure 5b. Les mesures expérimentales et les prédictions numériques sont indiquées.

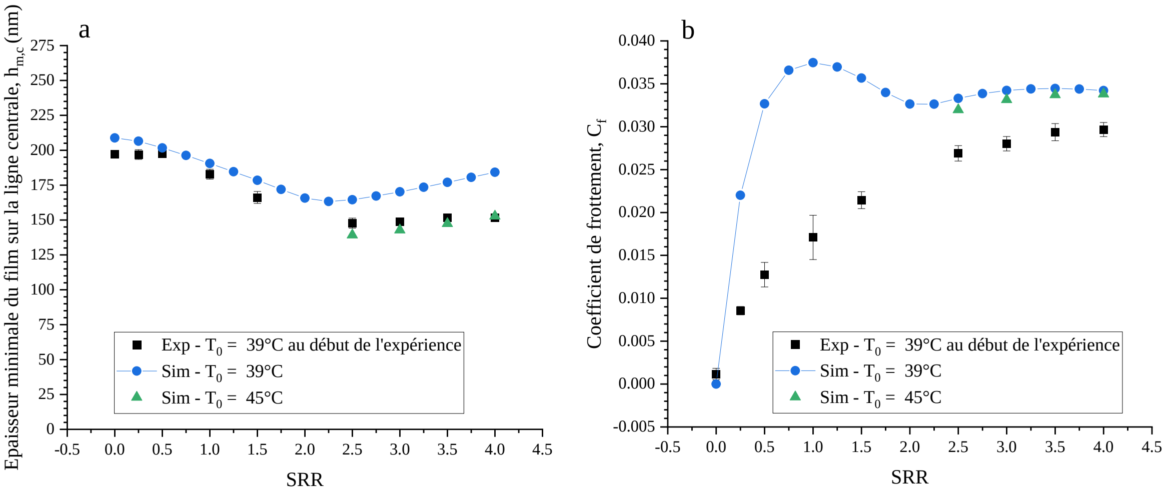

Figure 5: (a) Variation de l'épaisseur minimale de film sur la ligne centrale $h_{m,c}$ avec SRR. Quelques résultats de simulation à $T_0 = 45°C$ sont également montrés. (b) Variation du coefficient de frottement avec SRR. Les conditions opératoires sont $p_{Hz}^{2D} = 504\ MPa$, $T_{ext} = 45°C$, et $u_e = 1\ m/s$.

L'épaisseur de film minimale diminue avec l'augmentation de SRR de 0 à 2. Ce comportement s'explique par le comportement rhéofluidifiant et l'augmentation de la température du lubrifiant dans la région d'entrée en raison de l'échauffement par cisaillement. La condition de glissement pur ($SRR = 2$) constitue un point d'inflexion pour la variation de l'épaisseur de film avec SRR dans le cas des surfaces thermo-conductrices. Pour $2 < SRR \leq 4$, les mesures montrent une augmentation de $h_{m,c}$ avec l'augmentation du SRR. Ceci est due à l'effet « viscosity wedge » caractériser par la présence d'un « dimple » dans la zone centrale du contact, observé expérimentalement et numériquement. On notera que le modèle numérique peut prédire quantitativement la forme du profil d'épaisseur de film et la valeur de $h_{m,c}$ à fort glissement ($SRR > 2$) lorsqu'une température d'entrée plus élevée est considérée. Ceci est due à une accumulation de chaleur au cours de l'essai qui fait que la température ambiante du contact vers la fin de l'essai est plus élevée que celle du début de l'essai.

Pour un SRR compris entre 0 et 2, l'écart en frottement entre les prédictions numériques et les mesures provient principalement de l'ignorance du phénomène de contrainte de cisaillement limite (limiting shear stress, LSS) dans le modèle ainsi que de l'utilisation d'un modèle de contact linéique pour représenter un contact elliptique. En revanche, pour $2 < SRR \leq 4$, les prédictions de frottement sont proches des mesures. Cela confirme la prédominance des effets thermiques et non-Newtoniens sur l'effet LSS à fort glissement.

Effets de changement des conditions opératoires

L'effet des conditions de fonctionnement simultanément sur l'épaisseur de film EHL et le coefficient de frottement simultanément, en particulier en cas de glissement extrême (par exemple, $SRR > 2$) est quasiment absent de la littérature. Les effets de la température d'entrée du lubrifiant, de la charge normale et de la vitesse d'entraînement sur l'épaisseur de film et le coefficient de frottement sont étudiés grâce au modèle numérique du contact linéique.

Les conditions de fonctionnement testées sont résumées dans la légende de la Figure 6 qui montre la variation de l'épaisseur minimale de film et du coefficient de frottement avec SRR pour les différentes conditions testées.

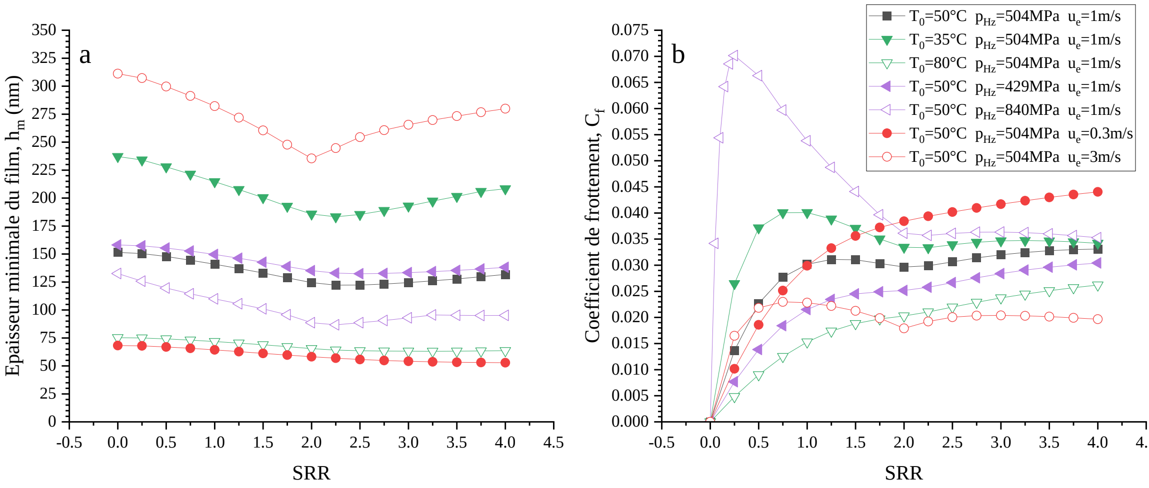

Figure 6: Variations (a) de l'épaisseur minimale de film et (b) du coefficient de frottement avec SRR. Les différentes conditions de fonctionnement sont représentées en couleurs et le cas de référence en noir.

D'une part, il a été constaté dans la Figure 6a que la température d'entrée et la vitesse d'entraînement influencent largement l'épaisseur minimale de film d'un point de vue qualitatif et quantitatif. Pour une température d'entrée plus basse ou une vitesse d'entraînement plus élevée, l'épaisseur minimale de film a tendance à augmenter pour un SRR donné. En outre, les effets thermiques et non-Newtoniens, qui contrôlent la variation de l'épaisseur minimale de film en fonction de SRR, deviennent plus prononcés pour une température plus basse ou une vitesse plus élevée. Il en résulte un taux de diminution plus rapide avec le SRR entre 0 et 2 et un taux d'augmentation plus rapide avec le SRR entre 2 et 4 (grâce à l'effet « viscosité wedge »). D'autre part, les effets de la variation de la charge normale (ou de la pression hertzienne maximale) sur l'épaisseur minimale de film sont plus faibles que les effets de la température d'entrée ou de la vitesse d'entraînement, comme l'indiquent les modèles semi-analytiques classiques de la littérature [151]. L'augmentation de la charge normale entraîne une diminution de l'épaisseur minimale de film pour un SRR donné.

En revanche, la Figure 6b montre que la variation de la charge normale a une influence significative sur le frottement, en particulier pour $0 \leq SRR \leq 2$, en raison de la forte dépendance viscosité-pression lorsque les effets thermiques et non-Newtoniens sont faibles. Dans les simulations actuelles, le coefficient de frottement est surestimé dans certaines conditions car le comportement "LSS" n'est pas pris en compte. Lorsque le SRR augmente au-delà de 2, l'influence de la modification de la charge devient moins importante. Pour un SRR donné, l'augmentation de la charge augmente le coefficient de frottement. De plus, à faible SRR ($SRR \leq\ 2$), la viscosité est très sensible aux changements de température. Ainsi, une augmentation de la température d'entrée diminue la viscosité et, par conséquent, le coefficient de frottement à un SRR donné. De plus, l'impact de la variation de la vitesse d'entraînement est moins important pour les faibles SRR ($SRR \leq 0{,}75$) en raison des faibles effets thermiques et rhéofluidifiant. Cependant, dès que SRR augmente, une différence remarquable dans le coefficient de frottement est observée entre les cas avec différentes vitesses d'entraînement en raison de la dominance des effets thermiques et rhéofluidifiant. Pour $SRR \geq 1$, le coefficient de frottement est plus faible pour une vitesse d'entraînement plus élevée à un SRR donné.

D'une manière générale, à glissement opposé, l'épaisseur de film dépend surtout des conditions du lubrifiant dans les zone convergentes (du part et d'autre du contact). En revanche, le coefficient de frottement dépend des conditions au centre du contact.

Expression semi-analytique

Des résultats numériques à différentes condition de fonctionnement (221 simulations au total) sont utilisés pour créer une expression semi-analytique pour l'estimation de l'épaisseur minimale de film dans le cas d'un contact linéique (1D) à SRR élevé. La vitesse d'entraînement, la charge normale, la température d'entrée et le SRR sont variés tout en gardant la géométrie et les matériaux inchangés. Dans les cas simulés :

$$U \in [2.41 \times 10^{-12}, 2.41 \times 10^{-11}] \qquad G \in [4184, 5614]$$

$$W_{1D} \in [1.33 \times 10^{-5}, 5.11 \times 10^{-5}] \qquad SRR \in [0, 4]$$

avec U, G, et W_{1D} les paramètres adimensionnés de Dowson et Higginson [23] utilisés classiquement dans les expressions d'estimation d'épaisseur minimale de film lubrifiant dans le contact EHL.

Dans un premier temps l'épaisseur minimale de film est estimée par une expression classique (Dowson [151] par example) en roulement pur ($SRR = 0$). Cette valeur devrait être corrigé pour prendre en compte les effets non-Newtoniens ($H_{m,corr}$). Enfin, l'expression (8) peut être utilisé pour estimer l'épaisseur minimale adimensionné H_m^* à SRR entre 0 et 4.

$$H_m^* = \begin{cases} H_{m,corr} - SRR^a U^b G^c W^d, & 0 \leq SRR \leq 2 \\ H_{m,corr} - 2^a U^b G^c W^d + (SRR-2)^{a'} U^{b'} G^{c'} W^{d'}, & 2 < SRR \leq 4 \end{cases} \tag{8}$$

L'épaisseur minimale de film est calculée à partir de H_m^* et du rayon de courbure R par l'expression $h_m = H_m^* \times R$. Les paramètres de l'expression (8) sont ajustés pour avoir la meilleure adéquation aux données numériques et leurs valeurs sont les suivantes :

$a = 1.390, \qquad b = 0.967, \qquad\qquad a' = 1.192, \qquad b' = 2.535,$

$c = 1.915\,, \qquad d = 0.530, \qquad\qquad c' = 7.256, \qquad d' = 1.207$

Cette expression a été validée par rapport à des mesures expérimentales et à des expressions similaires dans la littérature. Cependant, la précision de l'expression semi-analytique n'est pas garantie dans des conditions trop éloignées de celles utilisées pour la créer.

6 Contact TEHL : rôle des surfaces thermiquement isolantes

Dans un premier temps, la capacité prédictive du modèle numérique est évaluée pour un contact TEHL avec des surfaces thermiquement isolantes par une double approche expérimentale et numérique similaire à celle présentée dans la section précédente. Ensuite, l'effet de l'utilisation de revêtements DLC est étudié simultanément sur l'épaisseur de film et le coefficient de frottement dans un contact TEHL linéique. Enfin, les effets de la variation de la conductivité thermique du revêtement et de son épaisseur sur l'épaisseur de film de lubrifiant et le coefficient de frottement sont explorés.

Une double approche expérimentale et numérique : surfaces thermiquement isolantes

Des essais sont réalisés sur le tribomètre tonneau-sur-disque avec le tonneau en acier revêtu DLC et le disque en verre revêtu DLC. Les résultats sont présentés dans la Figure 7. Ils montrent que le modèle est capable de prédire l'épaisseur de film à glissement faible. En revanche, à glissement élevé, le modèle surestime l'épaisseur probablement à cause du réchauffement des surfaces au cours de l'essai (les simulations à $T_0 = 50°C$ sont en accord avec les mesures). L'effet « viscosity wedge » est atténué, et contrairement au cas des surfaces thermo-conductrices, l'épaisseur minimale de film n'augmente pas en augmentant SRR entre 2 et 4. Ceci s'explique par l'absence de « viscosity wedge » dans ce cas.

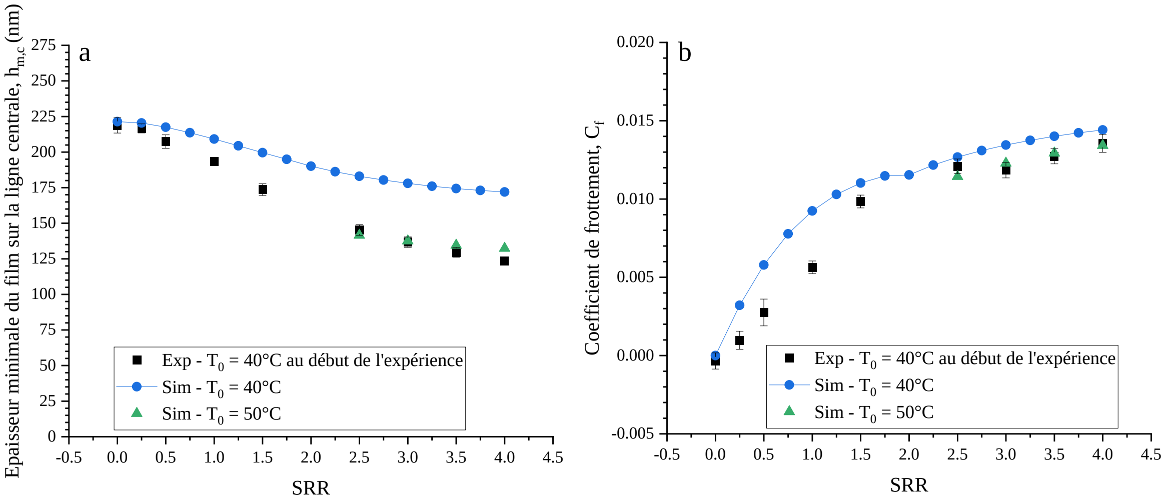

Figure 7: (a) Variation de l'épaisseur minimale de film sur la ligne centrale $h_{m,c}$ avec SRR. Quelques résultats de simulation à $T_0 = 50°C$ sont également montrés. (b) Variation du coefficient de frottement avec SRR. Les conditions opératoires sont $p_{Hz}^{2D} = 276\ MPa, T_{ext} = 45°C$, et $u_e = 1\ m/s$.

Les simulations surestiment le coefficient de frottement pour toutes les conditions de glissement, mais la surestimation dans la plage $SRR < 1.5$ n'est pas aussi importante que dans le cas des matériaux conducteurs illustrés à la Figure 5b. La pression du lubrifiant est relativement faible dans le cas des surfaces isolantes car la pression Hertzienne maximale est faible par rapport au cas des surfaces conductrices (276 MPa pour la première contre 504 MPa pour la seconde).

Dans l'ensemble, le modèle numérique peut capturer des mécanismes physiques complexes qui dépendent des propriétés thermiques des surfaces en contact et peut prédire quantitativement le coefficient de frottement et l'épaisseur de film lorsque l'augmentation de la température dans les expériences au fil du temps est prise en compte dans les simulations.

Rôle du revêtement DLC dans un contact TEHL linéique

Des études précédentes [119-121, 123] traitant l'effet du revêtement DLC dans les contacts TEHL se limitaient à un faible glissement ($SRR < 1$) où l'épaisseur de film n'est pas une préoccupation de premier ordre. Habchi [165] a montré numériquement que le coefficient de frottement dans les contacts EHL peut être réduit en utilisant des revêtements à faible inertie thermique sans affecter l'épaisseur de film. Cela est vrai pour des SRR allant jusqu'à 0.5 (la plage explorée dans [165]). À la connaissance de l'auteur, la littérature manque d'une étude de l'effet des revêtements thermiquement isolants simultanément sur l'épaisseur de film et le frottement dans des conditions allant du roulement pur au glissement opposé. Cette section résume les résultats d'une étude numérique dans un contact linéique (1D) de l'effet d'un revêtement DLC a-C:H sur une large gamme de conditions de glissement ($0 \leq SRR \leq 5$). Un contact acier-acier est considéré comme un cas de référence pour comparer avec le cas des surfaces revêtues DLC. Le DLC à une épaisseur de 2.8 μm et une conductivité thermique de 2.2 $W/m.K$ tandis que pour l'acier la conductivité est de 21 $W/m.K$.

La Figure 8 regroupe les variations de l'épaisseur minimale de film et de coefficient de frottement avec SRR pour les cas de surfaces revêtues DLC et non revêtues.

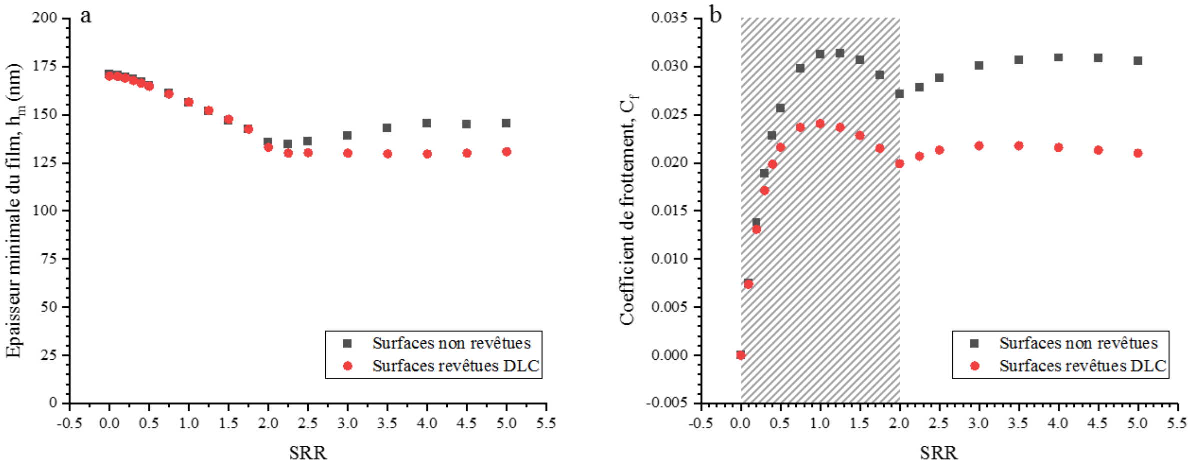

Figure 8: Variation (a) de l'épaisseur minimale de film et (b) du coefficient de frottement en fonction du SRR de 0 à 5 pour les surfaces non revêtues (en noir) et les surfaces revêtues de DLC (en rouge). Résultats issus du modèle numérique pour les conditions opératoires $p_{Hz}^{2D} = 500\ MPa, T_0 = 45°C$, et $u_e = 1\ m/s$

Les résultats sont en accord avec les études de la littérature [118,120,166] en ce qui concerne la réduction du frottement par l'utilisation d'un mince revêtement thermo-isolant dans les contacts

EHL fonctionnant dans des conditions de glissement-roulement. En outre, dans ces conditions ($SRR < 2$), l'épaisseur de film n'est pratiquement pas affectée par la présence du revêtement. Cependant, cette conclusion n'est pas applicable aux contacts fonctionnant dans des conditions de glissement opposées ($SRR > 2$) où les résultats montrent que l'utilisation des revêtements DLC conduit non seulement à une diminution du frottement (d'environ 30 % dans certains cas), mais également à une diminution de l'épaisseur de film (jusqu'à 10 %).

La Figure 9 résume les mécanismes par lesquels un revêtement à faible conductivité thermique peut entraîner simultanément une réduction du coefficient de frottement et de l'épaisseur de film dans les contacts EHL fonctionnant dans des conditions de glissement opposées ($SRR > 2$).

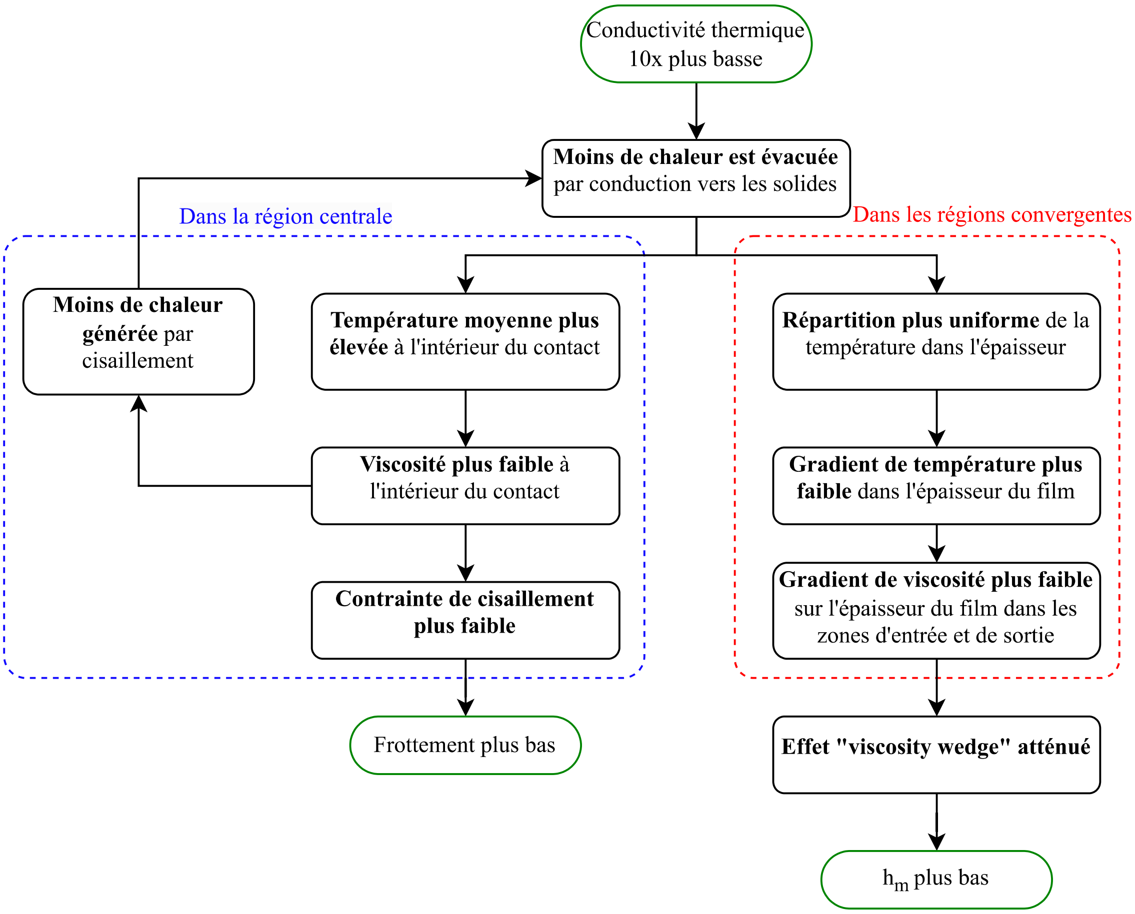

Figure 9: Mécanisme de réduction de coefficient de frottement et d'épaisseur de film par un revêtement DLC à faible conductivité thermique.

Le revêtement isolant à faible conductivité thermique entrave l'évacuation de la chaleur générée par le cisaillement du fluide vers les substrats solides plus froids. D'une part, l'isolation entraîne une augmentation de la température du lubrifiant, ce qui diminue sa viscosité. En conséquence, la contrainte de cisaillement et le coefficient de frottement diminuent par rapport au cas non revêtu. D'autre part, l'isolation thermique rend la distribution de la température plus uniforme sur l'épaisseur de film dans les zones d'entrée et de sortie, ce qui réduit le gradient de température et le gradient de viscosité sur l'épaisseur de film. Ainsi, l'effet « viscosity wedge » est atténué et l'épaisseur minimale de film diminue par rapport au cas sans revêtement. Les résultats montrent que dans des conditions de glissement opposées, non seulement le coefficient de frottement est réduit en raison de l'utilisation d'un revêtement thermo-isolant, mais aussi l'épaisseur de film. Il faut donc tenir compte de la perte d'épaisseur de film lors de l'application d'un revêtement thermo-isolant pour réduire le frottement dans les applications fonctionnant dans des conditions de glissement extrêmes ($SRR > 2$).

Influence de la conductivité thermique et de l'épaisseur des revêtements thermo-isolants

Les influences de l’épaisseur du revêtement h_{coat} et de sa conductivité thermique k sur la réduction de frottement et d’épaisseur de film du lubrifiant sont exploré grâce au modèle numérique. En plus du cas de référence ($h_{coat} = 2.8\,\mu m$; $k = 2.2\,W/m.K$), des simulations réalisées au différentes épaisseurs de revêtement ($h_{coat} \in \{0.2, 0.5, 1, 5, 10\}\,\mu m$) et pour différentes conductivité ($k \in \{0.2, 0.4, 0.7, 1, 5, 10\}\,W/m.K$) permettent d’identifier et de quantifier cette influence.

La Figure 10 montre la distribution la température dans le lubrifiant à l'intérieur du contact pour trois cas de conductivité thermique du DLC et le cas des surfaces non revêtues. La Figure 11 complète en montrant l’influence de différentes épaisseurs de revêtement.

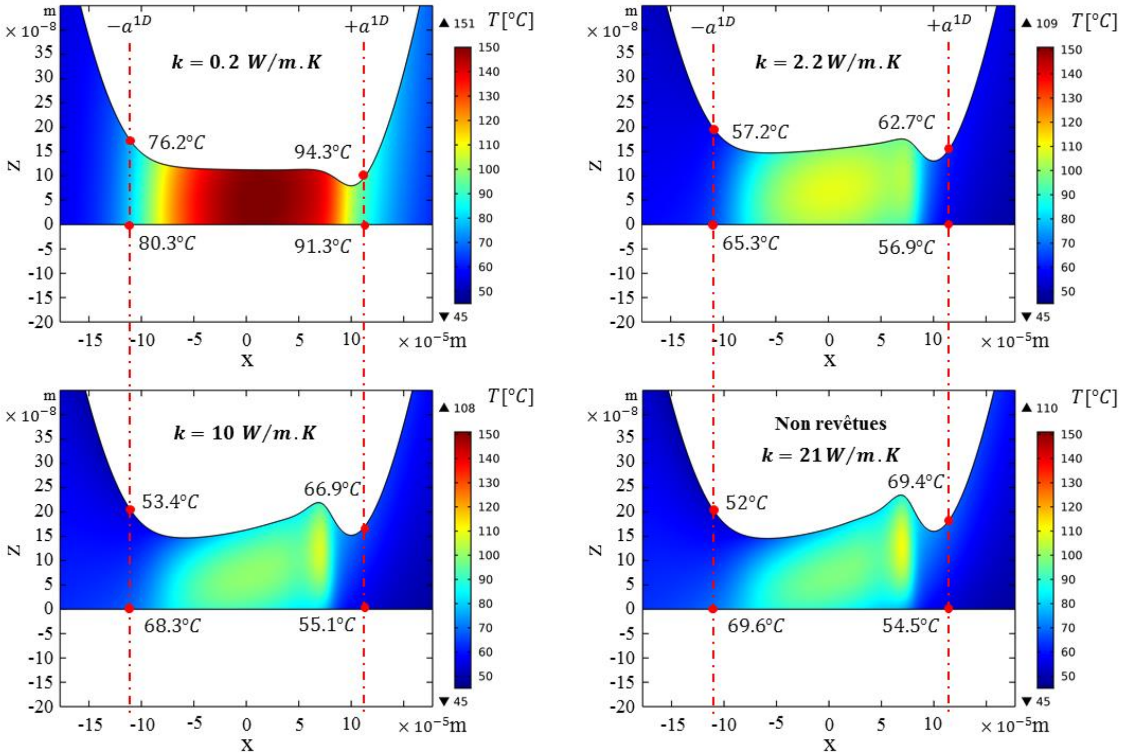

Figure 10: Distribution de la température dans le lubrifiant à l'intérieur du contact pour trois cas de conductivité thermique ($k = 0{,}2$, $2{,}2$ et $10\ W/m.K$) et le cas des surfaces non revêtues à $SRR = 5$ et $h_{coat} = 2.8\mu m$.

Pour des conductivités thermiques élevées ou des épaisseurs de revêtement faibles, les épaisseurs de film et les distributions de températures sont similaires à celles du cas non revêtu. En revanche, pour un k faible et un h_{coat} élevé, ces deux paramètres jouent un rôle important dans la régulation de la dissipation de la chaleur du fluide chaud vers les solides plus froids et influencent de manière significative la distribution de température dans le contact et celle du lubrifiant entrant dans le contact et donc sa viscosité et l'épaisseur de film de lubrifiant qui en résulte. L'effet « viscosity wedge » et plus faible pour une conductivité thermique moins élevée.

Le coefficient de frottement est principalement contrôlé par la viscosité et le taux de cisaillement du lubrifiant dans la région centrale du contact. Il est donc très différent pour les cas de revêtement ayant une conductivité thermique ou une épaisseur différente. Pour un SRR donné, le coefficient de frottement est plus faible dans le cas où k est plus faible suivant les mécanismes résumés dans la Figure 9. De même, si le revêtement est plus épais, l'isolation thermique est plus importante, ce qui diminue le coefficient de frottement.

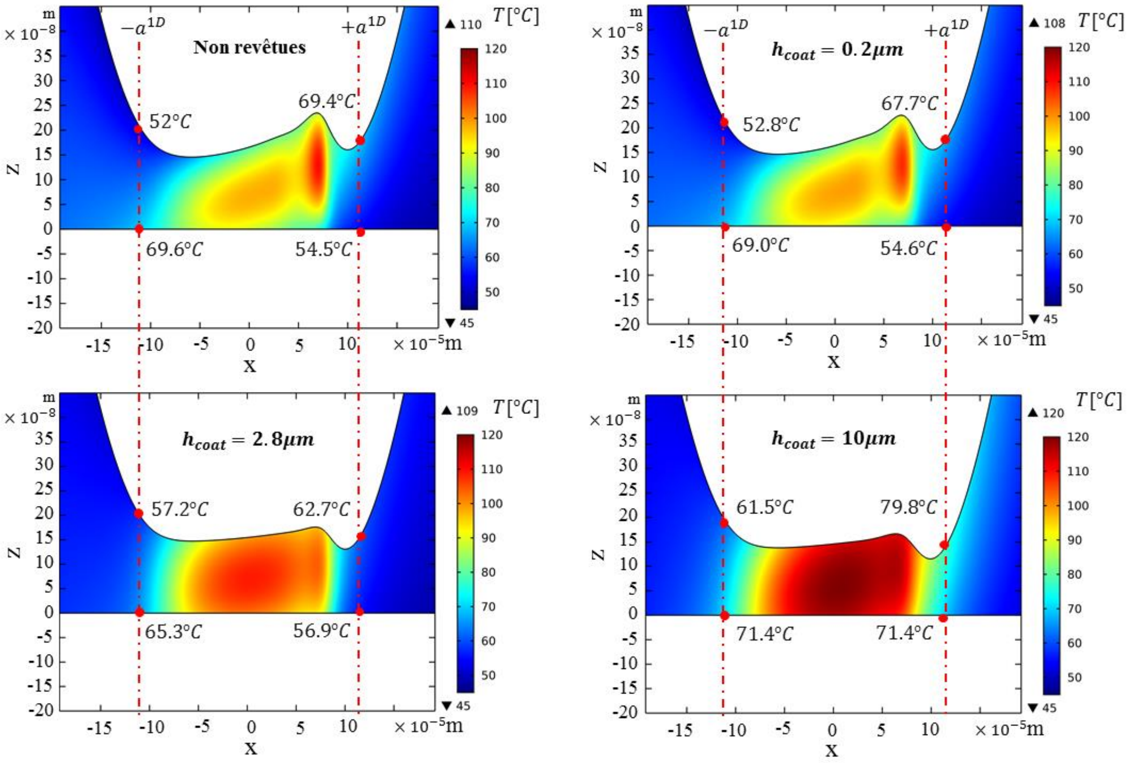

Figure 11: Distribution de la température dans le lubrifiant à l'intérieur du contact pour trois cas d'épaisseur de revêtement ($h_{coat} = 0{,}2{,}2{,}2{,}8$, et 10 μm) en plus du cas des surfaces non revêtues à $SRR = 5$ et $k = 2.2\ W/m.K$

L'influence de h_{coat} et k est quantifiée par des facteurs de correction de l'épaisseur minimale de film de lubrifiant et de coefficient de frottement à fort glissement. Des expressions semi-analytiques de ces facteurs de corrections dépendent des paramètres adimensionnels $\bar{h}_{coat} = \frac{h_{coat}}{R}$ et $\bar{k} = \frac{k}{C_p \rho u_e R}$ définies dans l'Annexe E. L'expression (9) représente le facteur de correction de l'épaisseur minimale de film de lubrifiant applicable pour des SRR entre 2 et 4.

$$\varphi_{coat} = \frac{H_m(\bar{k}, \bar{h}_{coat}, SRR)}{H_m(Non\ revêtu, SRR)} = \begin{cases} 1 - 0.021\left(\frac{\bar{h}_{coat}}{\bar{k}}\right)^{0.481} \times (SRR-2), & \frac{\bar{h}_{coat}}{\bar{k}} \leq 2.55 \\ 1.06\left(\frac{\bar{h}_{coat}}{\bar{k}}\right)^{-0.0624} - 0.021\left(\frac{\bar{h}_{coat}}{\bar{k}}\right)^{0.481} \times (SRR-2), & sinon \end{cases} \quad (9)$$

L'expression (10) représente le facteur de correction de coefficient de frottement à SRR élevé ($3 \leq SRR \leq 5$) supposé indépendant de SRR.

$$\psi_{coat} = \frac{\sum_{SRR=3}^{5}\left(\frac{C_f\left(\bar{k}, \bar{h}_{coat}, SRR\right)}{C_f(Non\,rev\hat{e}tu, SRR)}\right)}{5} = \begin{cases} 1, & \frac{\bar{h}_{coat}}{\bar{k}} \leq 0.248 \\ 0.855\left(\frac{\bar{h}_{coat}}{\bar{k}}\right)^{-0.0352\ln\left(\frac{\bar{h}_{coat}}{\bar{k}}\right)-0.160}, & sinon \end{cases} \tag{10}$$

Les coefficients des expressions semi-analytiques sont choisis pour avoir le meilleur accord avec les simulations numériques.

Les expressions (9) et (10) permettent de cartographier la réduction de l'épaisseur minimale de film et la réduction du coefficient de frottement à fort glissement pour $k \in [0.1{,}10]\ W/m.K$ et $h_{coat} \in [0.1{,}10]\ \mu m$. La Figure 12 illustre l'influence combinée de k et de h_{coat} sur l'épaisseur minimale de film et le coefficient de frottement pour un cas de contact revêtu par rapport à un cas de contact non revêtu à $SRR = 4$. Les réductions sont calculées comme $1 - \varphi_{coat}$ et $1 - \psi_{coat}$ respectivement pour l'épaisseur minimale de film et le coefficient de frottement, et sont indiquées en pourcentage. La Figure 12 montre que les réductions de l'épaisseur de film et de frottement coexistent dans le cas de fort glissement dû au revêtement thermiquement isolant. La région où la réduction minimale de l'épaisseur de film est la plus importante correspond également à la réduction la plus importante du frottement. Par ailleurs, dans le cas de référence (indiqué par le carré noir dans la Figure 12), une diminution d'environ 30 % du coefficient de frottement s'accompagne d'une diminution d'environ 10 % de l'épaisseur minimale de film.

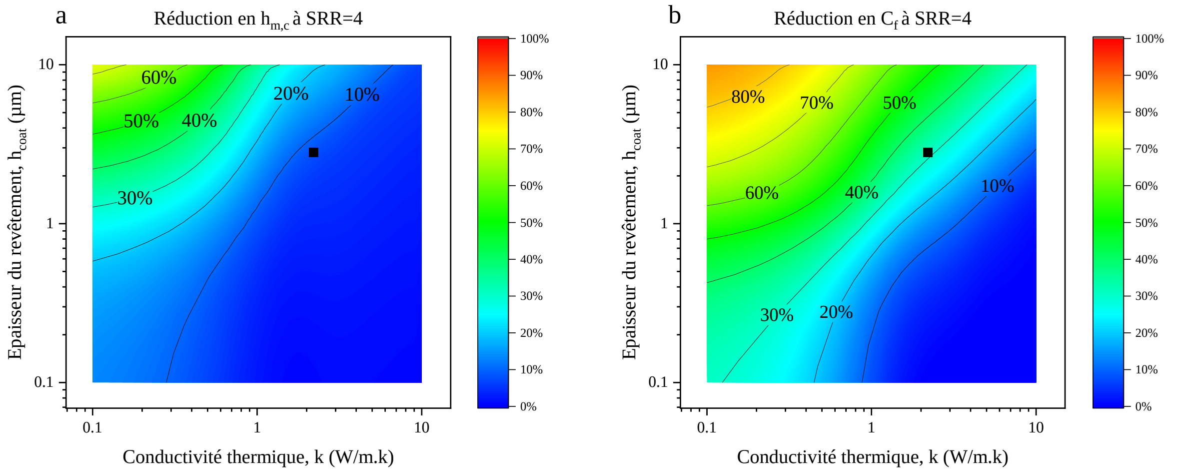

Figure 12: (a) Réduction de l'épaisseur minimale de film $1 - \varphi_{coat}$ et (b) réduction du coefficient de frottement $1 - \psi_{coat}$ due à l'utilisation d'un revêtement isolant de conductivité thermique k et d'épaisseur h_{coat} à $SRR = 4$. Les valeurs sont calculées à l'aide des expressions semi-analytiques (9) et (10).

7 Contact came-linguet : Effets des revêtements DLC sur les performances tribologiques

Les effets du revêtement DLC sur les performances d'un contact came-linguet sont étudiés expérimentalement à l'aide du banc d'essai Monocam et numériquement à l'aide d'une approche TEHL quantitative transitoire. Une large gamme de vitesses de rotation de l'arbre à cames est prise en compte (350 tr/min, à 2030 tr/min). Trois températures de lubrifiant à l'entrée ($25 \pm 2°C$, $50 \pm 1°C$, et $77 \pm 1°C$) et trois configurations de surfaces (Acier/Acier, Acier/DLC, et DLC/DLC) sont testées.

Les vitesses de rotation couvrent une large gamme de conditions correspondant à des régimes moteur compris entre 700 tr/min et 4060 tr/min, typiques d'un moteur à quatre temps de voitures de tourisme.

Le modèle numérique donne accès à la variation de l'épaisseur de film, de sorte que le paramètre d'épaisseur de film λ est calculé sur la base des résultats numériques et des mesures de rugosité après les expériences sur le banc d'essai Monocam. La Figure 13 représente la variation du paramètre d'épaisseur de film λ avec la vitesse de rotation de l'arbre à cames (axe de droite). Les variations du coefficient de frottement moyen obtenues expérimentalement et numériquement sont également représentées (axe gauche). Les résultats correspondant aux configurations acier/acier et DLC/DLC sont présentés respectivement en (a) et (b). La plage de λ suggère que le contact came-linguet fonctionne entre la lubrification mixte et la lubrification par film complet à la température intermédiaire (c'est-à-dire 50°C).

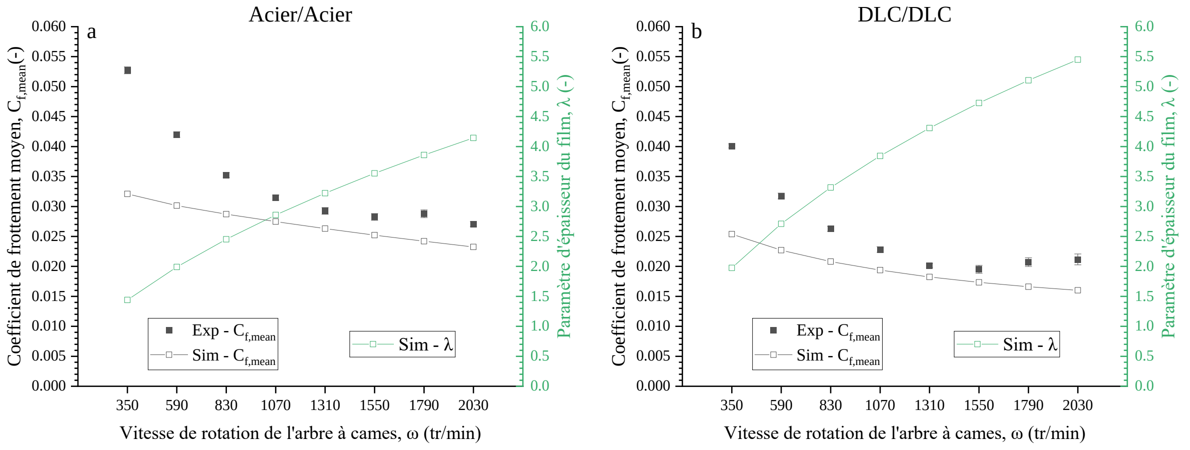

Figure 13: Variation, en fonction de la vitesse de rotation de l'arbre à cames, du coefficient de frottement moyen (axe de gauche) obtenu numériquement et expérimentalement, ainsi que de la variation du paramètre d'épaisseur de film (axe de droite) calculé sur la base de l'épaisseur minimale moyenne de film $h_{m,mean}$ à partir des simulations TEHL et des mesures de rugosité. Les résultats correspondant aux configurations Acier/Acier et DLC/DLC sont respectivement présentés en (a) et (b). Les expériences et les simulations sont réalisées à $T_{in} = 50 \pm 1°C$ et $T_0 = 50°C$ respectivement.

Les résultats de la Figure 13 ont montré que l'approche numérique peut prédire le frottement à 50°C avec une erreur acceptable (~13% de sous-estimation en moyenne) à des vitesses de rotation élevées ($\omega \geq 1310\ tr/min$) pour toutes les configurations de surface. En revanche, en raison des limites du modèle qui ne simule que les régimes de lubrification à film complet, l'erreur de prédiction a atteint environ 40 % à la vitesse de rotation la plus faible (350 tr/min). À faible vitesse de rotation, la réponse au frottement est principalement dictée par le frottement des aspérités plutôt que par le frottement fluide. Le modèle numérique n'est donc pas adapté à cette condition.

Le modèle numérique est exploité pour quantifier le transfert de chaleur en calculant les flux thermiques évacués de l'intérieur du contact dans différentes directions. Le flux thermique total q^*_{tot} est la somme des flux dans toutes les directions. La configuration DLC/DLC diminue considérablement q^*_{tot} par rapport à la configuration acier/acier en raison de l'effet d'isolation thermique. L'effet d'isolation thermique devient plus important à des vitesses de rotation plus élevées. Cela confirme l'idée d'utiliser le revêtement DLC pour ses propriétés thermiques dans les applications où le contact fonctionne à des vitesses élevées, comme dans le sport automobile par exemple.

Les expériences montrent que dans un régime de lubrification complète ou mixte, le contact revêtu DLC est plus performant que le contact non revêtu en termes de réduction du coefficient de frottement et de la perte de puissance. La Figure 14 montre la perte de puissance par frottement obtenue à partir d'expériences à différentes températures, pour différentes configurations de surface et trois vitesses de rotation (350, 1310 et 2030 tr/min).

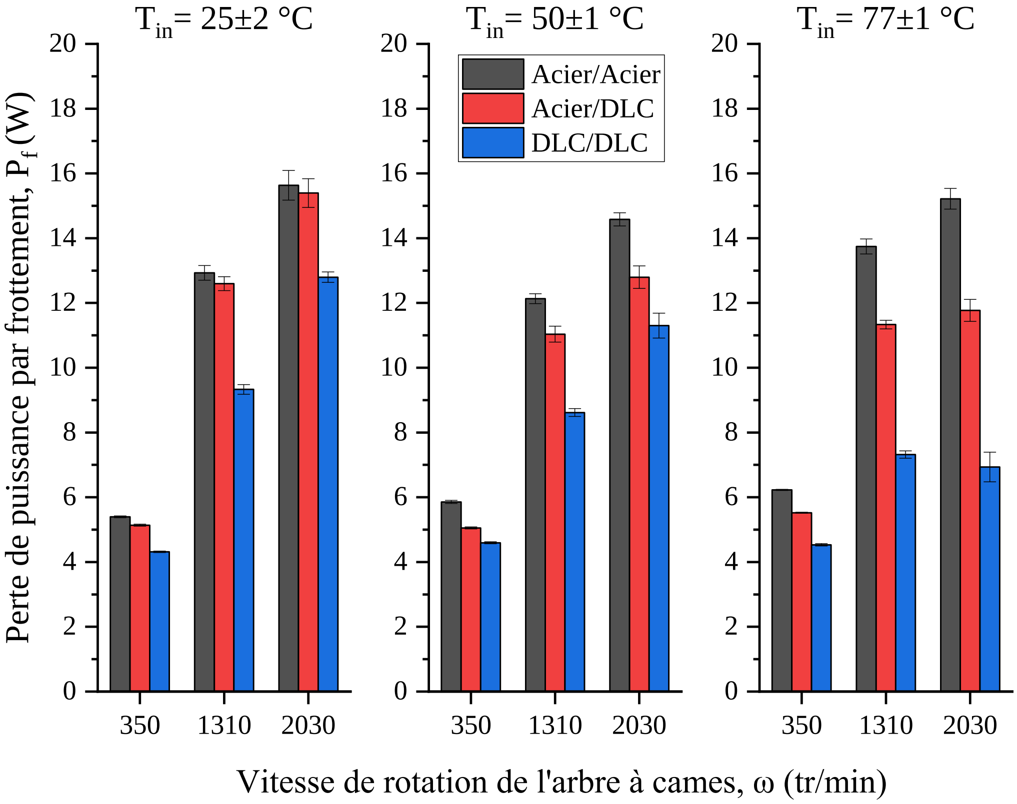

Figure 14: Perte de puissance par frottement P_f pour différentes configurations de surface à différentes vitesses de rotation pour différentes températures d'entrée du lubrifiant.

La diminution de la perte de puissance par frottement avec l'utilisation du DLC est dû à la contribution de trois mécanismes : le faible frottement d'aspérité du DLC, le paramètre d'épaisseur de film λ plus élevé (dans des conditions équivalentes) et l'effet d'isolation thermique. Par exemple, à une température d'entrée $T_{in} = 50°C$, la réduction du travail de frottement due aux revêtements sur les deux surfaces varie entre 22 % et 30 % en fonction de la vitesse de rotation de l'arbre à cames. Cette réduction est amplifiée lorsque la température du lubrifiant est plus élevée.

En outre, l'utilisation du revêtement DLC comme revêtement résistant à l'usure est démontrée par une comparaison des profils de surface pour différents linguets et cames utilisés au cours de la campagne expérimentale réalisée dans ce travail. Les surfaces en acier non revêtues présentaient des cicatrices d'usure importantes, alors que le revêtement DLC était presque intact, bien qu'elles aient été soumises aux mêmes conditions d'essai.

8 Conclusion

Dans les moteurs à combustion interne, la réduction du frottement et de l'usure des contacts lubrifiés augmente l'efficacité énergétique globale et la durée de vie des composants du moteur. Les revêtements DLC ont gagné en popularité dans les applications tribologiques ces dernières années en raison de leur capacité à réduire le frottement et l'usure. D'autre part, le remplacement d'une surface conductrice en acier par une surface isolante tel que le revêtement DLC modifie de manière significative le transfert de chaleur dans le film lubrifiant et les surfaces soumises à des applications à fort glissement telles que le contact came-linguet.

L'objectif principal de cette thèse est d'approfondir la connaissance des effets thermiques qui se produisent dans les contacts EHL dans des conditions de glissement élevé, en mettant l'accent sur le rôle des revêtements DLC thermiquement isolants.

Contributions

Les contributions de cette thèse au domaine de tribologie se résument par les points suivants :

- Le Chapitre 3 de cette thèse vise à étudier simultanément l'épaisseur de film et le frottement dans un contact elliptique large par une double approche expérimentale et numérique, depuis le roulement pur jusqu'aux conditions de glissement opposé. Les résultats mettent en évidence la capacité de l'approche quantitative de modélisation EHL à prédire à la fois l'épaisseur de film et le frottement, en particulier dans des conditions de glissement opposé. En outre, les effets de la variation des conditions de fonctionnement sont explorés et une expression semi-analytique est proposée, pour la première fois, pour prédire l'épaisseur minimale de film dans un contact linéique sur une large gamme de conditions de glissement ($0 \leq SRR \leq 4$).
- Le Chapitre 4 vise à approfondir la compréhension des effets thermiques des revêtements thermo-isolants sur l'épaisseur de film et le frottement simultanément dans un contact EHL, en particulier dans le cas de glissement élevé. Les résultats suggèrent que dans des conditions de glissement opposé ($SRR > 2$), cette réduction du frottement due à l'effet d'isolation thermique s'accompagne d'une diminution de l'épaisseur de film de lubrifiant en raison d'une atténuation de l'effet « viscosity wedge ». Ainsi, lorsque l'on utilise des revêtements thermo-isolants pour réduire le frottement, il faut être conscient que l'épaisseur de film peut également diminuer et que, par conséquent, le régime de lubrification peut passer à une lubrification mixte où le frottement peut augmenter en raison du contact entre aspérités. De plus, l'influence de la conductivité thermique et de l'épaisseur du revêtement est étudiée. Des expressions semi-analytiques de facteurs de correction pour l'épaisseur de film et le coefficient de frottement en cas de glissement élevé sont proposées.
- Le Chapitre 5 se concentre sur les effets des revêtements DLC sur les performances tribologiques d'un contact came-linguet. Les expériences sont réalisées sur un banc d'essai

imitant la géométrie et les conditions de fonctionnement des composants réels du moteur. En parallèle, des simulations ont été réalisées à l'aide d'une approche quantitative transitoire TEHL. Les résultats numériques suggèrent que dans la plupart des conditions de fonctionnement (vitesse de rotation faible à intermédiaire, et température intermédiaire à élevée), le contact fonctionne dans le régime de lubrification mixte. Cependant, dans le cas des surfaces revêtues DLC, le frottement reste inférieur à celui des surfaces en acier. Ce phénomène s'explique par le faible frottement de contact des aspérités avec le DLC par rapport aux contacts acier-acier conventionnels. En outre, les revêtements DLC offrent une meilleure résistance à l'usure que les surfaces en acier dans les mêmes conditions de fonctionnement. Les caractéristiques du matériau DLC génèrent à la fois moins de frottement et moins d'usure que le contact acier-acier.

Limitations

Les deux dispositifs expérimentaux utilisés dans la présente étude ont leurs limites. D'une part, dans le tribomètre tonneau-disque l'utilisation des disques transparents est nécessaires pour mesurer l'épaisseur de film par la technique optique DCI. Il n'a donc pas été possible de tester des configurations de surface telles qu'un disque en acier revêtu DLC et un tonneau. En revanche, un disque en saphir revêtu d'un DLC transparent a été utilisé. En outre, l'installation actuelle ne permet pas de mesurer avec précision la température du lubrifiant entrant dans le contact.

Le banc d'essai came-linguet-soupape permet de mesurer directement le couple de l'arbre à cames. Pour extraire les résultats du coefficient de frottement, une analyse dynamique simplifiée du mécanisme avec de nombreuses hypothèses est utilisée, ce qui ajoute une couche d'incertitude à ces résultats expérimentaux.

L'approche numérique présente également certaines limitations. Bien que le lubrifiant soit caractérisé par des mesures rhéologiques indépendantes, la description de son comportement dans le modèle numérique ne tient pas compte de l'effet dit de "contrainte de cisaillement limite" (limiting shear stress, LSS). Dans des conditions de roulement-glissement ($0 \leq SRR \leq 2$), le modèle numérique n'a pas été capable de prédire avec précision la réponse du frottement dans des cas à charge normale élevée.

L'environnement thermique du contact réel est beaucoup plus compliqué que celui modélisé ici avec une température constante imposée. Plusieurs modèles thermiques impliquant différentes échelles devraient être envisagés pour capturer le changement de température à l'entrée du contact en cas de glissement élevé.

Perspectives

Les travaux actuels ont contribués à la littérature en termes de frottement et d'épaisseur de film dans les contacts TEHL dans des conditions de glissement élevé avec l'effet thermique du revêtement isolant. Toutefois, certaines questions restent sans réponse et constituent un bon point de départ pour de futures recherches.

- Les modèles EHL basés sur le Eléments Finis tels que celui utilisé dans cette étude peuvent être complétés par une compréhension approfondie et une description précise de l'effet de contrainte de cisaillement limite. Pour ce faire, une caractérisation rhéologique indépendante hors contact pourrait être couplée à une simulation de dynamique moléculaire pour créer des modèles rhéologiques capables de capturer le plateau de frottement à un cisaillement modéré, en fonction de la pression et de la température [150]. Cette approche se limite cependant à des fluides simples.

- L'ajout d'un modèle de contact d'aspérité similaire à celui utilisé par Marian et al [124] permettra probablement d'obtenir des prédictions plus proches de la réalité dans les cas de lubrification mixte. Cependant, il faut être prudent dans le choix du "coefficient de frottement de contact d'aspérité" qui est influencé par les conditions de fonctionnement, les additifs de lubrifiant, le type de surfaces de contact, etc. Il est donc nécessaire de poursuivre les recherches à l'échelle des contacts d'aspérités en termes de déformation des aspérités individuelles et de frottement à cette échelle, où la composition chimique du lubrifiant et son interaction avec les surfaces ne peuvent pas être négligées.
- Les expressions semi-analytiques créées dans le présent travail sont applicables dans une gamme limitée de conditions de fonctionnement et pour un lubrifiant spécifique. Par conséquent, des études numériques plus complètes couvrant d'autres conditions de fonctionnement et d'autres lubrifiants sont nécessaires pour créer des expressions plus générales à l'aide de la même méthodologie que celle développée ici.
- L'approche numérique utilisée dans le présent travail et les expressions semi-analytiques pourraient être intégrées à des simulations dynamiques afin de fournir une meilleure description du comportement à grande échelle de systèmes complexes tels que le mécanisme came-linguet-soupape. Ceci pourra accélérer les phases de conception et d'optimisation de ces systèmes.

En conclusion, cette thèse a contribué au domaine de la tribologie en comblant les principales lacunes de la littérature et en faisant progresser la compréhension des divers effets qui influencent les performances des contacts lubrifiés. Grâce à l'expérimentation et aux simulations numériques, des connaissances significatives ont été acquises sur le comportement des contacts TEHL, en particulier ceux qui fonctionnent dans des conditions de glissement opposées et avec des surfaces revêtues, thermiquement isolantes. Les résultats présentés ici ne se limitent pas au contexte dans lequel ils ont été développés (c'est-à-dire le contact came-suiveur). Ils peuvent être utiles pour d'autres applications où le frottement et l'usure des contacts lubrifiés sont un enjeu, par exemple les futurs moteurs à combustion avec des carburants alternatifs, les voitures électriques, les roulements, les applications biomédicales, etc.

General Introduction

In the quest for sustainable and efficient transportation, reducing friction within internal combustion engines has gained importance over the years. Frictional losses significantly impact the overall efficiency and performance of these engines, leading to more fuel consumption and CO_2 emissions. Lubrication is employed in engines to mitigate the negative effects of friction. However, stringent regulations are being passed in different countries pushing automotive manufacturers to produce more efficient engines. As a result, research efforts have been directed toward developing innovative techniques to minimize friction and wear in engines. One of these techniques is DLC-coated surfaces of some engine components that are in relative motion such as in the valve-train system.

The lubricated cam-follower contact undergoes rapid changes in load, surface geometry, and velocity. Over a significant part of the working cycle, very high sliding occurs, where thermal effects are suspected. Therefore, replacing (thermally conductive) steel surfaces with (thermally insulating) DLC-coated surfaces could lead to major modifications of lubricant film build-up and friction.

That is why this thesis aims to investigate the thermal effects of DLC coatings on friction and lubricant film thickness in lubricated contacts with a focus on high sliding operations.

Chapter 1 introduces the background and significance of the current research. It presents some experimental and numerical advances in the field of elastohydrodynamic lubricated contacts in addition to an overview of thin-film DLC coatings. Finally, it highlights research objectives in relation to gaps identified in the literature.

Chapter 2 describes the two experimental setups employed in this work. These include a barrel-on-disk tribometer and a single cam-follower-valve test rig. Moreover, the theoretical background of the numerical approach is laid out in addition to its implementation in a finite element code. Finally, the material properties of different solid components are presented alongside the results of a rheological characterizing of a commercial engine lubricant used throughout this work.

Chapter 3 uses a dual experimental-numerical approach to study simultaneously the lubricant film thickness and friction coefficient in a wide-elliptical contact for a wide range of sliding conditions. The effects of several operating conditions (varying temperature, load, and entrainment velocity) at high sliding are also explored.

Chapter 4 focuses on the effects of DLC coating in a line contact on friction and film thickness reduction, especially under opposite sliding conditions. Moreover, the influence of coating properties (thermal conductivity and thickness) is investigated.

Chapter 5 focuses on the industrial application of concern in this thesis: the cam-follower contact. The numerical approach is confronted with experimental friction measurement and provides insight into the effects of DLC coating in real engine components.

The final chapter concludes this work by pointing out its main contributions and limitations. It also provides some perspectives for future research.

Chapter 1: Introduction

According to the “Fit for 55” [1] European package, greenhouse gas emissions should be reduced by 55 % in 2030 compared to 1990. Similar stringent regulations are being passed in Japan [2] and the US [3]. With the tightening of environmental targets, researchers are racing to find more efficient technologies in all sectors, especially in transportation. The development of friction reduction techniques in tribological systems constitutes an essential step toward sustainable mobility. One technique is the coating of mechanical components with Diamond-Like Carbon (DLC) thin films to reduce friction and increase the lifespan of these components. This thesis provides insights into the effect of DLC coatings on lubricant film thickness and friction in highly-loaded lubricated contacts at high shear.

The Jost report [4] introduced the word “tribology” and showed that, at the time, applying new technologies to tribological systems could save 1.36 % of the Gross National Product (GNP) of the United Kingdom annually. In 2017, Holmberg et al. [5] studied the impact of tribology on global energy consumption, costs, and emissions. They found that in total, tribological contacts are responsible for 23 % of the global energy consumption. Of which, 20 % is consumed to overcome friction. Holmberg et al. [5] also found that by implementing new friction reduction and anti-wear technologies, around 25 % energy saving is possible in the transportation sector shortly (in less than 10 years). In the transportation area, a non-negligible part of fuel energy is lost due to friction inside an internal combustion engine (ICE). Holmberg et al. [6] presented a breakdown of passenger car energy consumption shown in Figure 1.1 where friction in the engine accounts for 11.5 % of total chemical fuel energy.

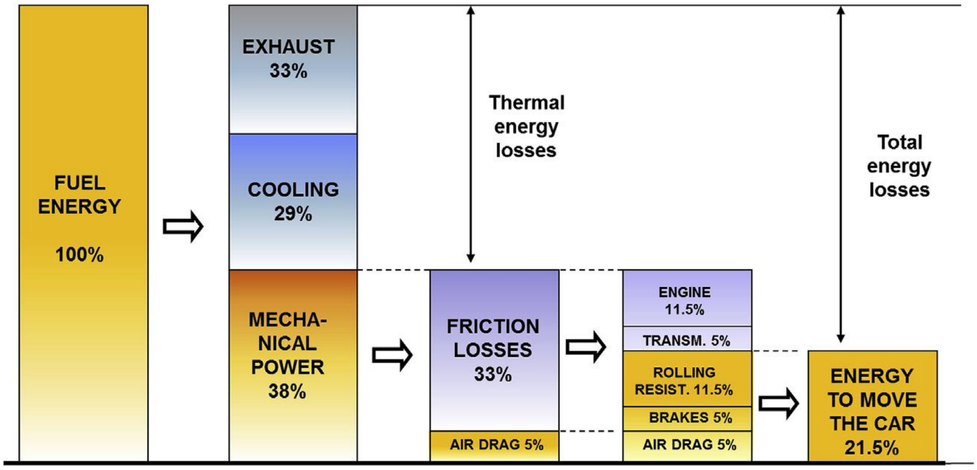

Figure 1.1: A breakdown of ICE-powered passenger car energy consumption. Taken from [7].

Friction originates from different contacting parts in relative motion such as piston rings moving against the cylinder liner and cams in contact with valves tappets or finger followers. Any friction reduction at the level of these tribological contacts is advantageous for fuel efficiency and engine emissions.

This thesis is concerned with friction reduction that could be achieved by DLC-coating some parts in the valve train system of an ICE, more specifically the cam-finger follower contact. The latter is introduced in section 1.1. Then, in section 1.2, an overview of lubricated contacts is presented in terms of different lubrication regimes via theoretical and experimental methods. Next, in section 1.3, an overview of DLC coatings is given with details about depositions methods and material properties. Finally, the objectives and outline of this thesis are presented in section 1.4.

1.1 The Cam-Finger Follower Contact

Before going into the details of the cam-finger follower contact, a quick overview of the working cycle of an ICE is presented. As the name suggests, an ICE is powered by the combustion of the air-fuel mixture inside a combustion chamber (i.e. cylinder) to release the chemical energy stored in the fuel. Figure 1.2 illustrates the operation of a 4-strokes ICE.

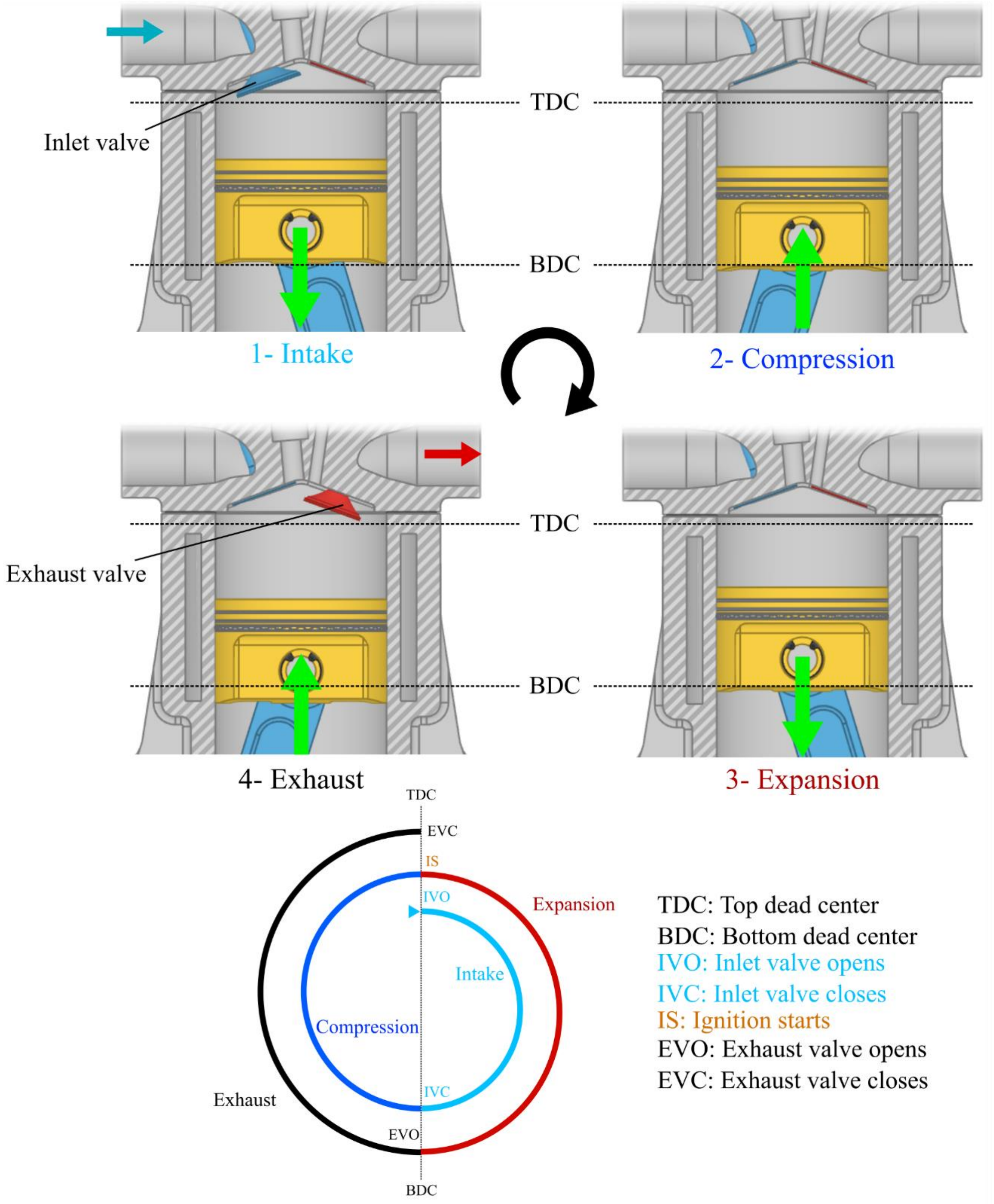

Figure 1.2: Schematic representation of the theoretical operation of a 4-strokes engine. The green arrows describe the movement of the piston during a stroke, the blue arrow represents the flow of air (or air-fuel mixture) into the cylinder, and the red arrow represents the flow of exhaust gases out of the cylinder. The illustration of different parts of the mechanism is taken from [8]. A theoretical valve timing diagram is shown at the bottom of the figure.

A 4-strokes engine operates by repeating a succession of 4 stages:

1. Intake: air (or air-fuel mixture) is introduced into the cylinder through the opening of the inlet valve.
2. Compression: the gases in the cylinder are compressed due to the upward motion of the piston. Towards the end of this stroke, ignition starts typically via a spark plug.
3. Expansion (or power stroke): chemical energy stored in the fuel is released by combustion and transmitted in the form of pressure to the piston which is pushed downwards. The linear downward motion of the piston is transformed into rotation of the crankshaft.
4. Exhaust: burned gases are exhausted out of the cylinder through the opening of the exhaust valve and the upwards motion of the piston.

A theoretical valve timing diagram for a 4-strokes engine is shown at the bottom of Figure 1.2. In practice, the valve opening and closing do not occur exactly at the top dead center (TDC) or bottom dead center (BDC). Instead, the time of opening and closing of the valves during the engine cycle is controlled by cams which are carefully designed and positioned on a camshaft. In the engine design phase, engineers take great care in designing the cam profile to get the desired valve lift profile essential for an efficient engine operation. There exist various mechanisms to transmit the rotary motion of the cam to the valve such as cam-roller follower, cam-tappet, or cam-finger follower. The latter has been used in Formula 1 engines due to its lightweight and ability to increase maximum valve lift [9] and is the mechanism of interest in the current work. More specifically, the lubricated contact between the cam and the top pad of the finger follower is the subject of this study. Throughout this thesis, the term cam-follower contact will be used to refer to this contact. Figure 1.3 is a schematic representation of the cam-follower-valve mechanism studied in Chapter 5.

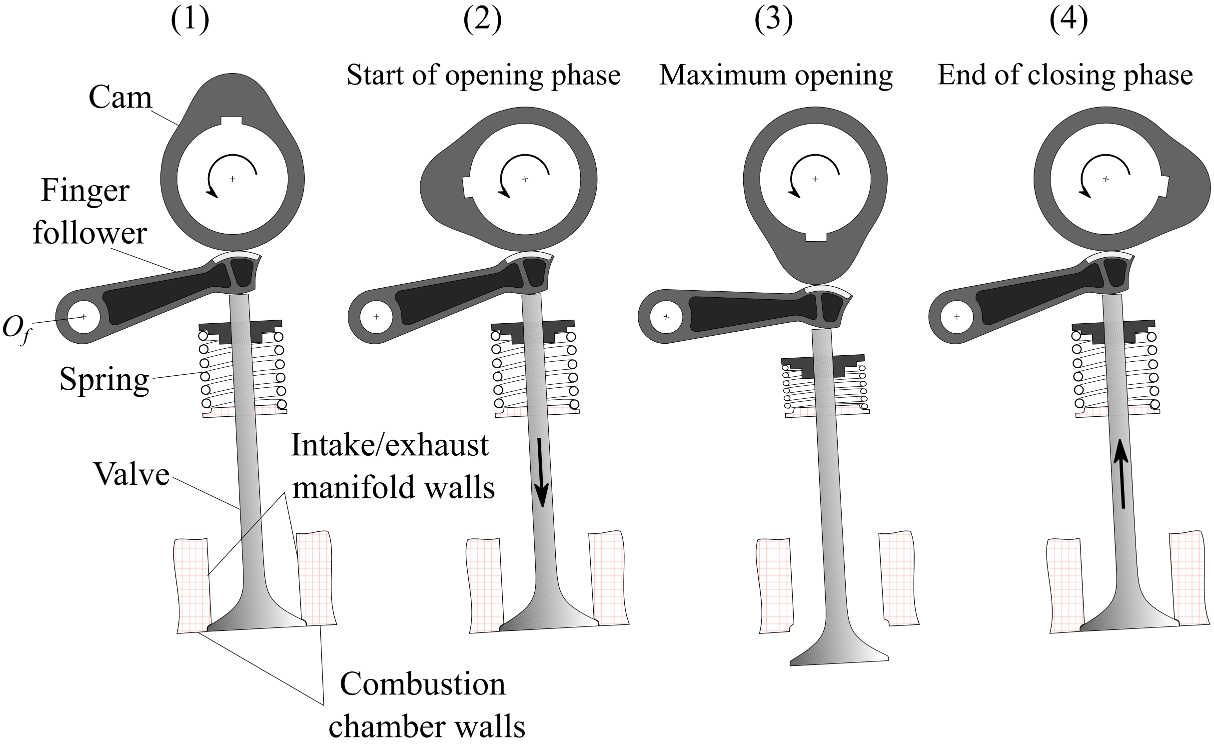

Figure 1.3: Schematic drawings of cam-follower-valve mechanism. Each of drawings (1) through (4) corresponds to a position during the rotation cycle of the cam.

The translation motion of the valve is governed by the cam profile. A full cam rotation completes a valve opening/closing cycle. In Figure 1.3, between positions (1) and (2) there is no contact between the back of the cam and the finger follower which stays in its initial position and the valve is fully closed. Between (2) and (3) the cam starts to push the finger follower which rotates around a pin at O_f and moves the valve downwards while compressing the spring. A maximum valve opening is reached at position (3) when the nose of the cam is pushing the finger follower. The cam continues its rotation and the valve becomes fully closed due to spring action at position (4) where the back of the cam is no longer in contact with the follower. The latter oscillates back to its original position and the cycle repeats. On one hand, if the valve belongs to the intake manifold, inlet air (or fuel-air mixture) enters the combustion chamber between positions (2) and (4). On the other hand, if the valve belongs to the exhaust manifold, gases are evacuated after combustion between positions (2) and (4). The lift, speed, and acceleration of the valve are plotted as a function of the cam rotation angle in Figure 1.4. Also, the different phases of the cycle are indicated.

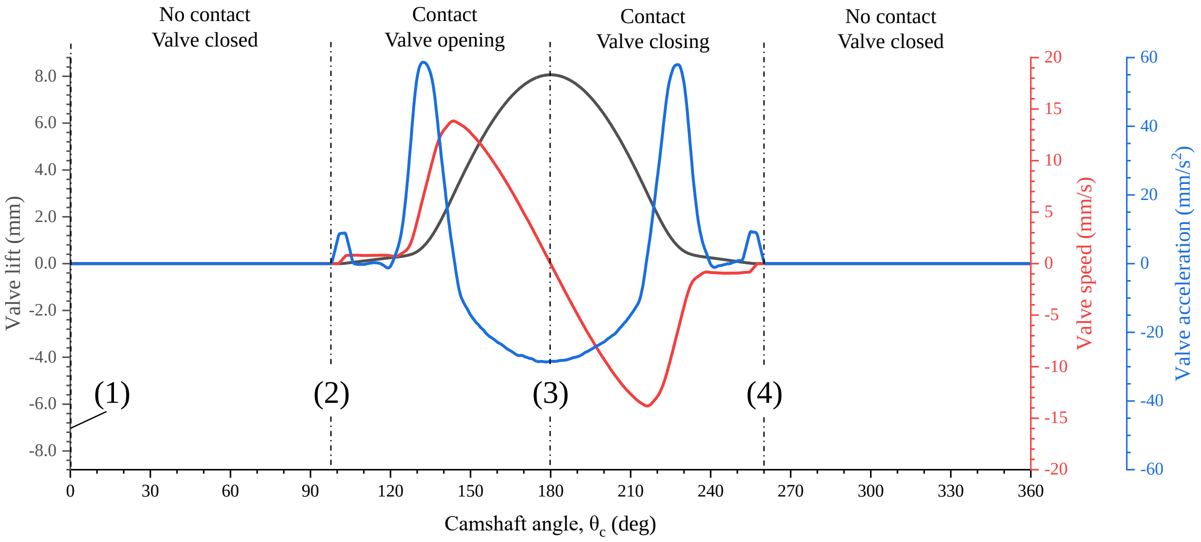

Figure 1.4: Variation of valve lift, speed, and acceleration with the rotation of the cam. Different opening and closing phases are indicated. These profiles correspond to a counter-clockwise rotation of the cam at 1550 rpm.

The rotation speed of the camshaft in a 4-strokes engine is equal to half of the crankshaft rotation speed. With engine speeds exceeding 10000 rpm in some cases [10] and up to 15000 rpm in Formula 1 engines where a full cam cycle takes less than 10 milliseconds to complete. The speeds of the surfaces, the normal load, and the radii of the curvature of the contacting bodies are rapidly changing during each cam cycle. The contact alternates from being conformal to non-conformal and surfaces change from moving in the same direction to opposite directions. Figure 1.5 shows these changes during one rotation cycle of the cam.

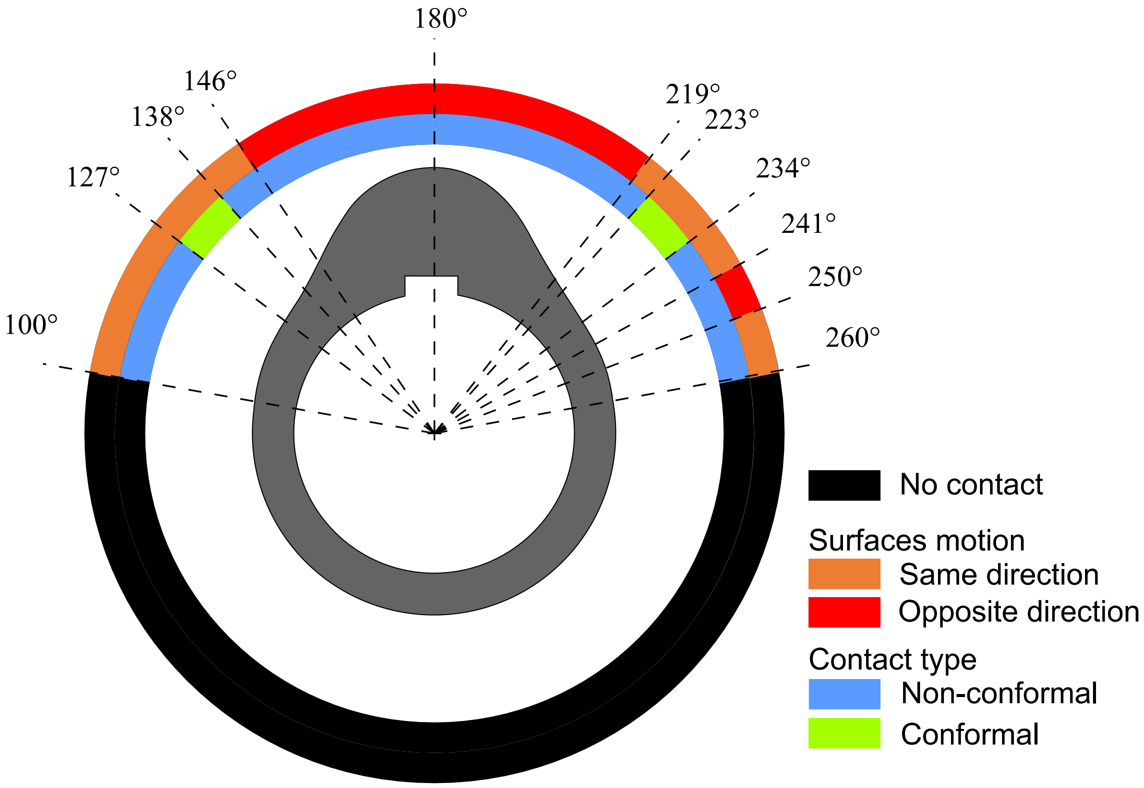

Figure 1.5: Changes in cam-follower contact type and surfaces motion during a cam cycle. The angles correspond to the counter-clockwise rotation camshaft angle.

Depending on the geometrical design of the cam and finger follower mechanism the variation of the speed and motion direction of the contact point can be theoretically calculated [11]. As a consequence, the cam surface velocity, u_1, and the follower surface velocity, u_2, with respect to the contact point can be found. The entrainment velocity, u_e, and the slide-to-roll ratio, SRR, are expressed respectively by equation (1.1) and equation (1.2).

$$u_e = \frac{u_1 + u_2}{2} \tag{1.1}$$

$$SRR = \frac{u_1 - u_2}{u_e} \tag{1.2}$$

The variation of SRR with the rotation angle of the cam is shown in Figure 1.6. Note that only the part of the cam cycle where there is contact between the cam and the follower is plotted (i.e. camshaft angle between 100° and 260° for a counter-clockwise rotation).

It is found that for the mechanism studied in this thesis (presented in Figure 1.3), the SRR is greater than 0.5 for the entire time when the cam is in contact with the finger follower. Also, more than half this time, SRR is greater than 2. In this case, contacting surfaces move in opposite directions. Furthermore, SRR reaches a maximum of 10.

Due to high sliding, the friction in a cam-follower contact affects the overall efficiency of the engine and the lifespan of the parts involved. Lubrication is employed in an ICE to limit friction and wear by introducing a fluid that separates the solid parts and prevents direct contact. Understanding the lubrication mechanisms of highly dynamic and highly-loaded contacts is crucial to ensure the proper functioning of such complex mechanical systems. In this context, the following section presents the state-of-the-art of lubricated contacts in terms of theoretical and experimental advances.

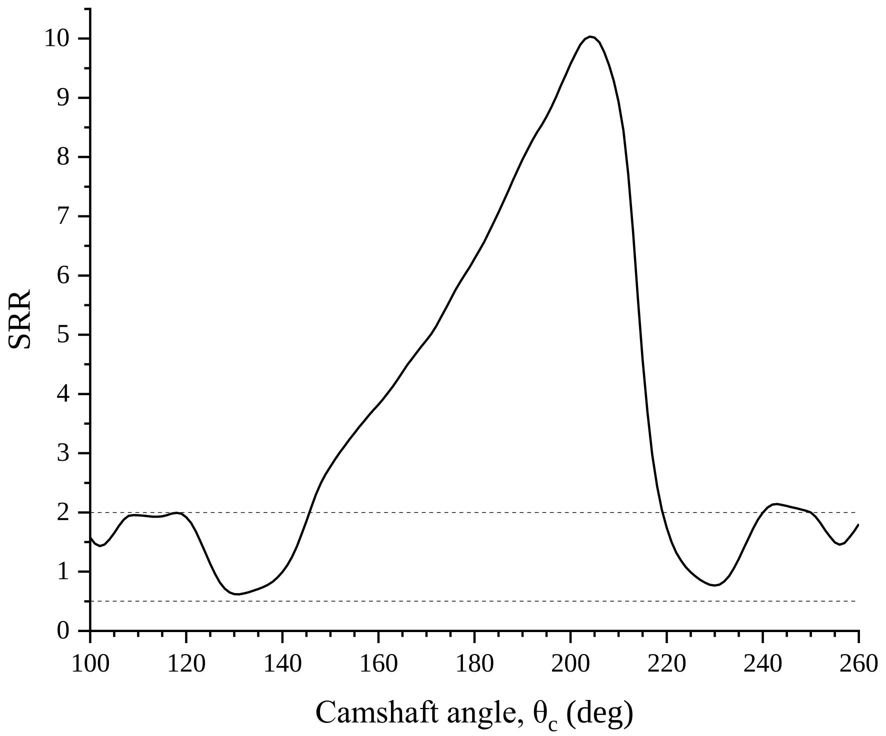

Figure 1.6: Variation of SRR with camshaft rotation angle in the cam-follower contact. The angles correspond to the counter-clockwise rotation angle of the cam.

1.2 Lubricated Contact

In contrast with the dry contact where two solid surfaces are in direct contact, the lubricated contact is formed when a lubricant (fluid or grease) is introduced to separate the two solid surfaces. The entrapment of a lubricant in the convergent region of a contact results in a load-bearing capacity that separates the contacting surfaces by a lubricant film. In an ideal case, the surfaces are perfectly smooth and even a very thin lubricant film prevents the solid surfaces from touching. However, in reality, surfaces are not perfectly smooth, hence, asperity contact may occur if the lubricant film is not thick enough. The composite roughness of two rough surfaces is defined as $R_q = \sqrt{R_{q,1}^2 + R_{q,2}^2}$ where $R_{q,1}$ and $R_{q,2}$ are root mean squared roughness of surfaces 1 and 2 respectively. The film thickness parameter, λ, is defined in (1.3) as the ratio of the average lubricant thickness h_a between the two surfaces to their composite roughness R_q.

$$\lambda = \frac{h_a}{R_q} \tag{1.3}$$

Figure 1.7 illustrates the famous Stribeck curve created by Stribeck in 1902 [12]. It represents the variation of friction coefficient with the dimensionless parameter proportional to viscosity and sliding velocity and inversely proportional to normal load. The friction coefficient is defined as the ratio of the tangential friction force over the normal load.

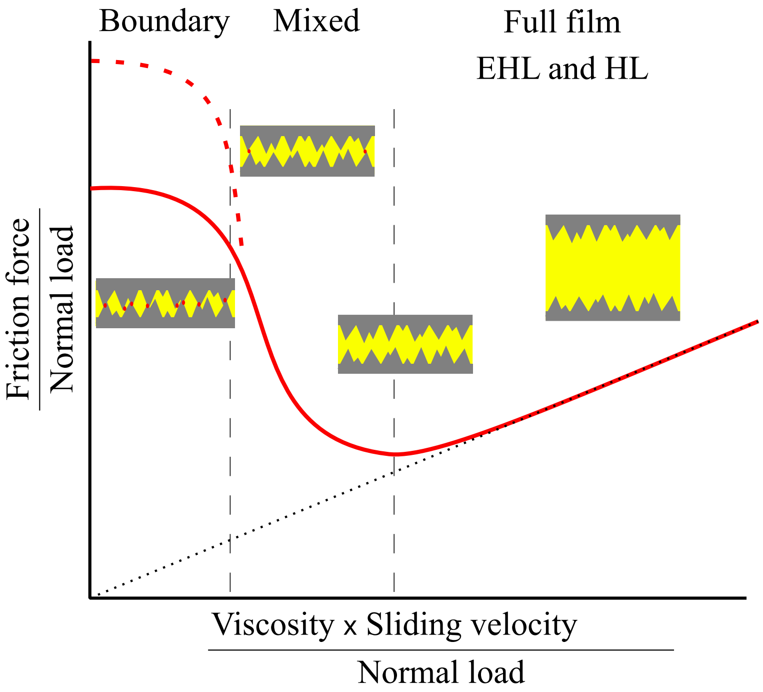

Figure 1.7: Schematic of Stribeck curve adapted from [13] with different lubrication regimes.

The curve can be roughly divided into three regions based on the value of the film thickness parameter λ. Each region corresponds to a lubrication regime. Gohar and Ranejet [14] indicated that $\lambda = 1$ and $\lambda = 3$ mark the transitions between the different lubrication regimes. These transitions can shift depending on the operating conditions. In general, for $\lambda \leq 1$, direct contact occurs between the surfaces, and the regime is called **boundary lubrication (BL).** The friction coefficient in the boundary regime can be affected by lubricant additives and by mechanical and surface properties of the contacting solids among other factors. To reflect these dependencies, a dashed part of the Stribeck curve is shown in the boundary lubrication region of Figure 1.7. For $1 \leq \lambda \leq 3$, a more regular lubricant film separates the surfaces however it is not thick enough to prevent all asperity contact. This is called the **mixed lubrication (ML)** regime. The friction in this regime is lower than that in boundary lubrication. In BL and ML regimes, asperity contact causes surface wear and decreases the lifespan of mechanical components. For λ higher than the upper limit of the ML regime, a full film separation is assumed because the film thickness is at least three times the composite roughness of the surfaces. A minimum friction coefficient occurs near the transition from mixed to full film lubrications. At low contact pressure, as in conformal contacts, the full film regime is called **hydrodynamic lubrication (HL).** In contrast, when the pressure generated inside the contact is high enough to elastically deform the surfaces, the regime is called **elastohydrodynamic lubrication (EHL).** This is a common type of lubrication found in numerous applications such as gears, roller bearings, and cam finger follower mechanisms usually involving two non-conforming solid surfaces. According to [14], the film thickness is usually less than 1 μm in EHL contacts. The current work focuses on EHL contacts at high sliding. Hence, a brief history of theoretical and numerical methods in EHL is presented next.

1.2.1 Theoretical and numerical methods in EHL

EHL film thickness

In 1886, Reynolds [15] derived from the Navier-Stokes equation a relation between the pressure of the lubricant, the geometry, and the motion of the solids. Kingsbury [16] and Michell [17] were able to apply this equation to contacts operating under the HL regime where the solids are considered undeformed. A few decades later, Ertel [18] was able to uncover the EHL fundamentals by using Hertz elastic deformation and Barus [19] piezo-viscosity relation in the Reynolds equation. Cameron [20] uncovered the story of the publication of Ertel's work under Grubin's name in 1949 [21].

With advances in numerical methods in the second half of the 20th century many researchers solved the EHL problem using the semi-system approach. This approach was first used by Dowson and Higginson [22] to study lubricated line contact. They calculated the thickness and pressure profiles along the entrainment direction. Figure 1.8 is an example of the solution proposed by Dowson and Higginson [22] for the EHL line contact. Figure 1.8 includes the dry Hertzian pressure profile in addition to the calculated thickness and pressure profiles along the x-direction. They showed that at high loads the pressure profile approaches that of dry contact. Later, the same authors [23] curve-fitted the expression (1.4) relating dimensionless minimum film thickness H_m to other dimensionless parameters given in (1.5) for simple estimation of minimum film thickness h_m.

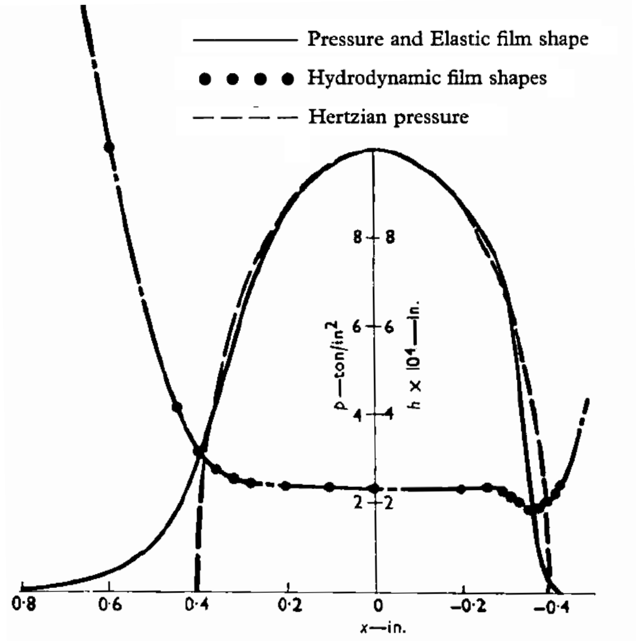

Figure 1.8: An example of calculated thickness and pressure profiles in lubricated EHL in addition to the Hertzian pressure profile. Taken from [22] for maximum Hertzian pressure equal to 10 ton/in^2 (137.9 MPa).

$$H_{m,Dowson-Higginson} = 1.6U^{0.7}G^{0.6}W_{1D}^{-0.13} \tag{1.4}$$

$$U = \frac{\mu_0 u_e}{E'R^{1D}} \qquad G = \alpha E' \qquad W_{1D} = \frac{w_{1D}}{E'R^{1D}} \qquad H_m = \frac{h_m}{R^{1D}} \tag{1.5}$$

where u_e is the entrainment velocity calculated as an average of the velocity of the contacting surfaces, μ_0 is the viscosity at atmospheric pressure at a given lubricant temperature T_0, α is the viscosity-pressure coefficient at T_0, and h_m is the minimum film thickness along the entrainment direction. In addition, w_{1D} is the normal load applied to the contact, R^{1D} is the reduced radius of curvature, and E' is the reduced Young's modulus. Expressions of u_e, R^{1D}, and E' are given later in Chapter 2.

Furthermore, a relation of dimensionless parameters to minimum and central film thickness in circular or point contacts was suggested by Evans and Sindle [24]. Also, Hamrock and Dowson [25] proposed a relation for elliptical contact with lubricant flowing along the minor axis. Later Chittenden et al. [26] used the same approach and suggested expressions (1.6) and (1.7) to estimate central and minimum film thickness respectively in an elliptical contact.

$$H_{c,Chittenden} = 4.31\, U^{0.68}\, G^{0.49}\, W_{2D}^{-0.073} \left(1 - e^{-1.23\left(\frac{R_y}{R_x}\right)^{2/3}}\right) \tag{1.6}$$

$$H_{m,Chittenden} = 3.68\, U^{0.68}\, G^{0.49}\, W_{2D}^{-0.073} \left(1 - e^{-0.67\left(\frac{R_y}{R_x}\right)^{2/3}}\right) \tag{1.7}$$

Note that the definitions of the load parameter and dimensionless thickness for the elliptical contact case are slightly different than those of the line contact case and are given in (1.8). In this case, h_c is the central film thickness and R_x^{2D} is the reduced radius of curvature in the entrainment direction given later by expression (2.23) of Chapter 2.

$$W_{2D} = \frac{w_{2D}}{E'(R_x^{2D})^2} \qquad H_m = \frac{h_m}{R_x^{2D}} \qquad H_c = \frac{h_c}{R_x^{2D}} \tag{1.8}$$

Note that the aforementioned semi-analytical expressions only give an estimation of central or minimum lubricant film thickness under pure (or nearly pure) rolling conditions (i.e. $SRR = 0$ or very close to 0).

The accuracy of the numerical solutions improved over the years. In 1987, Lubrecht et al. [27] introduced multigrid methods and were able to solve the EHL equations discretized on a dense finite difference grid while achieving a better convergence rate at a lower computational cost. This technique was later improved by Venner [28,29] for highly loaded contacts.

With advances in computational techniques such as the Finite Element Method (FEM), Computational Fluid Dynamics (CFD), and Fluid-Structure Interaction (FSI) a new approach emerged for solving EHL equations: the full-system approach. As the name suggests, it consists in solving the various EHL equations simultaneously in a single step instead of iteratively solving each equation separately. In 2008, Habchi [30] developed a finite element model based on the full-system approach to solve the lubricated point contact problem. Wheeler [31] later added the possibility of simulating non-circular contacts. Raisin et al. further developed the model to include transient calculation [32] and the possibility to simulate coated surfaces [33]. The current work is derived from these state-of-the-art models so more details are provided in a dedicated section of Chapter 2.

EHL under high-sliding conditions

In 1989, the generalized Reynolds equation derived by Najji et al. [34] enabled the variation of viscosity and density through the film thickness. Non-Newtonian fluids and thermal effects could then be modeled. This was a major advancement due to the importance of these effects when sliding occurs. On one hand, heat generation by shear heating occurs when the lubricant is subjected to shear stresses. Thus, under sliding conditions the temperature of the lubricant increases. Due to the strong temperature dependency of the viscosity, EHL models must include thermal effects when simulating sliding conditions. On the other hand, lubricants can be non-Newtonian at high shear rates. Meaning that the viscosity of the lubricant not only depends on its temperature and pressure but also the shear rate. Hence, the importance of modeling non-Newtonian fluids in EHL contacts under sliding conditions. As mentioned before, the classical semi-analytical expressions are limited to near-zero sliding cases where thermal and non-Newtonian effects are negligible. More recent expressions/correction factors are becoming available to estimate minimum or central film thickness under higher sliding conditions. In 2020, Marian et al. [35] provided an extensive review of different prediction expressions for film thickness along with thermal and non-Newtonian correction factors.

Early experimental observations showed that the behavior of EHL contacts at high-sliding conditions is different than what the classical theory predicts. While the latter predicts zero film thickness under zero entrainment velocity (ZEV) condition, experiments showed that a fluid gap exists even at this extreme sliding condition ($SRR = \infty$). In the 1950s, Cameron [36] coined the term viscosity wedge referring to the load-bearing capacity by a viscosity gradient created in a lubricated contact even with ZEV. Dyson and Wilson [37] showed using a twin-disk setup and capacitive thickness measurement that surfaces moving in opposite directions at the same speed are still separated by an oil gap. In the year 2000, an original numerical solution of TEHL line contact at high sliding (up to infinity) by Yang et al. [38] and Guo et al. [39] was used to explain the thermal origins of the viscosity wedge observed in the experimental results of Dyson and Wilson [37]. In addition, the new solution by [38,39] responded to the need for a new EHL theory to explain the shape of a non-flat central film thickness profile (i.e. dimple) observed previously by Kaneta et al. [40] using optical interferometry.

Guo and Wong [41] studied numerically the film formation in EHL point contacts under ZEV conditions. Based on the flow, temperature, and viscosity analysis in the contact region they mainly attributed the film formation in the studied conditions to the thermal viscosity wedge effect. Later, Yagi et al. [42] reached the same conclusion experimentally by measuring the film thickness and temperatures of the surfaces. More recently, Bruyere et al. [43] used a fluid-structure interaction approach to solve Navier-Stokes equations coupled with elasticity and energy equations for a sliding TEHL line contact. By analyzing the order of magnitude of the different terms of the Navier-Stokes equations they identified the term responsible for the viscosity wedge effect: $\frac{\partial \eta}{\partial y} \cdot \frac{\partial u}{\partial y}$. Figure 1.9, taken from [43], presents the distribution across the deformed lubricant gap of (a) the viscosity wedge term and (b) the pressure gradient along the entrainment direction.

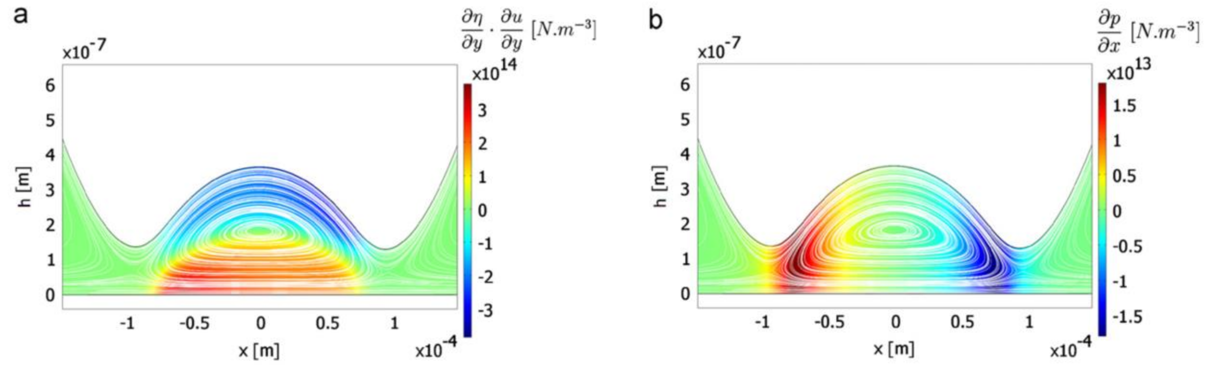

Figure 1.9: Distribution in the deformed oil gap of (a) the viscosity wedge term and (b) the horizontal pressure gradient. Taken from Bruyère et al. [43]

The viscosity wedge term becomes more significant when the viscosity gradient across the film thickness is greater. Note that in [43] the thickness of the film is in the y-direction. The idea behind the thermal viscosity wedge is that in opposite sliding, the lubricant is entrained in and out of the contact from both sides. At a given location in the entrainment direction, there exists a large temperature gradient throughout the oil gap due to the difference in the temperature of surfaces entering and exiting the contact. The temperature gradient leads to a viscosity gradient throughout the oil gap which provokes a pressure gradient in the entrainment direction contributing to the development of a high-pressure zone (commonly called "dimple") and also to the increase in the load-bearing capacity of the lubricant. More recent studies of the thermal viscosity wedge effect in TEHL contacts include a study by Raisin et al. [33] and Meziane et al. [44]. The former investigated the effects of DLC coatings on point contacts under ZEV conditions. They found that the use of low inertia coatings can disturb the heat balance in the contact and leads to an attenuation of the thermal viscosity wedge effect. The latter approached experimentally and numerically the film thickness build-up in wide elliptical contacts under ZEV conditions. They investigated the influence of operating conditions such as surface velocity, normal loads, and external temperatures. In general, according to [44], an increase in the surface velocity (i.e. sliding speed $\Delta u = u_1 - u_2$) leads to an increase in minimum film thickness. Also, an increase in the external normal load increases the central film thickness. Finally, an increase in the external temperature results in less significant viscosity gradients and lower minimum and central film thicknesses.

EHL in valve-train contacts

Contacts in a valve-train system are characterized by their complexity due to the dynamic nature of the mechanisms. Namely, the speed and geometry of surfaces, and the contact load vary rapidly during a rotation cycle.

In 1992, Dowson et al. [45] investigated from a tribological perspective the transient cam-follower contact and offered an analytical approach to optimize the design of this mechanism and ensure lubrication under critical conditions. Messe and Lubrecht [46] applied the multigrid technique developed in [27] to study the transient cam-tappet contact from an isothermal point of view. They compared their results with those obtained by a quasi-steady approach and found that for most of the cycle, the film thickness results are close except at the critical points in the contact (i.e. when the entrainment velocity is zero). Quasi-steady approach predicted a total collapse of film thickness at the critical points whereas the transient approach predicted a lubricant gap even under ZEV conditions. The authors attributed this observation to the squeeze-film effect originating from the entrapment of the lubricant inside the contact. Later, Wang and Yang [47] used a Thermal-EHL numerical model to study the effect of a transient load on eccentric cam-tappet pair. They revealed that not only the squeeze-film effect plays a role in maintaining a film thickness under ZEV conditions but also the thermal viscosity wedge. Moreover, they pointed out that assuming isothermal conditions may lead to inaccurate results in terms of film thickness and pressure predictions. This was later confirmed by Raisin et al. [10] who investigated the importance of thermal, shear-thinning, and transient effects on the performance of a cam-follower contact using a TEHL line contact model (similar to the one used in this work). They concluded that the thermal and shear-thinning effects significantly influence friction coefficient and film thickness results. Therefore, they should be considered when simulating a cam-follower contact. Furthermore, when transient effects were considered, the variation of friction coefficient and film thickness is smoother over the cycle compared to a quasi-steady simulation without a significant difference.

EHL friction

In addition to the study of EHL film thickness researchers are interested in studying and predicting the friction behavior in EHL contacts. EHL friction is usually represented by a friction (or traction) curve showing the variation of friction coefficient C_f with SRR. The friction coefficient is defined as the ratio of the tangential friction force F_T over the normal load w_N (1.9). Note that F_T is expressed in $[N/m]$ in the case of 1D line contact where $w_N = w_{1D}$ and is expressed in $[N]$ in the case of 2D contact where $w_N = w_{2D}$ resulting in a dimensionless C_f in both cases.

$$C_f = \frac{F_T}{w_N} \tag{1.9}$$

On one hand, F_T and w_n can be measured experimentally in twin-disk, ball-on-disk, or other tribological setups by multi-axis piezoelectric or strain gauge sensors. On the other hand, theoretically, the friction force F_T is the integral of the shear stress τ_{zx} at the fluid-solid interface ($z = 0$ or $z = h$) over the entire contact area A_c and is given by equations (1.10) and (1.11) for 1D line contact and 2D elliptical contact respectively. τ_{zx} depends on the rheology of the lubricant.

$$F_T^{1\mathrm{D}} = \int_{A_c} \tau_{zx} dx \tag{1.10}$$

$$F_T^{2\mathrm{D}} = \iint_{A_c} \tau_{zx} dx dy \tag{1.11}$$

In **classical EHL**, twin-disk machines were used to extract rheological properties of lubricants such as Eyring stress and the pressure-viscosity coefficient as in Johnson and Tevarwerk's work [48]. This approach was later proved inaccurate based on rheological measurements outside EHL contact by Bair [49] who showed that the assumption that the friction curve is equivalent to the lubricant flow curve is erroneous. Over the years, **quantitative EHL** [50] viscosity models were fitted to independent rheological measurements outside of EHL. In this approach though, rheological characterization of the lubricant (under pressures and shear rates suitable for rheological measurements) has to be completed by a limiting value of shear stress,τ_{xz}, to model the so called "limiting shear stress" (LSS) phenomenon observed in EHL experiments. Based on the quantitative EHL approach and using a validated-by-experiment numerical model, Habchi et al. [51] proposed four friction regimes:

1) Linear regime: The isothermal Newtonian viscous shear causes a linear increase of friction with increasing SRR.
2) Non-linear viscous regime: Non-Newtonian shear thinning and/or thermal effects influence the friction response which becomes non-linear with increasing SRR. Friction response can also be influenced by the limiting shear stress phenomenon.
3) Plateau regime: Friction stabilizes at an asymptotic value indicating the major influence of the limiting shear stress of the lubricant.
4) Thermoviscous regime: Friction decreases with further increasing of SRR. In this regime, thermal and shear-thinning effects are dominant over the limiting shear stress phenomenon.

Figure 1.10 represents the different friction regimes mentioned above with varying SRR.

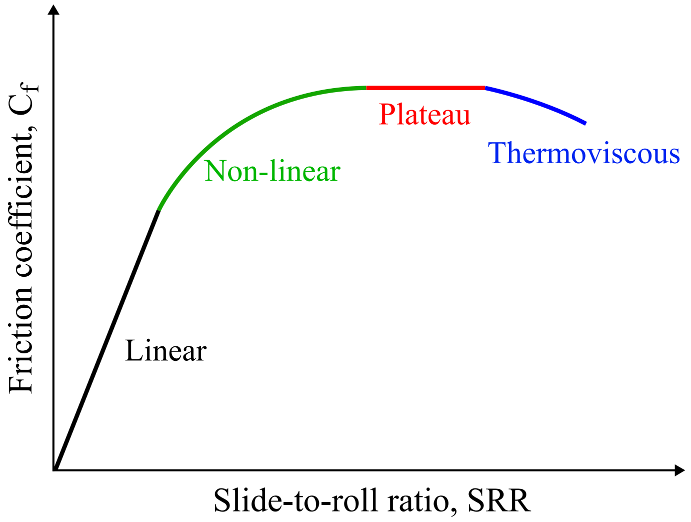

Figure 1.10: Friction regimes with varying SRR. Reproduced from [52].

This concludes the overview of the theoretical and numerical approaches to studying EHL film thickness and friction. Over the years, these went hand-in-hand with experimental methods to deepen the understanding of EHL contacts. Next, some experimental methods developed in the last 70 years are described.

1.2.2 Experimental methods in EHL

Experimental methods for investigating EHL contacts were developed in the second half of the 20th century to validate the already available theoretical solutions and deepen the understanding of lubricated contacts. In 2016, Albahrani et al. [53] presented an extensive review of in-situ methods for studying different aspects of EHL contacts. The EHL aspects of interest to researchers mainly include the lubricant film thickness, temperature, and pressure among others. In this section, an overview of the most widely used methodologies is presented.

Film thickness measurement

First, the measurement of the electrical resistance across the lubricated contact was one of the first techniques that aimed to measure lubricant film thickness in a contact between two conductive solids [54,55]. However, the authors were not able to deduce an accurate quantitative film thickness from resistance measurements due to variations in the electrical conductivity of mineral oils and differences in the electrical properties of thin oil films compared to bulk oil. Thus, this electric resistance technique was used mostly to identify transitions between mixed and full-film lubrication regimes.

Another electrical method based on capacitance measurements between two contacting surfaces separated by a lubricant was first used by Lewicki [56] in 1955 to measure the film thickness between two disks. The measured capacitance is proportional to the contact area and the lubricant's dielectric constant and inversely proportional to the distance separating the two surfaces (i.e. the lubricant film thickness) which can then be calculated. At first, this technique did not consider the changing shape of the lubricant gap under high load. In 1958 Crook [57] improved this measurement technique by applying it not to the lubricant inside the contact (where the deformation of the surfaces is significant) but to the lubricant films remaining on both disks after exiting the contact (where the disks are undeformed). After some calculations, they were able to deduce the lubricant film thickness in the contact region. Later, Dyson and Wilson [58] were able to apply the same method to validate Dowson-Higginson estimation for a variety of lubricants and thicknesses ranging from 30 nm to 1000 nm. They attributed some of the discrepancies between measurements and Dowson-Higginson estimations to non-Newtonian effects. One limitation of this technique is its low spatial resolution when the capacitance is measured directly between the two surfaces in contact. To overcome this limitation, Hamilton and Moore [59] measured the capacitance between one surface and a small capacitive gauge deposited on the other surface. They were able to measure the film thickness in a piston-ring/cylinder-wall contact. A major advancement in capacitive lubricant film measurement was brought by the instrument called "Lubcheck" developed by Heemskerk et al. [60]. This instrument was able to reduce the high-frequency noise of the electrical signals and to detect the occurrence of asperity contact in rough rolling element bearings. Jablonka et al. [61] simultaneously used optical and capacitance measurements (using the "Lubcheck" instrument) of film thickness on a ball-on-disk setup. Measurements in both methods were in good agreement with estimations by the Hamrock-Dowson formula as shown in Figure 1.11.

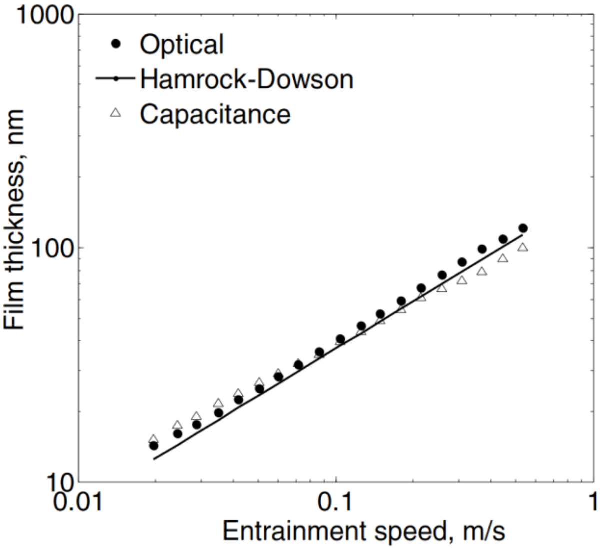

Figure 1.11: Comparison between theoretical and experimental (optical and capacitance) film thickness methods. Taken from Jablonka et. al [61].

More recently, capacitive measurements were applied to study grease-lubricated radial-loaded bearings by Cen et al. [62,63] and Zhou et al. [64]. For more details about the capacitive method for EHL film thickness measurements, readers are referred to a recent review by Cen et al. [65].

According to Albahrani et al. [53], optical interferometry of lubricant films contributed the most to lubricated contact understanding. An early version of optical interferometry was developed by Kirk [66]. This technique is based on the illumination by a light beam of a lubricated contact of an opaque ball and a transparent disk (usually made of glass or sapphire) separated by a lubricant. The light reflects from the oil-disk interface and then from the surface of the ball. The optical path difference between these reflected beams creates an interference pattern that depends on the thickness of the lubricant film. The resulting interference pattern can be interpreted as a contour map of the film thickness based on a previous calibration. The light beam can be a monochromatic light as in the experiments of Cameron and Gohar [67] in 1966 who were the first to use monochromatic interferometry in a steel ball on glass disk setup to observe a lubricant film gap in an EHL contact. Two years later, Foord et al. [68] introduced semi-reflective chromium-coated disks that improved the contrast of the resulting images. An important contribution of Westlake and Cameron [69] was the introduction of a thin silica spacer layer which enable the decrease of the lower limit of possible thickness measurement from 50nm to 10nm. With the advancement in computer technology and the availability of relatively cheap cameras, image analysis techniques were applied to optical interferometric patterns of EHL contacts. Gustafsson et al. [70] were the first to use the image analysis technique. This greatly improved the accuracy of the measurement by eliminating the problem of bias and low sensitivity of the naked eye. At the turn of the century, Hartl et al. [71] and Molimard et al. [72] simultaneously developed a technique called differential colorimetric interferometry (DCI) to measure film thickness in lubricated circular contact. They used RGB data (Red Green Blue) from images of interference patterns formed by reflected chromatic light beams. They were able to measure thicknesses ranging from 5 nm to 800 nm with a resolution of 1nm. This technique was used by Yagi et al. [42] who focused on contacts operating under infinite sliding conditions and investigated the film thickness profile in addition to temperature measurements. In another study, Nakaharara and Yagi [73] observed the evolution of film thickness optically for a circular contact from pure rolling up to $SRR = 1.8$. They found that the central film thickness decreases with increasing sliding velocity and that the central region thickness profile is no longer flat as predicted by theory. The DCI technique was extended by Wheeler et al. [74] to measure film thickness contacts of any shape (not limited to circular contacts). The main limitation of the optical film thickness measurements techniques is the requirement of a transparent material and mechanical components are usually made of opaque materials, such as steel. However, this technique is still one of the most widely used film thickness measurement methods in the field of EHL contact. In the current work, this optical technique is used for film thickness measurements on a barrel-on-disk tribometer.

Other less popular techniques for film thickness measurement include acoustic [75] and X-ray transmission [76] methods. These techniques are non-invasive and do not require transparent materials (so they can be applied directly to mechanical components). However, they are more complicated and more expensive than the above-mentioned capacitive and optical methods.

Pressure and temperature measurement

In addition to film thickness, researchers were interested in measuring the temperature and pressure of the lubricant inside an EHL contact. Transducers were manufactured with specific materials and deposited on one of the contacting surfaces and the changes in the transducer's resistance can be correlated to changes in temperature or pressure. Kannel et al. [77] were the first to use an electrical transducer made of manganin (copper, manganese, and nickel alloy) to measure the pressure of the lubricant in an EHL contact. Cheng and Orcutt [78,79] later added a platinum transducer for simultaneous pressure and temperature measurement in a twin-disk setup under rolling-sliding conditions. One limiting factor of these transducers was their low spatial resolution due to the large size of the transducer compared to the measured features. The spatial resolution of pressure measurements was improved by Hamilton and Moore [80] and later by Safa et al. [81] who respectively used gauges with widths 40 μm and 1 μm. They were able to confirm the presence of the pressure spike at the exit of the contact that was already predicted by the EHL theory. With the advancement of manufacturing techniques these pressure and temperature transducers got smaller and more widely used. In 2008, Miyata et al. [82] used a platinum thin-film sensor for temperature measurement in an elliptical contact at high entrainment speed and very low slip ratio. Figure 1.12 shows the temperature rise along the central line in EHL contact from Miyata et al. [82]. The results showed higher temperature rise in the lubricant subjected to higher slip conditions. The entrainment velocity in the case presented here is 11.77 m/s and the slip ratio "s" (defined differently than SRR) correspond to SRR from 0 to 0.038.

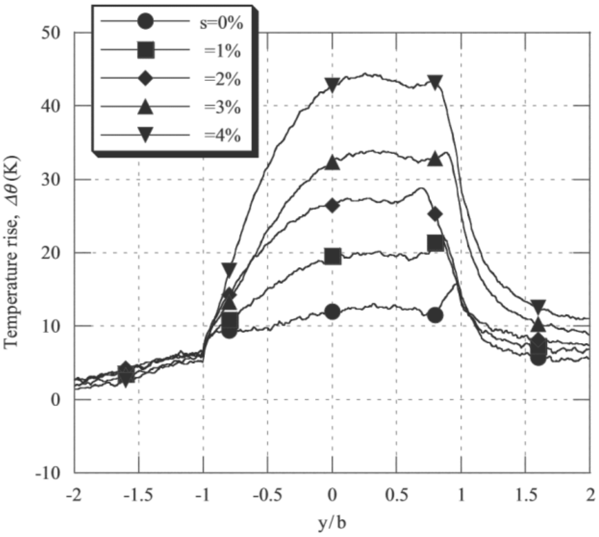

Figure 1.12: Comparison of the temperature rise with varying slip conditions along the central line in elliptical EHL contact with entrainment velocity 11.77 m/s, maximum Hertzian pressure 980 MPa, and bulk temperature 50 $°C$. Taken from Miyata et al. [82].

The large temperature rise ($\Delta\theta > 40\ K$ in the highest slip ratio case) is expected due to the high entrainment velocity and high load. Habchi and Vergne [83] demonstrated using a TEHL model that even at pure rolling in a highly loaded contact (with maximum Hertzian pressure 1.37 MPa) the maximum temperature rise inside the fluid can reached 7 K at for an entrainment velocity of 10 m/s due to compressive heating.

More recently, Ebner et al. [84] used thin film sensors for different bulk and coating materials on a twin-disk experimental setup. They were able, with the help of TEHL simulations, to confirm the thermal insulation effects, especially on the friction coefficient. According to Albahrani et al. [53], some limitations are faced by users of transducers for pressure and temperature measurements. These include the sensitivity of the transducers to the presence of impurities in the lubricant, the requirement of having extremely thin transducers to not influence the lubricant flow in the contact, and the short lifespan of the transducers used in severe EHL contacts, especially under high sliding conditions.

Another technique for pressure measurements in EHL contacts is Raman spectroscopy. The main advantage of this technique is that it is non-intrusive. A monochromatic light is used to illuminate a pressurized lubricant sample. Some of the absorbed light is reemitted with energy change due to variations of excitation energy within the sample molecules. This is called Ramen scattering. The Ramen spectrum is related to the vibrational energy of the sample. The pressure measurement technique consists of tracking the shift in the peaks of the Ramen spectrum which is related to the pressure applied to the sample. This technique was first applied to tribology by Gardiner et al. [85] for direct measurement of pressure in a static lubricant entrapment between a steel ball and a glass flat. Later in the 2000s, Jubault et al. [86–88] published a series of papers about pressure measurements in an EHL contact between a steel ball and a sapphire disk. They were able to achieve good special resolution and pressure sensitivity ($10\ \mu m$ and $30\ MPa$). Limitations of the Raman spectroscopy are its low signal-to-noise ratio and it necessitating a laborious calibration process compared to techniques using transducers for pressure measurements.

As for temperature measurements in EHL contacts by a non-intrusive technique, there exists a technique called Infrared (IR). It is based on detecting the infrared emissions from different parts of the contact (i.e. the solid surfaces and the lubricant) and calculating their temperatures. One of the first attempts at temperature measurement by IR thermography in EHL was by Turchina et al. [89]. They reported lubricant film and surface temperature in a point contact between a steel ball and a sapphire flat. Later in the mid-2000s, Spikes et al. [90] improved the spatial resolution of IR temperature measurement in an EHL contact between a steel ball and a sapphire disk. The sapphire disk was divided into three parts: uncoated, chromium-coated, and aluminum-coated. The different properties of the coatings and the bulk material enabled the authors to isolate radiations originating from the ball or the disk. Hence, this method gives the surface temperature of the disk and ball in the contact. Yagi et al. [42] realized IR thermography measurements in addition to optical thickness measurements to study the EHL behavior at high sliding, especially the mechanisms of “dimple” formation. With the assumption of parabolic temperature variation across the film thickness, they were able to deduce a temperature distribution in the film thickness based on the measured temperature of the ball and disk surfaces. They found a maximum temperature rise reaching $275\ K$ in the dimple zone under infinite sliding with a sliding velocity of $2\ m/s$ and a mean Hertzian pressure of $0.97\ GPa$. It was suspected that in the dimple zone the lubricant would solidify under the extreme pressures, however, the measurements in [42] demonstrated that the temperature rise in the high-pressure zone can keep the oil in its liquid state. Improvements to the sensitivity and resolution of IR thermography were brought by Reddyhoff et al. [91]. More recently, Lu et al. [92,93] presented a new IR microscopy technique to measure not only the temperature of the surfaces but also that of the lubricant film in all three directions. This technique required a calibration phase to measure the emissivity of the lubricant which varied with the lubricant film thickness and temperature.

This concludes the description of the state-of-the-art of experimental methods in EHL. Next, friction reduction techniques by DLC coatings are discussed in addition to an overview of the composition, deposition methods, and properties of DLC coatings.

1.3 Friction Reduction Techniques and DLC Coatings

Researchers are exploring different techniques for friction reduction in lubricated contacts operating under different lubrication regimes. According to Lee et al. [94], friction reduction can be achieved by using low-viscosity lubricants. However, this applies mostly to contacts operating at high speed/low load where a full film separation condition is satisfied since the film thickness is directly related to the rheology of the lubricant. In contrast, at low speed/high load conditions, mixed and boundary lubrication may occur because the low viscosity lubricant cannot separate the surfaces. In this case, friction and wear increase. Oil additives and surface coating can be used to reduce the risk of excessive wear in ML and BL. Kano [95] and Dobreniski et al. [96] showed experimentally the advantageous use of DLC-coated cam and tappet on friction in BL and ML at low engine speeds. In addition, these coatings were more wear-resistant than uncoated steel under equivalent operating conditions.

Diamond-like carbons were first discovered in the late 1960s [97] and were originally called Diamond seed crystals. Over the years different types were elaborated by various deposition methods. Researchers found various applications for DLCs, especially as protective coatings due to their high hardness and chemical inertness. In 2002, Robertson [98] presented a comprehensive review of deposition methods and mechanisms, characterization methods, and electrical, optical, and mechanical properties in addition to some applications of DLCs. In the following section, the atomic composition and microstructure of DLC are first presented. Next, the deposition methods are described. Finally, some of the properties of DLC are noted.

1.3.1 Composition and microstructure of DLC

As the name indicates, Diamond-like carbon is formed mainly of Carbon atoms. These atoms are in an amorphous form as opposed to the crystalline form of graphite and diamond. These structures are called amorphous carbon (a-C). Two types of hybridizations (sp^3 and sp^2) exist in a DLC. Hybridization refers to the way atoms form bonds with neighboring atoms. In diamond, the sp^3 configuration results in strong bonds between atoms which are arranged in a 3D tetrahedral form. Each atom is strongly bonded to 4 other atoms. This arrangement gives the diamond its high hardness, and thermal conductivity. In graphite, the sp^2 configuration results in a strong bond in 2D planes in addition to a weak bond with the neighboring plane. Each atom is strongly bonded to three other atoms in the same plane and weakly bonded to an atom of the neighboring plane. This arrangement gives graphite its highly anisotropic properties in different directions. In DLC, a portion of bonds are of the sp^3 type and another portion is of the sp^2 type. Also, hydrogen can be added resulting in hydrogenated amorphous carbon (a-C:H). Recently, Ohtake et al. [99] classified 74 types of amorphous carbon film and created an updated ternary diagram representing different amorphous carbon-hydrogen films in terms of concentrations of sp^3 bonds, sp^2 bonds, and hydrogen in the material. This diagram is shown in Figure 1.13.

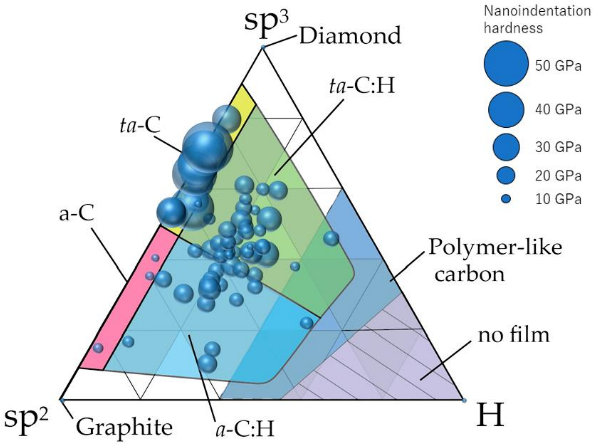

Figure 1.13: Distribution of 74 types of amorphous carbon films on the ternary diagram (sp^2-sp^3-H). The diameter of the circle corresponds to the nanoindentation hardness of each amorphous carbon film. Taken from [98].

Note that when the proportion of sp^3 bonds is high (higher than 70%) the coating is called tetrahedral amorphous carbon (ta-C). With increased hydrogen content it is referred to as hydrogenated tetrahedral amorphous carbon (ta-C:H).

1.3.2 DLC deposition methods

DLC films can be deposited by various atomic deposition processes divided into two main families: Physical Vapor Deposition (PVD) and Chemical Vapor Deposition (CVD). Films are deposited either directly on the surface of the substrate or on a sub-layer already deposited on the substrate. Both types of methods are realized in a vacuum chamber to avoid impurities in the resulting films. In PVD processes the carbon atoms are sourced from the vaporization of a solid block of material (usually graphite) while in CVD carbon atoms originate from the dissociation of bigger molecules (usually from a vapor) through electron impacts. Here, more details are given about CVD and more specifically Plasma-Assisted (or Plasma-Enhanced) Chemical Vapor Deposition (PACVD/PECVD) which was used to create the coatings on components used in this thesis.

In CVD processes, the source gas and the transport medium chemically react at the substrate surface (in case of non-assisted CVD) or in the medium itself before touching the substrate surface (in case of assisted CVD) [100]. In all cases, at least one solid product is produced and deposited on the surface of the substrate. Other products (usually gases) are pumped out of the vacuum chamber. In non-assisted CVD, the substrate needs to be heated to temperatures above 500°C to provide the energy needed for the chemical reaction. Not all materials can withstand such high temperatures. This is where assisted CVD is more advantageous. Given that the chemical reaction happens during the transport (not directly on the surface of the substrate), there is no need to heat the substrate to very high temperatures. Such methods allow the deposition of DLC on almost any type of surface. In addition, PACVD is suitable for depositing thin films on surfaces with complex geometries [101].

PACVD is based on the creation of plasma by an electric discharge between two electrodes in the presence of a gas (usually argon) in a vacuum reactor. Vapor reactants (usually acetylene C_2H_2) are ionized and dissociated by plasma electron impact. The impact produces chemically active ions and radicals that undergo a chemical reaction at or near the substrate surface and result in a thin film deposition [100]. The resulting DLC type and properties are strongly dependent on the parameters of the process. These include, among others, the reactive gas used, the pressure and temperature inside the reactor, and the electric bias between the anode and the cathode.

Deposition methods and their parameters greatly influence the composition and as a consequence the properties of DLC films. In the next section, some of their mechanical, tribological, and thermal properties are presented.

1.3.3 Properties of DLC coatings

The properties of DLC coatings strongly depend on the type of bonds, the hydrogen content, and the type and parameters of the deposition method. In this section, the properties of DLC films are discussed.

In terms of mechanical properties, the hardness of DLC coatings is very high relative to other materials and approaches that of the diamond the higher the content of the sp^3 bonds. It ranges between 5 GPa for soft DLCs with low sp^3 and high H contents to 80 GPa for hard DLCs with high sp^3 content and no H [98,102]. Also, Young's modulus of elasticity spans a wide range from 30 GPa to 800 GPa.

In terms of tribological properties, amorphous carbon coatings present extraordinarily low dry friction and high wear resistance. Grill [102] mentioned that according to [103] friction coefficient between two DLC-coated surfaces can be as low as 0.05 in ambient air. The low dry friction was attributed to the formation of a transfer layer with low shear strength according to Grill [104]. In addition, Grill [104] noted that the properties of the transfer layer can be affected by the type of DLC, the environment, the contact conditions (load and sliding speeds), and the material of the sliding counterpart. Erdemir et al. [105] suggested that the transfer layer is formed by a transformation of the top layer of DLC film into a material of low shear strength. The transformation is caused by thermal and strain effects generated in the sliding contact.

In terms of thermal properties, Tallant et al. [106] tested the thermal stability of DLC at increasing temperatures. They found that the structure and properties of DLC are preserved for temperatures under 260 $°C$. For higher temperatures, the sp^3-bonded carbon starts to convert to sp^2-bonded resulting in nano-crystalline graphite (also referred to as glassy graphite). The conversion is completed for a temperature range of $450 - 600\ °C$ in an inert environment. Robertson [107] showed that hydrogenated DLC has lower thermal stability than non-hydrogenated DLC because of the loss of hydrogen at higher temperatures. experienced by the material. Moreover, the thermal conductivity of thin DLC coatings is not easy to estimate due to its dependence on the sp^3 bond content, the amount of structural disorder, the temperature of the coating, and the interfacial resistance between the coating and the substrate (or sub-layers if present). In literature, thermal conductivity of DLC films was measured by a number of researchers [108–115]. Table 1.1 lists some of the thermal conductivity measurements available in the literature. Values ranged from as low as 0.1 $W/m.K$ in some a-C:H films up to 5 $W/m.K$ in some ta-C films. These values indicate that applying a DLC coating to a steel substrate can thermally insulate the steel depending on the thermal conditions.

Furthermore, DLC coatings are very good electrical insulators with resistivities ranging from $10^2\ \Omega \cdot m$ to $10^{16}\ \Omega \cdot m$ depending on the different types of bonds, hydrogen content, and deposition conditions [116].

Table 1.1: Thermal conductivity data of some DLC thin films from the literature.

Reference	**Measurement method**	**Deposition method**	**Type and composition of DLC**	**Coating thickness (nm)**	**Thermal conductivity $(W/m.K)$**
Morath et al. (1994) [108]	Picosecond thermoreflectance	PACVD	a-C:H with 37 %H	120	0.28 ± 0.1
				240	0.45 ± 0.1
Hurler et al. (1995) [109]	Photothermal method using mirage effect	RF plasma reactor *	a C:H	1000-6200	0.5-1.01
Bullen et al. (2000) [110]	3ω method	PACVD	a-C:H with C:H ratio of 2:1	120	0.1-0.35
				280	0.35-1
				3800	0.5-1.1
Chen et al. (2000) [111]	Pulsed photothermal reflectance	Filtered cathodic vacuum arc	ta-C	20	5.2 ± 1.7
				40	4.25 ± 0.3
				60	4.5 ± 0.25
				80	4.5 ± 0.15
				100	4.3 ± 0.2
Shamsa et al. (2006) [112]	3ω method	PACVD	a-C:H with 28 %H	18-100	0.69
			a-C:H with 30 %H		0.566
		ECWR **	ta-C:H with 28 %H		1.3
			ta-C:H with 30 %H		0.77
		Single band FCVA †	ta-C		2.7
		S-band FCVA †	ta-C		2.2
Arlein et al. (2008) [113]	Ultrafast optical pump probe	PACVD	a-C:H 70 %C and 27 %H	450	0.65
			a-C:H 56 %C and 42 %H	458	0.89
			a-C:H 60 %C and 40 %H	469	0.88
			a-C:H 69 %C and 30 %H	800	1.37
Kim et al. (2010) [114]	3ω method	ion gun	a-C:H	200	0.9
				600	1.6
				1200	1.85
				1800	2.15
Vera et al. (2018) [117]	SThM ‡	PACVD	a-C:H	NA	2.2

* Capacitively coupled parallel plate RF plasma reactor

** ECWR: electron cyclotron wave resonance

† FCVA: filtered cathodic vacuum arc

‡ SthM: Scanning thermal microscopy

1.3.4 DLC in full-film lubrication regime

As mentioned above in section 1.3.3 the DLC films exhibit very low dry friction compared to traditional materials such as steel. Furthermore, DLC coating is used in some applications with a lubricated contact operating under the full-film lubrication regime (i.e. no asperity contact). Many research teams showed a friction reduction in TEHL contacts operating under such conditions when surfaces are coated with an amorphous coating compared to uncoated control cases.

On one hand, some researchers attributed this reduction to wall-slip at the fluid/solid interface [118,119]. They argued that the oleophobic tendency of the coating increases the wall-slip behavior and results in a reduction of up to 20 % in friction. On the other hand, others [84,120–122] showed that the low thermal conductivity of amorphous carbon coating is responsible for friction reduction mainly using numerical simulations. These included a no-slip condition at the fluid/solid interface and were able to demonstrate that thermal insulation alone plays a significant role in friction reduction. However, it is difficult to decisively claim that the thermal properties of the coating are responsible for friction reduction and not the wetting properties [123]. In a recent study, Marian et al. [124] provided an overview of friction reduction techniques by surface modifications and studied experimentally and numerically the effect of using a DLC coating in a cam-tappet contact. They found that friction is reduced by at least 17 % in a DLC-coated contact compared to an uncoated case at all cam rotation speeds. Note that in [124] the numerical model also considered asperity contacts because for low cam rotation speeds the contact operated under a mixed lubrication regime. Björling et al. [120] investigated the effect of thermal insulation by a DLC coating (of thickness $2.8\,\mu m$) on friction in a ball-on-disk experimental setup and corresponding numerical simulations based on the quantitative EHL approach. A 39 % reduction in friction was noted in the case where surfaces were coated with a thin thermal insulation layer compared to the case of the uncoated surface. Similar results were obtained by Bobzin et al. [123] who conducted friction experiments on different DLC coating using a twin-disk test rig. Habchi et al. [121] provided an extensive numerical thermal analysis of circular contact coated with an insulating layer. The thermal insulation layer limits the transfer of shear-generated heat from the lubricant to the contacting solids. This increases the temperature of the lubricant and as a consequence lowers its viscosity. A lower viscosity translates to lower friction with the use of thermal insulation coatings.

In some cases, the use of thermally insulating coatings can attenuate the thermal viscosity wedge effect. Thus, the thermal insulation not only decreases the friction coefficient but also the lubricant film thickness in EHL contacts operating under opposite sliding conditions. Hence, it is important to understand the effects of DLC coatings simultaneously on the film thickness and friction coefficient in opposite sliding conditions (i.e. $SRR > 2$).

This concludes the discussion on the composition, elaboration, and properties of DLC films in addition to their impact on friction in full-film lubrication. Next, the gaps in the literature are identified and the objectives and outline of this thesis are presented.

1.4 Objectives and Outline of the Thesis

Although great advances in experimental and numerical methods have been made in the field of EHL, extreme sliding conditions still represent a challenge.

To the author’s best knowledge, **(i)** there are no studies simultaneously covering film thickness and friction coefficient in EHL contact for a wide range of slide-to-roll ratios especially for opposite sliding ($SRR > 2$) using experimental and numerical methods. Furthermore, **(ii)** EHL literature lacks an investigation of the effect of using thermally insulating coatings simultaneously on film thickness and friction coefficient at $SRR > 2$. Moreover, at such high sliding conditions, the thermal viscosity wedge that is supposed to be one of the most important phenomena allowing good lubrication may be greatly disturbed by the presence of thermally insulating coatings. Finally, most works in the literature concerning DLC coating for friction reduction in the valve train system focused on the benefits in the boundary and mixed lubrication regimes [95,96]. However, **(iii)** little importance is given to high-speed operations where the lubricant gap fully separates the surfaces of the contacting bodies.

This thesis addresses these gaps to deepen the understanding of the thermal effects in EHL contacts at high sliding while focusing on the insulating role of DLC coatings. In Chapter 2, experimental and numerical methodologies are presented along with the materials (solids and fluid) used in this work. In Chapter 3, a dual experimental-numerical investigation of film thickness and friction in wide elliptical TEHL contact is presented for a wide range of sliding conditions (SRR from 0 to 4). Chapter 3 addresses issue **(i)** and highlights the quantitative prediction capacity of the numerical approach. Chapter 4 deals with the thermal effects of DLC coatings in TEHL line contacts related to the issue **(ii)**. Next, Chapter 5 is a dual experimental-numerical study of the influence of DLC-coating on the performance of a cam-follower contact addressing the issue **(iii)**. The numerical model validated in Chapters 3 and 4 is used in transient mode to consider the rapidly changing contact conditions. Experiments are realized on a single-cam test rig replicating a real cam-follower-valve mechanism. Finally, Chapter 6 concludes this work and gives future perspectives.

Chapter 2: Methodology

This chapter presents the experimental and numerical methods used throughout this work. The chapter is divided into two main sections. First, in section 2.1, the experimental methods are presented in addition to the materials used throughout this work. Then, in section 0, the theory and the numerical models are described.

2.1 Experimental Approach

In this work, experiments are realized on two different test rigs:

- A barrel-on-disk tribometer belonging to the "**La**boratoire de **M**écanique des **Co**ntacts et des **S**tructures" (LaMCoS) in Lyon, France, called "JEROTRIB".
- A single cam-follower-valve test rig that replicates a real mechanism taken from a passenger car engine. This test rig called "Monocam", belongs to the "**I**nstitut de **R**echerche **E**n **I**ngenierie des **S**urfaces" (IREIS) in Saint-Etienne, France.

JEROTRIB is a typical EHL laboratory tribometer that enables the study of fundamental contact phenomena in relatively simple geometries. In contrast, the contact studied on the Monocam test rig is closer to the real-world application.

On one hand, the tribometer is used to validate the stationary numerical model by simultaneous film thickness and friction coefficient measurements. On the hand, the cam-follower-valve test rig is used to validate the transient numerical model and investigate the effects of DLC-coatings on the friction coefficient in a cam-follower contact.

2.1.1 Barrel-on-disk tribometer

JEROTRIB is a ball-on-disk tribometer developed at LaMCoS (INSA Lyon) by Molimard et al. [72] to measure film thickness and friction in EHL contacts. This setup was initially developed to measure lubricant film thickness in a point contact between a transparent disk and an opaque ball. Thickness measurement is achieved by Differential Colorimetric Interferometry (DCI). This technique, developed by Molimard et al. [72] for circular contact, was then extended by Wheeler et al. [74] to measure film thickness in elliptical contacts (barrel-on-disk contacts). DCI is based on the idea that the oil gap between the barrel and the disk introduces a difference in the optical path of beams originating from the same light source. As a consequence, reflected light beams produce a color interference pattern. The pattern is captured in an RGB image where colors are representative of the separating film thickness. In [74], Wheeler et al. explained the technique in more detail along with the calibration process. In addition, the test rig is equipped with a multi-axis gauge sensor that records tangential friction force and normal force in the contact zone during the experiment from start to finish.

Kinematics

JEROTRIB setup is schematically represented in Figure 2.1 and is similar to that of Meziane et al. [44].

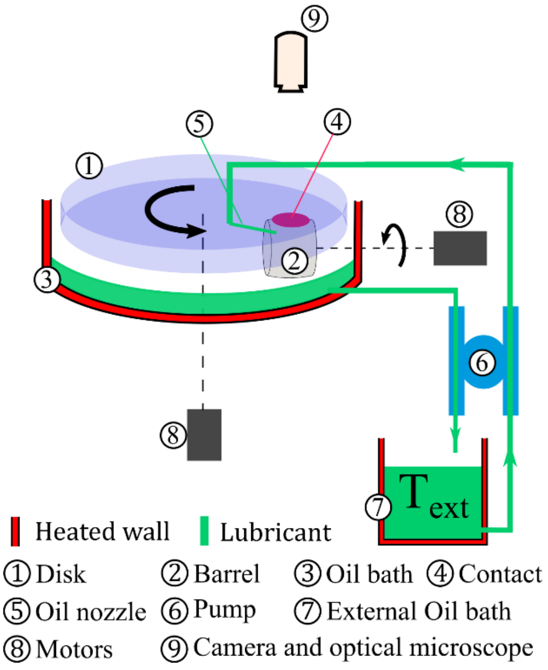

Figure 2.1 Schematic representation of the JEROTRIB setup inspired by [44].

The disk and barrel are mounted on vertical and horizontal axes respectively. Radial runout of the barrel lower than $1 \pm 0.5\ \mu m$ and axial runout of the disk lower than $1.2 \pm 0.6\ \mu m$ are ensured to avoid the cyclic normal contact force during the experiments. The rotations of the disk and barrel are controlled by two independent motors able to rotate in both directions. This is a mandatory feature for this study where a wide range of SRR will be studied. For pure rolling ($SRR = 0$), the tangential surface velocities of both the disk and the barrel are equal and in the same direction at the point of contact. For rolling-sliding ($0 < SRR < 2$), the surface velocities are in the same direction but that of the disk is lower than that of the barrel. The difference in surface velocities causes the sliding at the point of contact. Furthermore, for pure sliding ($SRR = 2$), the disk surface is stationary and the barrel is moving. Finally, for opposite-sliding ($SRR > 2$), the surface velocities are in opposite directions and become equal at ZEV condition ($SRR = \infty$).

The position of the horizontal axis on which the barrel is mounted is controlled by a lever arm, a spring, and a plate so that the barrel can be pushed upward toward the disk. In this manner, the normal load, w_N, of the contact is precisely adjusted.

Solid materials

Two types of transparent disks are used in tribological tests on the JEROTRIB test rig:

- Sapphire disk coated with a very thin ($< 20\ nm$) semi-reflective chromium layer.
- Glass disk (N-BK7) coated with a semi-reflective layer of a-C:H DLC with a silicon (Si) sub-layer to ensure good adhesion of the DLC on glass (SiO_2) material.

Figure 2.2 shows on the left the sapphire disk mounted on the vertical axis of JEROTRIB and the right the DLC-coated glass disk. Transparent materials are required to enable optical measurements and semi-reflective layers are essential for the DCI technique to improve the interference contrast and then the film thickness measurement.

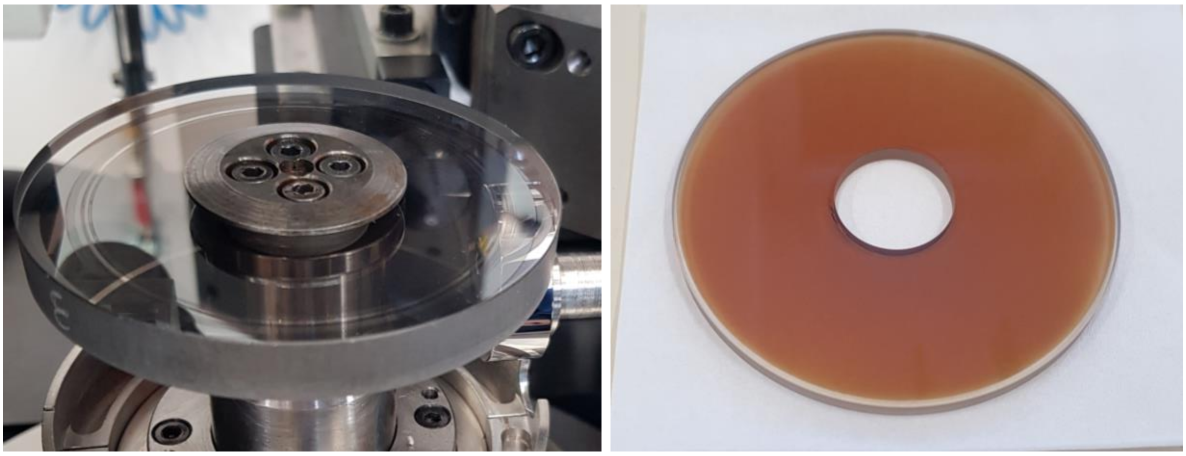

Figure 2.2: Sapphire disk mounted on the vertical axis of JEROTRIB (left). Glass disk coated with a semi-reflective DLC coating (right).

Both disks have the same diameter of 85 mm. The thickness of the sapphire disk is 10 mm to ensure global rigidity in highly-loaded contact cases. In contrast, the thickness of the glass disk is limited to 4 mm to enable the deposition of the DLC coating. The PACVD deposition method described in chapter 1 is applied. The DLC coating thickness is measured to be around 100 nm. A metallic bracket, 6 mm thick, serves to fit the coated glass disk in the test rig and reinforce it. This installation is shown in Figure 2.3.

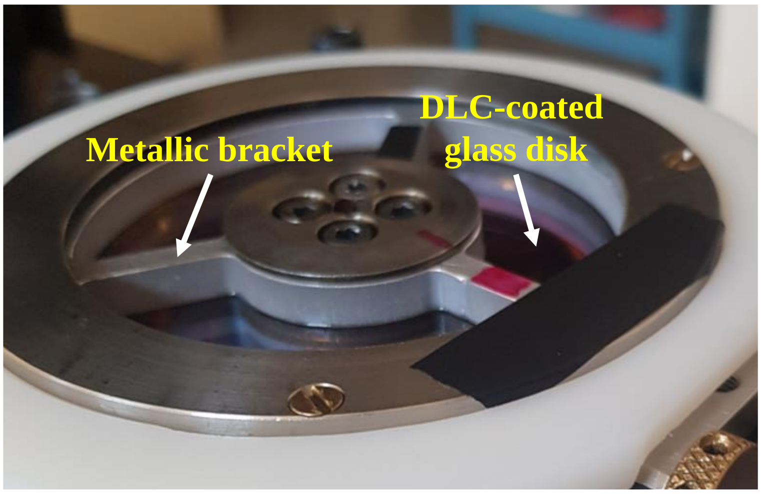

Figure 2.3: Mounted DLC-coated glass disk with a metallic bracket positioned above the disk to compensate for the thickness of the disk and reinforce it.

The DLC coating hardness and Young's modulus were measured by IREIS using nano-indentation on a 2.5 μm thick coating deposited by the same process and in the same conditions as that deposited on the disk. Nano-indentation cannot be used on very thin coatings because indentation depth must be limited to 10 % of the total coating thickness [98]. Hardness is found to be 12.75 GPa while the Young's modulus is calculated to be 99 GPa assuming a Poison's ratio equal to 0.2.

It is very challenging to characterize all the properties of thin DLC coatings needed as input to the numerical model, especially thermal properties. To estimate these properties, other known properties are coupled with those of DLC coatings already characterized in the literature. Shamsa et. al [112] measured the thermal properties of a comprehensive set of DLC films ranging from a-

C:H to ta-C:H with thicknesses between 18.5 and 100nm (see Table 1.1). In [112], the properties of an a-C:H film prepared by PECVD, with a hydrogen content of around 28 % correspond to the coating applied on the glass disk. Moreover, Young's modulus of the sample is measured in [112] to be 95 GPa which is very close to the 99 GPa measured for the current coating. Shamsa et. al [112] also reported the thermal conductivity ($0.69\ W/m.K$) and the density ($1760\ kg/m3$). These values are considered for the coating applied on the glass disk in this work. Furthermore, Hakovirta et al. [125] proposed an expression to estimate the heat capacity Cp of DLC films. This expression is given by (2.1)

$$Cp\ (J/g.K) = A + 0.006\ c_H \tag{2.1}$$

with

$$A\ (J/g.K) = \begin{cases} 0.79, & for\ pure\ sp^2 \\ 0.62, & for\ pure\ sp^3 \end{cases}$$

and c_H the Hydrogen percentage. Here $c_H = 25\ \%$ is assumed resulting in Cp between 0.77 (pure sp^3) and 0.94 (pure sp^2). By assuming that for the current a-C:H coating the sp^3 content is about 50 %, and by interpolating the value of A, the heat capacity is calculated by (2.1) to be $Cp = 0.855\ J/g.K = 855\ J/kg.K$.

The main physical properties (Young's modulus, Poisson's ratio, and density) in addition to thermal properties (conductivity and heat capacity) of the materials of the disks and the semi-reflective DLC coating are given in Table 2.1.

Table 2.1: Physical and thermal properties of the sapphire disk, the N-BK7 glass disk, and the semi-reflective DLC coating.

Property	**Unit**	**Value**		
		Sapphire	N-BK7 glass	Semi-reflective DLC coating
Young's Modulus, E	Pa	360 x 10^9	81 x 10^9	99 x 10^9 *
Poisson's ratio, ν	$-$	0.34	0.208	0.2
Density, ρ	kg/m^3	4000	2510	1760 †
Thermal conductivity, k	$W/m.K$	40	1.114	0.69 †
Heat capacity, Cp	$J/kg.K$	750	858	855 ‡

* Measured by IREIS with the assumption of $\nu = 0.2$

† Taken from a similar DLC coating in Shamsa et al. [112]

‡ Calculated using equation (2.1) taken from Hakovirta et al. [125]

On one hand, the sapphire disk is chosen because its mechanical and thermal properties have the same order of magnitude as that of steel (see Table 2.2). Sapphire disk is used in experiments against a steel barrel to mimic a steel-steel contact. In such conditions, the contacting surfaces are thermally conductive. On the other hand, the coated glass disk is used in experiments against a DLC-coated barrel. In this configuration, the contacting surfaces are considered thermally insulating.

In addition to the disks presented above, two barrels were used in the experiments on JEROTRIB. Two identical steel barrels with radii are $R_{b,x} = 13\ mm$ and $R_{b,y} = 330\ mm$ are machined from 100C6 steel rollers similar to that shown in Figure 2.4.

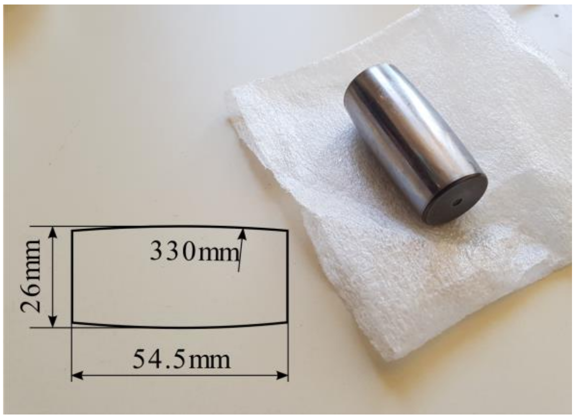

Figure 2.4: 100C6 hardened steel roller. With main dimensions in mm.

After machining, the barrels are polished with a diamond paste of decreasing particle sizes until a mirror-like finish is reached. This ensures a root mean squared (RMS) roughness parameter $Rq < 8\ nm$. One of the barrels is coated by IREIS with a DLC coating commercially called Certess™ DDT. Coated and uncoated barrels are shown in Figure 2.5.

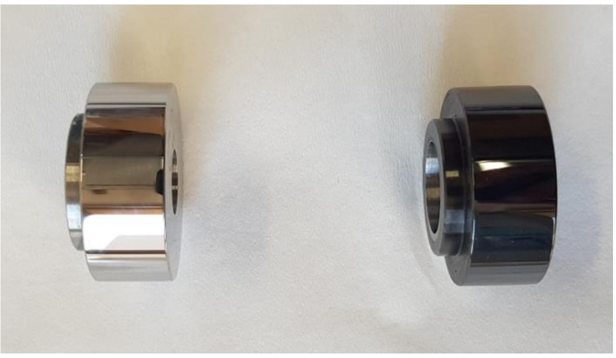

Figure 2.5: Uncoated steel barrel (left). DLC-coated steel barrel (right).

The coating is composed of a tungsten carbide/carbon (WC,C) adhesion sub-layer (0.7 μm thick) in addition to an a-C:H DLC layer (2.8 μm thick). The coating is deposited by PACVD resulting in 20-25 % hydrogen content.

In general, the surface finish of the coating is similar to that of the substrate in terms of roughness. However, during the deposition of the DLC, some needle-like aggregations of material may appear. These can reach a height of a few micrometers. These surface defects were easily broken using abrasive papers (P1200 grade) in preparation for tribological testing.

The coating used in Vera et al. [117] is similar to the one used in the current work. Its thermal conductivity was measured by Scanning Thermal Microscopy (SThM) to be 2.2 $W/m.K$. Furthermore, according to [110] and [112], thermal conductivity of an amorphous carbon coating increases with its density. Furthermore, equation (2.2) adapted from [112] is a linear fit to their measurements and it relates the thermal conductivity k to the density ρ.

$$\rho = \frac{1000(k + 2.82)}{1.77} \tag{2.2}$$

Considering that the thermal conductivity of the coating used on steel parts in this work is 2.2 $W/m.K$, its density is calculated from (2.2) to be around 2840 kg/m. The heat capacity of the coating deposited on the steel barrel is calculated in the same way as that of the semi-reflective coating on the glass disk.

Table 2.2 summarizes some physical and thermal properties of 100C6 steel and a-C:H DLC coating.

Table 2.2: Physical and thermal properties of the 100C6 steel, and a-C:H DLC coating.

Property	**Unit**	**Value**	
		100C6 steel	a-C:H DLC coating
Young's Modulus, E	Pa	210 x 10^9	-
Poisson's ratio, ν	$-$	0.3	-
Density, ρ	kg/m^3	7850	2840 †
Thermal conductivity, k	$W/m.K$	21*	2.2 ‡
Heat capacity, Cp	$J/kg.K$	470	855§

* Measured by Reddyhoff et al. [126] for hardened steel

† Calculated using equation (2.2) taken from Shamsa et al. [112]

‡ Measured by Vera et al. [117] using SThM for a similar DLC coating

§ Calculated using equation (2.1) taken from Hakovirta et al. [125]

Lubrication and temperature regulation

The lubricant is supplied directly to the contact via a nozzle and by entrainment of the lubricant partly submerging the bottom part of the barrel as shown in Figure 2.6.

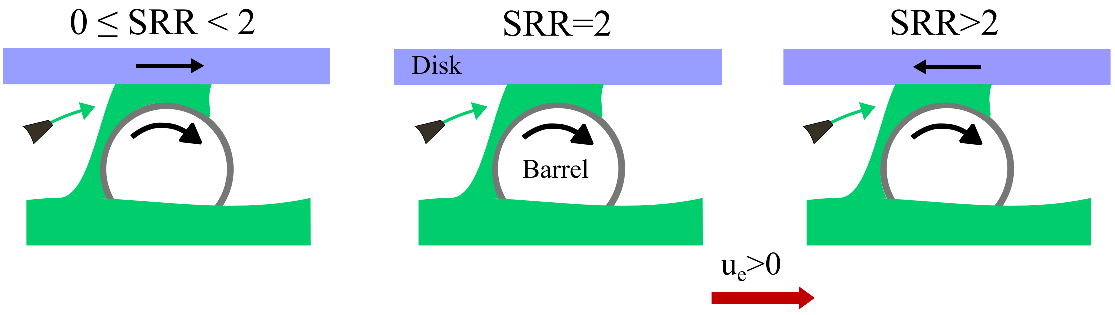

Figure 2.6: Representation of possible configurations of the rotating barrel and disk. In addition, contact lubrication via the nozzle and by lubricant entrainment is illustrated.

An external oil bath serves as a lubricant reservoir. The walls (colored in red in Figure 2.1) of the main and external oil baths (#3 and #7 in Figure 2.1 respectively) and the spindles of the motors are maintained at a constant temperature by an external thermal regulator. The temperature of the heating fluid is fixed by the regulator to a higher temperature than the desired temperature entering the contact (T_0) for a given test. The heating fluid passing through the walls of the bath is set Lubricant is pumped from and to the external bath by a peristaltic pump with a volumetric flow rate of 350 ml/min measured at room temperature (i.e. 20°C). A thermocouple placed at a fixed position inside the external oil bath records the temperature T_{ext} throughout the experiment. However, the exact temperature T_0 of the lubricant entering the contact is influenced by different factors. First, it is influenced by the temperature of the lubricant in the bottom of the main oil bath which is entrained by the barrel into the contact. Due to the difficulty of instrumenting the lubricant in this oil bath by a thermocouple, its temperature is not exactly known. Second, T_0 is influenced by the temperature of the oil projected from the nozzle which is potentially at a different temperature than that of the bath. Third, the inlet temperature depends on the temperatures of the surfaces entering into the contact which are unknown. All these factors make knowing T_0 with enough precision very difficult. Details about overcoming this issue are given in Chapter 3.

Test procedure

One hour before starting the calibration process and the test, the thermal regulator is turned on to get all parts of the system to the desired temperature. For the sapphire disk, the calibration phase consists of collecting pairs of interference images (white and monochromatic) for a lightly-loaded static contact ($w_N = 10\ N$). Calibration curves are obtained by applying the method developed in [74]. The calibration phase was slightly modified for the DLC-coated glass disk because its transmissivity is not uniform all around the disk. Different optical paths lead to different calibration curves at different locations on the disk and to a deterioration in the accuracy of thickness measurements. Details about how this challenge was overcome are in Appendix A.

Before starting the images and signals acquisition, the barrel and the disk are rotated in pure rolling ($SRR = 0$) with the desired entrainment velocity and no normal load for 15 minutes. Next, the load is applied, signal recording is started, and sliding conditions are tested one after the other going from pure rolling to opposite sliding with intermediate conditions. In the end, the pure rolling condition is revisited to control any deviation in the value of friction force measurement.

Measurements

At each tested condition, images are collected at least 7 minutes after the transition from the previous sliding condition for the temperature to stabilize. At least 30 images are collected for each condition of which 10 are randomly chosen for the analysis to ensure the repeatability of the measurements. An image analysis MATLAB program inspired by the work of Doki-Thonon [127] was developed. The image analysis process is schematized in Figure 2.7.

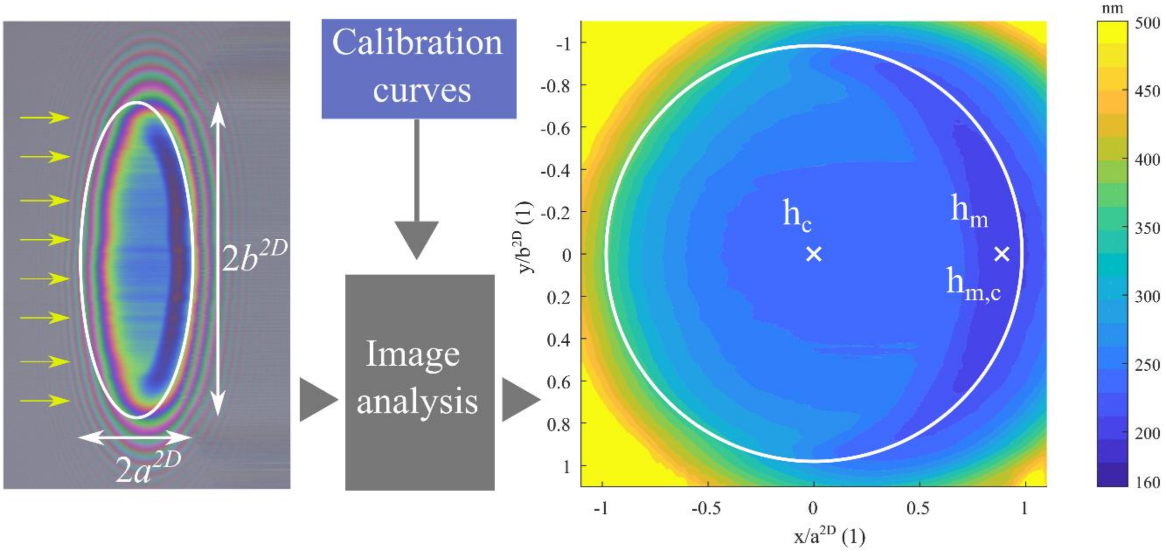

Figure 2.7: Process of image analysis of an interference pattern in an elliptical contact between a steel barrel and a sapphire disk at $SRR = 0$. The result is a 2D average map showing film thickness distribution in the contact region. a^{2D} and b^{2D} are semi-minor and semi-major axes length of the ellipse respectively. Yellow arrows indicate the lubricant's entrainment direction.

The left-side image is an example of the interference pattern of an elliptical contact between a steel barrel and a sapphire disk at $SRR = 0$. The contact region is defined by the ellipse whose semi-minor and semi-major axes lengths are a^{2D} and b^{2D} respectively. a^{2D} and b^{2D} are calculated using the dry contact Hertz theory detailed in section 2.2.1.

Note that x and y axes are normalized by a^{2D} and b^{2D} respectively resulting in a circular representation of the elliptical contact on the right side of Figure 2.7. Yellow arrows indicate the entrainment direction of the lubricant. Interference images are passed along with calibration curves through the image analysis program to obtain a single film thickness map (shown on the right side of Figure 2.7) by averaging results from 10 different images acquired at a given sliding condition. Different thickness levels are represented by different colors ranging from blue (lowest thickness) to yellow (highest thickness). A correction is applied to account for the pressure dependency of the refraction index of the oil by assuming a Hertzian pressure distribution. Minimum film thickness (h_m), minimum thickness on the central line ($h_{m,c}$), and central thickness (h_c) are calculated and their corresponding locations are marked with white "x" marks. Also, a standard deviation is calculated from the set of 10 different thickness values deduced from each image at a given sliding condition. The standard deviation is represented in results plots as error bars above and below the average value and reflects how well the average value is representative of all the individual measurements.

In terms of recorded signals, the initial acquisition frequency is 1000 Hz. Data is then exported at the frequency of 100 Hz and analyzed in a signal analysis program. In addition to normal and tangential forces, external lubricant bath temperature, and motors' speeds are recorded and exported. Next, the noise in the signals is filtered using the Savitzky-Golay filter, and any deviation in sensor measurements over time is corrected. The friction coefficient C_f for a given SRR is defined as the mean of the ratio $\frac{F_T}{w_N}$ over the time t_{SRR} elapsed in this sliding condition where F_T and w_N are respectively the force tangent to the entrainment direction and the force in the normal direction. Note that after noise filtering the force signals, a standard deviation from the mean value over t_{SRR} is calculated. This standard deviation is represented as error bars attached to resulting experimental data points and reflects the noise level in the filtered signals.

2.1.2 Monocam test rig

In addition to the tribometer described above, a single cam-follower-valve test rig is used to study the friction response of a cam-follower contact for different material configurations (uncoated steel and DLC-coated steel). The test rig replicates a real mechanism taken from an M9R Renault-Nissan passenger car engine.

Kinematics

Figure 2.8 is a simplified schematic representation of the Monocam setup. An electric motor, able to rotate in both directions up to a speed of 6000 rpm, is coupled to the shaft of a metallic flywheel. The latter ensures the stability of the speed of rotation. Its shaft is coupled from the other side to the camshaft. A torque-measuring flange system is mounted on the camshaft outside the metallic test chamber. It is composed of a rotor fixed on the camshaft which captures the torque generated in the camshaft using strain gauges and transmits the signal to a stator placed precisely underneath it (technical descriptions of these components are found in [128,129]). This system enables the measuring of highly dynamic torques found in a variety of automotive applications.

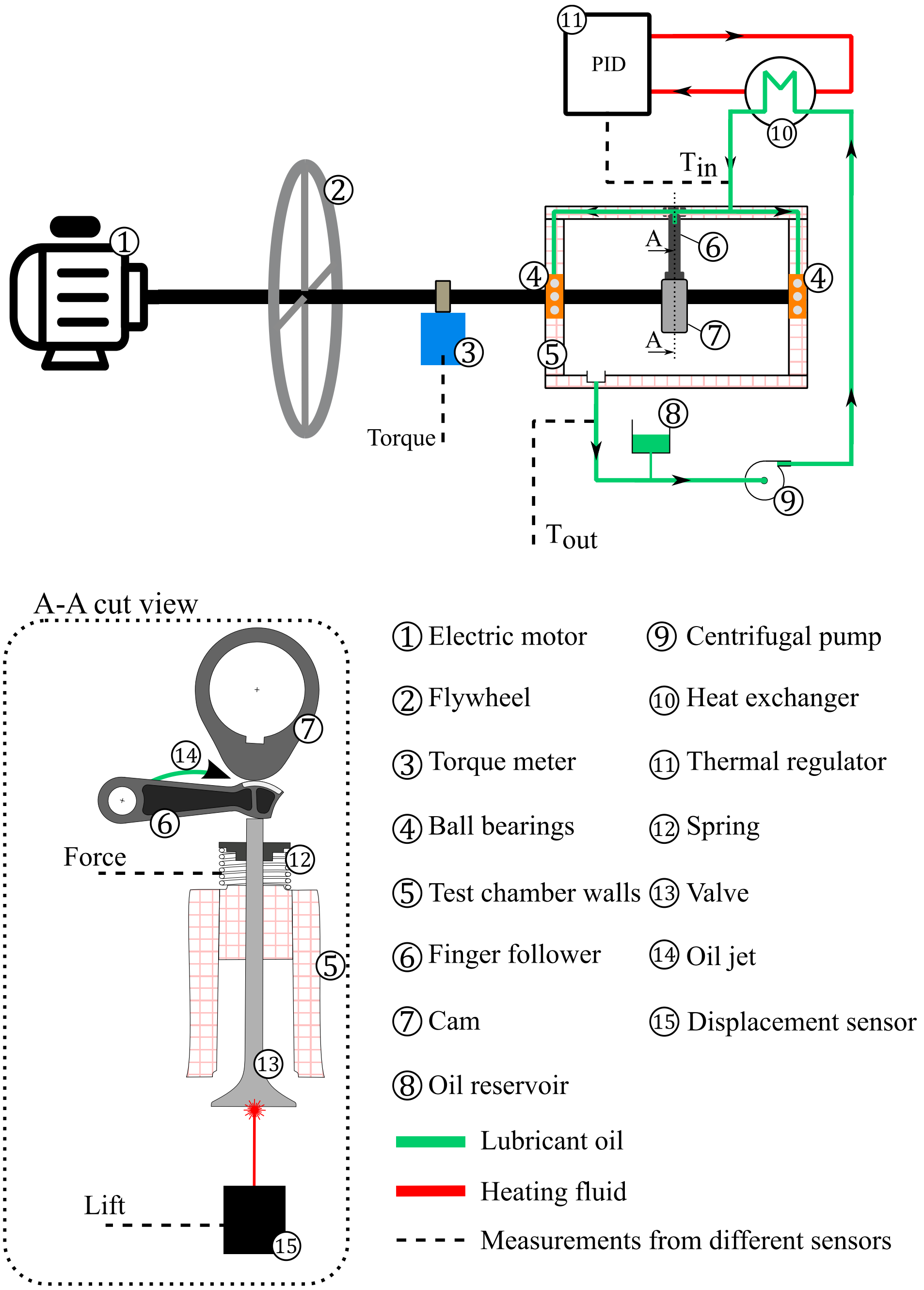

Figure 2.8: Schematic representation of the Monocam setup.

A finger follower is mounted on a pin to the side wall of the test chamber. The camshaft placed on top of the follower is held by two ball bearings allowing it to rotate freely while being constrained from translation motion. The A-A cut view shows the arrangement more clearly.

The cam can rotate in the clockwise (CW) or counter-clockwise (CCW) directions. Each rotation direction results in a different kinematic behavior of the contact point throughout the rotation cycle. Starting from the theoretical valve lift profile and the geometry of the cam-follower-valve mechanism, the equations in [11] are used to study this kinematic behavior of the cam-follower contact. The respective positions of the contact point on the upper pad during the CCW and CW rotations of the cam are presented in Figure 2.9.

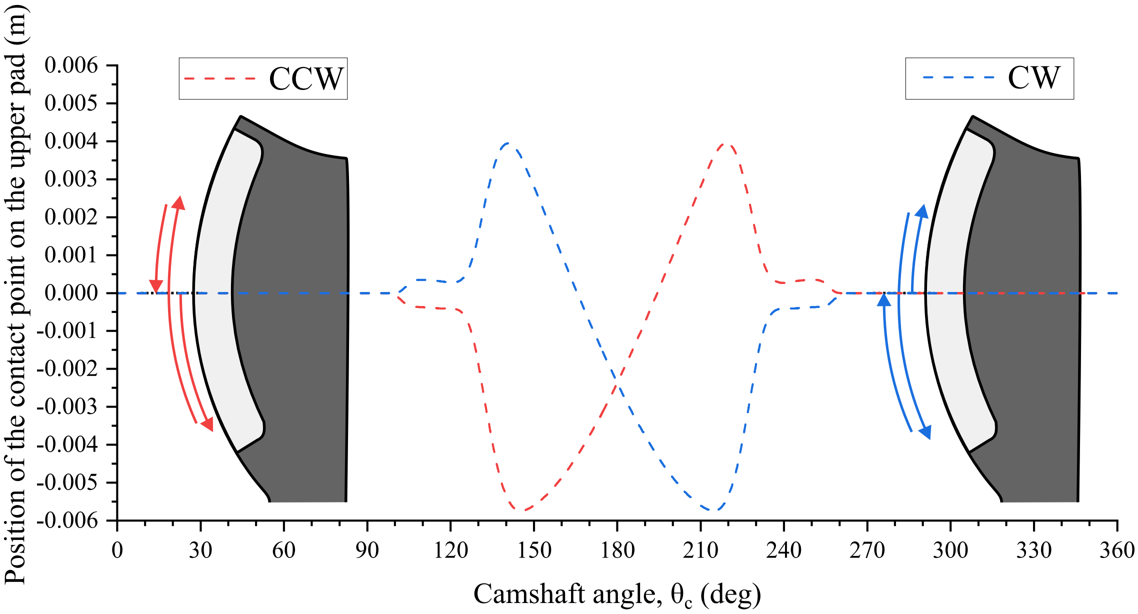

Figure 2.9: Variation of the position of the contact point on the upper pad of the follower with the camshaft rotation angle. In addition, the drawings show the motion of the point of contact on the upper pad.

Note that in the case of CCW rotation the point of contact moves in the negative direction first in contrast with the case of CW direction where the point of contact moves in the positive direction. The same extreme positions are reached in both cases but at different rotation angles during the rotation cycle. The position variation is independent of the rotation speed given that it is calculated based on the rotation angle of the cam.

Figure 2.10 and Figure 2.11 respectively show the variation of the velocity of the contact point on the upper pad and on the cam with the camshaft rotation angle.

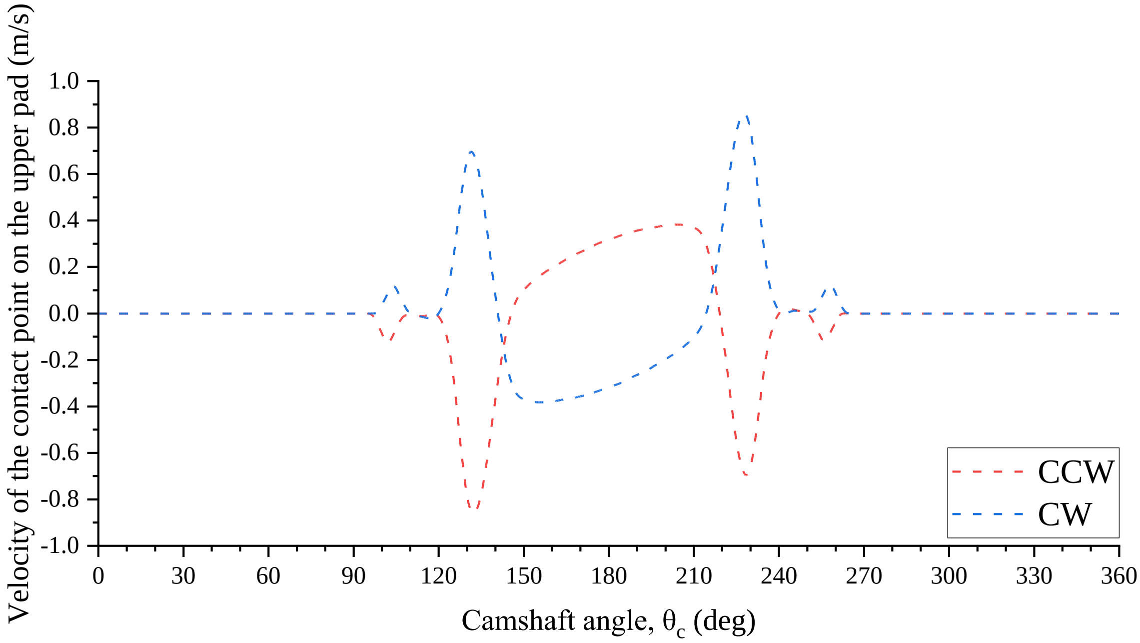

Figure 2.10: Variation of the velocity of the contact point on the upper pad of the follower with the camshaft rotation angle. The cam rotation speed is set to 350rpm.

For a given rotation direction, the velocity of the contact point on the upper pad alternates between positive and negative values reflecting the changes in the direction of motion shown in Figure 2.9.

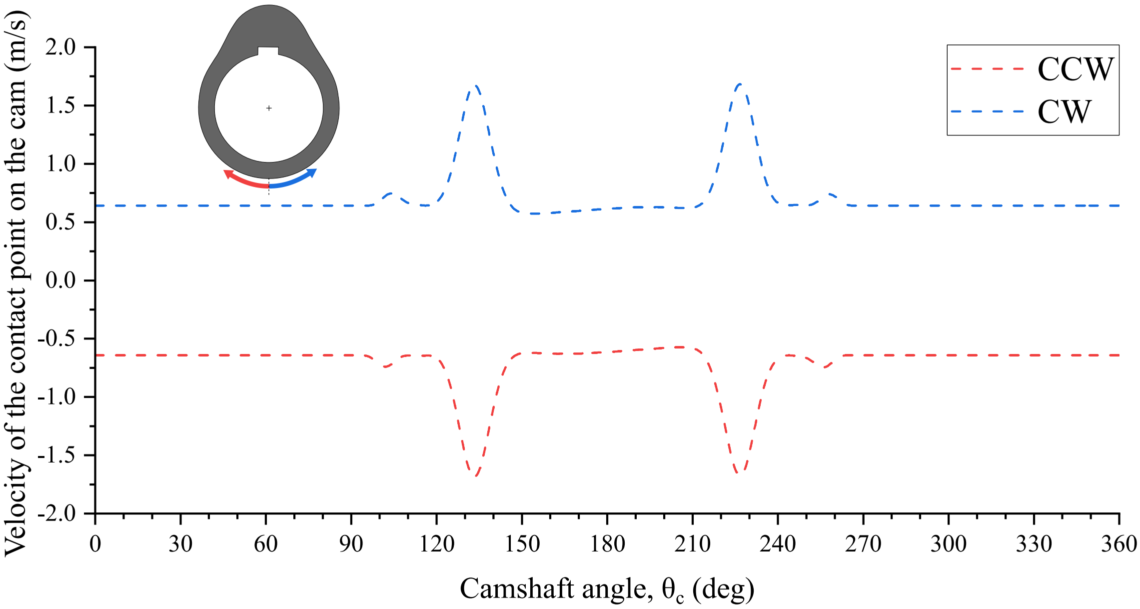

Figure 2.11: Variation of the velocity of the contact point on the cam with the camshaft rotation angle. The cam rotation speed is set to 350rpm.

In contrast, for a given cam rotation direction, the velocity of the contact point on the cam is either positive (if CW rotation) or negative (if CCW rotation). This is because the point of contact moves around the cam profile unidirectionally during a rotation cycle. The directions of motion of the contact point on the cam are depicted by arrows on the cam drawing in Figure 2.11. The magnitude of the velocities in Figure 2.10 and Figure 2.11 scales linearly with the rotation speed of the camshaft.

Instead of presenting the velocity of the point of contact with respect to the upper pad or the cam, one can present the velocities of the upper pad and cam surfaces with respect to the point of contact. Meaning that the frame of reference can be fixed to the contact point. This perspective is suitable to study the evolution of contact conditions during the rotation cycle. Hence, the velocities shown in Figure 2.10 and Figure 2.11 can be assigned to the upper pad and cam surfaces respectively. Furthermore, the mean entrainment velocity in the cam-follower contact is calculated and its variation is shown in Figure 2.12. The entrainment velocities (i.e. average velocity between the velocities of the surface of the cam and the upper pad given by (1.1)) are presented as positive values because from the perspective of the point of contact positive and negative entrainment velocities are equivalent. Moreover, the magnitude of the entrainment velocity scales linearly with the rotation speed of the camshaft.

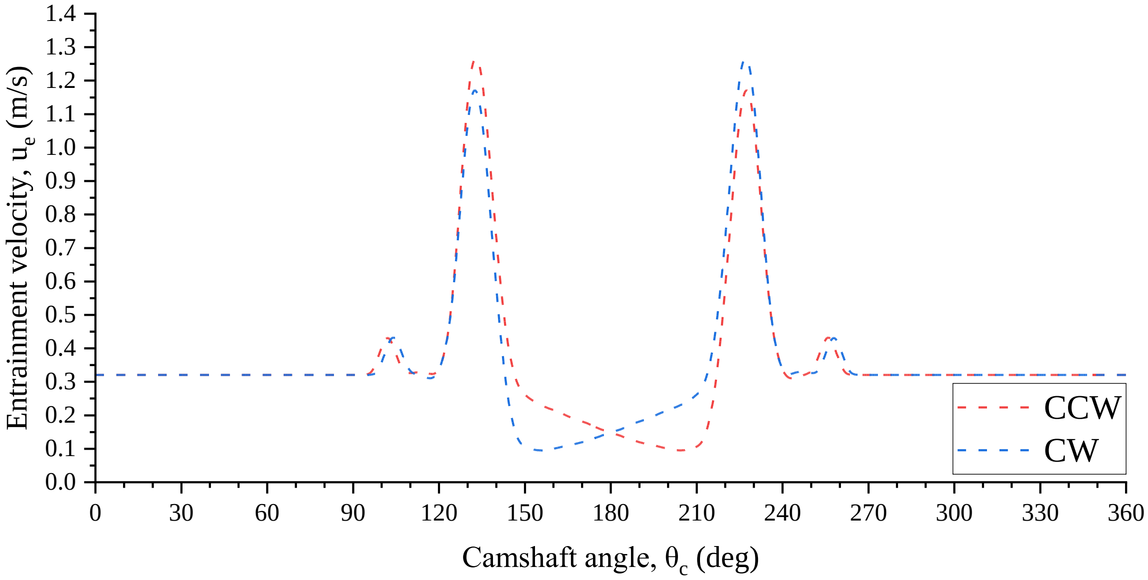

Figure 2.12: Variation of the entrainment velocity in the cam-follower contact. The cam rotation speed is set to 350rpm.

In addition to the entrainment velocities, the slide-to-roll ratios are calculated for CW and CCW camshaft rotation directions. Figure 2.13 presents the variation of the SRR given by (1.2) in the cam-follower contact with the camshaft rotation angle for CW and CCW rotation directions.

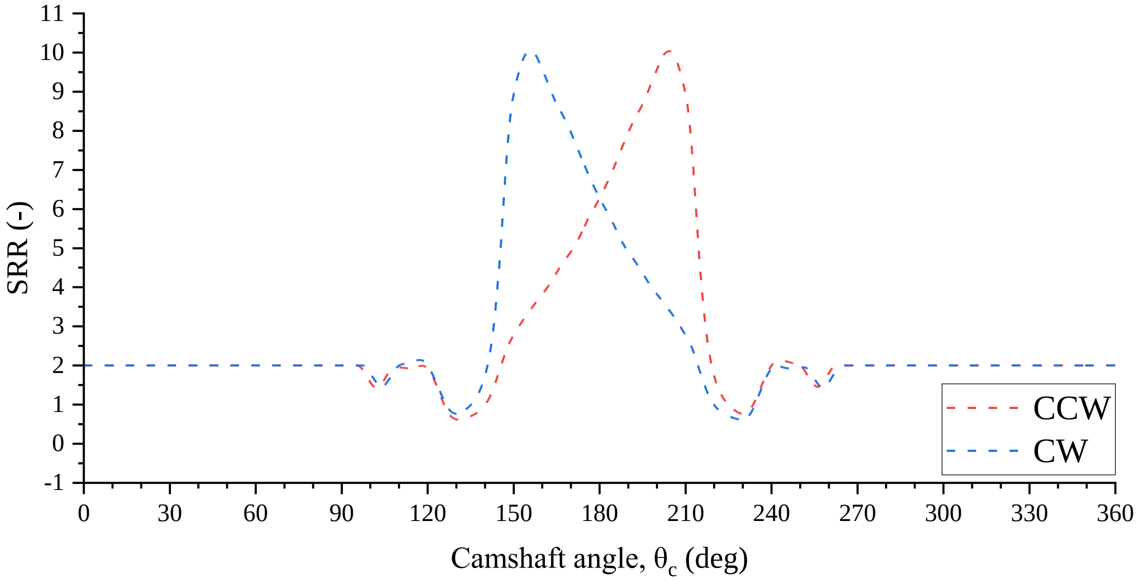

Figure 2.13: Variation of the SRR in the cam-follower contact with the camshaft rotation angle. The camshaft rotation speed is set to 350rpm.

It should be noted that the SRR is independent of the rotation speed of the camshaft. The SRR peaks at different angles during the rotation cycle for CW and CCW rotation directions. However, the SRR maximum occurs in the same location on the upper pad and the cam regardless of the rotation direction.

While the radius of curvature of the upper pad is fixed at 0.012 m, the radius of curvature of the cam (with respect to the point of contact) varies during the rotation cycle. A reduced radius, R, defined in (2.3) is useful to convert the contact from being between two curved surfaces (the pad and the cam) to a contact between a cylinder with a radius equal to R and a plane. In (2.3), R_t

and R_b are the radii of curvature of the surface of the cam and the upper pad of the follower respectively.

$$R = \frac{1}{\frac{1}{R_t} + \frac{1}{R_b}} \tag{2.3}$$

Figure 2.14 shows the variation of the reduced radius of curvature, R, with the camshaft angle. The two large peaks in the variation of R corresponds the passage of the concave parts of the cam (i.e. conformal contact).

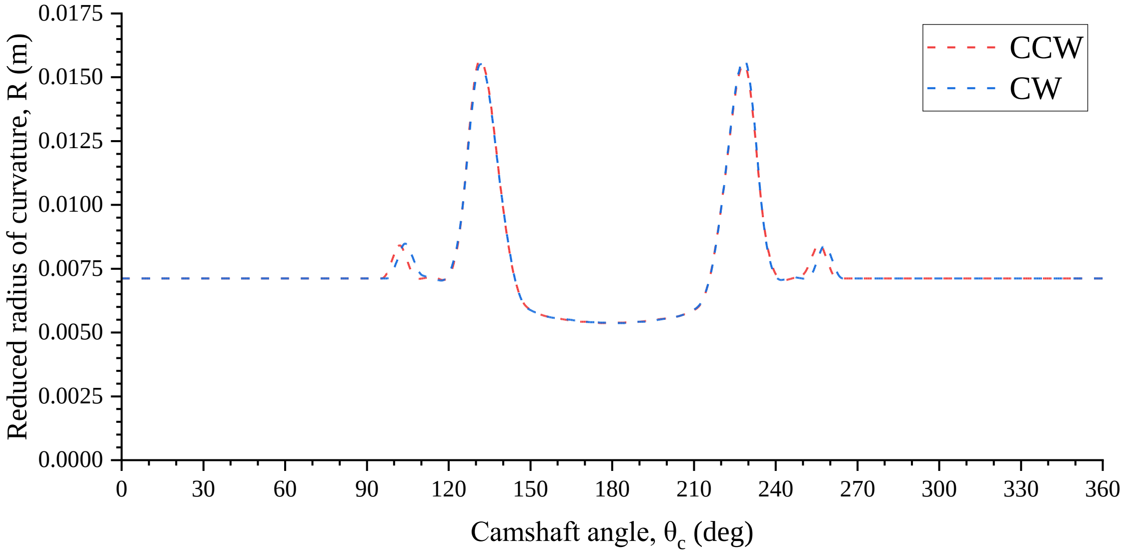

Figure 2.14: Variation of the reduced radius of curvature R with the camshaft rotation angle.

The normal load w_N supported by the cam-follower contact can be calculated based on the dynamics and geometry of the cam-follower-valve mechanism. Details about calculating w_N are provided in Appendix B. Figure 2.15 shows the variation of the normal load w_N with the camshaft rotation angle for 3 rotation speeds (350 rpm, 1070 rpm, and 2030 rpm) and for CCW and CW rotation directions.

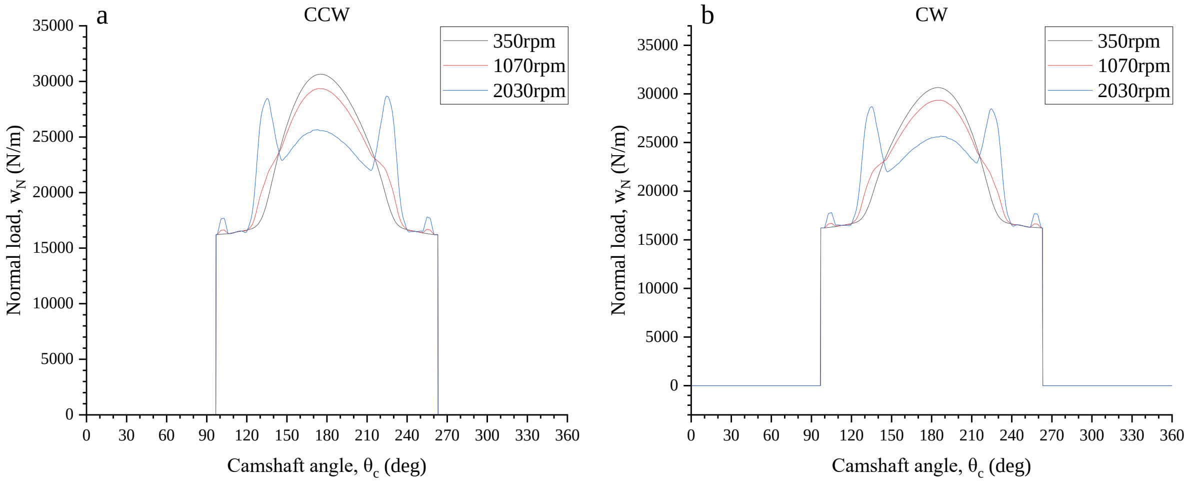

Figure 2.15: Variation of the normal load, w_N, with the camshaft rotation angle for 3 rotation speeds (350rpm, 1070rpm, and 2030rpm) and for (a) CCW and (b) CW rotation directions.

The large differences in the variation of w_N between different rotation speeds are caused mainly by inertial forces. At a low rotation speed, the contribution of the fluctuations in the acceleration of the valve is insignificant. Hence, the normal load is controlled mainly by the spring force which pushes the follower against the cam. At a higher rotation speed, however, the influence of inertia forces becomes more significant.

The variations of the different parameters discussed above are used as inputs to the transient TEHL contact simulations of Chapter 5.

Solid materials

Two identical cams made of hardened steel (100C6) are used for tests on the Monocam test rig. One of which is coated by PACVD with 2.8 μm layer of a-C:H DLC with an adhesion sublayer of tungsten carbide/carbon (WC,C). This coating is similar to that applied on the barrel of the JEROTRIB tribometer. Both cams are shown in Figure 2.16.

Figure 2.16: Photographs of the cams used in the experimental campaign on the Monocam test rig. Uncoated steel cam (left) and DLC-coated steel cam (right).

The profiles of the cams are measured to accurately calculate the theoretical valve lift profile essential to find the variation of the contact parameters during a rotation cycle.

Also, the RMS roughness parameter R_q of steel surfaces is found to be below 50 nm after polishing the surfaces. The roughness of the DLC coating is similar to that of the steel surface on which it is deposited ($R_q < 50\ nm$).

In addition to the cams, two identical hardened steel (W300) finger followers (shown in Figure 2.17) are tested. One of which is coated by PACVD with 2.8 μm layer of a-C:H DLC with adhesion sublayers of tungsten carbide/carbon (WC,C) and Chromium nitride (CrN).

The coating applied on the follower is commercialized under the name Certess™ DCZ and has properties similar to the coating applied on the steel cam and barrel (i.e. name Certess™ DDT). In addition, the surface roughness of the upper pads of both followers is characterized by $R_q < 50\ nm$. The upper limit of the resulting composite roughness for the cam-follower contact is calculated as $R_q = \sqrt{R_{q,1}^2 + R_{q,2}^2} = \sqrt{50^2 + 50^2} \cong 70\ nm$ where $R_{q,1}$ and $R_{q,2}$ are root mean squared roughness of the surfaces of the cam and follower respectively.

Table 2.3 lists some physical and thermal properties of the W300steel of which the cams and followers are made.

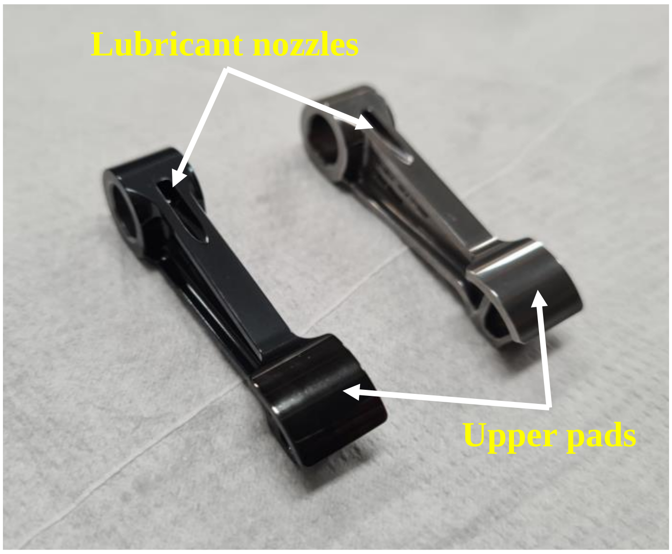

Figure 2.17: A photograph of the followers used in the experimental campaign on the Monocam test rig. DLC-coated steel follower (left) and uncoated steel follower (right).

Table 2.3: Physical and thermal properties of the W300 hardened steel, 100C6 hardened steel, and a-C:H DLC coating.

Property	**Unit**	**Value**		
		W300 steel ISODISC® **	100C6 steel	a-C:H DLC coating
Young's Modulus, E	Pa	215 x 10^9	210 x 10^9	-
Poisson's ratio, ν	$-$	0.3	0.3	-
Density, ρ	kg/m^3	7800	7850	2840 †
Thermal conductivity, k	$W/m.K$	24.9	21*	2.2 ‡
Heat capacity, Cp	$J/kg.K$	460	470	855§

* Measured by Reddyhoff et al. [126] for hardened steel
** Taken from the datasheet of the material [130]
† Calculated using equation (2.2) taken from Shamsa et al. [112]
‡ Measured by Vera et al. [117] using SThM for a similar DLC coating
§ Calculated using equation (2.1) taken from Hakovirta et al. [125]

The DLC coatings on the cam and the follower serve as an anti-wear protective layer in case mixed or boundary lubrication occurs. However, as referred to in Table 2.3, the DLC coatings have a thermal conductivity that is almost 10 times lower than that of steel. Thus, they also act as heat-insulating layers depending on the thermal conditions experienced by the materials. This can affect the tribological behavior of the cam-follower mechanism when operating under EHL conditions, which is one of the main concerns of this thesis.

Lubrication and temperature regulation

The cam-follower contact is lubricated by the direct projection of commercial engine oil from a nozzle in the follower (#14 in Figure 2.8). On one hand, if the cam is rotating in the CCW direction then the projected oil gets entrained into the contact by the motion of the cam. On the other hand, if the cam is rotating in the CW direction the projected oil lubricates the cam surface exiting the contact. Thus, the direction of rotation might influence the friction response of the cam-follower contact. In addition to the cam-follower contact, the ball bearings are lubricated with the same lubricant. Lubricant oil is drained through a sink at the bottom of the test chamber. An oil reservoir ensures that the lubricant circuit is always filled. The lubricant is pumped by an electric centrifugal pump at a pressure of 350 kPa. Then, it passes through a filter into a heat exchanger where it is heated by a heating fluid from a thermal regulator. The temperature to be controlled is T_{in} of the lubricant at the inlet of the test chamber. A thermocouple measures T_{in} and transmits the measurement to the proportional – integral – derivative (PID) controller of the thermal regulator which is set to the desired temperature. Thus, the heating power is automatically adjusted to accommodate T_{in} to the setpoint of the regulator. The pressure of lubricant flowing to the ball bearings is controlled by a valve set to 100 kPa. In addition to T_{in}, the temperature T_{out} of the lubricant exiting the chamber is measured by another thermocouple.

Test procedure

The following test procedure was used in the current work realized on Monocam test rig. The temperature of the lubricant T_{in} entering the test chamber is set to the desired temperature. CW and CCW cam rotation directions are tested to account for the differences in contact kinematics and lubrication. For each rotation direction, speed is varied in steps of 240 rpm from 350 rpm to 2030rpm in ascending and then descending to ensure the repeatability of the measurements. Signals are recorded at the end of each step after a stabilization period of 4 minutes (i.e. the time needed for the torque reading to stabilize).

The following steps are realized before every test:

- Power up the electronics (PC, signal recorder, sensors, etc.).
- Turn on the electric pump to increase the pressure in the lubricant system to 350 kPa.
- Turn on the thermal regulator if the test temperature is above room temperature.
- Wait until the temperature is stabilized.
- Align the flywheel/camshaft to have the nose of the cam pointing upwards which indicates its 0° angular position.
- Turn on the electric motor and start the test by increasing the rotation speed.
- If the cam and/or the follower are used for the first time a run-in period of 2 hours is required at an inlet oil temperature of $80°C$ and a rotation speed of 500 rpm, else if the cam and follower are already used the test can start directly.

Measurements

Signals from different sensors are recorded at a fixed sampling rate of 102.4 kHz. Signals over 5 camshaft cycles are then analyzed using a signal analysis script.

An optical displacement sensor is placed vertically underneath the moving valve. It records the cyclic variation of the lift of the valve during the rotation of the cam. Also, a piezoelectric force sensor measures the force generated due to the compression of the valve spring. Figure 2.18 shows an example of the experimental lift profile and the spring force variation with the camshaft rotation angle. The curves are obtained by averaging these quantities over 5 cam cycles and applying a filter to smooth the curves.

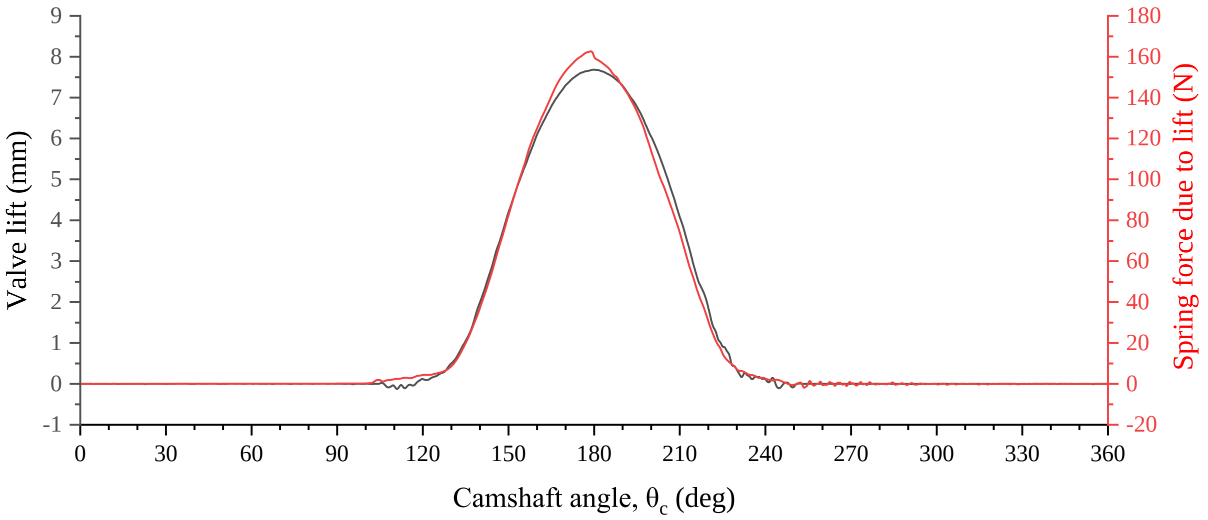

Figure 2.18: Variation of the experimental valve lift (left axis) and spring force (right axis) with camshaft angle. In this example, the cam and follower are made of uncoated steel and the rotation speed of the cam is 350 rpm in the CW direction at $T_{in} = 50°C$.

Note that even at zero valve lift the spring is pre-compressed and has a pre-compression force equal to 200 N. Hence, the total spring force is obtained by adding 200 N to the spring force due to the valve lift when the cam and follower are in contact (i.e. when the lift is not zero). The total spring force is used in the dynamic analysis of the cam-follower-valve mechanism detailed in Appendix B.

Similarly, the torque variation with the camshaft rotation angle is obtained by averaging the instantaneous torque, at a given camshaft angle, from each of the 5 cycles. Figure 2.19 presents the variation of the instantaneous cam torque with camshaft angle. Note that the envelope presents the standard deviation calculated from the 5 analyzed cycles. It indicates how representative is the final results of all the cycles.

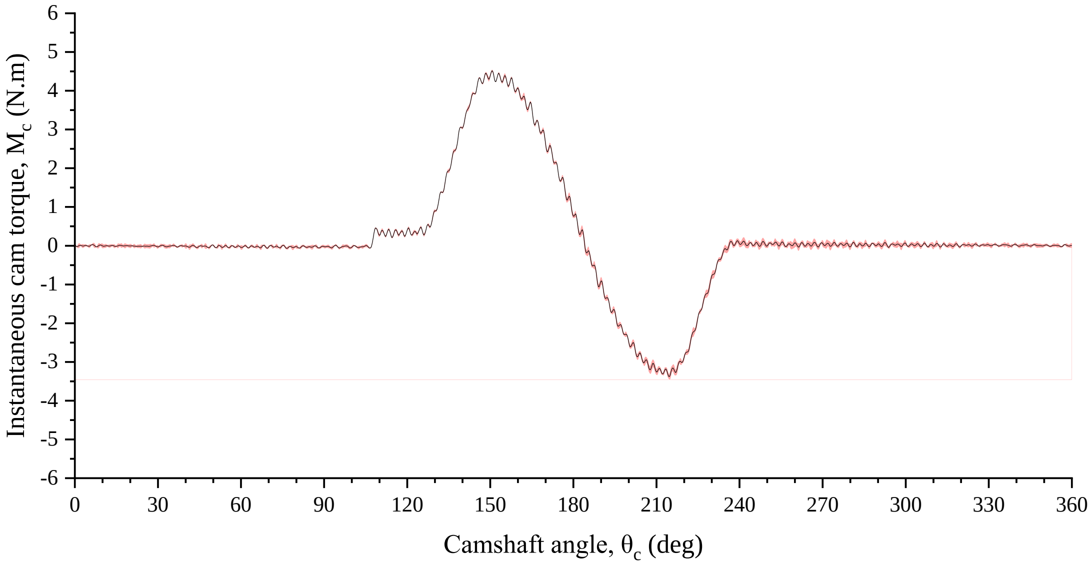

Figure 2.19: Instantaneous cam torque variation with camshaft angle. In this example, the cam and follower are made of uncoated steel and the rotation speed of the cam is 350 rpm in the CW direction at $T_{in} = 50°C$.

The above torque is the cam torque calculated by subtracting the mean bearing torque (calculated in the parts of the cycles where there is no contact) from the total camshaft torque measured by the torque meter.

In addition, the measured cam torque from each cycle is converted to friction coefficient based on the procedure presented in Appendix B. The resulting friction coefficient variation is averaged at each camshaft angle. Figure 2.20 is an example of the variation of friction coefficient with camshaft angle. Note that the envelope represents the standard deviation from the mean value at each camshaft angle.

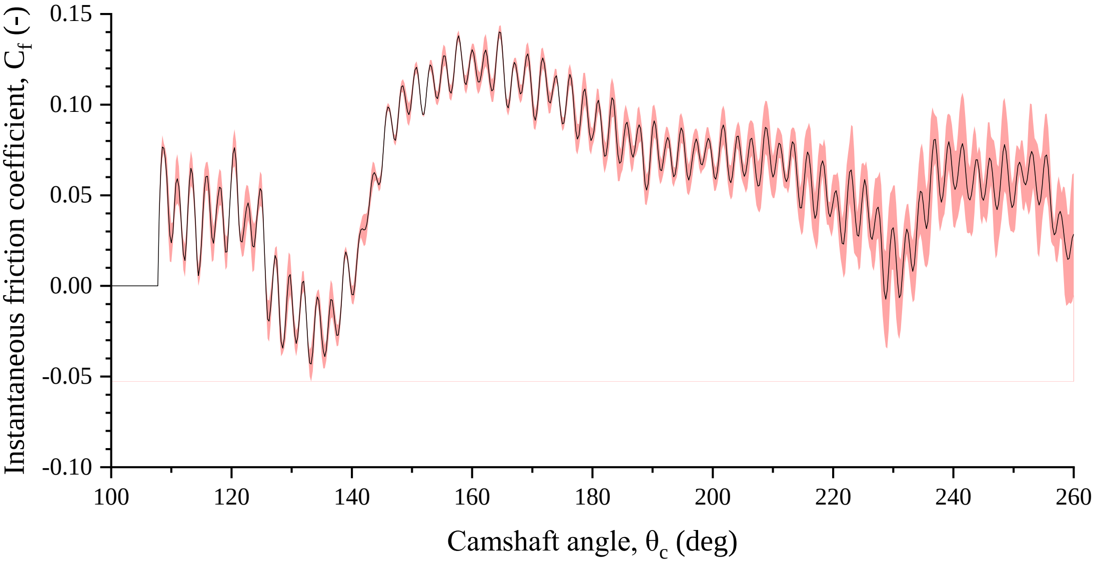

Figure 2.20: Instantaneous friction coefficient variation with camshaft angle. In this example, the cam and follower are made of uncoated steel and the rotation speed of the cam is 350rpm in the CW direction at $T_{in} = 50°C$.

An average cam-follower friction coefficient over the whole cycle is calculated for each rotation speed. The measurement uncertainty can be assessed by calculating the standard deviation of results from different cycles at the same rotation speed. The uncertainty is presented as error bars on results plots, reflecting the representativeness of the final average value. Figure 2.21 presents an example of the variation of the mean friction coefficient denoted $C_{f,mean}$ for a case at $T_{in} = 50\ °C$ and a CW rotation of the cam. Results from both ascending and descending rotation speeds are shown. The results of the mean friction coefficient can be compared to those obtained numerically by TEHL transient simulations of the cam-follower contact.

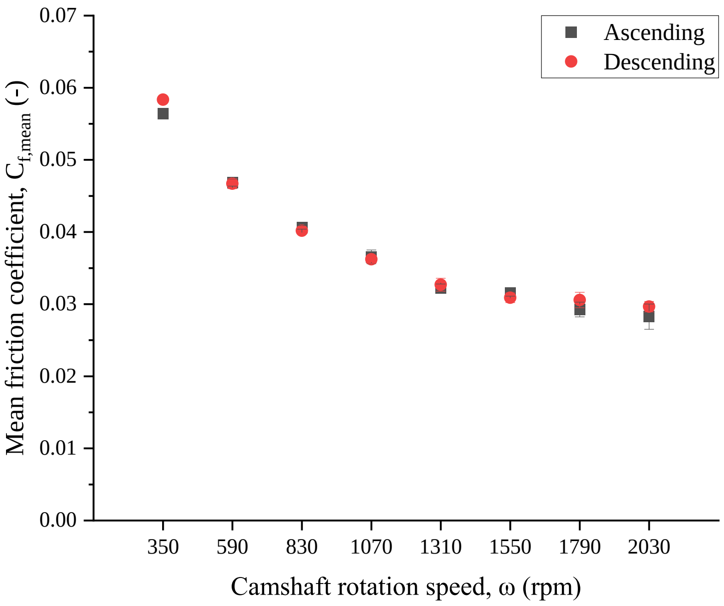

Figure 2.21: Variation of the mean friction coefficient with the camshaft rotation speed. In this example, the cam and follower are made of uncoated steel and the cam is rotating in the CW direction at $T_{in} = 50°C$. Results from ascending and descending speed are shown.

2.1.3 Lubricant characterization

Following the quantitative approach in EHL, an independent rheological characterization of the lubricant outside EHL contact is required. The lubricant used throughout this study is a commercial engine oil. Rheological characterization of the lubricant was realized in LaMCoS by Bouscharain [131].

The lubricant's density dependence on pressure and temperature is expressed by Tait's [132] equation of state (2.4).

$$\rho(p,T) = \rho_r \left(\frac{V_r}{V_0} \times \frac{V_0}{V}\right) \tag{2.4}$$

Where

$$\frac{V}{V_0} = 1 - \frac{1}{1 + K_0'} \ln\left[1 + \frac{p}{K_0}(1 + K_0')\right]$$

$$\frac{V_0}{V_r} = 1 + a_v(T - T_r)$$

$$K_0 = K_{00}\exp(-\beta_K T)$$

Viscosity was measured using three different rheometers:

- Low-pressure viscometer (Anton-Paar Physica MCR301): measures viscosity variation with temperature (15°C to 130°C) at atmospheric pressure and low shear rate (less than 3000 s^{-1}). The lubricant has a Newtonian behavior under these conditions.
- High-pressure viscometer: this instrument was made by Bair and described in his book [132]. It is a falling-body viscometer that measures the viscosity of fluids at pressures between 0.1 MPa and 800 MPa at a given temperature. In the current lubricant characterization, 4 different temperatures (40, 60, 100, and 130°C) were tested. Note that to cover the wide range of conditions different falling bodies were used. This viscometer

is essential to study the influence of pressure and temperature on the viscosity of the lubricant.

- High-pressure Couette rheometer: this instrument was designed for [133] by Bair based on his earlier design [134]. It is used to study the variation of viscosity with shear stress at a given temperature (between $40^\circ C$ and $60^\circ C$) and a given pressure (between 200 MPa and 400 MPa). The shear stress is varied from 0.4 kPa to 3.5 MPa.

For more details about the instruments used in the rheological characterizations, readers are referred to [133] where the same instruments were used.

The "Newtonian" viscosity, $\mu(p,T)$, of the lubricant used throughout this work is described by the WLF model improved by Yasutomi, Bair, and Winer [135] and is given by (2.5)

$$\mu(p,T) = \mu_g \times 10^{\frac{-C_1(T-T_g(p))F_m(p)}{C_2+(T-T_g(p))F_m(p)}} \tag{2.5}$$

where

$$T_g(p) = T_g(p_0) + A_1 \ln(1 + A_2 p)$$
$$F_m(p) = (1 + B_1 p)^{B_2}$$

As for non-Newtonian behavior, it is described by the modified Carreau-Yasuda model [132] given by (2.6)

$$\eta(p,T,\tau) = \mu(p,T)\left(R_{CY} + \frac{1 - R_{CY}}{\left[1 + \left(\frac{\tau}{G_{CY}}\right)^{a_{CY}}\right]^{(\frac{1}{n_{CY}}-1)/a_{CY}}} \right) \tag{2.6}$$

where $\mu(p,T)$ is the Newtonian viscosity and $\tau = \sqrt{\tau_{zx}^2 + \tau_{zy}^2}$ is the fluid shear stress with τ_{zx} and τ_{zy} the shear stresses along the x and y directions.

The above viscosity models were fitted to the measured viscosity on state-of-the-art rheological instruments independently from any tribological tests. Figure 2.22 presents the fitting of the modified Carreau-Yasuda model (2.6) to viscosity measurements from the high-pressure Couette rheometer at $40^\circ C$ and pressures 200 MPa, 300 MPa, and 400 MPa.

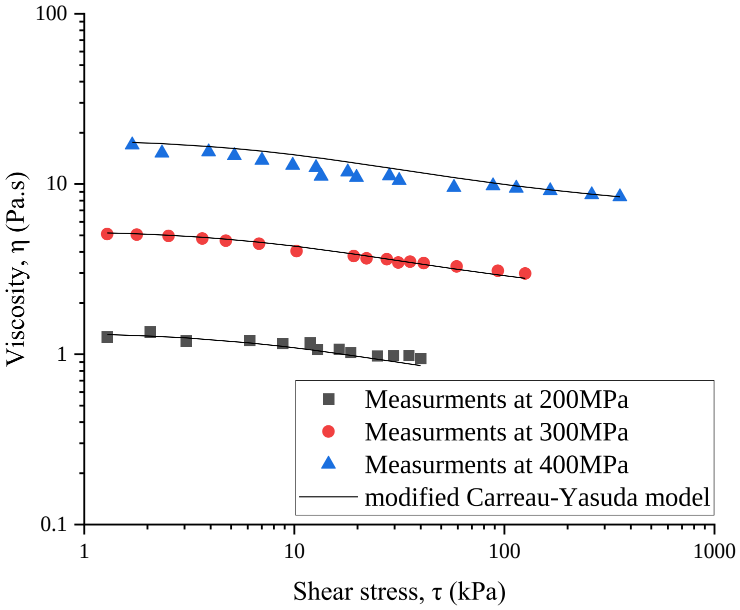

Figure 2.22: Example of fitting the modified Carreau-Yasuda model (2.6) to viscosity measurements from the high-pressure Couette rheometer at 40°C and pressures 200 MPa, 300 MPa, and 400 MPa. Data are taken from [131].

All the parameters used in the models along with reference state conditions are summarized in Table 2.4. The parameters represent the best fit to measured viscosity with less than 10% RMS error. These parameters are used in numerical simulations to define the properties of the lubricant. For completeness, Table 2.5 gives values of the lubricant's viscosity at atmospheric pressure μ_0 and viscosity-pressure coefficient α^* at various temperatures. These values will be useful in later chapters.

Table 2.4: Properties of the lubricant at the reference state in addition to the parameters of different lubricant models (2.4), (2.5), and (2.6).

Property	Unit	Value	Property	Unit	Value
Reference State			WLF model		
T_r	K	288.15	A_1	K	42.043
P_{atm}	Pa	1 x 10^5	A_2	$1/Pa$	2.48 x 10^{-9}
ρ_r	kg/m^3	850	B_1	$1/Pa$	5.92 x 10^{-9}
μ_r	$Pa.s$	0.156	B_2	–	-0.52
			C_1	–	16.17
Tait model			C_2	K	28.23
K_{00}	Pa	9.00 x 10^9	T_g	K	179.33
K'_0	–	11	μ_g	$Pa.s$	10^{12}
a_v	$1/K$	8.00 x 10^{-4}			
β_k	$1/K$	0.0065	Modified Carreau-Yasuda model		
			R_{CY}	–	0.3534
Lubricant thermal properties			a_{CY}	–	1.1137
k_f	$W/m.K$	0.14	n_{CY}	–	0.6752
Cp_f	$J/kg.K$	2400	G_{CY}	Pa	8.20 x 10^3

Table 2.5: Values of viscosity at atmospheric pressure μ_0, and viscosity-pressure coefficient α^* of the lubricant at different temperatures.

Property	**Unit**	**Value**					
Temperature	$°C$	35	39	40	45	50	80
Viscosity at atmospheric pressure, μ_0	$Pa.s$	0.054	0.046	0.044	0.036	0.030	0.012
Viscosity-pressure coefficient, α^*	$1/GPa$	19.1	18.5	18.4	17.73	17.1	14.2

This concludes the experimental methods and materials employed in the current work. Next, the theoretical background of the numerical models used is presented along with details about the implementation in a finite element code.

2.2 Numerical Approach

Instrumenting experimental test rigs to collect data and knowledge about relevant physical phenomena is rarely an easy task. In this case, numerical models come in handy, coupled with experiments to test hypotheses and validate predictions. Advanced numerical models leverage the available computational power and provide insights into phenomena that are hardly accessible by experimental methods. As exposed in Chapter 1, the numerical models used in this study are finite element models based on the full system approach, first proposed by Habchi [30]. Wheeler [31] added the possibility to simulate non-circular contacts. Raisin et al. developed it further to include transient calculation [32] and the possibility to simulate coated surfaces [33]. In this section, the numerical models used in this study are detailed but first, the Hertzian dry contact theory is presented.

2.2.1 Hertzian dry contact

Pressure distribution and the dimensions of a dry contact are determined depending on the geometry of the contacting bodies and the applied load according to the theory of Hertz [136]. To model a barrel-on-disk contact or a cam-follower contact two geometries can be considered. Figure 2.23 illustrates (a) an elliptical contact and (b) a line contact.

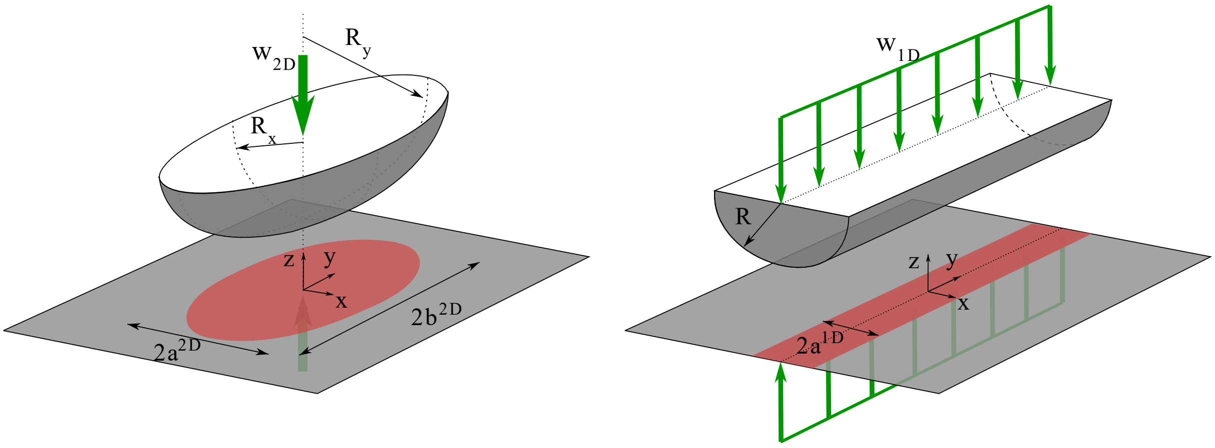

Figure 2.23: (a) 2D elliptical contact and (b) 1D line contact. The red “Hertzian” area is magnified for clarity. In practice $a^{2D} \ll R_x$ and $a^{1D} \ll R$.

On one hand, a 2D elliptical contact between a semi-infinite ellipsoid and a plane is represented in Figure 2.23a, where, R_x and R_y are the radii of curvature in the x and y directions respectively. a^{2D} and b^{2D} are the minor and the major axes half-lengths of the elliptical area of contact respectively. a^{2D} and b^{2D} are calculated by the equations (2.7).

$$a^{2D} = \frac{b^{2D}}{k_e} \quad \text{and} \quad b^{2D} = \left(\frac{6k_e^2 F_2 R_{eq} w_{2D}}{\pi E'}\right)^{1/3} \tag{2.7}$$

where w_{2D} is the normal load applied to the contact, R_{eq} is the equivalent radius of curvature given by (2.8), E' is the reduced Young's modulus given by (2.9), and k_e and F_2 the elliptical integrals given by their corresponding equations in (2.10) from [137].

$$R_{eq} = \frac{1}{\frac{1}{R_x} + \frac{1}{R_y}} \tag{2.8}$$

$$E' = \frac{2}{\frac{1-\nu_1^2}{E_1} + \frac{1-\nu_2^2}{E_2}} \tag{2.9}$$

where (E_1, ν_1) and (E_2, ν_2) are Young's modulus and Poisson's ratio of solids 1 and 2 respectively.

$$\begin{gathered} k_e = D^{0.6268}\,[1 + 0.0632\sin(0.6315\ln(D))] \\ F_2 = \left[1 + \left(\frac{\pi}{2} - 1\right) D^{-1.0238}\right][1 + 0.0486 D^{-1.3358}(\ln(D))^{1.0997}] \end{gathered} \tag{2.10}$$

where $D = \frac{R_x}{R_y}$ is the radii ratio.

The resulting pressure distribution is given by (2.11)

$$p(x,y) = \begin{cases} p_{Hz}^{2D}\sqrt{1 - \left(\frac{x}{a^{2D}}\right)^2 - \left(\frac{y}{b^{2D}}\right)^2} & \text{if } \left(\frac{x}{a^{2D}}\right)^2 + \left(\frac{y}{b^{2D}}\right)^2 \leq 1 \\ 0, & \text{otherwise} \end{cases} \tag{2.11}$$

where p_{Hz}^{2D} is the maximum Hertzian pressure at $x = y = 0$ is given by (2.12)

$$p_{Hz}^{2D} = \frac{3w_{2D}}{2\pi a^{2D} b^{2D}} \tag{2.12}$$

Note that circular (or point) contact is a special case of elliptical contact where $R_x = R_y$. As the name suggests the area of contact is circular instead of elliptical.

On the other hand, a 1D line contact is represented in Figure 2.23b between a cylinder and a plane, where R is the radius of the cylinder and a^{1D} is the half-length of the contact given by (2.13).

$$a^{1D} = \left(\frac{8w_{1D}R}{\pi E'}\right)^{1/2}, \tag{2.13}$$

where w_{1D} is the load per unit length applied to the contact. w_{1D} is expressed in $[N/m]$ contrary to w_{2D} that is expressed in $[N]$.

The pressure distribution is given by (2.14).

$$p(x,y) = \begin{cases} p_{Hz}^{1D}\sqrt{1 - \left(\frac{x}{a^{1D}}\right)^2}, & if \ |x| \leq a^{1D} \\ 0, & otherwise \end{cases} \tag{2.14}$$

where p_{Hz}^{1D} is the maximum Hertzian pressure at $x = 0$ and is given by (2.15).

$$p_{Hz}^{1D} = \frac{2w_{1D}}{\pi a^{1D}} \tag{2.15}$$

2.2.2 Geometries and equations of EHL contact

As opposed to dry contact where the solid surfaces are touching, a lubricated contact is between two solids separated by a lubricant film. When the lubricant fully separates the solids and the contact pressure is high enough to elastically deform the surfaces the contact is said to be an EHL contact.

The EHL problem is represented by a set of equations: the Reynolds equation (classical or generalized), the elastic deformation equation, and the load balance equation. In this section, the geometries of the models used in this work are presented along with the relevant equations.

Two numerical models are presented in this section: the 2D elliptical contact and the 1D line contact. Each of the two models is constructed on two geometries:

- Geometry 1: used for solving the lubricant pressure, the solid elastic deformation, and the load balance equation. This geometry is illustrated in Figure 2.24.
- Geometry 2: used for solving the energy equation and calculating the variables across the thickness of the lubricant. This geometry is illustrated in Figure 2.25.

The spatial dimensions of the geometries are without units based on the dimensionless variables defined later in (2.21).

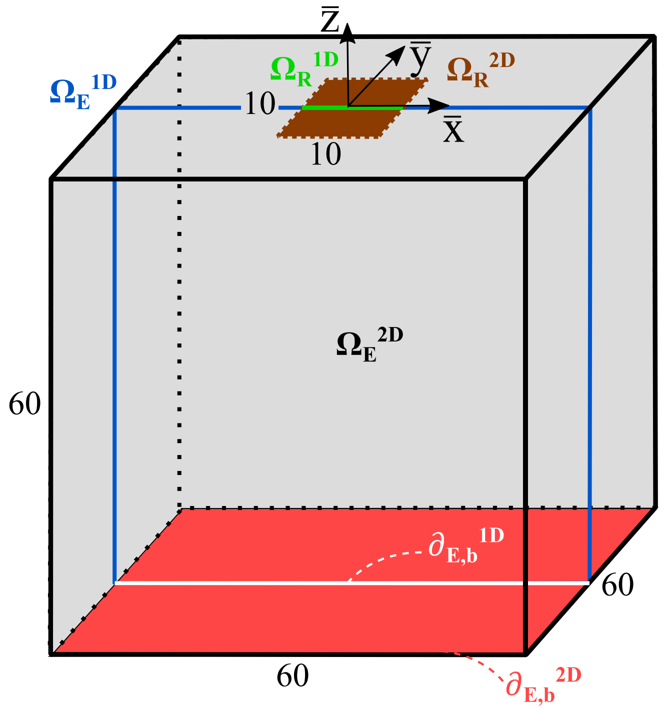

Figure 2.24: Geometry 1 of the elastohydrodynamic component of the numerical models. The 1D geometry is obtained by slicing the 2D geometry at $\bar{y} = 0$. Different domains are denoted by the Greek letter Ω with subscripts “R” and “E” corresponding to Reynolds and elastic domains respectively. In addition, superscripts “1D” and “2D” are used to distinguish the domains belonging the 1D and the 2D contacts respectively. The boundaries of the elastic domains are denoted by the symbol “∂”. This figure is inspired by Meziane [138].

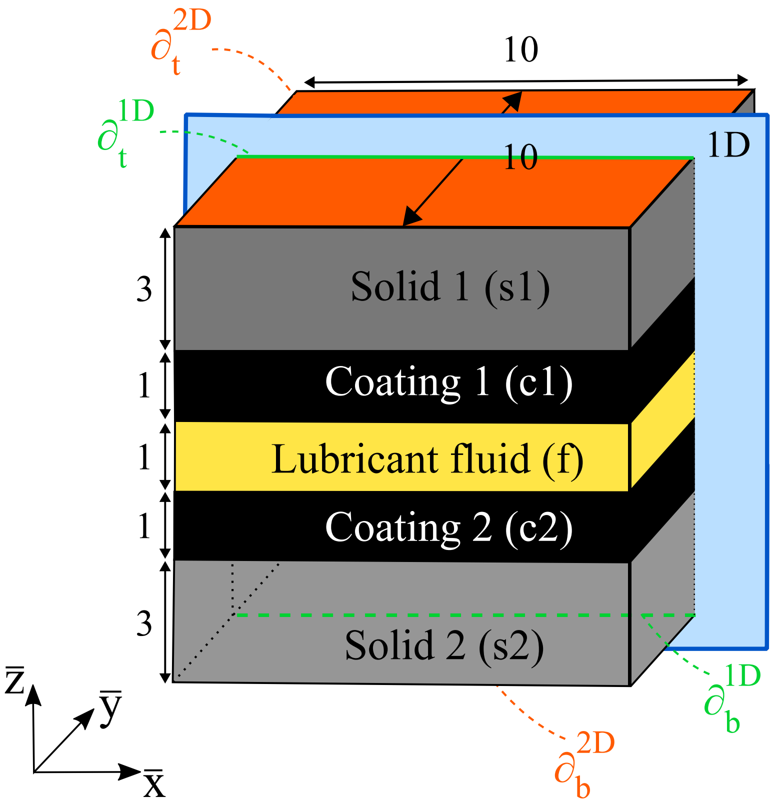

Figure 2.25: Geometry 2 of the energy equation component of the numerical models. The 1D geometry is obtained by slicing the 2D geometry at $\bar{y} = 0$.

Reynolds equation

The Reynolds equation (2.16) relates the pressure of the lubricant p, the local geometry of the fluid gap h, and the motion of the solids. The terms corresponding to the y-direction can simply be dropped from this equation if it is used in a 1D line contact model.

$$\frac{\partial}{\partial x}\left[\frac{\rho h^3}{12\mu}\frac{\partial p}{\partial x}\right]+\frac{\partial}{\partial y}\left[\frac{\rho h^3}{12\mu}\frac{\partial p}{\partial y}\right]-u_{e,x}\frac{\partial}{\partial x}(\rho h)-u_{e,y}\frac{\partial}{\partial y}(\rho h)=0 \tag{2.16}$$

where μ and ρ are respectively the viscosity and density of the lubricant generally given by constitutive laws describing their dependence on pressure. $u_{e,x}$ and $u_{e,y}$ are the entrainment velocities in the x and the y directions respectively and given by (2.17).

$$\begin{aligned} u_{e,x} &= \frac{u_{1,x}+u_{2,x}}{2} \\ u_{e,y} &= \frac{u_{1,y}+u_{2,y}}{2} \end{aligned} \tag{2.17}$$

with, $u_{1,x}$ and $u_{2,x}$ the velocities in the x-direction of the solids 1 and 2 respectively. Also, $u_{1,y}$ and $u_{2,y}$ are the velocities in the y-direction of the solids 1 and 2 respectively.

Equation (2.16) was derived from the Navier-Stokes equations based on several assumptions:

- Thin film approximation (h<<a^{2D}, b^{2D} and a^{1D})
- Full-film separation
- No-slip at the fluid/solid interfaces
- Laminar flow
- Newtonian lubricant

- Viscosity and density are constant in the z-direction
- Inertial and gravitational forces are neglected compared to viscous forces

These assumptions limit the applicability of the Reynolds equation to a relatively narrow set of contact conditions. For instance, the lubrication with fluids manifesting a non-Newtonian behavior under high sliding conditions could not be modeled. This equation is presented here for completeness. However, in the models used throughout this work, the generalized Reynolds equation (detailed next) is implemented.

Generalized Reynolds equation

The generalized Reynolds equation enables the variation of viscosity and density through the film thickness. Hence, the non-Newtonian fluids and thermal effects could be modeled. It was first derived in [34] and can be written as equation (2.18) based on the form given in [139]. It is solved on the domain Ω_R^{2D} and Ω_R^{1D} respectively, in the 2D and 1D models. The terms corresponding to the y-direction are dropped from this equation in the 1D model.

$$\frac{\partial}{\partial x}\left[\left(\frac{\rho}{\eta}\right)_e \frac{\partial p(x,y,t)}{\partial x}\right] + \frac{\partial}{\partial y}\left[\left(\frac{\rho}{\eta}\right)_e \frac{\partial p(x,y,t)}{\partial y}\right] - \frac{\partial}{\partial x}(\rho_x^*) - \frac{\partial}{\partial y}(\rho_y^*) - \frac{\partial}{\partial t}(\rho_e) = 0 \tag{2.18}$$

where

$$\begin{gathered}\left(\frac{\rho}{\eta}\right)_e = \frac{\eta_e}{\eta_e'}\rho_e' - \rho_e'', \\ \rho_x^* = \rho_e'\eta_e\big(u_{1,x}(t) - u_{2,x}(t)\big) + \rho_e u_{2,x}(t), \\ \rho_y^* = \rho_e'\eta_e\big(u_{1,y}(t) - u_{2,y}(t)\big) + \rho_e u_{2,y}(t),\end{gathered} \tag{2.19}$$

Variables with subscript "e" refer to equivalent quantities considering the variations of the lubricant's density ρ and viscosity η through the film thickness. These quantities are expressed by the following integrals.

$$\begin{gathered}\rho_e = \int_0^{h(x,y,t)} \rho(p,T)dz \qquad \frac{1}{\eta_e} = \int_0^{h(x,y,t)} \frac{1}{\eta(p,T,\tau)}dz \\ \rho_e' = \int_0^{h(x,y,t)} \rho(p,T)\left(\int_0^z \frac{1}{\eta(p,T,\tau)}dz'\right)dz \qquad \frac{1}{\eta_e'} = \int_0^{h(x,y,t)} \frac{z}{\eta(p,T,\tau)}dz \\ \rho_e'' = \int_0^{h(x,y,t)} \rho(p,T)\left(\int_0^z \frac{z'}{\eta(p,T,\tau)}dz'\right)dz\end{gathered} \tag{2.20}$$

In the equations (2.20), p and h are the lubricant pressure and film thickness respectively, and are both dependent on the position (x, y) and time t. Relations describing the dependency of density on pressure and temperature and the dependency of viscosity on pressure, temperature, and shear stress are detailed in section 2.1.3 based on an independent rheological characterization.

Different variables are written in dimensionless forms defined in (2.21).

$$\bar{x} = \frac{x}{a_{ref}}, \quad \bar{y} = \frac{y}{b_{ref}}, \quad \bar{z} = \begin{cases} z/h, & in\ fluid \\ z/h_{coat}, & in\ coatings \\ z/a_{ref}, & in\ solids \end{cases},$$
$$R_t = \frac{R(t)}{R_{ref}}, \quad W_t = \frac{w_n(t)}{w_{ref}}, \quad \bar{p} = \frac{p}{p_{Hz_{ref}}},$$
$$U_{e,x} = \frac{u_{e,x}(t)}{u_{e,x_{ref}}}, \quad U_{e,y} = \frac{u_{e,y}(t)}{u_{e,y_{ref}}},$$
$$H = \frac{hR_{ref}}{a_{ref}^2}, \quad \bar{\rho} = \frac{\rho}{\rho_0}, \quad \bar{\eta} = \frac{\eta}{\mu_0}, \quad \bar{t} = \frac{tu_{e,x_{ref}}}{a_{ref}} \tag{2.21}$$

In transient simulations, contact conditions and dimensions may change. Meaning that the normal load w_n (which is equal to either w_{1D} or w_{2D} in the 1D and 2D models respectively), the surface velocities $u_{1,x}$, $u_{2,x}$, $u_{1,y}$, and $u_{2,y}$ in addition to the reduced radius of curvature R, can all be time-dependent. To guarantee a correct scaling of the model regardless of how the contact conditions change over time, the reference instant t_{ref} is chosen such that a_{ref} represents the largest Hertzian half-width in the x-direction during the entire simulation. Note that variables with subscript "ref" are calculated at the reference instant t_{ref}.

R is calculated by (2.22) in the 1D model or by (2.23) in the 2D model.

$$R = R^{1D} = \frac{1}{\frac{1}{R_1^{1D}} + \frac{1}{R_2^{1D}}} \tag{2.22}$$

where in the 1D model the solids are presented as cylinders with respective radii of curvature R_1^{1D} and R_2^{1D}.

In x-direction:
$$R = R_x^{2D} = \frac{1}{\frac{1}{R_{1,x}^{2D}} + \frac{1}{R_{2,x}^{2D}}}$$

In y-direction:
$$R = R_y^{2D} = \frac{1}{\frac{1}{R_{1,y}^{2D}} + \frac{1}{R_{2,y}^{2D}}} \tag{2.23}$$

where $R_{1,x}^{2D}$ and $R_{1,y}^{2D}$ are the radii of curvature of solids 1 in the x and y-directions respectively. Also, $R_{2,x}^{2D}$ and $R_{2,y}^{2D}$ are the radii of curvature of solids 2 in the x and y-directions respectively. In the 2D model, the solids are presented as ellipsoids.

In the 2D model, the lengths L_x^{2D} and L_y^{2D} of Reynolds domain in the x and y direction are respectively equal to 10 in both x and y directions. These dimensions of the domain are greater than the classical domain dimensions suggested by Habchi et al. [139] to accommodate a wider pressure distribution. The domain is symmetric with respect to the axes $x = 0$ and $y = 0$. The symmetry is required because lubricant can be entrained from both sides of the contact in case of opposite sliding ($SRR > 2$) which is a common condition throughout this thesis. Moreover, two versions of the 1D model are used in this thesis with Reynolds domain length L_x^{1D} equal to 10 or 20 respectively. The smaller length is used for comparing the 1D model with the 2D model (as in Appendix C) while the larger length is used elsewhere for numerical studies and comparisons with experiments (as in Chapters 3, 4, and 5).

Zero pressure is imposed at the boundaries of Ω_R^{1D} and Ω_R^{2D}. At the contact outlet, negative pressure may occur. The penalty method first presented by Wu [140] is used to address this issue. It consists of adding a penalty term to the Reynolds equation that makes negative pressures very close to zero without affecting positive pressures of the validity of the Reynolds equation. Cavitation is neglected in the models employed in the current work because negative pressures are less significant in opposite sliding cases where the lubricant enters and exits the contact simultaneously at both sides.

Elastic deformation equation

The elastic deformation equation (2.24) is solved in a deformable domain denoted respectively by Ω_E^{1D} and Ω_E^{2D} for the 1D and 2D models in Figure 2.24.

$$\nabla \cdot \boldsymbol{\sigma} = 0 \tag{2.24}$$

with, $\boldsymbol{\sigma} = \boldsymbol{C\epsilon}(u, v, w)$ being the stress tensor expressed as a function of stiffness tensor $\boldsymbol{C}$ and strain tensor $\boldsymbol{\epsilon}$. The latter is a function of the displacements u, v, and w in the x, y, and z directions respectively. The equivalent Young's modulus E_{eq} and equivalent Poisson's ratio ν_{eq} are assigned to the elastic domain and are defined by equations (2.25) and (2.26) from [30]

$$E_{eq} = \frac{E_1 E_2^2 (1+\nu_1)^2 + E_2 E_1^2 (1+\nu_2)^2}{\big(E_2(1+\nu_1) + E_1(1+\nu_2)\big)^2} \tag{2.25}$$

$$\nu_{eq} = \frac{E_2 \nu_1 (1+\nu_1) + E_1 \nu_2 (1+\nu_2)}{E_2(1+\nu_1) + E_1(1+\nu_2)} \tag{2.26}$$

Where (E_1, ν_1) and (E_2, ν_2) are Young's modulus and Poisson's ratio of bulk solids 1 and 2 respectively.

The elastic domain has a fixed constraint at the bottom boundary $\partial_{E,b}^{1D}$ or $\partial_{E,b}^{2D}$ in the 1D and 2D models respectively. All other boundaries are free. Moreover, the pressure p calculated by the generalized Reynolds equation is applied to the top boundary of the elastic domain. Solving (2.24) with these boundary conditions gives the displacement of the equivalent solid domain, $\delta(x, y, z = 0, t) = w(x, y, z = 0, t)$. δ represents the sum of the displacement of the two real surfaces.

Load balance equation and film thickness expression

In addition to the Reynolds equation and the elastic deformation equation, the load balance equation (2.27) ensures equilibrium between the generated hydrodynamic pressure p and normal load w_n.

$$\begin{aligned} &\text{1D} \qquad \int_{\Omega_R^{1D}} p(x,t)\,dx = w_n(t) = w_{1D}(t) \\ &\text{2D} \qquad \iint_{\Omega_R^{2D}} p(x,y,t)\,dx\,dy = w_n(t) = w_{2D}(t) \end{aligned} \tag{2.27}$$

The lubricant film thickness h can be expressed as in (2.28) where h_0 is the rigid body displacement, δ is calculated by the elasticity equation and the terms in the middle represent the equivalent geometry of the gap.

$$\text{1D} \qquad h(x,t) = h_0(t) + \underbrace{\frac{x^2}{2R_{eq}^{1D}}}_{} + \delta(x,t)$$

$$\text{equivalent geometry of the gap} \tag{2.28}$$

$$\text{2D} \qquad h(x,y,t) = h_0(t) + \overbrace{\frac{x^2}{2R_{eq,x}^{2D}} + \frac{y^2}{2R_{eq,y}^{2D}}}^{} + \delta(x,y,t)$$

Energy equation

The energy equation is solved on geometry 2 shown in Figure 2.25. The energy equation can be written in a general form (2.29).

$$\rho_i Cp_i \left(\underbrace{\overrightarrow{u_i} \nabla T}_{advection} + \underbrace{\frac{\partial T}{\partial t}}_{transient} \right) - \underbrace{\nabla(k_i \nabla T)}_{conduction} = \underbrace{Q_i}_{heat\ source} \tag{2.29}$$

In the above equation the index "i" is replaced by "s1", "s2", "c1", "c2", or "f" to represent the properties or the variables in each sub-domain of Figure 2.25. This form of the equation is used in the 2D model. It can be used in the 1D model by dropping the y-components of the different terms.

On one hand, for the fluid domain ($i = f$), the vector $\overrightarrow{u_i}$ becomes the fluid velocity vector $\overrightarrow{u_f}(x,y,z,t)$ in the 3D fluid domain and is given (2.30).

$$\overrightarrow{u_f}(x,y,z,t) = \begin{pmatrix} \frac{\partial p}{\partial x} \left(\int_0^z \frac{z'}{\eta} dz' - \frac{\eta_e}{\eta_e'} \int_0^z \frac{1}{\eta} dz' \right) + \eta_e \left(u_{1,x} - u_{2,x} \right) \int_0^z \frac{1}{\eta} dz' + u_{2,x} \\ \frac{\partial p}{\partial y} \left(\int_0^z \frac{z'}{\eta} dz' - \frac{\eta_e}{\eta_e'} \int_0^z \frac{1}{\eta} dz' \right) + \eta_e \left(u_{1,y} - u_{2,y} \right) \int_0^z \frac{1}{\eta} dz' + u_{2,y} \\ 0 \end{pmatrix} \tag{2.30}$$

Note that the z-component of $\overrightarrow{u_f}$ is zero indicating that the lubricant flow in the z-direction is negligible compared to the flow in the xy-plane (thin-film assumption). Accordingly, the heat advection in (2.29) in the z-direction is neglected. In contrast, heat advection dominates over heat conduction in the x and y directions. Thus, only the z-component of the conduction term is used in (2.29). In addition, the source term Q_i becomes the sum of Q_s and Q_c which represent the shear and compressive heat sources respectively, and are given by (2.31) and (2.32).

$$Q_s = \eta \left[\left(\frac{\partial u_{f,x}}{\partial z} \right)^2 + \left(\frac{\partial u_{f,y}}{\partial z} \right)^2 \right] \tag{2.31}$$

$$Q_c = -\frac{T}{\rho_f} \frac{\partial \rho_f}{\partial T} \left(\overrightarrow{u_f} \nabla p + \frac{\partial p}{\partial t} \right) \tag{2.32}$$

The material properties ρ_f, k_f, and Cp_f are replaced by the properties of the lubricant detailed in section 2.1.3.

On the other hand, for the solid domains ($i = \{s1,\ s2,\ c1,\ c2\}$), the vector $\overrightarrow{u_i}$ represents the velocity of the solids. The advection in the z-direction is neglected compared to the advection in the xy-plane. In the case of solids, conduction can happen in all directions. Hence, all the components of the conduction term are used in (2.29). In addition, the source term Q_i is set to zero given that no heat is generated in the solid domains. The material properties ρ_i, k_i, and Cp_i in each domain are replaced by the properties of the different types of solids and coatings. In case no coating is used, the thermal properties of solids 1 and 2 are applied to coatings 1 and 2 respectively.

The ambient temperature T_0 is imposed on boundaries ∂_t^{2D} and ∂_b^{2D} in the 2D model and on boundaries ∂_t^{1D} and ∂_b^{1D} in the 1D model. Also, the same temperature is imposed on the side boundaries, denoted by ∂_i, if the material (solids or fluid) is moving toward the contact center. This condition is described by equation (2.33). In contrast, if the material at a boundary is moving away from the contact center then a zero conductive heat flux is assumed across this side boundary. This condition is described by equation (2.34).

$$T|_{\partial_i} = T_0, \qquad if\ \vec{u_i} \cdot \vec{n} \leq 0 \tag{2.33}$$

$$\begin{aligned} &\partial_i \text{ parallel to yz-plane:} && \left.\frac{\partial T}{\partial x}\right|_{\partial_i} = 0, \qquad if\ \vec{u_i} \cdot \vec{n} > 0 \\ &\partial_i \text{ parallel to xz-plane:} && \left.\frac{\partial T}{\partial y}\right|_{\partial_i} = 0, \qquad if\ \vec{u_i} \cdot \vec{n} > 0 \end{aligned} \tag{2.34}$$

with $\vec{n}$ the outwards-pointing vector normal to the boundary. In practice, these boundary conditions reflect the idea that the material entering the contact is at the ambient temperature T_0. In contrast, the temperature of the lubricant or the solids exiting the contact is dictated by what the material experiences during its travel through the contact.

Moreover, equations (2.35) to (2.38) imply that the conductive heat flux is conserved in the z-direction across the fluid/coating and the coating/solid interfaces. Note that the "+" and "−" signs are used to distinguish between the gradients calculated in the domains just above and below the interface respectively.

$$k_f \left.\frac{\partial T}{\partial z}\right|_{\partial_{f/c1}^-} = k_{c1} \left.\frac{\partial T}{\partial z}\right|_{\partial_{f/c1}^+} \tag{2.35}$$

$$k_f \left.\frac{\partial T}{\partial z}\right|_{\partial_{f/c2}^+} = k_{c2} \left.\frac{\partial T}{\partial z}\right|_{\partial_{f/c2}^-} \tag{2.36}$$

$$k_{c1} \left.\frac{\partial T}{\partial z}\right|_{\partial_{c1/s1}^-} = k_{s1} \left.\frac{\partial T}{\partial z}\right|_{\partial_{c1/s1}^+} \tag{2.37}$$

$$k_{c2} \left.\frac{\partial T}{\partial z}\right|_{\partial_{c2/s2}^+} = k_{s2} \left.\frac{\partial T}{\partial z}\right|_{\partial_{c2/s2}^-} \tag{2.38}$$

Transient effects

According to Raisin et al. [32], the film thickness and friction coefficient in a TEHL contact can be significantly impacted by transient fluctuations if these fluctuations occur faster than the contact can accommodate the resulting physical effects.

The characteristic time associated with a phenomenon indicates how fast this phenomenon reaches a steady state after a fluctuation. The authors of [32] provided an overview of the main characteristic times in a TEHL contact. They found that the characteristic times associated with the hydrodynamic fluid flow and thermal effects are much longer than the characteristic times associated with other phenomena such as the elasticity of the solids. For this reason, transient effects are considered in the generalized Reynold equation (2.16) and the energy equation (2.29) but not in the elasticity equation (2.24).

Calculating friction coefficient

A no-slip condition at the fluid/coating interfaces is assumed along with smooth surfaces and full-film separation. Thus, there are no mixed or boundary lubrication regimes. The numerical friction coefficient is calculated by equations (2.39) and (2.40) in the 1D and 2D models respectively.

1D
$$C_f = \frac{\int_{\partial_{f/c1}^{1D}} \tau_{zx}\, dx + \int_{\partial_{f/c2}^{1D}} \tau_{zx}\, dx}{2 \times w_N} \tag{2.39}$$

2D
$$\begin{aligned} C_{f,x} &= \frac{\iint_{\partial_{f/c1}^{2D}} \tau_{zx}\, dxdy + \iint_{\partial_{f/c2}^{2D}} \tau_{zx}\, dxdy}{2 \times w_N} \\ C_{f,y} &= \frac{\iint_{\partial_{f/c1}^{2D}} \tau_{zy}\, dxdy + \iint_{\partial_{f/c2}^{2D}} \tau_{zy}\, dxdy}{2 \times w_N} \end{aligned} \tag{2.40}$$

where τ_{zx} and τ_{zy} are the shear stresses calculated in the fluid domain. These are integrated over the fluid/coating interfaces $\partial_{f/c1}^{1D}$ and $\partial_{f/c2}^{1D}$ for the 1D model and $\partial_{f/c1}^{2D}$ and $\partial_{f/c2}^{2D}$ for the 2D model. The integration results in the friction force at the top and bottom boundaries of the fluid domain. Finally, the mean friction force is divided by the normal load w_N to obtain the friction coefficient.

Note that in equations (2.39) and (2.40) the shear stresses cannot be expressed simply as $\tau_{zx} = \eta \frac{\partial u_{f,x}}{\partial z}$ and $\tau_{zy} = \eta \frac{\partial u_{f,y}}{\partial z}$ due to the circular dependency with the viscosity as expressed in (2.6). To resolve the issue, $\frac{\partial u_{f,x}}{\partial z}$ and $\frac{\partial u_{f,y}}{\partial z}$ are calculated by deriving $u_{f,x}$ and $u_{f,y}$ given in (2.30) once with respect z then multiplying by η which results in expressions (2.41) where η does not appear explicitly.

$$\begin{aligned} \tau_{zx} &= \frac{\partial p}{\partial x}\left(z - \frac{\eta_e}{\eta_e'}\right) + \eta_e(u_{1,x} - u_{2,x}) \\ \tau_{zy} &= \frac{\partial p}{\partial y}\left(z - \frac{\eta_e}{\eta_e'}\right) + \eta_e(u_{1,y} - u_{2,y}) \end{aligned} \tag{2.41}$$

The integral terms named $\frac{1}{\eta_e}$ and $\frac{1}{\eta_e'}$ in (2.20) and appearing in (2.41) are calculated, similarly to [32], by the solution of two additional partial differential equations (PDEs) given in (2.42) at all points of the 3D fluid domain colored in yellow in Figure 2.25 in the case of using the 2D model. In contrast, if the 1D model is used, these equations are solved at all points of the 2D fluid domain obtained by intersecting the 1D cut-plane ($y = 0$) with the 3D fluid domain.

$$\begin{aligned} \frac{\partial}{\partial z}\left(\frac{1}{\eta_e}\right) &= \frac{1}{\eta(p,T,\tau)} \\ \frac{\partial}{\partial z}\left(\frac{1}{\eta_e'}\right) &= \frac{z}{\eta(p,T,\tau)} \end{aligned} \tag{2.42}$$

with $\eta(p,T,\tau)$the non-Newtonian viscosity given in (2.6).

2.2.3 Numerical implementation

The equations detailed in previous sections are implemented in their dimensionless form in COMSOL 5.5 [141], a commercial multi-physics finite element analysis software. They are then solved by a Newton-Raphson approach until convergence is reached when the maximum relative difference in all variables between two consecutive iterations gets lower than 0.001. This convergence criterion is typical for this kind of thermal and non-Newtonian EHL models [139].

The same model can be used for parametric stationary and transient simulations. Parametric stationary studies are used when the contact operating conditions do not change over time (for example, simulating a barrel-on-disk contact). The different test conditions (SRR, normal load, etc.) are provided as parameters to a parametric sweep, and each combination is solved as a separate steady-state study. In contrast, transient studies are used when the contact conditions change over time (for example, simulating a cam-follower contact). In this case, the evolution of different variables with time can be investigated.

Mesh statistics

Table 2.6 presents some statistics about the numbers and types of elements used in the finite element models in addition to the resulting number of degrees of freedom (DOF). Note that the numbers of DOF given in the table correspond to the solution of the full stationary problem (i.e. Thermal non-Newtonian EHL).

Table 2.6: Statistics about the meshes used in the finite element models and the resulting number of degrees of freedom.

	2D model		**1D model**		**1D model**	
Ω_R dimensions	10 × 10		10		20	
Geometry	1	2	1	2	1	2
Elements*	53,974 tet	159,100 pri 126,813 tet	935 tri	4,810 tri 840 quad	3,032 tri	14,920 tri 2,670 quad
Total number of elements	339,887		6,585		20,622	
Degrees of Freedom (DOF)	783,263		19,331		60,735	

* Types of elements are abbreviated by “tet” for tetrahedral elements, “pri” for prism elements, “tri” for triangles, and “quad” for quadrangles.

Computation scheme

According to [32], analytical solutions fall short of providing a good first guess for all variables. Hence, approaching a correct initial condition by intermediate steps is required. The computation procedure is represented in Figure 2.26.

In the case of a transient study, a reference state is defined based on expected contact conditions during the whole simulation. Also, the operating conditions at $t = 0$ are defined. In contrast, if a parametric stationary study is considered then the first combination of parameters is used as initial operating conditions. After assembling the non-linear system of equations, the first solution of solid elastic deformation under Hertzian pressure is calculated. Then, an intermediate isothermal solution is computed with Newtonian lubricant behavior. Next, the full thermal non-Newtonian TEHL solution is computed. Note that each solution serves as an initial guess for the next step.

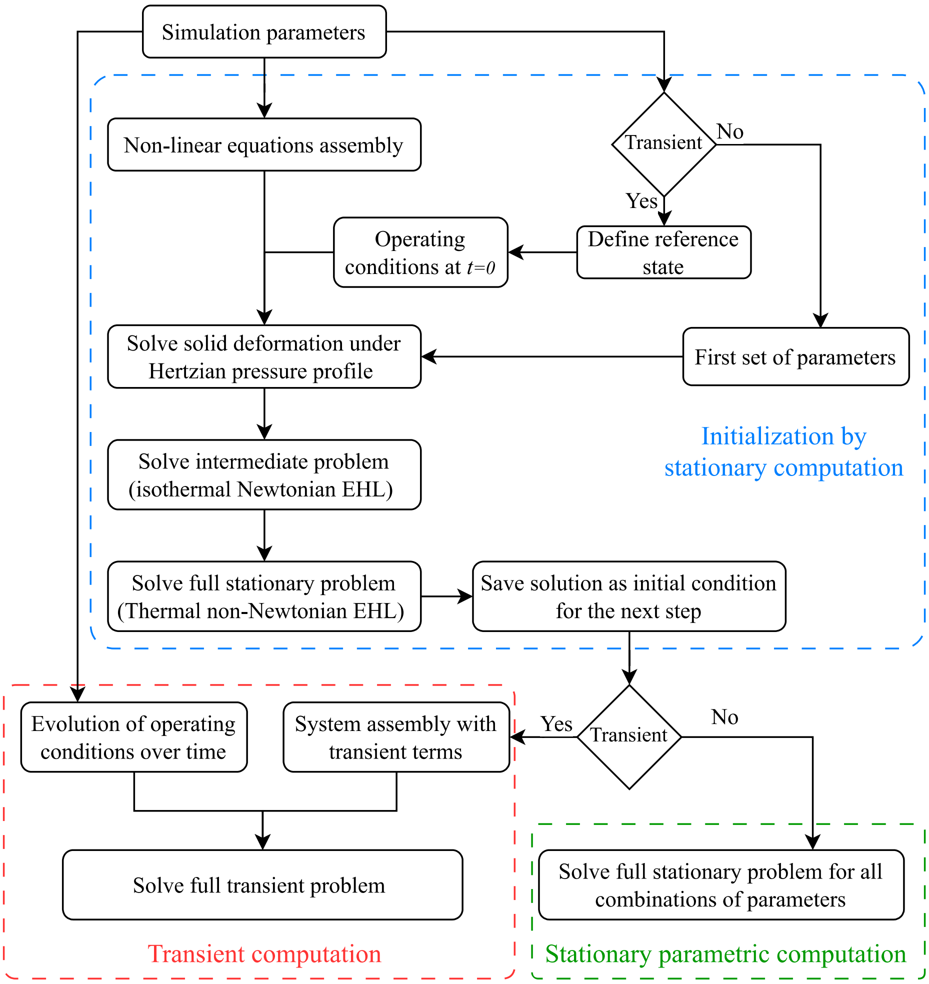

Figure 2.26: Schematic flowchart of the numerical computation procedure.

At this point, the initialization is complete. On one hand, if a parametric stationary study is considered, then the full stationary problem is solved for all required combinations of parameters. Each solution serves as an initial condition for the next step in the parametric sweep. In this manner, the initialization is realized only once. On the other hand, if a transient study is considered, then the system of equations is assembled with transient terms, and the evolution of operating conditions with time is imported into the transient solver.

The transient system is discretized and solved by a backward differentiation formula (BDF) scheme. The timestep size is automatically adjusted during the solution based on local error estimations compared to the tolerances. The timestep is either decreased or increased. It is also decreased if the solver does not converge within the specified maximum number of iterations set to 15 iterations per step. Only the predefined timesteps are saved for postprocessing.

Calculation time

On one hand, the 2D model simulations were performed on a workstation equipped with 64GB memory and an 8-core Intel Xeon processor with a clock speed of 3.5 GHz. On the other hand, both variants of the 1D model simulations ($L_x^{1D} = 10$ and 20) were performed on a PC equipped with 16GB memory and a 4-core Intel i7 processor with a clock speed of 1.9 GHz.

A typical parametric stationary study realized in this work consists of solving the full stationary problem (Thermal non-Newtonian EHL) for varying SRR from 0 to 4 with steps of 0.25.

This includes the initialization step at pure rolling condition ($SRR = 0$) then a parametric sweep solving the full stationary problem for each SRR value. A typical 2D model simulation took around 31.5 hours to finish while, for the same conditions, the 1D model simulations took 21 minutes and 34 minutes to finish respectively for the $L_x^{1D} = 10$ and $L_x^{1D} = 20$ variants.

2.2.4 Numerical outputs

A variety of results can be collected by numerically solving a TEHL non-Newtonian problem. Here some possible outputs are listed:

- The lubricant film thickness profile is calculated on the Reynolds domains Ω_R^{1D} and Ω_R^{2D}. In addition, values of minimum, central, and minimum on central line film thickness are deduced.
- The lubricant pressure distributions on Ω_R^{1D} and Ω_R^{2D} are also calculated.
- The friction coefficient is calculated by equations (2.39) and (2.40).
- The heat transfer and temperature distribution in different parts of the system are accessible by solving the energy equation.
- The lubricant variables such as velocity, viscosity, shear stress, and shear rate are obtained at all points of the 2D or 3D fluid domains respectively in the 1D and 2D models.

2.3 Conclusion

In this chapter, experimental and numerical methods used throughout this work were presented. On one hand, the JEROTRIB tribometer enables the investigation of barrel-on-disk elliptical contact by simultaneously measuring friction coefficient and lubricant film thickness. On the other hand, the Monocam test rig is used to study friction in a cam-follower contact replicating a real contact geometry and operating conditions. In addition to experimental methods, a transient TEHL non-Newtonian numerical model is detailed. The numerical approach explores physical phenomena not accessible by experimental measurements. The main physical and thermal properties of the different materials used in this work are presented including bulk components materials, coatings, and lubricant properties.

For simplicity, throughout the following chapters, different components will be referred to by their short names according to Table 2.7.

Table 2.7: List of short names used for simplicity designating the various components used throughout this work.

Short name	**Description**	**Used in ...**		
		Chapter	Test rig	TEHL Model
Steel-B	Uncoated steel barrel	3	JEROTRIB	Parametric stationary
DLC-B	DLC-coated steel barrel	3	JEROTRIB	Parametric stationary
Sapphire-D	Sapphire disk	4	JEROTRIB	Parametric stationary
Glass-DLC-D	DLC-coated glass disk	4	JEROTRIB	Parametric stationary
Steel-C	Uncoated cam	5	Monocam	Transient
Steel-F	Uncoated finger follower	5	Monocam	Transient
DLC-C	DLC-coated cam	5	Monocam	Transient
DLC-F	DLC-coated finger	5	Monocam	Transient

Chapter 3: TEHL contacts: From Pure Rolling to Opposite Sliding

---

N.B: the majority of the results in this chapter are published in an article [142] by the author and colleagues entitled: “Dual experimental-numerical study of oil film thickness and friction in a wide elliptical TEHL contact: From pure rolling to opposite sliding”. Tribology International 2023; 184:108466.

The main idea of this chapter is to assess the ability of quantitative TEHL modeling (involving independent rheological characterization of a commercial lubricant) to predict simultaneously the film thickness and friction coefficient. A dual experimental-numerical approach is presented where measurements and predictions are compared over a relatively wide range of sliding conditions, from pure rolling to opposite sliding. In addition, the numerical approach is used to investigate the simultaneous effects of varying operating conditions on film thickness and friction coefficient in a TEHL contact. Finally, a semi-analytical expression involving SRR is proposed to estimate the minimum film thickness in a TEHL line contact.

3.1 Dual Experimental-Numerical Approach: Thermally Conductive Surfaces

3.1.1 Experiments on the barrel-on-disk tribometer

Experiments are realized on the barrel-on-disk tribometer (JEROTRIB) described in detail in Chapter 2. The barrel Steel-B and the disk Sapphire-D are used. Table 3.1 presents the experimental conditions of tests realized on JEROTRIB.

Table 3.1: Experimental conditions for tests realized on JEROTRIB.

Parameter	**Unit**	**Value**
Normal load, w_{2D}	N	65
Maximum Hertzian pressure, p_{Hz}^{2D}	MPa	504
External bath temperature, T_{ext}	$°C$	45
Entrainment speed, u_e	m/s	1
Slide-to-roll ratio, SRR	$-$	0, 0.25, 0.5, 1, 1.5, 2.5, 3, 3.5, 4

The experiments are performed with external bath temperature $T_{ext} = 45°C$ and normal load $w_{2D} = 65\ N$ which corresponds to a maximum Hertzian pressure $p_{Hz}^{2D} = 504\ MPa$ calculated using equation (2.12) for the given geometry and materials. The entrainment velocity is fixed to $u_e = \frac{u_1+u_2}{2} = 1\ m/s$, with u_1 and u_2 the velocities of the surfaces, at the point of contact, of the barrel and the disk respectively. Sliding is quantified by the slide-to-roll ratio $SRR = \frac{u_1-u_2}{u_e}$ varied from 0 to 4 with intermediate steps.

As discussed in section 2.1.1, it is difficult to know the lubricant inlet temperature T_0 with enough precision. To overcome this challenge and determine T_0, measurements of film thickness in pure rolling condition at the start of the experiment are compared to estimates based on Chittenden's expressions [143] corrected for non-Newtonian behavior [144] (for more details see Appendix D). Minimum and central film thicknesses are calculated for the range of lubricant temperatures from $35°C$ to $42°C$. Estimations are shown in Figure 3.1 as scattered black squares and red dots for minimum and central film thickness respectively. In addition, black and red lines correspond to experimental measurements, and the shaded area refers to measurement uncertainty.

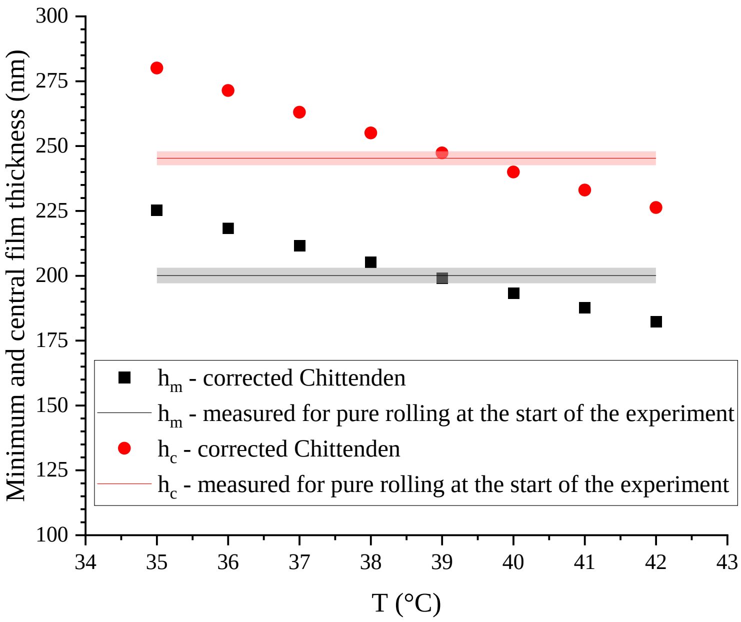

Figure 3.1: Corrected Chittenden estimations and measurements of minimum and central film thickness in the pure rolling condition for configuration 1.

The value of T_0 is the temperature at which estimations and measurements are the closest. T_0 is found to be equal to $39°C$. This value is used as inlet temperatures in the corresponding numerical simulations.

3.1.2 Simulations: TEHL line contact

The model used in this chapter is a stationary thermal-elastohydrodynamic line contact model. It has to be noted that according to Nijenbanning [145] for pure rolling EHL isothermal contacts, h_c and $h_{m,c}$ of the 2D wide elliptical contact are similar to those of a 1D line contact if the ellipticity parameter $D = \frac{R_{1,x}}{R_{1,y}}$ is less than 0.1, which is the case here ($D = 0.04$). In contrast with h_c and $h_{m,c}$ which are defined on the central line along the entrainment direction, the friction coefficient is calculated over the whole elliptical contact domain in the 2D case. Thus, an equivalence between 1D and 2D models in friction coefficient cannot be assumed without further justifications. Appendix C provides a comparison between 1D and 2D models in terms of film thickness parameters and friction coefficient. The loss of accuracy by using a 1D model is shown to be acceptable (even at high SRR) compared to the advantages of using it instead of a 2D model. These advantages include saving time and computational resources. More details about the use of the 1D line contact model instead of the 2D elliptical contact model are provided in Appendix C.

Throughout this work, a 1D model is used to confront experimental results from a barrel-on-disk contact. The 1D contact needs to have equal maximum Hertzian pressure and equal contact half-lengths as the 2D contact. The 1D radius of curvature R and normal loads w_{1D} are calculated by their corresponding equations (3.1) and (3.2) taken from [44].

$$\text{Condition to satisfy: } \begin{cases} p_{Hz}^{1D} = p_{Hz}^{2D} \\ a^{1D} = a^{2D} \end{cases} \qquad \text{this gives: } \begin{cases} R = \dfrac{E' a^{2D}}{4 p_{Hz}^{2D}} & (3.1) \\ w_{1D} = \dfrac{\pi p_H^{2D} a^{2D}}{2} & (3.2) \end{cases}$$

Expressions of E', a^{2D}, a^{1D}, and p_{Hz}^{1D} are given in section 2.2.1.

According to geometry, material properties, operating conditions, and the equation (3.1), the equivalent radius of curvature $R = 12.78\ mm$ is used throughout this chapter.

Simulations are performed with inputs corresponding to experimental conditions. That is, the inlet (or ambient) temperature T_0 is set to $39°C$ and the maximum Hertzian pressure is set to $504\ MPa$ resulting in $w_{1D} = 6.93 \times 10^4 N/m$ based on equation (3.2). The entrainment velocity u_e is fixed to 1m/s whereas SRR varies from 0 (pure rolling) to 4 (opposite sliding). Note that the solution of each sliding condition is used as an initial guess for the next sliding condition. The closer the two consecutive conditions are, the higher the chance of convergence for the higher sliding condition. For this reason, a step of 0.25 (in SRR) is chosen in simulations as opposed to a larger step as in experiments. Additional simulations are performed at the temperature $T_0 = 45°C$, these are used to explain the effect of accumulated heat in the surfaces of the solids during the experiments.

The lubricant properties and viscosity models presented in section 2.1.3 are used in the numerical simulations.

3.1.3 Film thickness results

During experiments and simulations, SRR varies from pure rolling ($SRR = 0$) to opposite sliding ($SRR = 4$). Values of central film thickness (h_c) and minimum film thickness on the central line ($h_{m,c}$) obtained by both methods can be compared.

Figure 3.2a and Figure 3.2b respectively show the variation of h_c and $h_{m,c}$ with respect to SRR for the experiments (black squares) with $T_0 = 39°C$ at the start of the experiment (i.e. at $SRR = 0$) and the simulation with $T_0 = 39°C$ (blue dots). Also, 4 points are shown corresponding to the simulation with $T_0 = 45°C$ (green triangles). In addition, the Chittenden thickness estimation corrected for non-Newtonian viscosity is shown in red at $SRR = 0$.

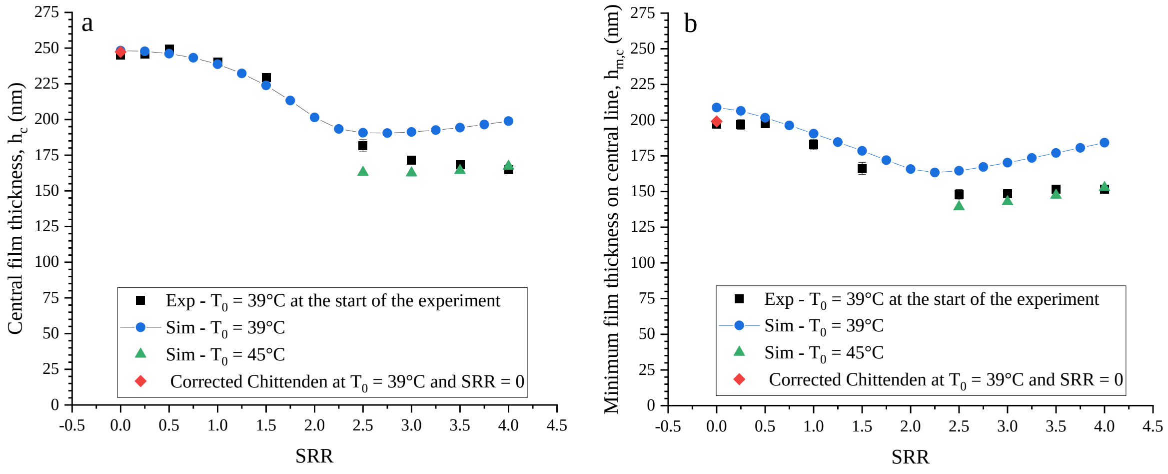

Figure 3.2: Variation of (a) the central film thickness h_c and (b) the minimum film thickness on central line $h_{m,c}$ with SRR. Some results of simulation at $T_0 = 45°C$ are also shown in addition to

the film thickness found by Chittenden's expression after correcting for non-Newtonian behavior at SRR=0 and $T_0 = 39°C$.

The error bars attached to experimental points correspond to the standard deviation calculated from 10 random measurements per sliding condition. Overall, the absolute error is lower than $\pm 4\ nm$ which translates to less than ± 2.8 % error on h_c and $h_{m,c}$, making the error bars hardly visible in Figure 3.2 as they have a similar size as the symbols.

For *0≤SRR<2*

The central film thickness h_c is almost constant with increasing SRR from 0 to 0.5 for measurements and simulations. With further increasing SRR to 1.5, h_c drops 6.4 % in experimental measurements and 9.8 % in simulations. Similarly, $h_{m,c}$ decreases with increasing SRR. The same effect on film thickness is reported in [73] and [146] for a circular contact and SRR varying from 0 to 1.8 and 0 to 1.6 respectively. The lower film thickness is attributed to a greater temperature rise in the inlet region and more shear-thinning with increased sliding. This lowers the lubricant's viscosity in the convergent region which results in a decrease in film thickness. Figure 3.3a shows film thickness profiles obtained experimentally (for $SRR = 0$ and 1) and numerically (for $SRR = 0$, 1, and 2) also Figure 3.3b shows the temperature rise along the x direction obtained from simulations at $T_0 = 39°C$.

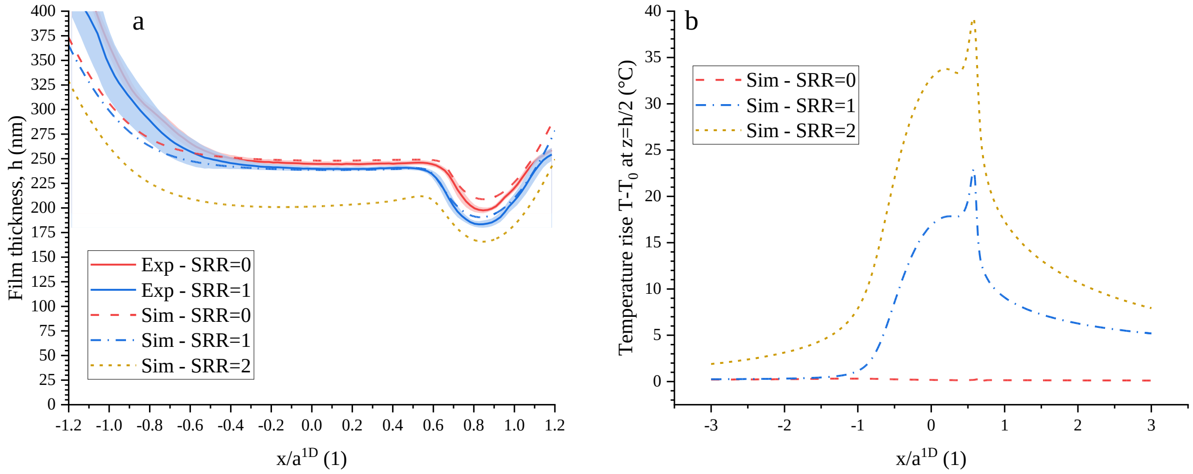

Figure 3.3: (a) Experimental and numerical film thickness profiles along the entrainment directions. (b) Numerical temperature rise in the lubricant's central line ($z = h/2$) compared to T_0. The latter is set to $39°C$ in simulations.

At the inlet ($x/a^{1D} = -1$), the temperature is higher at higher sliding. The effect of heating the lubricant upon entering the contact can be seen in Figure 3.3a by the decrease of film thickness in the central region ($-1 < x/a^{1D} < 1$). The envelope around experimental thickness profiles represents the standard deviation calculated from profiles extracted from 10 random images per sliding condition. It should be noted that the measurement uncertainty is highest at the entrance of the contact (on the left) and simulations underestimate the measured thickness. In contrast, experimental and numerical film thickness profiles are in good agreement elsewhere. Predictions are mostly within the measurement's uncertainty.

Figure 3.2a and Figure 3.2b show good agreement of numerical prediction corresponding to the inlet temperature $T_0 = 39°C$ with experiments in the range of SRR between 0 and 1.5. The prediction error for $h_{m,c}$ and h_c is less than 7.5 % and 2.5 % respectively. Thus, the model can reproduce quantitatively the lubricant film thickness for $0 \leq SRR \leq 1.5$.

For *SRR=2*

In both Figure 3.2a and Figure 3.2b, an inflection point in the thickness variation is noticed around the pure sliding condition ($SRR = 2$). This point marks the transition from surfaces moving in the same direction (rolling sliding) to moving in opposite directions (opposite sliding). Note that in the pure sliding condition, the disk is stationary and the barrel is rotating. This condition is only numerically simulated and not measured experimentally because the chromium coating of the sapphire disk was damaged probably due to local temperature rise and stress on the coating. Hence, no film thickness measurements were possible in this condition.

For *2<SRR≤4*

On one hand, the numerical model can reproduce qualitatively the measured increase in $h_{m,c}$ with SRR. This increase is attributed to the thermal viscosity wedge effect. A focus on the film thickness profiles in opposite sliding, involving a thermal viscosity wedge effect, is provided later in this section. On the other hand, a qualitative difference exists between the measured and calculated h_c variation with SRR. Meaning that, experimentally h_c continues to decrease with SRR while numerically it stabilizes and even increases slightly with SRR.

The prediction error is significant for SRR higher than 2. It reaches 21.3 % and 20.6 % at $SRR = 4$ respectively for $h_{m,c}$ and h_c. Note that experimental points were collected one after the other from SRR 0 to 4 in a single experiment. Throughout the experiment and due to heat dissipation from the lubricant to the contacting solids, the surface temperature of the disk and the barrel increases. As a consequence, the lubricant in the convergent region is at a higher temperature than that at the start of the test. This effect becomes more significant at higher sliding as more heat is generated by shearing inside of the fluid. With the increase in sliding, measurements become closer to a simulation at a higher inlet temperature $T_0 = 45°C$. This also explains the qualitative difference between measured and calculated h_c because the accumulation of heat in the solids is not considered in the numerical model.

Focus on film thickness profiles and the viscosity wedge effect in opposite sliding

In the current study, relatively high sliding conditions are tested (SRR up to 4). Figure 3.4 shows 2D thickness maps and film thickness profiles on the central line obtained by optical measurements for various sliding conditions. In addition, simulated film thickness profiles at $T_0 = 45°C$ are plotted along the entrainment direction. This temperature was chosen because the inlet lubricant temperature is thought to be higher at higher sliding compared to the pure rolling condition at the beginning of the experiment as explained at the end of section 3.1.1.

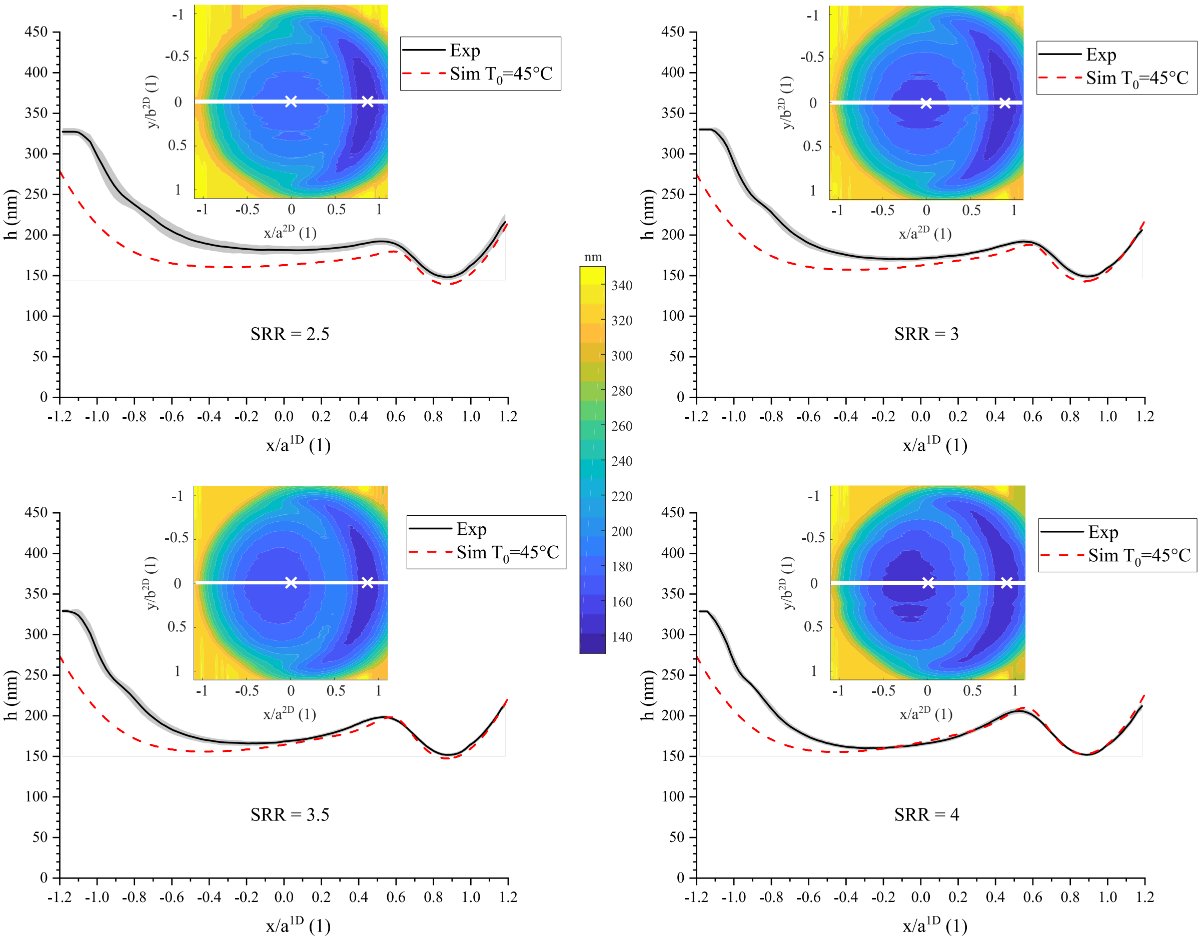

Figure 3.4: 2D thickness maps and thickness profiles along the x direction (experimental) and film thickness profiles (numerical at $T_0 = 45°C$) at SRR equal to 2.5, 3, 3.5, and 4. Note that x/a^{1D} and x/a^{2D} are equivalent because $a^{1D} = a^{2D}$ is a prerequisite for converting a 2D wide elliptical contact to 1D line contact.

Due to the dominance of thermal effects when a contact operates in opposite sliding ($SRR > 2$), the shape of the lubricant gap is no longer flat in the central region as in sliding-rolling conditions ($SRR < 2$) (see thickness profiles in Figure 3.3a and Figure 3.4). It should be noted that the numerical results considering $T_0 = 45°C$ in terms of thickness profiles fit very well the experimental results, especially in the region between the center and the right side of the contact ($0 \leq x/a^{1D} \leq 1.2$) and for the highest SRR.

In contrast, a quantitative difference between numerical and experimental thickness profiles on the left side of the contact is observed (similar to Figure 3.2a). A comparable difference is seen in Figure 11 of [74] showing experimental and numerical thickness profiles of a wide elliptical contact. In [74], no explanation was provided for this difference. In the present work, the influence of slightly changing Young's moduli of the materials or the radius of curvature R on the film thickness profiles was investigated. The profiles changed slightly but the changes were not enough to explain the large discrepancy on the left side of the contact between experimental and numerical profiles. Also, a comparison in Figure C.1b of Appendix C between the film thickness profiles from the 1D and 2D models revealed that, on the left side of the contact, the thickness profile from the 2D model is slightly lower than the profile from the 1D model and consequently further away from the experimental profile. Thus, the use of the 1D model to represent 2D elliptical contact is not the origin of the difference. A decisive physical explanation for the difference on the left side of the contact in Figure 3.4 is yet to be found.

A constant film thickness is observed at the extreme left of experimental profiles ($x/a^{1D} < -1$). This is due to an upper limit to film thickness set in the image analysis program to enable more accurate measurements in the zone of interest (i.e. $-1 < x/a^{1D} < 1$). The idea is to use a portion of the calibration curves (see Figure A.1) contained between a lower and an upper limit of film thickness. These were set respectively to 100 nm and 330 nm to get the profiles shown in Figure 3.4. In this manner, the image analysis program can only associate the colors of the interference pattern to the limited range of film thickness and avoids discontinuity in resulting film thickness profiles.

The variation of thickness profiles with increasing sliding indicates the development of a high-pressure zone known as a “dimple” due to the thermal viscosity wedge effect. The deformation caused by pressure build-up in the pressure zone becomes more important at higher sliding. Consequently, $h_{m,c}$ increases with increasing sliding.

Overall, the numerical model can capture complex physical mechanisms over a wide range of SRR. Also, it can accurately predict the film thickness when the temperature increase in experiments over time is accounted for.

3.1.4 Friction coefficient results

Figure 3.5 presents the variation of the friction coefficient C_f with SRR, where experimental and numerical results are shown.

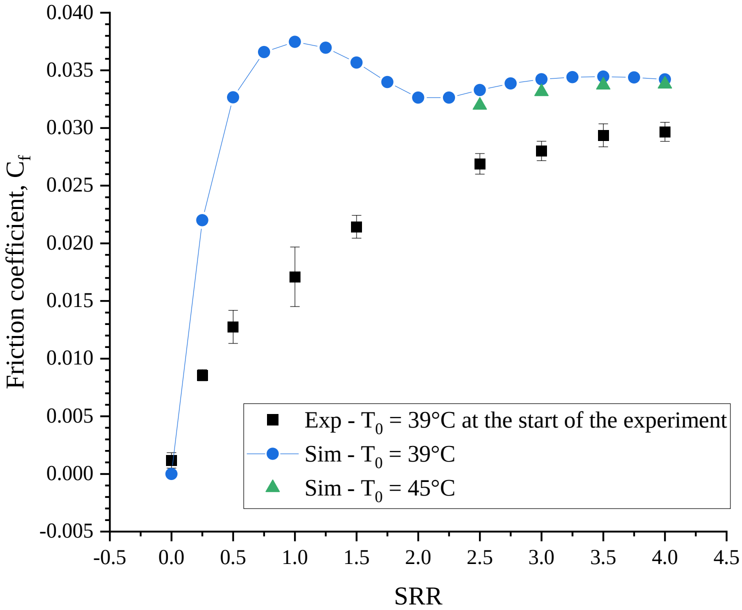

Figure 3.5: Friction coefficient variation with SRR. Experiment at $T_0 = 39°C$ at the start of the test and simulations at $T_0 = 39°C$ and $45°C$.

Experimentally the friction coefficient C_f increases with increasing SRR for the tested range. The rate of increase decreases with SRR. In contrast, a different behavior appears in numerical results. This behavior is similar to that found in [43] where the authors used a CFD model to study the performance of a TEHL contact over a wide range of sliding conditions ($SRR \in [0,8]$). Their model as well as the one used in the current work considers the pressure and temperature dependency of the properties of the lubricant. Furthermore, previous studies proved the importance of thermal and shear-thinning, especially in sliding-rolling contacts [147,51].

Results from simulations at $T_0 = 45°C$ are very close to those at $T_0 = 39°C$. This indicates that the inlet temperature has a low impact on the friction coefficient which is mostly controlled by the lubricant temperature in the high-pressure central region. More on this in section 3.2.

For *0≤SRR<2*

Numerically, C_f sharply increases from zero at pure rolling to a maximum at SRR around 1 then decreases. The shape of friction variation with SRR in simulations between pure rolling and pure sliding is attributed to the presence of two competing mechanisms. On one hand, increasing sliding leads to a higher shear rate, higher shear stress, and finally higher friction. On the other hand, due to shear heating, the lubricant's temperature increases and its viscosity decreases. In addition, shear-thinning further decreases the viscosity. After a critical SRR (here around $SRR = 1$), thermal and shear-thinning effects dominate and the friction coefficient starts decreasing (only in simulation).

Various causes can explain this discrepancy between experimental and numerical results. Habchi et al. [51] studied friction regimes in EHL contact along with the effect of considering (or not) thermal, shear-thinning, and limiting shear stress (LSS) effects on the frictional response. They found, using a numerical model similar to the one used in the current study, that the LSS is the most important factor to consider in friction prediction at moderate to high loads (i.e. when an apparent shear limit is reached). In [51] moderate and high loads correspond respectively to maximum Hertzian pressures $0.93 - 1.17\ GPa$ and $1.47\ GPa$. They described LSS as an upper bound to shear stress that depended on the pressure of the lubricant. However, the physical nature of LSS behavior and its dependency on contact conditions is not yet fully understood [148]. In the current state-of-the-art of lubricant rheology, it is very difficult to obtain independent viscosity measurements at extreme pressures and shear rates comparable to conditions found in EHL contacts. As a consequence, rheological models such as the ones used in this study cannot fully describe the behavior of the lubricant under extreme EHL conditions in terms of friction coefficient. Rheology of lubricants, especially at extreme shear rates, is still a very active research area [49,148–150] that is out of the scope of the current work.

Another possible reason for the discrepancy at relatively low sliding, mentioned in [120], is that in simulations the bulk temperature of the solids is considered equal to the lubricant inlet temperature T_0. However, in reality, heat accumulates in the solid surfaces which causes the viscosity in the neighboring fluid to drop, and consequently, the friction coefficient decreases. The influence of this mechanism on the friction response decreases as the average temperature in the contact increases. The sensitivity of the friction response to the change in temperature decreases at a higher temperature because viscosity itself is less sensitive to temperature variation at a high temperature compared to a low temperature. This is illustrated in Figure 3.6 showing the variation of average viscosity with average temperature both calculated in the contact region between $-a^{1D}$ and a^{1D}.

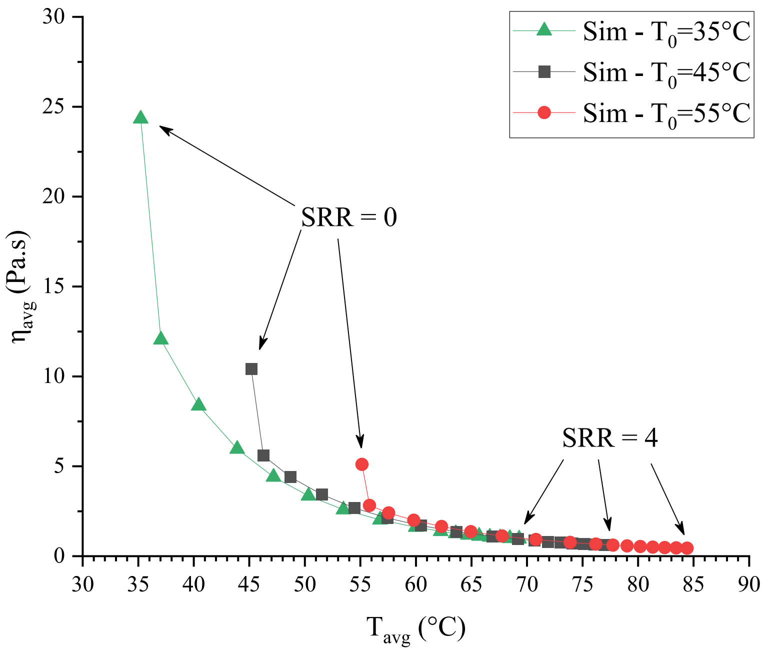

Figure 3.6: Average viscosity variation with the average temperature inside the contact for simulations at inlet temperatures 35, 45, and 55°C. The averages are calculated in the contact region between $-a^{1D}$ and a^{1D}.

Different curves are plotted each corresponding to a different ambient temperature where sliding goes from $SRR = 0$ (the left-most point) to $SRR = 4$ (the right-most point). At low SRR, the average temperature inside the contact is relatively low and heat from surfaces may largely influence the viscosity (notice the sharp decrease on the left side of each curve in Figure 3.6) and thus largely influence the friction coefficient. In contrast, at high SRR, the temperature inside the contact is relatively high and the influence of additional heat on viscosity and friction coefficient is less important (notice the slow decrease on the right side of each curve). This is true for all simulated temperatures.

It is important to remember that the friction coefficient is often overestimated by the 1D line contact model compared to a 2D wide elliptical contact with equal maximum Hertzian pressures and equal contact half-lengths along the entrainment direction. Figure 3.7 shows a comparison of the variation of friction coefficient with SRR resulting from 1D and 2D simulations described in Appendix C. It indicates that in rolling-sliding conditions ($0 < SRR < 2$), the friction coefficient calculated by the 1D line contact is, on average, 13 % higher than that calculated by the 2D elliptical contact. This overestimation is caused by the fact that the 1D model overestimates the lubricant pressure and shear rate in the y-direction if the contact was extended in the lateral dimension. The overestimation of the pressure leads to higher viscosity which in addition to the overestimation of the shear rate results in a higher friction coefficient calculated by the 1D model compared to the 2D model. However, this does not solely explain the discrepancy between predictions and measurements. Instead, errors from the three causes discussed above (i.e. not considering LSS, bulk temperature rise, and using the 1D model) accumulate in the final result.

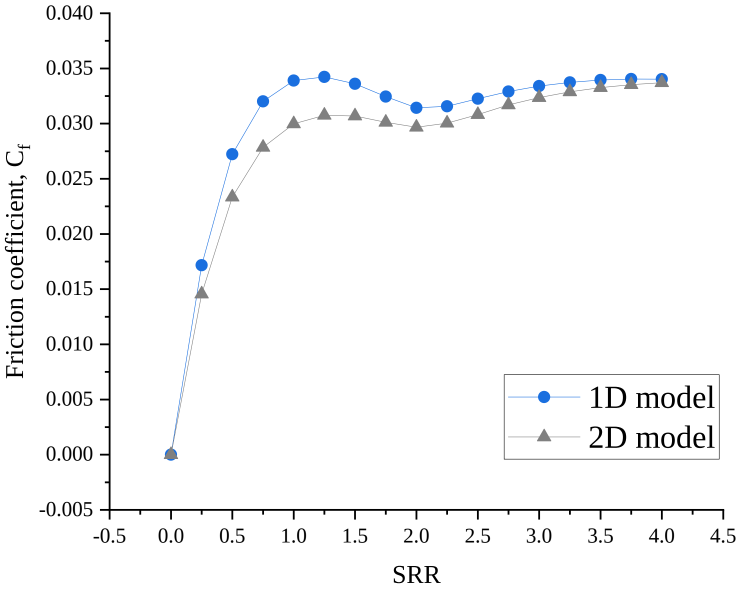

Figure 3.7: Friction coefficient variation with SRR. The results shown correspond to the 1D and 2D models used in Appendix C with $L_x^{1D} = L_x^{2D} = 10 = 10$ and $L_y^{2D} = 10$. The operating conditions are $T_0 = 45°C,\ p_{Hz}^{2D} = p_{Hz}^{1D} = 504\ MPa$, and $u_e = 1\ m/s$.

For *SRR=2*

At the pure sliding condition, the disk is stationary and the barrel rotates. The disk’s surface temperature increases and the “colder” fluid newly entering the contact heats up. Shear heating and convection from the disk surface contribute to lower viscosity and consequently friction. As soon as SRR becomes greater than 2, the friction coefficient increases because the convection of the fluid dissipates energy due to the motion of the disk. This leads to a minimum friction coefficient at $SRR = 2$. This behavior is observed only numerically where C_f is significantly overestimated for $SRR < 2$. In contrast, although experimentally measurements at $SRR = 2$ are not available, it could be inferred from the variation of C_f that a local minimum at $SRR = 2$ is unlikely to occur.

For *2<SRR≤4*

In the numerical results, for opposite sliding conditions ($2 < SRR \leq 4$), C_f increases slightly and then stabilizes at higher sliding. The numerical and experimental results are in good agreement with a mean relative prediction error of 19.5 % corresponding to a mean difference of 0.0055 between the predicted and measured friction coefficient. The discrepancy decreases with increasing sliding.

The authors in [51] showed that at high sliding and entrainment velocities ($SRR > 0.3$ and $u_e = 4\ m/s$), the thermal and shear-thinning effects dominate the friction response, and ignoring the LSS does not affect the model’s accuracy. It should be noted that the lubricant used in [51] (i.e. Shell T9), the geometry, and the operating conditions are very different than the ones used in the current work. Hence, only qualitative trends can be transferred to the current work. In [51], $SRR \in [0,0.5]$ while in the current study, the range of SRR extends to 4 and the numerical model does not include the LSS effect. Comparing experimental and numerical results confirms that at high sliding ($SRR > 2$) not considering the LSS effect has a less significant impact on the accuracy of the prediction compared to low sliding ($SRR < 2$).

The difference in friction coefficient, shown in Figure 3.7, between the 1D and 2D models decreases in opposite sliding conditions and with increasing SRR. As sliding increases, the temperature inside the contact also increases. By the same logic applied before, if one extends the 1D line contact into the y-direction a constant temperature along the y-direction is obtained. The higher pressure (normally leading to higher viscosity) in the extended 1D contact is compensated by a higher temperature which lowers the viscosity of the lubricant and the friction force compared to the 2D contact. One ends up with a friction coefficient closer to that found in the 2D model as sliding increases.

In conclusion, the difference between predictions and experimental measurements of friction coefficient results cannot be attributed to a single cause, instead, it is a result of contributions from the different phenomena discussed in this section. Mainly, the lack of a full description of the rheology of the lubricant at high pressure and high shear rate. However, a good agreement is obtained under high sliding conditions ($2 < SRR \leq 4$).

3.1.5 Conclusion

The wide elliptical TEHL contact performance was investigated for sliding conditions ranging from pure rolling ($SRR = 0$) to opposite sliding ($SRR = 4$). In all cases, film thickness (both h_c and $h_{m,c}$) decreases with increasing SRR from 0 to 2. This behavior is explained by shear-thinning and the increase of the temperature of the lubricant in the inlet region due to shear heating at higher sliding. The pure sliding condition ($SRR = 2$) constitutes an inflection point for the variation of film thickness with SRR in the case of conductive surfaces. For $2 < SRR \leq 4$, the thickness profile in the central region shows a dimple due to the thermal viscosity wedge. This causes an increase in $h_{m,c}$ with increasing SRR. Note that the numerical model can quantitatively predict the shape of the film thickness profile, especially at high sliding ($SRR > 2$) when the higher inlet temperature is considered. The average discrepancy is around 5 % between the measured film thickness profile and the calculated one (at $T_0 = 45°C$) over the contact area defined by $x \in [-a^{1D}, a^{1D}]$.

With SRR between 0 and 2, the discrepancy in C_f between the numerical predictions and measurements originates mainly from ignoring the limiting shear stress (LSS) phenomenon in the model. Meanwhile, for $2 < SRR \leq 4$, friction predictions are close to measurements. This confirms the dominance of thermal and shear-thinning effects over the LSS effect at high sliding.

Next, the numerical approach is used to explore the effects of varying operating conditions on film thickness and friction coefficient in a TEHL contact.

3.2 Effects of Varying Operating Conditions on Film Thickness and Friction Coefficient in a TEHL Line Contact for 0 ≤ SRR ≤ 4

Most of the semi-analytical expressions in the literature [18,23–25,143] are limited to pure rolling contact under isothermal conditions. Over the years, researchers came up with experimental and numerical methods that enable the study of EHL contacts under rolling-sliding conditions where thermal and shear-thinning effects are significant. Advances such as the generalized Reynolds equation [34] and the full-system approach [30] enabled deeper investigations of the effects of operating conditions on EHL contact performance. However, to the author's best knowledge, the literature lacks an investigation of the effects of varying operating conditions on EHL film thickness and friction coefficient simultaneously, especially under extreme sliding (for example, $SRR > 2$). In this section, the effects of changing the lubricant inlet temperature, the normal load, and the entrainment velocity on film thickness and friction coefficient are studied.

3.2.1 Materials and operating conditions

The geometry used here corresponds to a cylinder-on-plane contact with the plane made of sapphire and the cylinder made of steel. This mimics the barrel-on-plane experimental wide elliptical contact. Mechanical and thermal properties used for the solids are the same as those used in the previous sections and given in Table 2.1 (Sapphire) and Table 2.2 (100C6 steel). Also, the properties of the lubricant and the parameters of the viscosity models are given in Table 2.4. The parameters corresponding to different operating conditions are summarized in Table 3.2. For the reference case, the inlet temperature is $T_0 = 50°C$, the maximum Hertzian pressure is $p_{Hz} = 504\ MPa$, the contact half-length is $a^{1D} = 87.5\ \mu m$, and the entrainment velocity is $u_e = 1\ m/s$.

Table 3.2: Parameters used in the numerical model to simulate different operating conditions.

Parameters Units	$\boldsymbol{T_0}$ $°C$	$\boldsymbol{p_{Hz}}$ MPa	$\boldsymbol{w_{1D}}$ N/m	$\boldsymbol{a^{1D}}$ μm	$\boldsymbol{u_e}$ m/s
Reference case	50	504	6.93×10^4	87.5	1
Lower T_0	35	504	6.93×10^4	87.5	1
Higher T_0	80	504	6.93×10^4	87.5	1
Lower p_{Hz}	50	429	5.02×10^4	74.4	1
Higher p_{Hz}	50	840	19.22×10^4	145.7	1
Lower u_e	50	504	6.93×10^4	87.5	0.3
Higher u_e	50	504	6.93×10^4	87.5	3

For simplicity, cases with varying temperatures, normal loads, and entrainment velocities are studied separately in the following sections.

3.2.2 Effects of varying the inlet temperature

Film thickness

Firstly, the effects on the film thickness of different inlet temperatures $T_0 = 35, 50,$ and $80\ °C$ are considered. Figure 3.8 shows the variation of minimum lubricant film thickness h_m with SRR in a TEHL line contact under various inlet temperature conditions. In addition, the minimum film thickness by Dowson's expression (3.3) from [151] is corrected for non-Newtonian effects at $SRR = 0$ and represented in Figure 3.8 by green symbols corresponding to each operating condition.

$$H_{m,Dowson} = 2.65\ U^{0.7}\ G^{0.54}\ W_{1D}^{-0.13} \tag{3.3}$$

where U, G, and W_{1D} and $H_{m,Dowson}$ are the dimensionless parameters defined in (1.5).

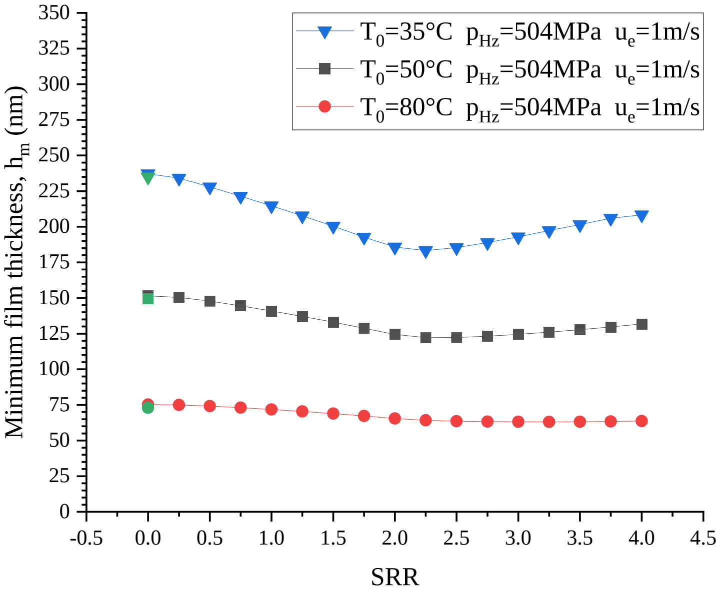

Figure 3.8: Variation with SRR of the minimum film thickness for various inlet temperatures. The reference case is presented in black and the other cases are colored in blue and red. In addition, green symbols represent the minimum film thickness found by Dowson's expression [151] after correcting for non-Newtonian behavior at $SRR = 0$.

For a given SRR between 0 and 4, h_m is lower for a higher temperature because the lubricant viscosity is lower.

For $0 \leq SRR \leq 2$, the increase in temperature in the convergent region caused by sliding is responsible for the decrease in film thickness (see section 3.1.3). Figure 3.9 shows the variation with SRR of the average temperature $T_{avg,x=-a^{1D}}$ and the average viscosity $\eta_{avg,x=-a^{1D}}$ for different values of T_0. These values are calculated by averaging across the film thickness at $x = -a^{1D}$.

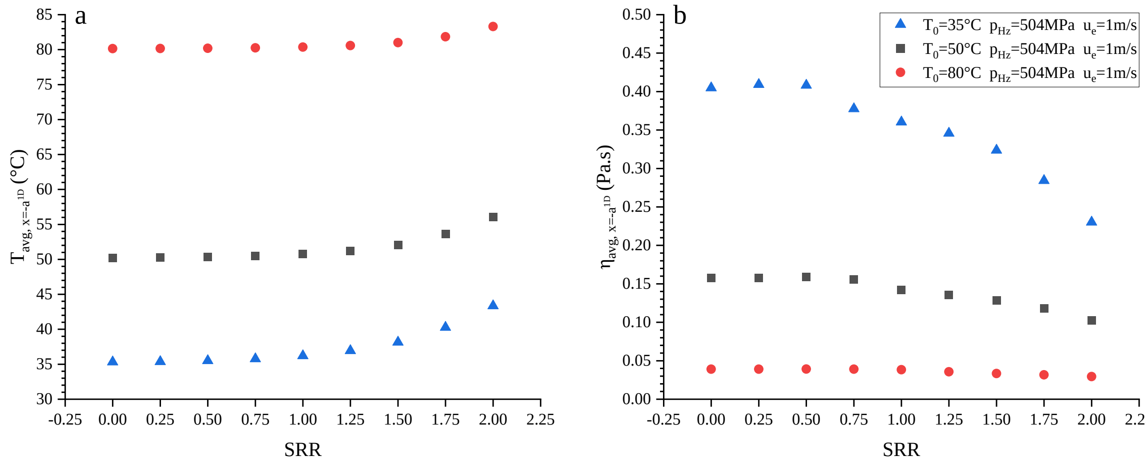

Figure 3.9: Variation with SRR of (a) the average temperature $T_{avg,x=-a^{1D}}$ and (b) the average viscosity $\eta_{avg,x=-a^{1D}}$ for various values of T_0. The values are calculated by averaging across the film thickness (z-direction) at the location $x = -a^{1D}$.

The increase of the average temperature at $x = -a^{1D}$ with SRR is more significant at lower T_0. Also, the decrease with SRR of the average viscosity at $x = -a^{1D}$ is more significant at lower T_0. This explains the higher rate of change in h_m with SRR for lower T_0.

For $2 < SRR \leq 4$, the difference in temperature $\Delta T = T|_{\partial_{f/s1}} - T|_{\partial_{f/s2}}$ across the film thickness at both entrances of the contact (i.e. $x = -a^{1D}$ and $x = a^{1D}$ due to opposite sliding) is lower for a higher T_0. This is shown in the following Table 3.3.

Table 3.3: Values of the difference in fluid temperature between the bottom and top fluid-solid interfaces at the positions $x = -a^{1D}$ and $x = a^{1D}$ for different T_0.

Variables	Values		
	$T_0 = 35°C$	$T_0 = 50°C$	$T_0 = 80°C$
$\|\Delta T_{x=-a^{1D}}\|$	15.7	13.0	7.6
$\|\Delta T_{x=a^{1D}}\|$	12.9	10.8	5.9

The lower $|\Delta T|$ at higher T_0 leads to a lower viscosity gradient $\frac{\partial \eta}{\partial z}$ across the film thickness in the fluid domain. Bruyère et al. [43] found that the term $\frac{\partial \eta}{\partial z} \times \frac{\partial u_f}{\partial z}$ is responsible for generating a pressure gradient in the entrainment direction (x-direction). In other word, it is responsible for the thermal viscosity wedge effect. Figure 3.10 shows the distribution of this “viscosity wedge term” in the deformed fluid domains for the highest simulated sliding ($SRR = 4$) at different inlet temperatures.

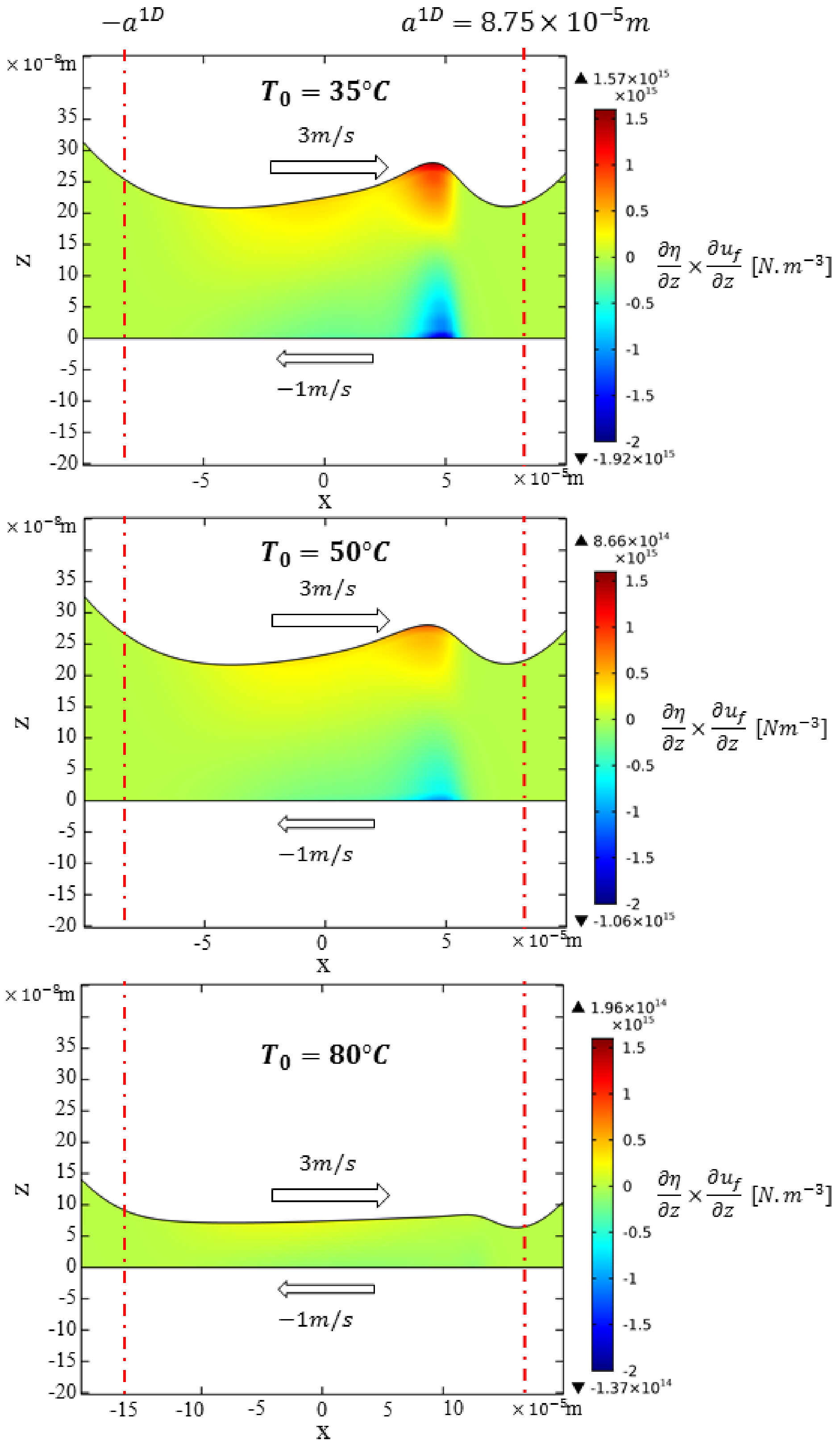

Figure 3.10: Distribution of the viscosity wedge term $(\frac{\partial \eta}{\partial z} \times \frac{\partial u_f}{\partial z})$ in the deformed fluid domain for $SRR = 4$, and $T_0 = 35°C, 50°C$, and $80°C$.

Note that the negative values in the above distributions correspond to the points where the fluid velocity u_f is in the negative x-directions notably near the bottom fluid-solid interface that is moving at 1 m/s in the negative x-direction. The magnitude of the term $\frac{\partial \eta}{\partial z} \times \frac{\partial u_f}{\partial z}$ is higher for lower T_0. Also, the thickness profile in the central region is mostly flat for $T_0 = 80°C$ while it shows a significant dimple in the lower temperature cases (i.e. $T_0 = 50°C$ and $35°C$). Hence, the thermal viscosity wedge effect becomes less significant when the inlet temperature T_0 is increased. A similar influence of inlet temperature on the thermal viscosity wedge effect was observed by Meziane et al. [44] under infinite sliding conditions.

Friction coefficient

Secondly, the effects of varying T_0 on the friction coefficient are discussed. Figure 3.11 shows the variation of the friction coefficient with SRR for various inlet temperatures.

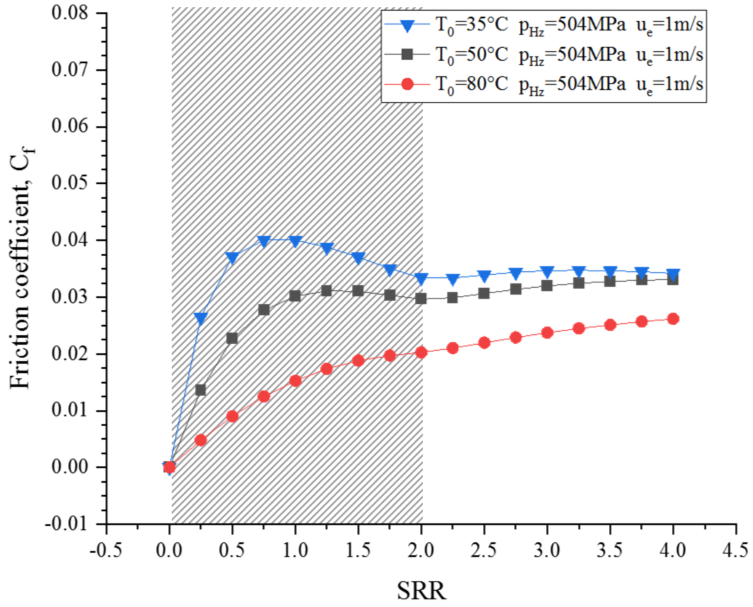

Figure 3.11: Variation with SRR of the friction coefficient for various inlet temperatures. The reference case is presented in black and the other cases are colored in blue and red. The gray zone indicates the range over which the friction coefficient is overestimated under certain conditions due to not considering the LSS.

The friction coefficient is significantly lower for a higher temperature at low SRR ($SRR \leq 1$). The influence of inlet temperature decreases with increasing sliding, especially for $SRR > 2$. In contrast to the film thickness, which is mostly controlled by the lubricant conditions at the convergent region, the friction coefficient is mostly controlled by the viscosity of the lubricant and the shear rate in the high-pressure region of the contact. To better understand the contribution of each of these quantities to the friction coefficient, the variations with SRR of the average viscosity and the average shear rate inside the contact are plotted in Figure 3.12 for all three lubricant temperatures.

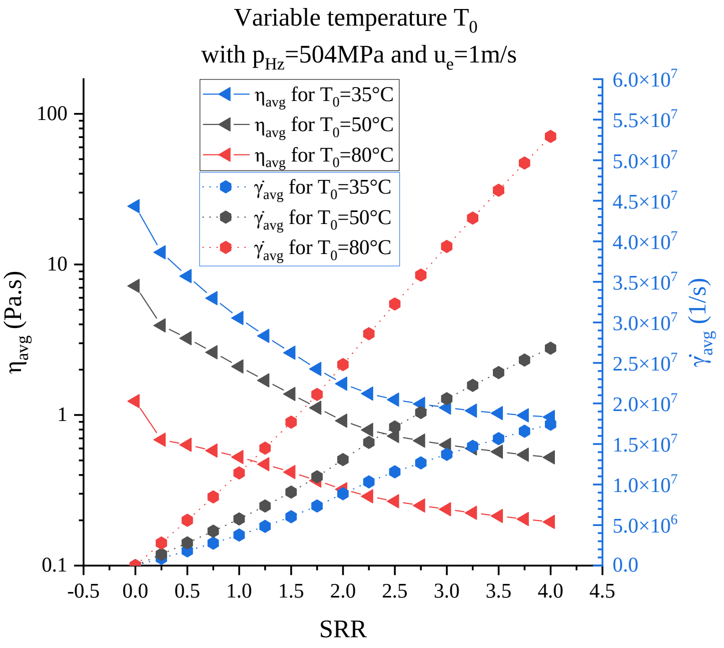

Figure 3.12: Variation with SRR of average viscosity (left axis) and average shear rate (right axis) inside the contact for various inlet lubricant temperatures. The averages are calculated over the 2D fluid domain in the contact region between $x = -a^{1D}$ and $x = a^{1D}$.

At a given $SRR > 0$, the average viscosity is significantly lower for a higher T_0 while the average shear rate is higher. The large difference in viscosity at low sliding conditions explains the significant difference in the friction curves between cases at different inlet temperatures. The shear stress is defined as $\tau_{zx} = \eta\dot{\gamma}$ increases with viscosity and shear rate. Moreover, given that the rheology models of the lubricant used in the numerical model do not include the LSS effect, the increase in shear stress is not bounded. For this reason, at a low inlet temperature, the friction coefficient sharply increases reaching a peak then decreases (when thermal and shear-thinning effects become important) to a minimum at $SRR = 2$. In contrast, at a high inlet temperature, the friction coefficient increases monotonously due to an already low shear stress. In this case, the LSS effect is dominated by the thermal effects.

Furthermore, the shear rate defined by $\dot{\gamma} = \frac{\partial u_f}{\partial z}$ is influenced by the film thickness (in the z-direction) and increases significantly when the film thickness decreases due to higher T_0. The decrease in viscosity and the increase in shear rate have the opposite effect on the friction coefficient. However, in the conditions presented here, the lower viscosity (due to higher inlet temperature) dominates the higher shear rate. Hence, the friction coefficient is lower for a higher lubricant temperature.

The diagram in Figure 3.13 summarizes the mechanisms discussed above by which the variation of the inlet temperature T_0 influences the minimum film thickness and the friction coefficient in a TEHL contact.

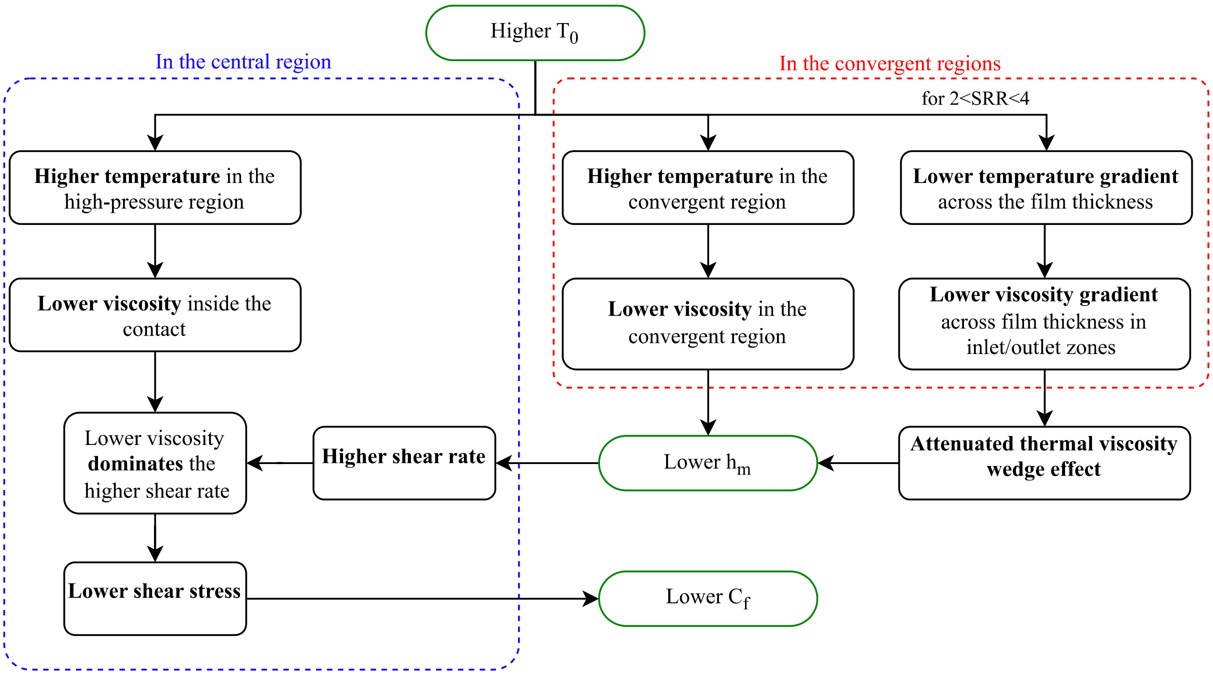

Figure 3.13: Diagram summarizing the mechanisms by which a higher inlet temperature leads to a lower minimum film thickness and lower friction coefficient in a TEHL contact.

3.2.3 Effects of varying the normal load

This section focuses on the effects of varying the normal load w_{1D} which is equivalent to varying maximum Hertzian pressure p_{Hz} given that the materials and geometries are unchanged. Two maximum Hertzian pressures, 429 MPa and 840 MPa, are investigated in addition to the reference case at 504 MPa. While studying the effect of varying the normal load, all other contact parameters were unchanged (including the inlet temperature and the entrainment velocity). Under the current contact conditions, excessively lowering the normal load may cause the transition of the lubrication from the elastohydrodynamic regime to the hydrodynamic regime. For this reason, the lowest tested maximum Hertzian pressure was limited to 429 MPa.

Film thickness

The results of the film thickness variation with SRR are shown in Figure 3.14. For all sliding conditions, the minimum film thickness decreases with increasing load.

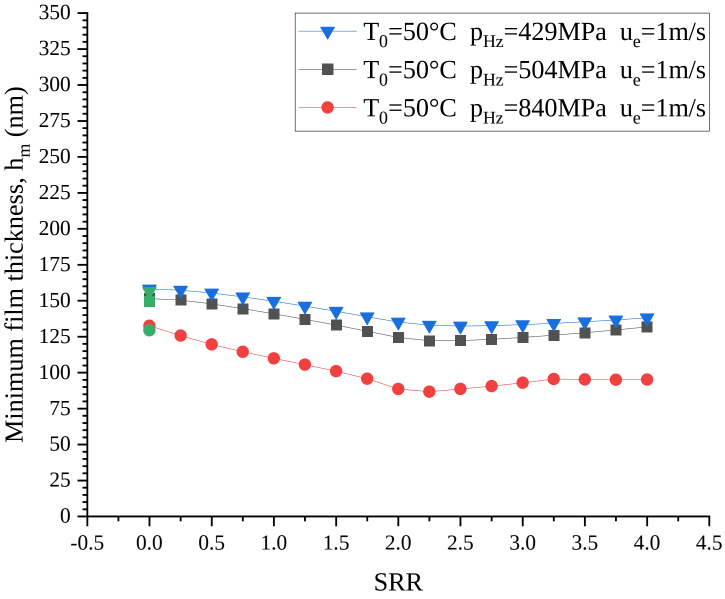

Figure 3.14: Variation of minimum film thickness with SRR for various normal loads. The reference case is presented in black and the other cases are colored in blue and red. In addition, green symbols represent the minimum film thickness found by Dowson's [151] expression after correcting for non-Newtonian behavior at $SRR = 0$.

As mentioned before, the film thickness is governed mainly by the viscosity of the lubricant at the convergent region. The viscosity depends on pressure, temperature, and shear rate. In the pure rolling case, however, the shear rate and temperature rise are negligible. Hence, the only thing that can influence the viscosity in the convergent region when changing the normal load is the pressure. Figure 3.15 shows the pressure profiles of the three normal load cases at pure rolling ($SRR = 0$) plotted on the normalized x-direction.

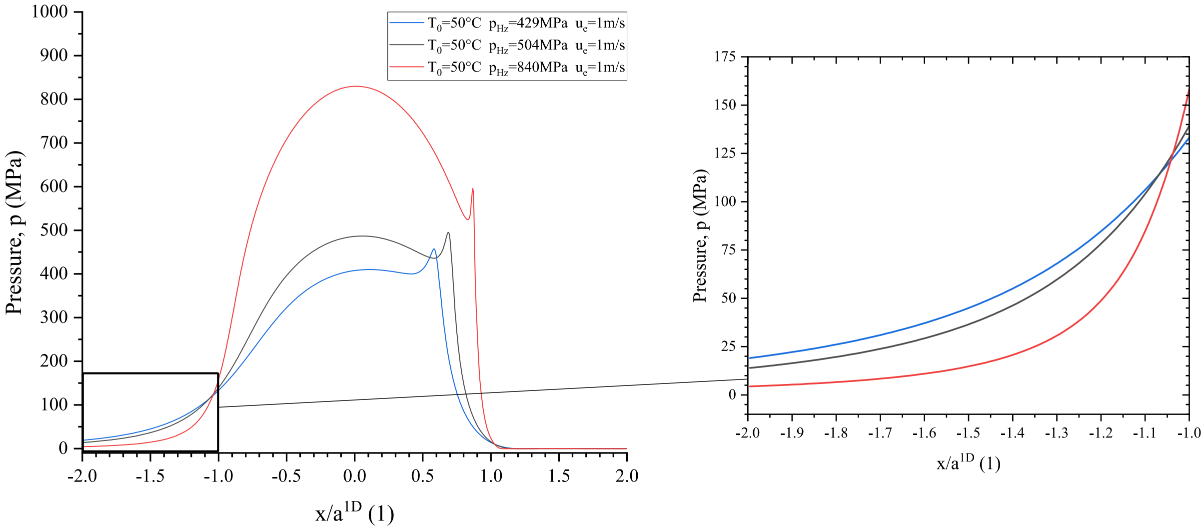

Figure 3.15: Pressure profiles along the normalized x-direction for various normal loads at pure sliding ($SSR = 0$). A zoom-in view of the convergent is shown on the right plot.

In the convergent region ($x/a^{1D} < -1$), the lubricant pressure is lower in the case of the highest load ($p_{Hz} = 840\ MPa$) compared to the reference case ($p_{Hz} = 504\ MPa$). This lower pressure leads to a lower viscosity and as a consequence h_m decreases with normal load at a given SRR.

Friction coefficient

The results of the friction coefficient variation with SRR are shown in Figure 3.16.

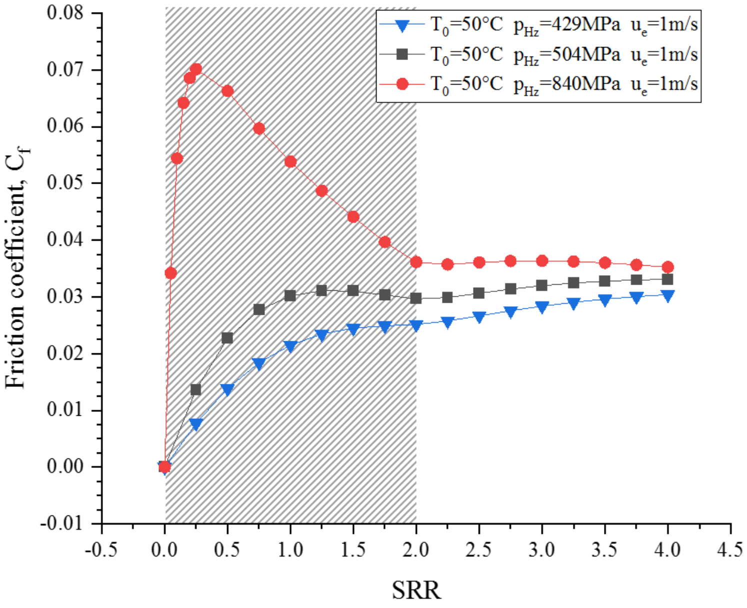

Figure 3.16: Variation of friction coefficient with SRR for various normal loads. The reference case is presented in black and the other cases are colored in blue and red. The gray zone indicates the range over which the friction coefficient is overestimated under certain conditions due to not considering the LSS.

The friction response is dictated by the fluid behavior inside the contact where pressure is the highest. Also, the temperature is the highest inside the contact (in case SRR>0). Figure 3.17 presents the temperature of the lubricant along the central line ($z = \frac{h}{2}$) for all three normal load cases at $SRR = 1$.

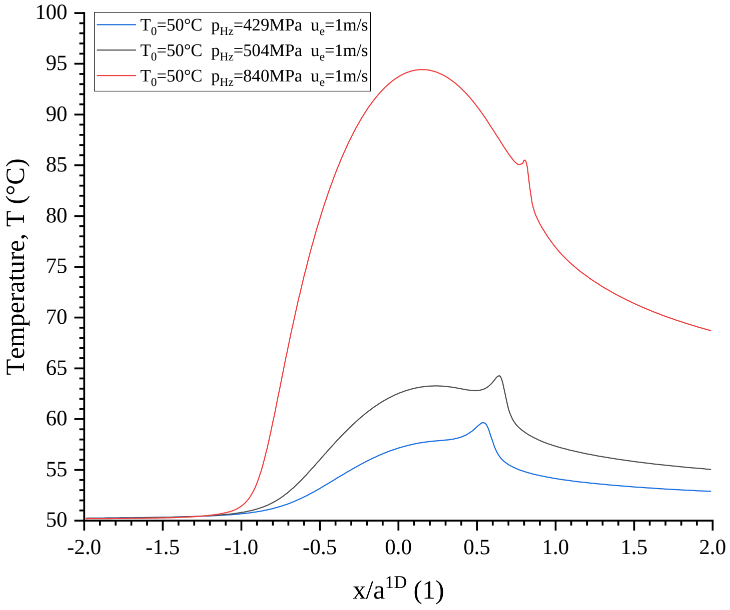

Figure 3.17: Temperature of the lubricant along the central line ($z = \frac{h}{2}$) for different normal loads at $SRR = 1$.

With increasing normal load, the temperature of the lubricant inside the contact increases significantly. An increase in temperature usually leads to a decrease in viscosity. However, in the tested cases the viscosity is dominated by the pressure increase. This could be inferred from Figure 3.18 showing that the average viscosity inside the contact is always higher for a higher load.

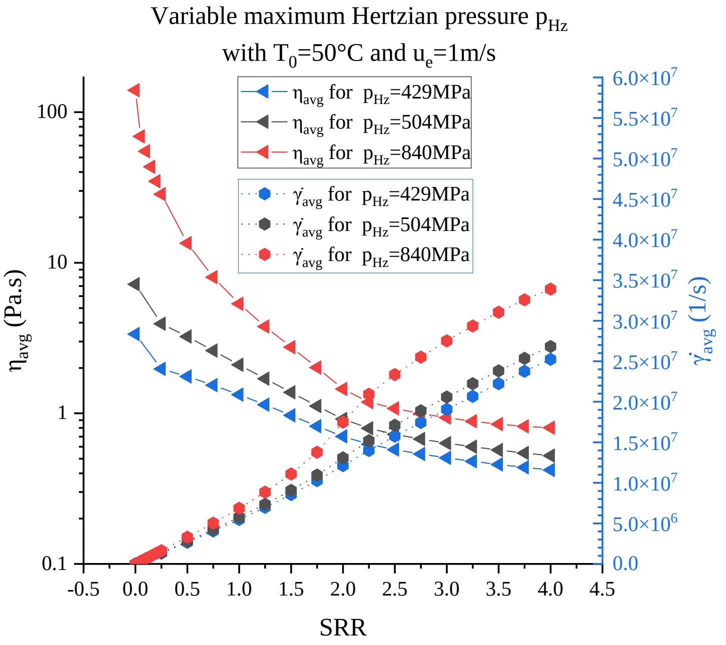

Figure 3.18: Variation with SRR of average viscosity (left axis) and average shear rate (right axis) inside the contact for various maximum Hertzian pressures. The averages are calculated in the contact region between $x = -a^{1D}$ and $x = a^{1D}$.

In the case of $p_{Hz} = 840\ MPa$ and at $SRR = 0.25$ the viscosity is significantly higher than all the other cases because of the dependence of viscosity on pressure. Values of friction coefficient are probably overestimated because the LSS effect is not considered. This explains the qualitative difference in friction curves between cases at different loads seen in Figure 3.16 at low SRR. Note that, similarly to the temperature variation cases, the difference in viscosity between various load cases becomes smaller at bigger sliding. Also, note that the difference in average shear rate is almost constant with SRR under opposite sliding conditions. This explains the tendency of friction coefficient variation of different load cases to converge at very high sliding.

The diagram in Figure 3.19 summarizes the mechanisms discussed above by which the variation in the normal load influences the minimum film thickness and the friction coefficient in a TEHL contact.

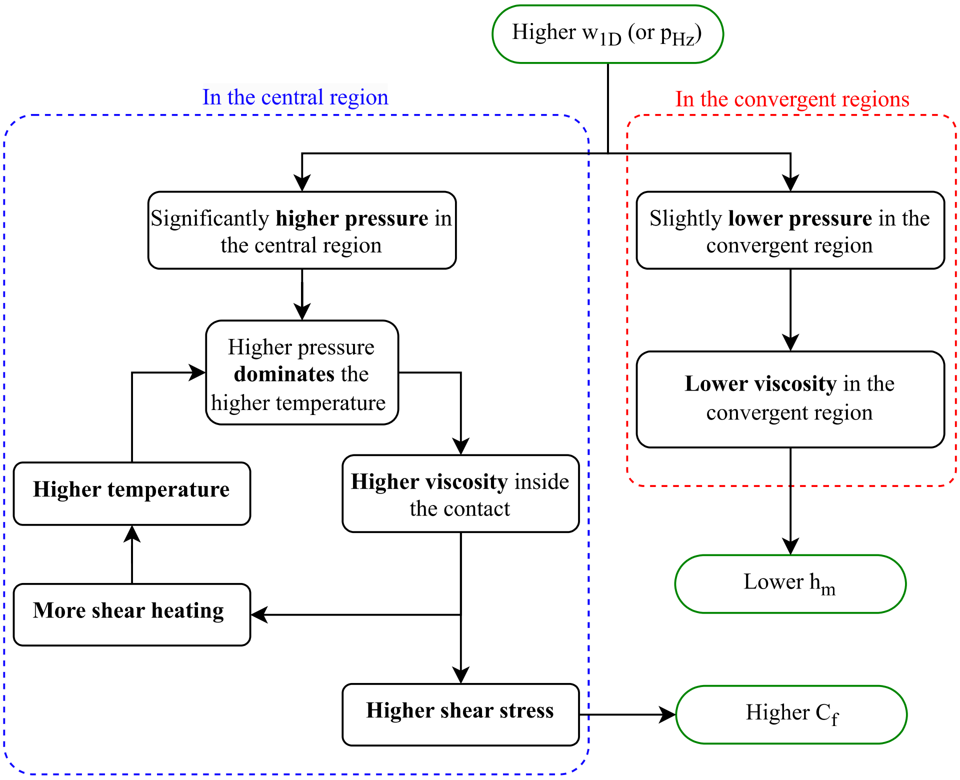

Figure 3.19: Diagram summarizing the mechanisms by which a higher normal load leads to lower minimum film thickness and higher friction coefficient in a TEHL contact.

3.2.4 Effects of varying the entrainment velocity

This section focuses on the effects of changing the entrainment velocity on the minimum film thickness and friction coefficient. It should be noted that, at a given SRR, increasing the entrainment velocity is synonymous with increasing the surface speeds u_1 and u_2 of solids 1 and 2 respectively. u_1 and u_2 are related to SRR and u_e by equations (3.4).

$$\begin{aligned} u_1 &= u_e(2+SRR)/2 \\ u_2 &= u_e(2-SRR)/2 \end{aligned} \tag{3.4}$$

Their values for some simulated conditions are listed in Table 3.4.

Table 3.4: Values of u_1 and u_2 for all simulated conditions.

	u_e (m/s)					
	0.3		1		3	
SRR	u_1(m/s)	u_2(m/s)	u_1(m/s)	u_2(m/s)	u_1(m/s)	u_2(m/s)
0	0.3	0.3	1	1	3	3
1	0.45	0.15	1.5	0.5	4.5	1.5
2	0.6	0	2	0	6	0
3	0.75	-0.15	2.5	-0.5	7.5	-1.5
4	0.9	-0.3	3	-1	9	-3

Film thickness

Figure 3.20 presents the variation of h_m with SRR for different entrainment velocities.

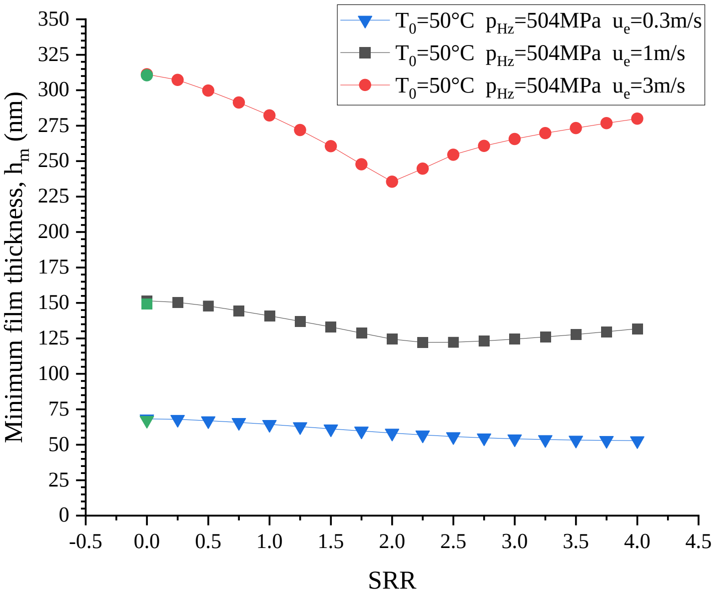

Figure 3.20: Variation of minimum film thickness with SRR for various entrainment velocities. The reference case is presented in black and the other cases are colored in blue and red. In addition, green symbols represent the minimum film thickness found by Dowson's [151] expression after correcting for non-Newtonian behavior at $SRR = 0$.

The minimum film thickness increases with increasing the entrainment velocity. This is in agreement with early semi-analytical film thickness expressions, such as (3.3) from Dowson [151], that showed a proportional relation between h_m and $u_e^{0.7}$ at $SRR = 0$. This is due to a greater convergent wedge at higher entrainment velocity.

In this Figure 3.20 a distinction is made in the variation of h_m with SRR between different entrainment velocities. For higher velocity, the rate of change of h_m with SRR is higher for both rolling-sliding and opposite-sliding conditions where h_m is respectively decreasing and increasing.

For $\mathbf{2 \leq \mathit{SRR} \leq 4}$, h_m increases more rapidly with SRR for the highest entrainment velocity. In contrast, for $u_e = 0.3\ m/s$, h_m continues the decrease indicating the negligible contribution of the thermal viscosity wedge effect. Under opposite sliding conditions, at each side of the contact, the colder surface enters more rapidly and the hotter surface exits more rapidly if the entrainment velocity is increased (see Table 3.4). Consequently, the temperature gradient through the film thickness becomes higher. Figure 3.21 shows the temperature distribution inside the lubricant film at $u_e = 0.3\ m/s$ and $3\ m/s$. Velocity directions and magnitudes of the surfaces are also shown for top and bottom surfaces. The temperature of the fluid near the surfaces at $x = -a^{1D}$ and $x = a^{1D}$ are indicated.

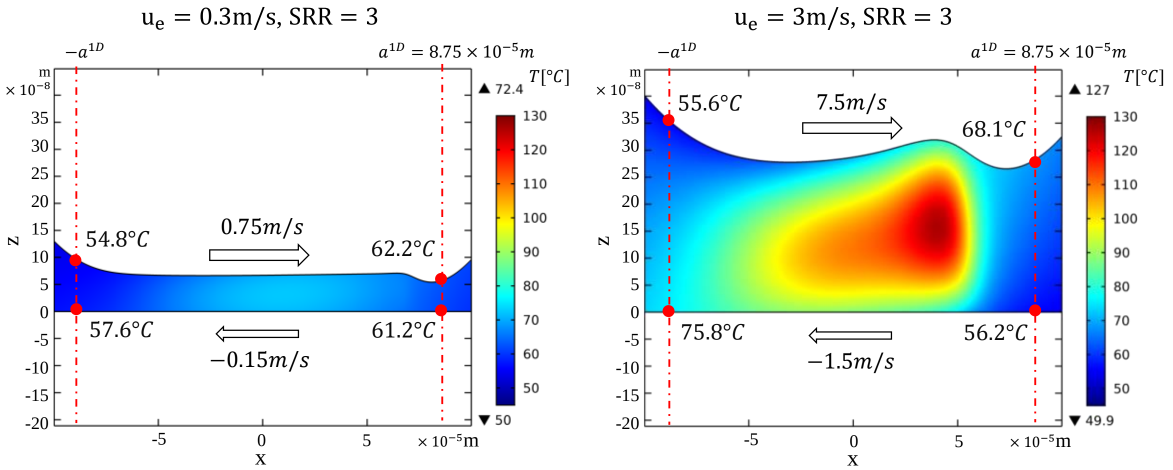

Figure 3.21: Temperature distribution inside the lubricant at SRR=3 for two different entrainment velocities (left) 0.3 m/s (right) and 3 m/s. Directions and speed of surface motion are shown for top and bottom surfaces. Also shown, is the temperature of the fluid near the surfaces at $x = -a^{1D}$ and $x = a^{1D}$.

For instance, at $x = -a^{1D}$, the differences between the lubricant temperatures near the top and the bottom surfaces are $2.8°C$ and $20.2°C$ for $u_e = 0.3\ m/s$ and $u_e = 3\ m/s$ respectively. The difference in temperature through the thickness between the top and bottom surfaces creates a difference in viscosity. Hence, for a higher entrainment velocity, this difference is greater and the thermal viscosity wedge effect is amplified. In contrast, in the case of $u_e = 0.3\ m/s$, no thermal viscosity wedge is observed.

Friction coefficient

Figure 3.22 shows the variation of friction coefficient with SRR for different entrainment velocities.

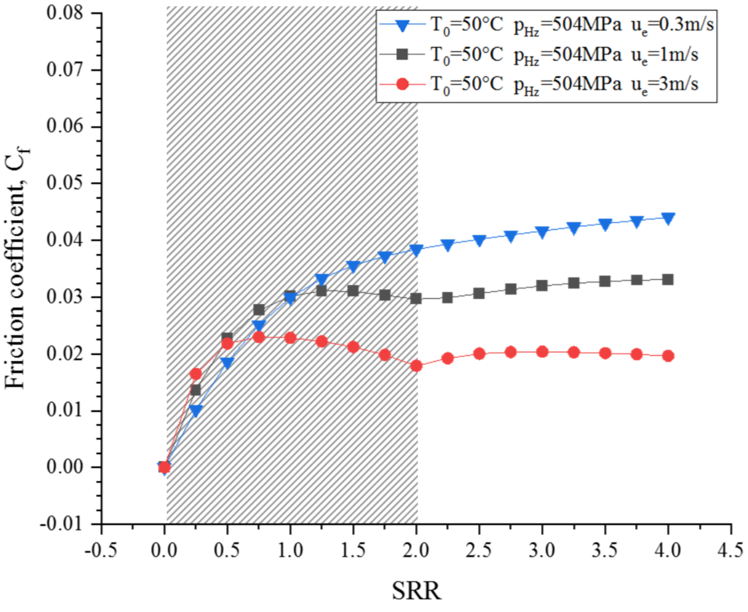

Figure 3.22: Variation of friction coefficient with SRR for various entrainment velocities. The reference case is presented in black and the other cases are colored in blue and red. The gray zone indicates the range over which the friction coefficient is overestimated under certain conditions due to not considering the LSS.

For $SRR \leq 0.5$, the values of friction coefficient from simulations at different entrainment velocities are close to one another at a given SRR. However, at higher sliding, thermal and shear-thinning effects start to influence the friction response. The values of C_f at different entrainment velocities become further apart at a given SRR. The influence of thermal and shear-thinning effects is greater for higher entrainment velocity because of higher shear rate and shear heating. Thus, C_f is lower for higher u_e for all sliding conditions when $SRR > 1$.

A plateau of friction coefficient is reached at high SRR for all entrainment velocities cases. Here, two competing mechanisms influence the friction response when increasing SRR. Namely, the viscosity decreases, and simultaneously the shear rate increases (see Figure 3.23).

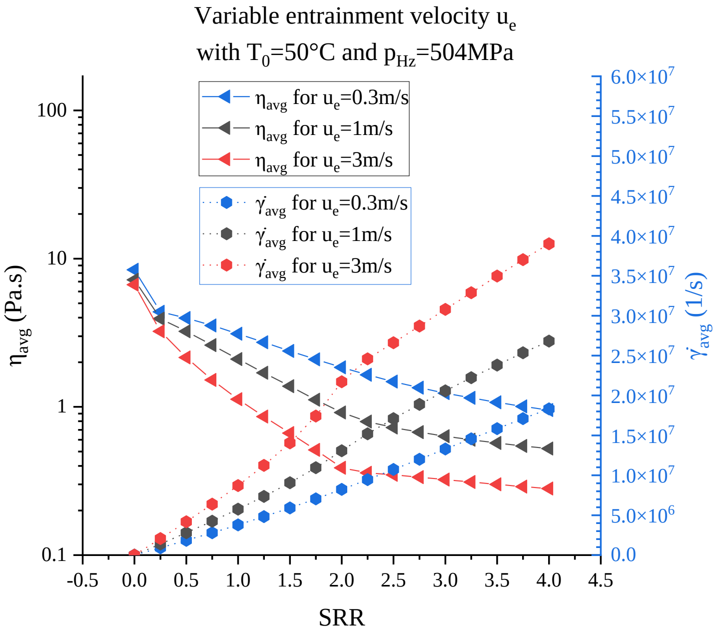

Figure 3.23: Variation with SRR of average viscosity (left axis) and average shear rate (right axis) inside the contact for various entrainment velocities. The averages are calculated in the contact region between $-a^{1D}$ and a^{1D}.

On one hand, the decrease in viscosity is caused by an increase in the temperature of the lubricant (see Figure 3.21) due to shear heating. On the other hand, the shear rate increases due to higher fluid velocity. In the presented cases, at high sliding ($SRR > 2.5$), these effects cancel each other out so an increase in sliding does not influence the friction coefficient significantly.

The diagram in Figure 3.24 summarizes the mechanisms discussed above by which the variation in the entrainment velocity influences the minimum film thickness and the friction coefficient in a TEHL contact.

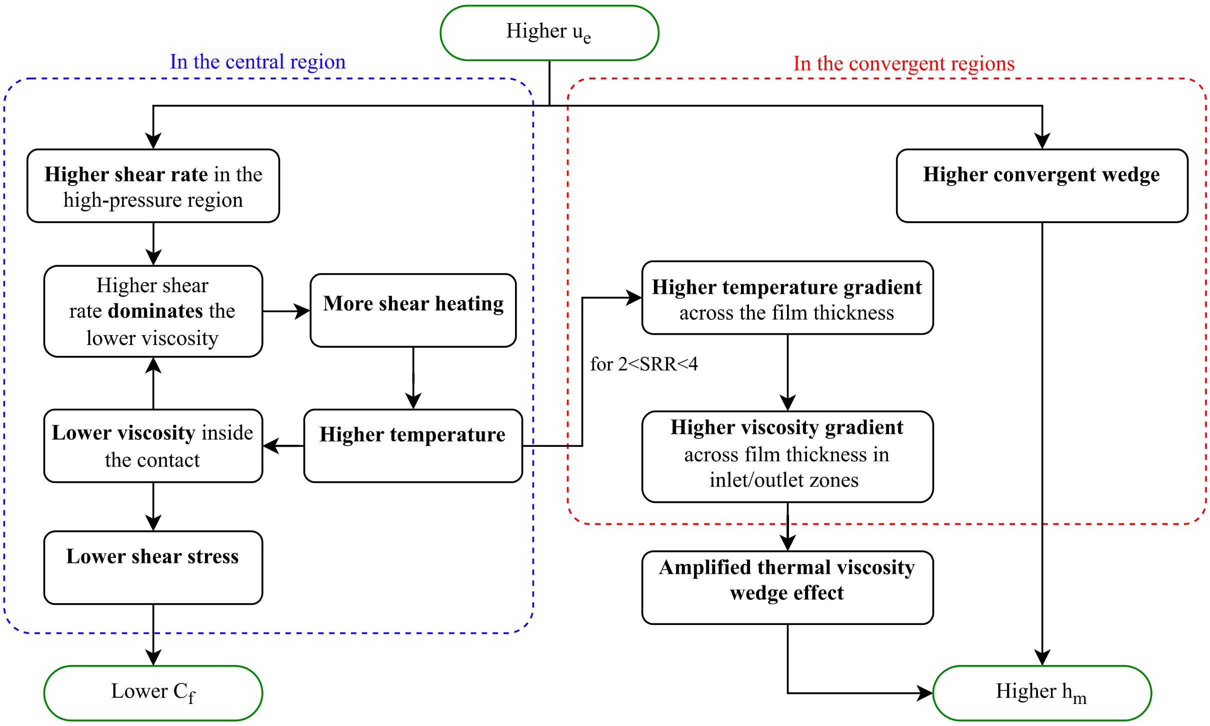

Figure 3.24: Diagram summarizing the mechanisms by which a higher entrainment velocity leads to a higher minimum film thickness and a lower friction coefficient in a TEHL contact.

3.2.5 Conclusion

The effects of varying the inlet temperature, the normal load, and the entrainment velocity on film thickness and friction coefficient were numerically studied. Table 3.5 summaries the effects of increasing T_0, u_e, and w_{1D} on minimum film thickness and friction coefficient. Note that a distinction is made in terms of sliding conditions.

Table 3.5: Summary of the effects of increasing T_0, u_e, and w_{1D} on minimum film thickness and friction coefficient.

	Higher T_0		Higher u_e		Higher w_{1D}	
	h_m	C_f	h_m	C_f	h_m	C_f
$SRR \in]0,2]$	$--$	$--$	$++$	$-$	$-$	$++$
$SRR \in]2,4]$	$--$	$-$	$++$	$--$	$-$	$+$

"$--$" indicates a significant decrease, "$-$" indicates a less significant decrease
"$++$" indicates a significant increase, "$+$" indicates a less significant increase

On one hand, it was found that the inlet temperature and the entrainment velocity largely influence the minimum film thickness qualitatively and quantitatively. For lower inlet temperature or higher entrainment velocity, the minimum film thickness tends to increase for a given SRR. Also, the thermal and shear-thinning effects, controlling the variation of the minimum film thickness with SRR, become more pronounced for lower temperature or higher velocity. This results in a faster rate of decrease with SRR between 0 and 2 and a faster rate of increase with SRR between 2 and 4 (due to the thermal viscosity wedge). On the other hand, the effects of varying the normal load (or the maximum Hertzian pressure) on minimum film thickness are weaker than the effects of inlet temperature or entrainment velocity as indicated by classical semi-analytical models from the literature. Increasing the normal load leads to a decrease in the minimum film thickness for a given SRR.

In contrast, varying the normal load has a significant influence on the friction response especially for $0 \leq SRR \leq 2$ due to the strong viscosity-pressure dependency when thermal and shear-thinning effects are weak. In current simulations, the friction coefficient is overestimated under certain conditions because the "LSS" behavior is not considered. As SRR increases beyond 2, the influence of changing the load becomes less important. For a given SRR, increasing the load increases the friction coefficient. Moreover, at low SRR ($SRR \leq 2$), the viscosity is very sensitive to changes in temperatures. Thus, an increase in inlet temperature lowers the viscosity and as a consequence lowers the friction coefficient at a given SRR. Furthermore, the impact of varying the entrainment speed is less significant for SRR ($SRR \leq 0.75$) due to weak thermal and shear-thinning effects. However, as soon as SRR increases, a remarkable difference in friction coefficient is observed between cases with different entrainment velocities due to the dominance of thermal and shear-thinning effects. For $SRR \geq 1$, the friction coefficient is lower for a higher entrainment velocity at a given SRR.

3.3 Semi-analytical Expression for Estimating the Minimum Film Thickness in 1D Line Contact at High SRR

3.3.1 Motivation

Semi-analytical expressions for estimating film thickness in line contact under pure rolling conditions exist in the literature [18,21,151–154], and their accuracy and limits were improved over time. A correction factor for thermal effects was suggested by Greenwood and Kauzlarich [155], Murch and Wilson [156], and Jackson [157] for pure rolling contact operating with entrainment speeds higher than a few meters per second. They argued that inlet thermal effects cannot be neglected at such velocities. Later, Wilson and Sheu [158] and Pandey and Ghosh [159] incorporated sliding up to $SRR = 2$ and $SRR = 0.5$ respectively in their thermal correction factors. With the development of the quantitative EHL approach due to new rheological characterization methods and non-Newtonian fluid models, researchers were able to analyze the shear-thinning in EHL contacts [160,161]. Bair [162] and Jang et al. [163] suggested correction factors for the non-Newtonian behavior in EHL contacts with lubricants modeled by a single-Newtonian Carreau-like model. These correction factors were established for SRR ranging from 0 to 1. Similarly, Habchi [144] proposed a correction factor for the non-Newtonian behavior in rolling EHL contacts with lubricants modeled by double-Newtonian Carreau-like models.

As shown in the previous section 3.2, operating conditions (including SRR) have significant effects on the minimum film thickness of the lubricant in EHL line contacts. To the author's knowledge, there are no minimum film thickness estimation equations or correction factors for high sliding conditions ($SRR > 2$). In this section, a new minimum film thickness expression is presented based on line contact simulations of 221 different operating conditions.

3.3.2 New semi-analytical expression

Numerical results are used as the basis for a semi-analytical expression since the model is well-controlled for the conditions of interest in this study (mainly extreme sliding) as opposed to experiments where the temperatures of the lubricant and the surfaces are hard to control. In addition, using simulations, operating conditions otherwise unreachable in experiments can be tested. For instance, low-speed or high-temperature cases result in a minimum film thickness under 80 nm that cannot be measured by the current optical method (limited to a minimum of 100 nm).

Entrainment velocity, normal load, inlet temperature, and SRR were varied while keeping the geometry and materials unchanged and similar to the previous section 3.2. In the simulated cases:

$$U \in [2.41 \times 10^{-12}, 2.41 \times 10^{-11}] \qquad G \in [4184, 5614]$$

$$W_{1D} \in [1.33 \times 10^{-5}, 5.11 \times 10^{-5}] \qquad SRR \in [0, 4]$$

Central and minimum fluid film parameters are given respectively by:

$$H_c = \frac{h_c}{R} \quad \text{and} \quad H_m = \frac{h_m}{R} \tag{3.5}$$

These can be estimated for a line contact at pure rolling using expressions (3.6) and (3.7) from [151] and [154] respectively.

$$H_{m,Dowson} = 2.65\, U^{0.7}\, G^{0.54}\, W_{1D}^{-0.13} \tag{3.6}$$

$$H_{c,Dowson-Toyoda} = 3.06\, U^{0.69}\, G^{0.56}\, W_{1D}^{-0.1} \tag{3.7}$$

The inlet Weissenberg number Γ [164] is calculated based on the Newtonian central thickness following the expression (3.8) .

$$\Gamma = \frac{\mu_0\, u_e}{H_{c,Dowson-Toyoda}\, R G_{cy}} \tag{3.8}$$

Where G_{cy} is a parameter in the modified Carreau-Yasuda model given in Table 2.4.

Film thickness values are then corrected for non-Newtonian behavior at $SRR = 0$ by the correction factors from Habchi [144] (as in Appendix D) in the case of a double-Newtonian shear-thinning behavior or from Bair [162] if the fluid has a single-Newtonian shear-thinning behavior. The corrected minimum film thickness estimation at $SRR = 0$ is calculated by (3.9), where $\varphi_{m,nN}$ is the correction factor and is lower than 1.

$$H_{m,corr} = \varphi_{m,nN} \times H_{m,Dowson} \tag{3.9}$$

To take the effect of sliding into account, an advanced semi-analytical formula is proposed in (3.10). On one hand, the expression corresponding to $0 \leq SRR \leq 2$ is based on the idea that the minimum film thickness decreases with SRR from a value that can be estimated by $H_{m,corr}$. The rate of this decrease is dependent on operating conditions described by dimensionless parameters U, G, and W. Thus, a term combining these parameters and SRR is required to describe the minimum film thickness for $0 \leq SRR \leq 2$. On the other hand, the first two terms of the second expression (corresponding to $2 < SRR \leq 4$) gives the film thickness at $SRR = 2$. As SRR increases beyond 2, the viscosity wedge effect causes the film thickness to increase depending on the operating conditions. Hence, the third term describes this increase in film thickness.

$$H_m^* = \begin{cases} H_{m,corr} - SRR^a U^b G^c W^d, & 0 \le SRR \le 2 \\ H_{m,corr} - 2^a U^b G^c W^d + (SRR-2)^{a'} U^{b'} G^{c'} W^{d'}, & 2 < SRR \le 4 \end{cases} \tag{3.10}$$

The exponents in (3.10) are determined by minimizing the squared error between the estimations and the numerical results. The Generalized Reduced Gradient (GRG) method is used for this optimization, first on results with $0 \le SRR \le 2$ to calculate a, b, c, and d, then on results with $2 < SRR \le 4$ to calculate a', b', c', and d'. The exponents are found to have the following values:

$$a = 1.390, \quad a' = 1.192,$$

$$b = 0.967, \quad b' = 2.535,$$

$$c = 1.915\,, \quad c' = 7.256,$$

$$d = 0.530, \quad d' = 1.207$$

It has to be noted that to calculate the exponents only numerical results are compared to estimations from expression (3.10). Experimental results presented in Chapter 3 and obtained from the literature will serve to confront the new estimation expression in the following section.

3.3.3 Validation

Minimum film thickness estimations calculated by expression (3.10) are plotted in Figure 3.25 against the numerical and experimental minimum film thickness. The closer the points are to the diagonal line, the better the prediction.

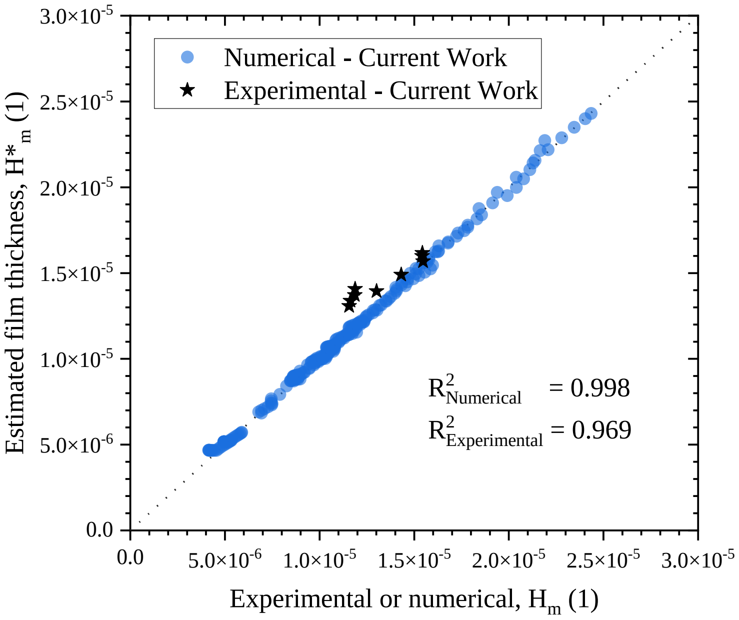

Figure 3.25: Dimensionless minimum film thickness prediction by expression (3.10) vs numerical or experimental dimensionless minimum film thickness.

The coefficient of determination (R^2) is a measure of the accuracy of the predictions against numerical calculations and experimental measurements of the minimum film thickness. $R^2_{Numerical}$ is very close to 1 indicating that expression (3.10) indeed captures very well the behavior of numerical simulations. The estimation expression can predict experimental thickness from configuration 1 of Chapter 3 with good accuracy ($R^2_{Experimental} = 0.969$). The experimental conditions correspond to parameters $U = 1.22 \times 10^{-11}$, $G = 5450$, $W = 1.84 \times 10^{-5}$, and $0 \leq SRR \leq 4$.

To the author's best knowledge, the literature lacks experimental studies on lubricant film thickness in line contact for high sliding conditions, i.e. at $SRR > 1$. To test the current expression, experimental thickness measurements by Dyson and Wilson [58] are used. These were made by capacitance measurements in a twin-disk setup with a silicone lubricant. The material and geometrical properties are given in [163]. Figure 3.26 presents a comparison between experimental measurements from Dyson and Wilson [58] and predictions using the current expression (3.10), and expressions from Bair [162] and Jang et al. [163]. The velocity parameter U is varied between 1.6×10^{-11} and 2.3×10^{-10} while all other parameters are constant: $G = 4054$, $W = 2.58 \times 10^{-5}$, and $SRR = 1$.

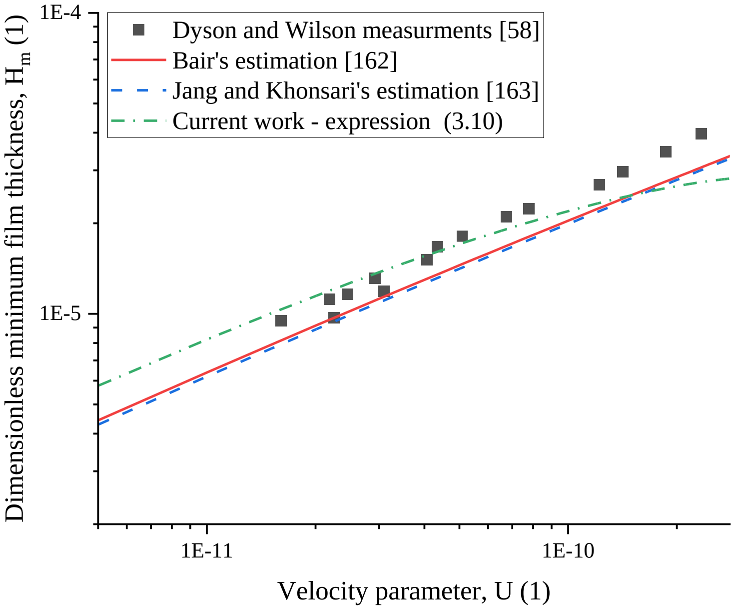

Figure 3.26: Dimensionless minimum film thickness estimated by current expression (3.10), Bair's estimation [162], and Jang and Khonsari's estimation [163] in addition to dimensionless minimum film thickness measured experimentally by Dyson and Wilson [58] for rolling-sliding contact at SRR = 1.

The current expression of minimum film thickness is in better agreement with measurements compared to the other estimation expressions from the literature for U up to 1.4×10^{-10} as shown in Figure 3.26. Note that at higher U the current expression underestimates the film thickness because U on the right-side of Figure 3.26 is almost 10 times larger than the upper limit of U (i.e. 2.41×10^{-11}) in the simulations used to fit the analytical expression.

In conclusion, the new semi-analytical expression proposed in this section can accurately predict minimum film thickness in a line contact under operating conditions close to those used to create it.

3.4 Conclusion

In this chapter, numerical results were compared to experimental measurements of film thickness and friction coefficient from barrel-on-disk tests. The ability of the quantitative EHL modeling approach was highlighted for a wide elliptical contact, especially when operating under opposite sliding conditions. However, both experimental and numerical approaches had their limitations. From the experimental point of view, maintaining a fixed lubricant temperature at the inlet of the contact proved to be challenging for experiments involving high sliding, where changes in inlet temperature influence the film thickness results. From the numerical point of view, the current rheology of the lubricant lacks a description of the complex LSS behavior leading to an overestimation of the friction coefficient.

Moreover, a numerical study was realized under various operating conditions (T_0, w_{1D}, and u_e) for a line contact that mimics a wide elliptical contact. The effects of varying these operating conditions simultaneously on film thickness and friction coefficient were explored.

Furthermore, using numerical results, a semi-analytical equation was created to estimate the minimum film thickness in line contact for SRR ranging from 0 to 4. This expression was validated against experimental measurements and similar expressions in literature. However, the accuracy of the semi-analytical expression is not guaranteed under conditions far from those used to create it.

In the next chapter, the ability of the numerical approach is assessed using experimental measurements from barrel-on-disk tests with thermally insulating materials. Also, the effects of using insulating coatings on film thickness and friction are explored.

Chapter 4: TEHL Contacts: Role of Thermally Insulating Surfaces

The ability of the 1D line contact numerical model to predict film thickness and friction in a 2D wide elliptical contact was discussed in Chapter 3 for conductive surfaces. In section 4.1, the predictive ability of the numerical model is assessed for a TEHL contact with thermally insulating surfaces by a dual experimental-numerical approach. Section 4.2 investigates the effect of using DLC coatings on film thickness and friction coefficient in a TEHL line contact. Finally, in section 4.3 the effects of varying the thermal conductivity of the coating and its thickness on the lubricant film thickness and friction coefficient are explored.

4.1 Dual Experimental-Numerical Approach: Thermally Insulating Surfaces

This section assesses the ability of the numerical approach to simultaneously predict film thickness and friction coefficient in a wide elliptical TEHL contact with thermally insulating surfaces.

4.1.1 Materials and operating conditions

On one hand, the barrel-on-disk tribometer (JEROTRIB) described in Chapter 2 is used with a DLC-coated glass disk (Glass-DLC-D) and a DLC-coated steel barrel (DLC-B) whose properties are given in section 2.1.1.

Table 3.1 presents the experimental conditions of tests realized on JEROTRIB.

Table 4.1: Experimental conditions for tests on realized on JEROTRIB.

Parameter	**Unit**	**Value**
Normal load, w_{2D}	N	60
Maximum Hertzian pressure, p_{Hz}^{2D}	MPa	276
External bath temperature, T_{ext}	$°C$	45
Entrainment speed, u_e	m/s	1
Slide-to-roll ratio, SRR	$-$	0, 0.25, 0.5, 1, 1.5, 2.5, 3, 3.5, 4

Note that the relatively low p_{Hz}^{2D} result from the low Young's modulus of glass that is equal to 81 GPa compared to 360 GPa for sapphire. This means that a maximum Hertzian pressure of 276 MPa can elastically deform the glass surface. The entrainment velocity is fixed to $u_e = 1\ m/s$ and sliding varied from 0 to 4 with intermediate steps. Moreover, the external bath temperature is set to the same temperature T_{ext} as in Chapter 3 and the inlet lubricant temperature at the start of the experiment is estimated by the same method resulting in $T_0 = 40°C$.

On the other hand, the 1D line contact, representing the wide elliptical contact, is used to simulate the above operating conditions with the material properties corresponding to Glass-DLC-D, DLC-B, and the lubricant given in Chapter 2. Note that a maximum Hertzian pressure of 276 MPa corresponds to a 1D normal load $w_{1D} = 4.9 \times 10^4\ N/m$ calculated using equation (3.2). Also, the equivalent radius of curvature is calculated by equation (3.1) to be $R = 12.78\ mm$.

4.1.2 Film thickness results

Experimental and simulated variations of h_c and $h_{m,c}$ with SRR are respectively shown in Figure 4.1a and Figure 4.1b along with some numerical results at $T_0 = 50°C$. The film thickness found by

Chittenden's expression after correcting for non-Newtonian behavior at $T_0 = 40°C$ and $SRR = 0$ is also plotted. The measurement uncertainty for all tested conditions is below $\pm 6\ nm$.

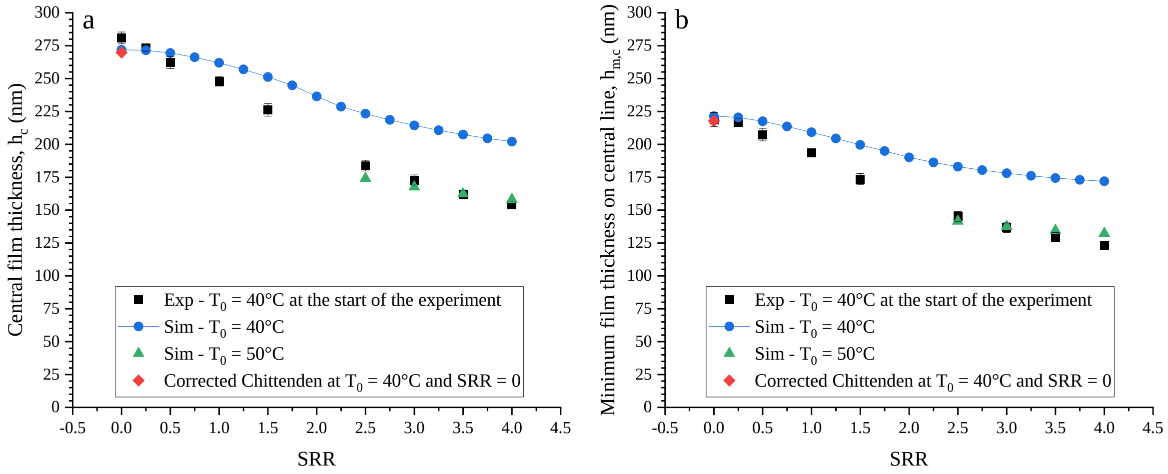

Figure 4.1: Variation of (a) the central film thickness h_c and (b) the minimum film thickness on central line $h_{m,c}$ with SRR for experiment and simulation of thermally insulating surfaces. Some results of the simulation at $T_0 = 50°C$ are also shown in addition to the film thickness found by Chittenden's expression after correcting for non-Newtonian behavior at SRR=0 and $T_0 = 40°C$.

Measured and calculated h_c and $h_{m,c}$ decrease with SRR from a maximum at pure rolling ($SRR = 0$) to a minimum at $SRR = 4$. The decrease in film thickness is attributed to both thermal and shear-thinning effects similar to section 3.1.3 for $SRR < 2$. For $SRR \leq 1$, the predictions are in good agreement with the measurements with a prediction error under 16 nm (8 %) for both h_c and $h_{m,c}$.

The discrepancy increases to 50 nm (40 %) between measured and simulated h_c and $h_{m,c}$ at $T_0 = 40°C$. On the contrary, simulations realized at the temperature $T_0 = 50\ °C$ are in much better agreement with measurements for $SRR \geq 2.5$. Note that the inlet temperature at the start of the test is $40°C$ and the same experimental protocol used in Chapter 3 is followed here. This indicates that the temperature of insulating surfaces increases over time (even more than conductive surfaces) by entrapping the heat generated in the fluid and hindering its dissipation to the bulk of the solids. Upon contact with the hot surfaces, the lubricant entering the contact is heated to a temperature higher than the one at the start of the test.

The trend of the variation of h_c and $h_{m,c}$ for $SRR > 2$ is different than that observed in section 3.1.3. Here, h_c and $h_{m,c}$ continuously decrease even in opposite sliding conditions. The thermal viscosity wedge is attenuated when thermally insulating surfaces are used. This can be observed in Figure 4.2, where the experimental and simulated lubricant film profiles along the x-direction are shown for SRR equal to 2.5, 3, 3.5, and 4. Note that simulations are realized at the temperature $T_0 = 50°C$ to show that the model at this temperature fits very well the experiments that are thought to be at a higher temperature.

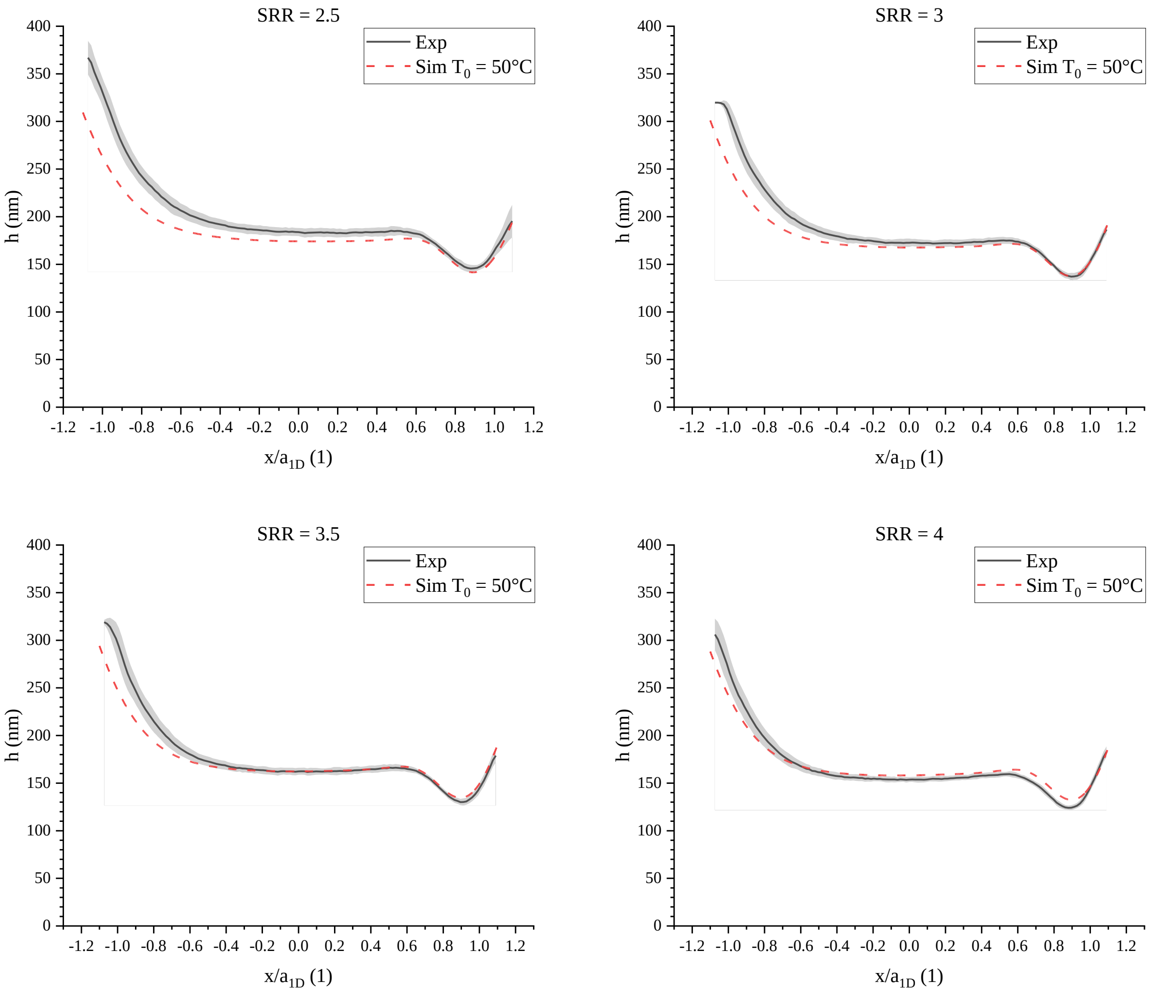

Figure 4.2: Experimental and simulated thickness for configuration 2 at SRR equal to 2.5, 3, 3.5, and 4. Simulations are realized at the $T_0 = 50°C$.

In simulations and experiments, an almost flat film thickness profile in the central region of the contact is observed even at the extreme sliding condition ($SRR = 4$). By comparing the profiles in Figure 4.2 to those in Figure 3.4 of Chapter 3 a significant difference is observed. In the case of insulating surfaces, the decrease of minimum film thickness is not countered by the thermal viscosity wedge effect at high sliding ($SRR > 2$). Detailed explanations of this behavior are given in section 4.2. An underestimation of film thickness in the convergent region similar to the one seen in Figure 3.4 is also observed here.

Overall, the numerical model can capture complex physical mechanisms that depend on the thermal properties of the contacting surfaces and can accurately predict the film thickness when the temperature increase in experiments over time is accounted for in simulations.

4.1.3 Friction coefficient results

Figure 4.3 shows the variation of measured and predicted friction coefficient with SRR for thermally insulating surfaces.

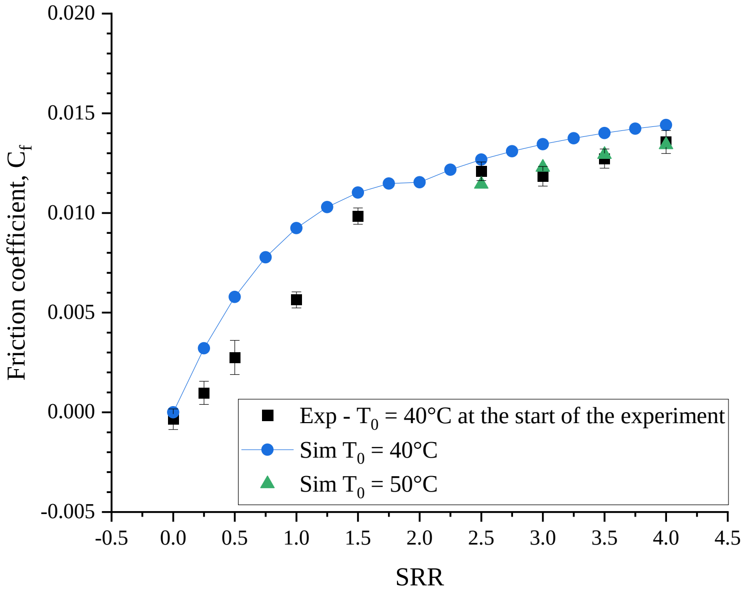

Figure 4.3: Friction coefficient variation with SRR for thermally insulating surfaces. Experiment at $T_0 = 40°C$ at the start of the test and simulations at $T_0 = 40°C$ and $50°C$.

The measured friction coefficient increases sharply with increasing SRR for SRR between 0 and 1.5. The increase is slower at higher sliding. Simulations overestimate friction coefficient for all sliding conditions however the overestimation in the range of $SRR < 1.5$ is not as significant in the case of conductive materials shown in Figure 3.5. The pressure of the lubricant is relatively low for the case of insulating surfaces since the maximum Hertzian pressure is low compared with the case of the conductive surface ($276\ MPa$ for the former versus $504\ MPa$ for the latter). According to [51], the limiting shear stress effect (responsible for lower friction coefficient in reality) is attenuated for low load cases. Thus, the discrepancy between experiments and a numerical model that does not consider LSS decreases when the normal load (or lubricant pressure) is lower. Here, the maximum prediction error is less than 0.004 at SRR=1. For $SRR \geq 2$, the prediction error is less than 0.002. Moreover, the simulation results at $T_0 = 50°C$ are in much better agreement with experimental results. The model can capture the friction coefficient variations qualitatively over the full range of SRR.

Next, the effects of applying insulating coatings on the lubricant film thickness and friction coefficient are explored for a wide range of sliding conditions ($0 \leq SRR \leq 5$).

4.2 Effects of Using Thermally Insulating DLC Coating on Film Thickness and Friction Coefficient in a TEHL Line Contact for 0 ≤ SRR ≤ 5

The effects of thin DLC coating on friction coefficient in a TEHL contact were studied by many researchers [119–121,123] (see section 1.3.4). However, the origin of friction reduction due to DLC coating is still an active area of research, and a decisive answer is yet to be found. Some argue that the lower surface energy of DLC coatings compared to steel is responsible for friction reduction [119]. Others attributed the reduction to the thermal insulation effect of DLC coatings [120,121,123]. The current numerical study does not consider wall-slip i.e. the lubricant sticks perfectly to the solid surfaces. Thus, friction reduction can only be studied in terms of the influence of the thermal properties of different contacting surfaces.

The aforementioned investigations were limited to an SRR of less than 1 and did not consider the effect of such coatings on the lubricant film thickness. Habchi [165] showed numerically that the friction coefficient in EHL contact can be reduced by using low thermal inertia coatings without affecting the film thickness. This was shown to be true for SRR up to 0.5 (the range explored in [165]). To the best of the author's knowledge, the literature lacks an investigation of the effect of thermally insulating coatings simultaneously on film thickness and friction over conditions ranging from pure rolling to opposite sliding.

This section presents a numerical study in a 1D line contact of the effect of a-C:H DLC coating over a wide range of sliding conditions ($0 \leq SRR \leq 5$). In section 4.1, a glass substrate was used to enable optical film thickness measurement which resulted in a relatively low lubricant pressure. In contrast, steel substrate is used in this section to mimic the effects of DLC coating in real EHL contact between real mechanical components. Thus, the lubricant pressure could be increased to a value typical for EHL contact (i.e. $p_{Hz} = 500\ MPa$).

4.2.1 Materials and operating conditions

The numerical study presented here represents a 1D line contact between a cylinder and a plane. Two surface configurations shown in Figure 4.4 are tested:

- Thermally conductive surfaces: uncoated steel cylinder and plane
- Thermally insulated surfaces: DLC-coated steel cylinder and plane

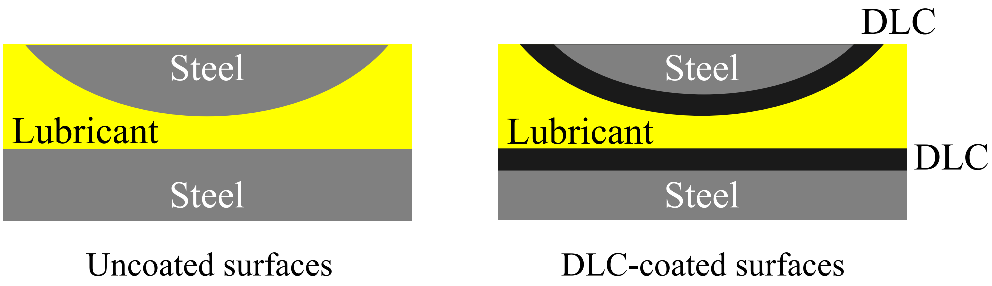

Figure 4.4: Surface configurations: (left) uncoated steel cylinder and plane and (right) DLC-coated cylinder and plane.

Mechanical and thermal properties of 100C6 steel and a-C:H DLC coating presented in Table 2.2 are attributed respectively to the bulk steel material and the DLC coating in this numerical study. It is to be noted that the thermal conductivity of the DLC coating is around 10 times lower than that of hardened 100C6 steel (2.2 $W/m.K$ versus 21 $W/m.K$). The coating thickness, h_{coat}, is set to 2.8 μm similar to that of the coating applied on the barrel used in the experiments of section 4.1. In addition, the same commercial lubricant whose properties are given in 2.1.3 is employed here.

The cylinder radius is set to $R = 12.78\ mm$ and the normal load is $w_{1D} = 8.7 \times 10^4\ N/m$ resulting in a maximum Hertzian pressure $p_{Hz} = 500\ MPa$. Only one temperature and one entrainment speed are tested to focus on the effects of DLC coating on friction and film thickness. SRR is varied from 0 to 5. All the operating conditions are summarized in the following Table 4.2.

Table 4.2: Operating conditions for the numerical study of coated or uncoated cylinder-on-plane contact.

Parameter	**Unit**	**Value**
Cylinder radius, R	mm	12.78
Normal load, w_{1D}	N/m	8.7×10^{-4}
Maximum Hertzian pressure, p_{Hz}	MPa	500
Contact half-length, a^{1D}	μm	110.6
Initial lubricant temperature, T_0	$°C$	45
Entrainment speed, u_e	m/s	1
Slide-to-roll ratio, SRR	$-$	0 to 5

4.2.2 Effects of DLC coating on film thickness

Figure 4.5 shows the variation of h_m, the minimum film thickness, with SRR from 0 to 5 for both uncoated and DLC-coated surface configurations.

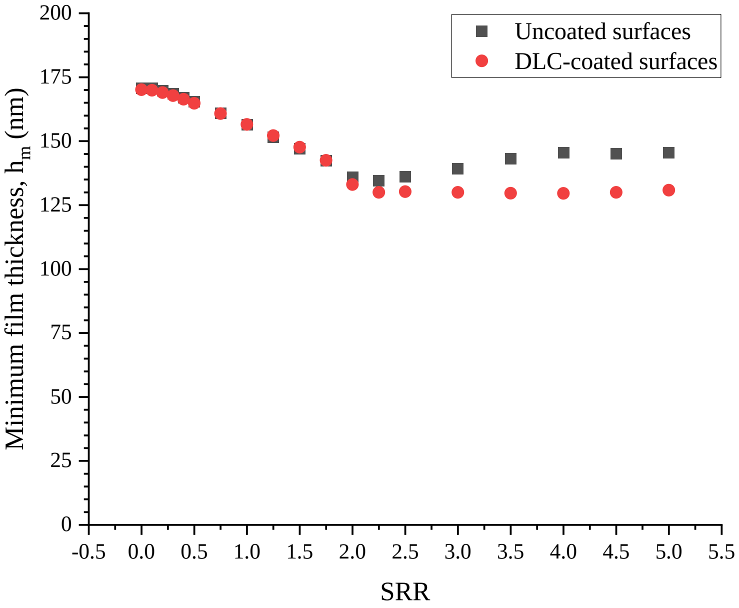

Figure 4.5: Minimum film thickness variation with SRR from 0 to 5 for uncoated surfaces (in black) and DLC-coated surfaces (in red).

For $0 \leq SRR < 2$, the minimum film thickness decreases with increasing sliding. The decrease is caused by thermal and shear-thinning effects becoming more pronounced as sliding increases. Note that in both DLC-coated and uncoated cases the values of h_m are almost identical with less than a 0.5 % difference in h_m for SRR between 0 and 1.75. This confirms and extends the findings of [165] about the disassociation of lubricant film thickness from the use or not of a thermally insulating coating.

In contrast, for SRR higher than 2, in the uncoated case, the minimum film thickness increases with SRR due to the thermal viscosity wedge. For the coated case, h_m is almost constant for $SRR > 2$. A decrease of more than 10 % (for $SRR = 4, 4.5,$ and 5) is found when DLC coating is used compared to the uncoated case. This indicates an attenuation of the thermal viscosity wedge effect when DLC coatings are used.

Temperature distributions in different parts of the system are plotted in Figure 4.6 to further investigate the mechanism by which the DLC-coating influences the lubricant film thickness at a high sliding condition ($SRR = 5$).

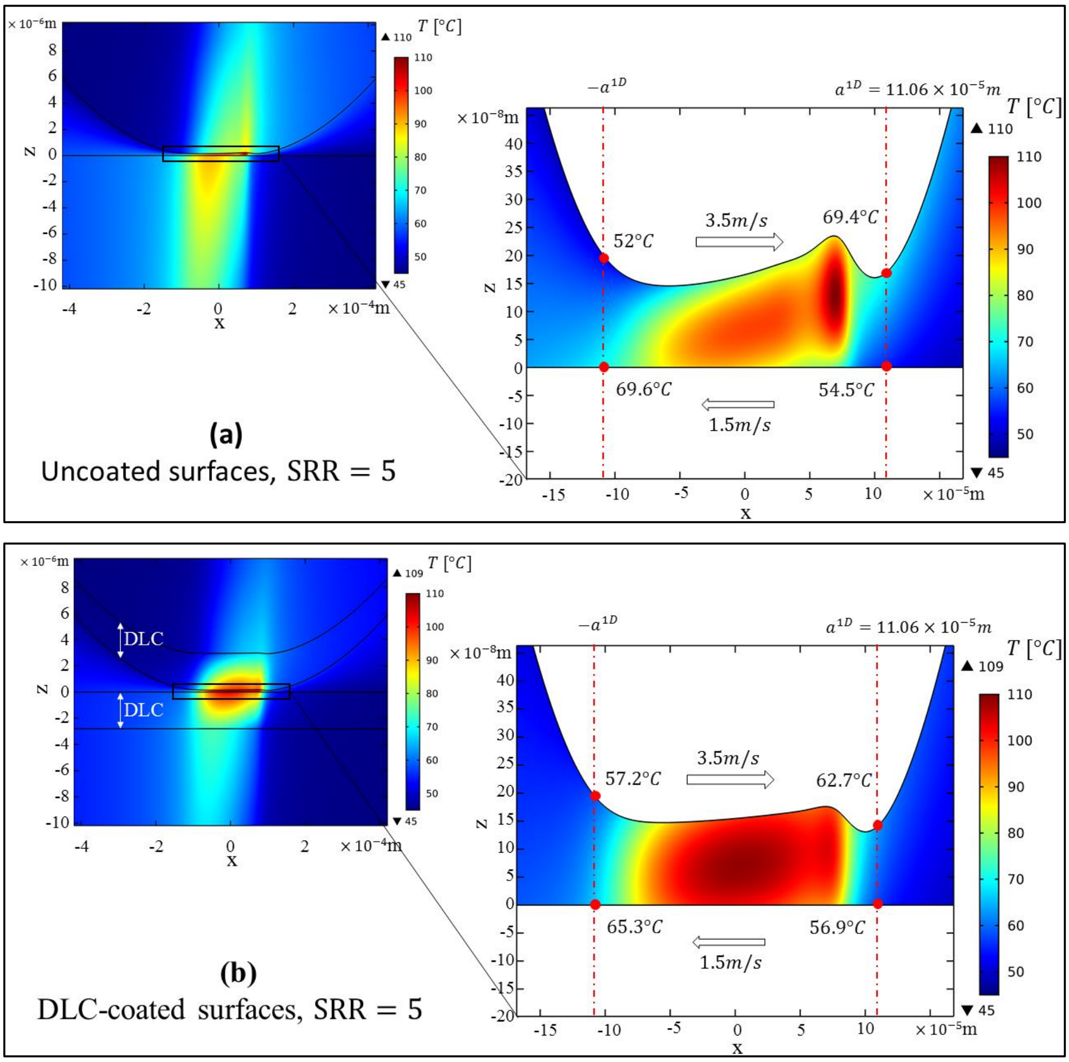

Figure 4.6: Temperature distribution in different parts of the system (solids and fluid) and a zoomed-in view of the lubricant inside the contact region. Temperatures of the lubricant at positions $x = +a^{1D}$ and $x = -a^{1D}$ are shown in addition to surfaces velocities. (a) corresponds to uncoated surfaces and (b) corresponds to DLC-coated surfaces, both at $SRR = 5$.

The colored plots to the left of Figure 4.6 represent the temperature distribution in the solids and coatings (in the DLC-coated case). In the uncoated surfaces case, heat is easily conducted from the lubricant (where it is generated mainly by shear heating) to the bulk of the solid which increases the temperature deep into the solids. In contrast, in the DLC-coated surfaces case, heat is trapped in the lubricant and the coating and is hardly transferred into the bulk steel solids because of the low conductivity of the DLC coating. Thus, the temperature increase of the bulk solids is restricted to near the contacting surfaces.

The colored plots to the right of Figure 4.6 represent zoomed-in views of the contact region where the temperature distribution inside the lubricant is plotted. Temperatures of the lubricant at the locations $x = +a^{1D}$ and $x = -a^{1D}$ near the top and bottom fluid/solid interfaces are also indicated in Figure 4.6. In the uncoated case (subfigure a), the maximum temperature is found in the high-pressure zone commonly referred to as the "dimple". In contrast, in the coated surfaces case the maximum temperature is located in the center of the contact ($x = 0$) and the increase in temperature is spread to a larger region in the x-direction compared to the uncoated case. Due to the insulating effect of the coating, the heat generated in the central region of the lubricant spreads to colder parts of the lubricant (i.e. the left and right sides). In opposite sliding, the surfaces move in opposite directions and lubricant is entrained from both sides of the contact so there is no distinct lubricant inlet and outlet. As shown in the plots on the right of Figure 4.6, the lubricant temperatures near the top and bottom interfaces are different. For the uncoated case, this difference is 17.6°C and 14.9°C at $x = -a^{1D}$ and $x = +a^{1D}$ respectively. While for the DLC-coated case, the difference is 8.1°C and 5.8°C at $x = -a^{1D}$ and $x = +a^{1D}$ respectively.

The magnitude of the temperature gradient controls the magnitude of the viscosity gradient in the z-direction. The viscosity variations across the normalized film thickness at the positions $x = +a^{1D}$ and $x = -a^{1D}$ are plotted respectively on the left and right graphs of Figure 4.7. Viscosity variations corresponding to uncoated and DLC-coated cases are shown in black and red respectively.

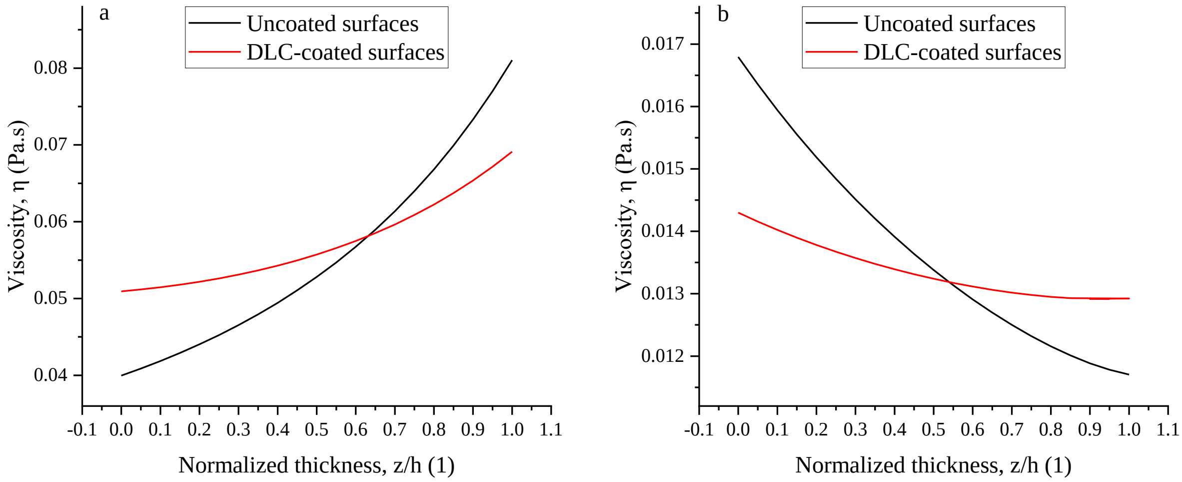

Figure 4.7: Variation of the viscosity of the lubricant across the normalized thickness at positions (a) $x = -a^{1D}$ and (b) $x = +a^{1D}$. The uncoated surfaces case is represented by black curves and the DLC-coated surfaces case is represented by red curves.

A significant difference is observed in the viscosity gradient between the different surface configurations. The viscosity gradient in the case of the DLC-coated surfaces is lower, leading to an attenuation of the viscosity wedge effect compared to the case of the uncoated surfaces. The same effect of the DLC coating was found by Raisin et al. [33] where they numerically studied DLC-coated point contact at zero-entrainment velocity (ZEV) condition (i.e. $SRR = \infty$).

Figure 4.8 shows, for different sliding conditions ($SRR = 0$ to 5), the pressure and film thickness profiles for coated and uncoated configurations.

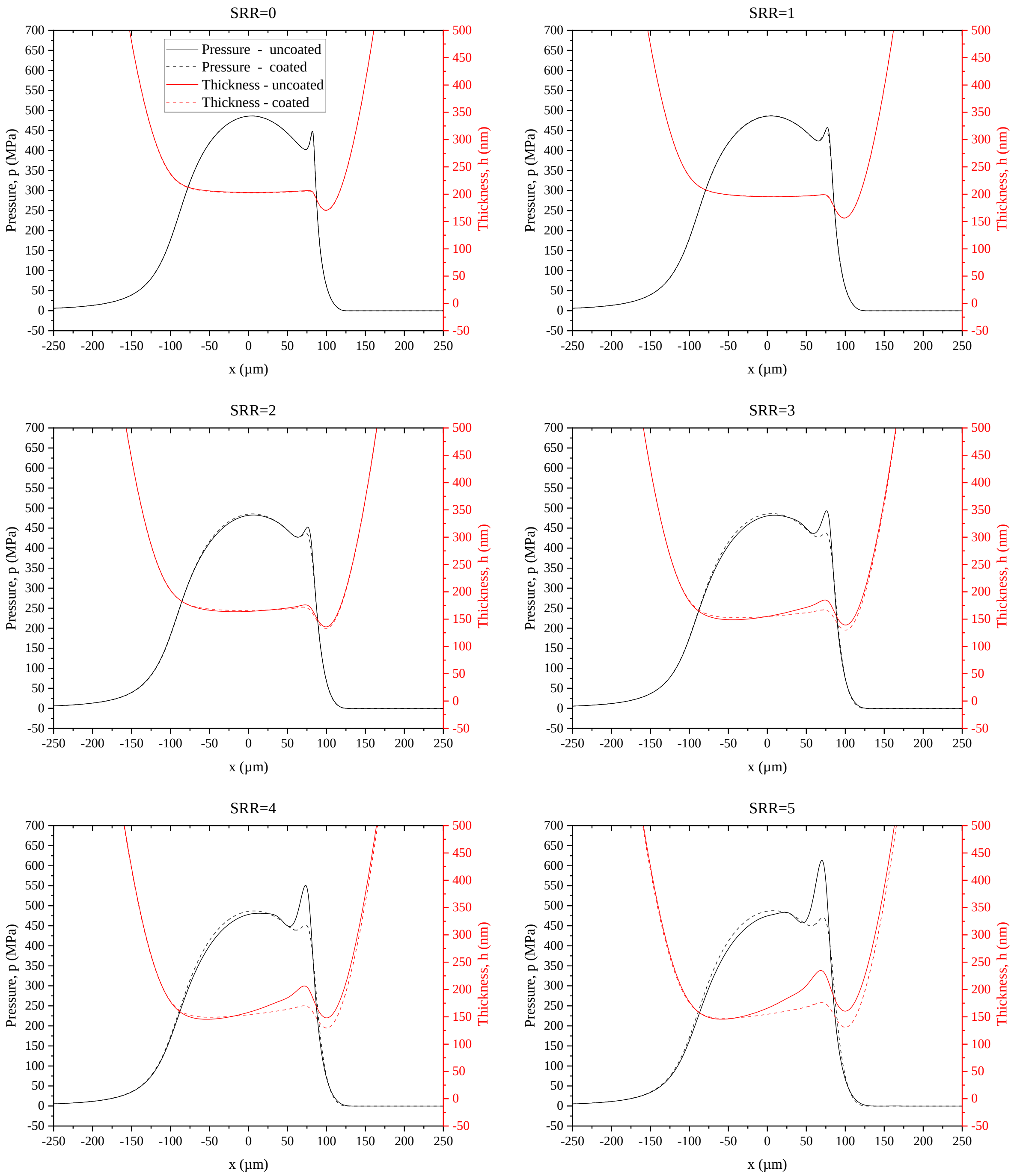

Figure 4.8: Pressure (black) and lubricant film thickness (red) profiles along the entrainment x-direction for different sliding conditions (SRR from 0 to 5). Uncoated and DLC-coated configurations are represented in solid and dashed lines respectively.

By comparing coated and uncoated configurations, it is noted that the pressure and film thickness profiles are almost identical for both configurations at relatively low sliding conditions (SRR=0 and 1). At SRR=2, one starts to distinguish between profiles of coated and uncoated cases. As sliding increases, the distinction becomes more pronounced. In the case of uncoated surfaces and due to a strong viscosity wedge effect, the pressure builds up in the “dimple” region which increases the minimum film thickness compared to the case with coated surfaces where the viscosity wedge effect is attenuated. Moreover, the maximum pressure is located at different locations for different configurations. In the case of coated surfaces, the maximum pressure of $486 \pm 1\ MPa$ is always at the center ($x = 0$) and the shape of the pressure profile hardly changes with the increase of SRR. In contrast, the shape of the pressure profile and the location of the maximum pressure change with increasing SRR for the uncoated configuration. The maximum pressure is located on the right side of the contact (no more in the center) and reaches $613\ MPa$ at $SRR = 5$.

4.2.3 Effects of DLC coating on friction coefficient

Figure 4.9 shows the variation of friction coefficient variation with SRR from 0 to 5 for uncoated and DLC-coated surfaces configurations respectively in black and red.

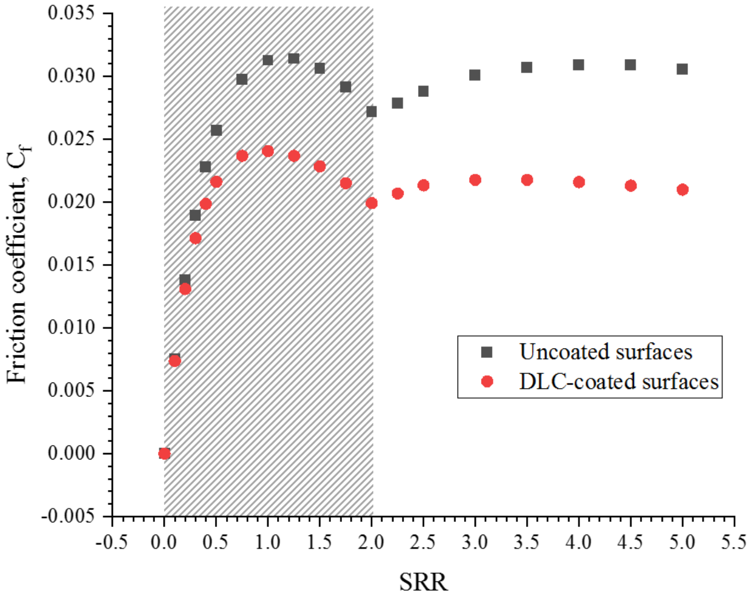

Figure 4.9: Friction coefficient variation with SRR from 0 to 5 for cases with (black) uncoated surfaces and (red) DLC-coated surfaces. The gray zone indicates the range over which the friction coefficient is overestimated due to not considering the LSS.

At low sliding ($SRR \leq 0.3$) C_f increases linearly with SRR for both coated and uncoated configurations. For $SRR > 0.4$, the thermal and shear thinning effects start to influence the friction response where the increase continues but at a less-than-linear tendency. A maximum friction coefficient is reached around $SRR = 1$ for both configurations after which thermal and shear-thinning effects dominate the friction response and contribute to the decrease of C_f ($1 < SRR < 2$). The friction coefficient is overestimated in the gray zone because the LSS behavior is not described by the rheological law used in the model. A local minimum of friction is reached at the pure sliding conditions ($SRR = 2$) where due to local heating of the stationary plane the lubricant temperature increases and its viscosity decreases, decreasing C_f. When the plane is in motion (i.e. $SRR \neq 2$) the local heating effect is lost and the friction coefficient increases creating a local minimum of C_f at $SRR = 2$. At higher sliding ($SRR \geq 3$) friction stabilizes for the uncoated case or slightly decreases in the DLC-coated case.

For low sliding conditions ($SRR \leq 0.2$), coated and uncoated configurations result in the same friction coefficient. However, at higher sliding ($SRR \geq 0.3$) and especially for $SRR \geq 1$ a significant difference in friction coefficient is observed between the different surface configurations. The friction coefficient between two DLC-coated surfaces is between 23% (at $SRR = 1$) and 31% (at $SRR = 5$) lower than the uncoated configuration. Comparable friction reductions were observed by [119,120,123] when comparing thin-film coated to uncoated contacts.

Heat is mainly generated by shear as expressed by the source term Q_s given in (4.1). The generated heat is proportional to the viscosity which in turn increases with increasing pressure and decreases with increasing temperature.

$$Q_s = \eta \left(\frac{\partial u_f(x,z)}{\partial z} \right)^2 \tag{4.1}$$

In addition to viscosity, shear heating depends on the shear rate $\partial u_f / \partial z$. The shear heat source is plotted in Figure 4.10 for coated and uncoated configurations at $SRR = 5$.

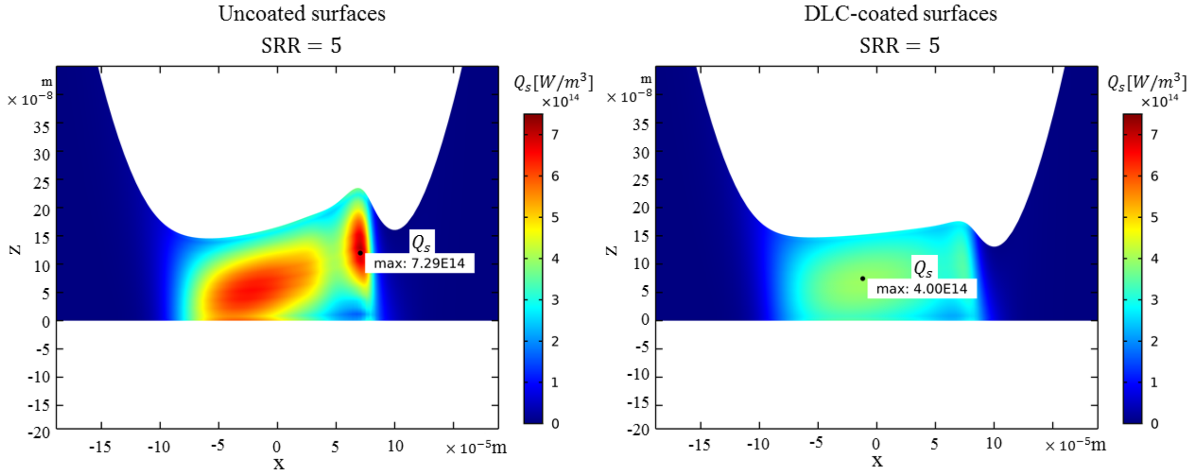

Figure 4.10: Shear heat source Q_s for the cases of (left) uncoated surfaces and (right) DLC-coated surfaces at $SRR = 5$.

It is noted that the maximum shear heat source is located near the location of maximum pressure in both cases (see Figure 4.8). However, in the case of uncoated surfaces, Q_s maximum is not in the center contrary to the case of DLC-coated surfaces. Also, the values of maximums are different with $7.29 \times 10^{14}\ W/m^3$ and $4.00 \times 10^{14}\ W/m^3$ for uncoated and coated cases respectively. Even though Q_s maximum is higher for the uncoated case (see Figure 4.10), the lubricant temperature decreases significantly near the conductive surfaces that evacuate heat more easily (see Figure 4.6). In contrast, insulating surfaces hinder heat evacuation and as a consequence, the average fluid temperature is higher compared to uncoated surfaces case.

Figure 4.11 show the variation with SRR of T_{avg}, the average temperature calculated inside the 2D fluid domain between $x = -a^{1D}$ and $x = +a^{1D}$.

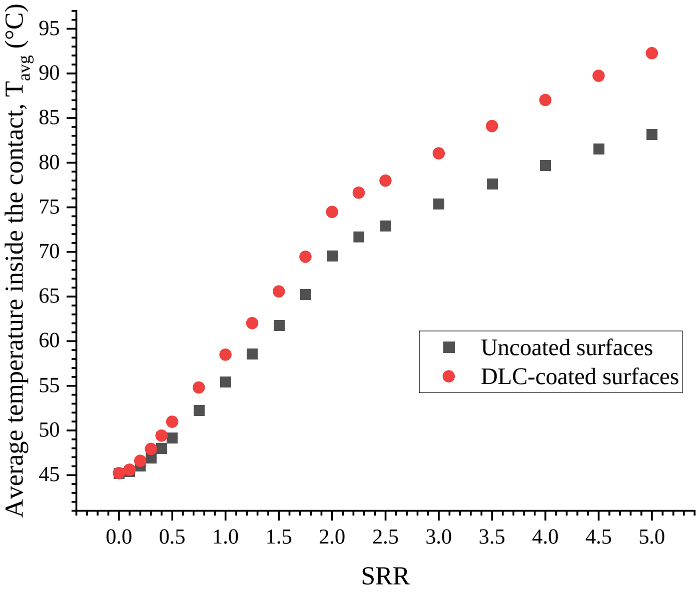

Figure 4.11: Average temperature variation with SRR from 0 to 5 for the case with (black) uncoated surfaces and (red) DLC-coated surfaces. T_{avg} is calculated inside the 2D fluid domain bounded by the top and bottom solid/fluid interfaces and by $x = -a^{1D}$ and $x = +a^{1D}$ from the left and right sides respectively.

The temperature at pure rolling ($SRR = 0$) is equal to the ambient lubricant and solids temperature ($45°C$) indicating negligible heat generation in the pure rolling condition. As soon as SRR starts increasing, T_{avg} also increases progressively with the increase of sliding. At the pure sliding condition ($SRR = 2$), T_{avg} reaches $69.5°C$ and $74.5°C$ for uncoated and DLC-coated cases respectively. T_{avg} increases even further with SRR increasing to 5. Furthermore, the difference in average temperature between coated and uncoated configurations becomes greater at higher SRR, it reaches $9°C$ at $SRR = 5$. The DLC-coated case results in a higher average temperature leading to lower average viscosity, lower shear stress, and finally lower friction coefficient compared to the uncoated case.

4.2.4 Conclusion

The findings of this section are in agreement with studies in the literature [118,120,166] in terms of friction reduction by the use of a thin thermally insulating coating in EHL contacts operating under sliding-rolling conditions. Also, in rolling-sliding conditions ($SRR < 2$), the film thickness is shown to be almost unaffected by the presence of the coating. A similar conclusion was made by Habchi [165] who study the influence of coating properties on circular EHL contact performance up to $SRR = 0.5$. However, this conclusion is not applicable for contacts operating under opposite sliding conditions where not only the friction coefficient but also the film thickness is influenced by the presence of the coating.

Figure 4.12 summarizes the mechanisms by which a low conductivity coating can lead simultaneously to a reduction in friction coefficient and film thickness in full-film EHL contacts operating in opposite sliding conditions ($SRR > 2$).

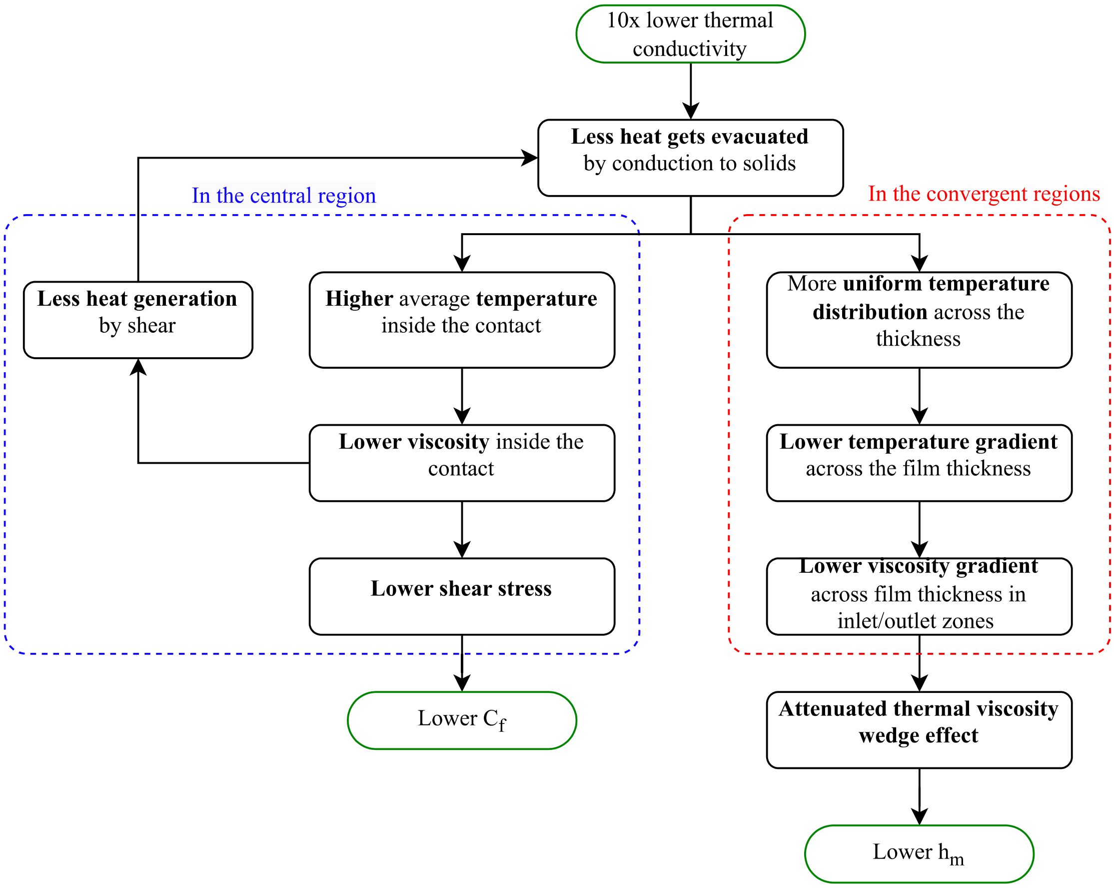

Figure 4.12: Diagram summarizing the mechanisms by which a low conductivity coating leads to a reduction in friction and film thickness in full-film EHL contacts operating in opposite sliding conditions ($SRR > 2$).

Insulating coating with lower thermal conductivity hinders the evacuation of heat generated by shear from the fluid to the colder solid substrates. On one hand, the insulation causes an increase in the temperature of the lubricant decreasing its viscosity. As a consequence, the shear stress and friction coefficient decrease compared to the uncoated case. On the other hand, the thermal insulation makes the temperature distribution more uniform across the film thickness in the inlet/outlet zones lowering the temperature gradient and the viscosity gradient across the film thickness. Thus, the viscosity wedge is attenuated and the minimum film thickness decreases compared to the uncoated case. Results show that in opposite sliding conditions not only the friction coefficient is reduced due to the use of thermally insulating coating but also the film thickness. Thus, one needs to be mindful of the loss in film thickness when applying thermally insulating coating to reduce friction in applications operating at extreme sliding conditions ($SRR > 2$). In the next section, the effects of changing the properties of the coating (namely, its thermal conductivity and thickness) are explored.

4.3 Effects of Varying Thermal Conductivity and Thickness of Thermally Insulating Coatings

The importance of the thermo-mechanical properties of the coating was pointed out in the works of Habchi [165,167] who used a numerical finite-element model to investigate the influence of varying Young's modulus ($52.5\ to\ 420\ GPa$), thickness ($20\ to\ 160\ \mu m$), and thermal properties of the coating on EHL contact performance. He found that friction can be reduced significantly when a more insulating coating is used while the film thickness is unaffected. The sliding conditions tested were limited to SRR from 0 to 0.5. To the author's knowledge, the literature lacks a study of the effects of coating properties on EHL contact performance for more extreme sliding (for instance, $SRR > 2$). As shown in section 4.2, the influence of thermally insulating coating on film thickness cannot be neglected under opposite sliding conditions. This section presents a numerical investigation of the effects of varying the thermal conductivity and the thickness of the DLC coating simultaneously on friction coefficient and film thickness for SRR ranging from 0 to 4.

The reference case here is identical to the DLC-coated case presented in section 4.2. It is a cylinder-on-plane contact of two bulk solids made of 100C6 steel with a-C:H DLC coating of thickness $h_{coat} = 2.8\ \mu m$ on both solids with thermal conductivity $k = 2.2\ W/m.K$. Operating conditions, in terms of load, inlet temperature, geometry, and entrainment velocity are the same as those summarized in Table 4.2.

For simplicity, the effects of varying the thermal conductivity and the thickness of the coating are explored separately at first in 4.3.1 and 4.3.2 respectively. Then, their combined effect is quantified in 4.3.3.

4.3.1 Effects of varying the thermal conductivity of the contacting surfaces

In practice, the thermal conductivity depends on the deposition process, the microstructure, and the hydrogen content of the DLC coating among other factors. The properties of interest to coating manufacturers are usually mechanical properties such as hardness and wear resistance. The thermal conductivity is a consequence of the choices made to control these properties. However, in this section, varying the thermal conductivity is intended to give general insights which apply to thermally insulating coating not limited to DLC coatings. Hence, the effects of varying the thermal conductivity of the coatings on lubricant film thickness and friction coefficient are discussed.

In addition to the reference case ($k = 2.2\ W/m.K$), simulations were realized with thermal conductivity $k \in \{0.2, 0.4, 0.7, 1, 5, 10\}\ W/m.K$. Other material properties are unchanged and the thickness of the coatings is fixed to $h_{coat} = 2.8\ \mu m$ (same as the reference case).

Effects on lubricant film thickness

Figure 4.13 shows the variation of minimum film thickness with SRR for different surfaces' thermal conductivities.

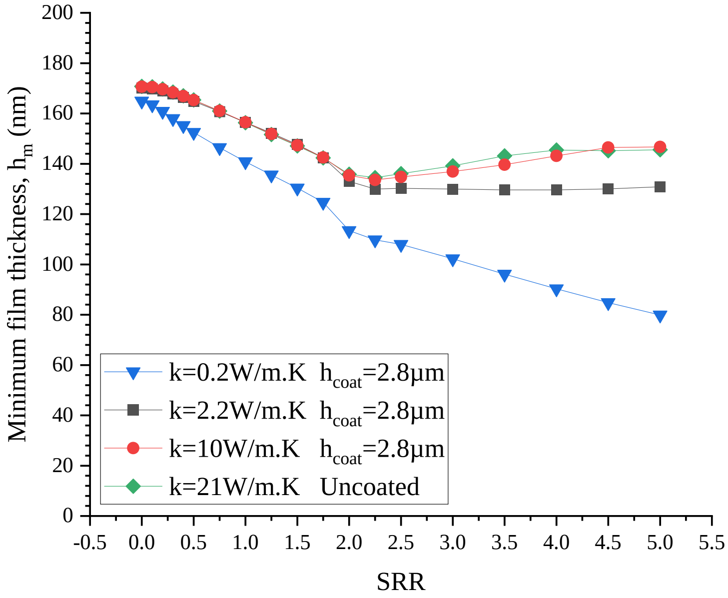

Figure 4.13: Variations of minimum film thickness with SRR for cases with different thermal conductivities in addition to the case of uncoated surfaces. Various conditions are represented in colors as opposed to the reference case represented in black.

In the range of **SRR between 0 and 2**, the reference coating case (black), the higher thermal conductivity coating case (red), and the uncoated surfaces case (green) are almost equivalent in terms of minimum film thickness variation. However, in the case of lower thermal conductivity (blue), the minimum film thickness is lower than all other cases for the whole range of $0 \leq SRR \leq 2$. This indicates that for the given operating conditions, using a coating with a thermal conductivity a hundred times lower than that of steel causes a decrease in the film thickness even under pure rolling conditions. Figure 4.14 shows the temperature rise compared to T_0 along the entrainment direction at the midplane of the lubricant film $(z = h/2)$ for cases with different thermal conductivities at $SRR = 0$ and 1.

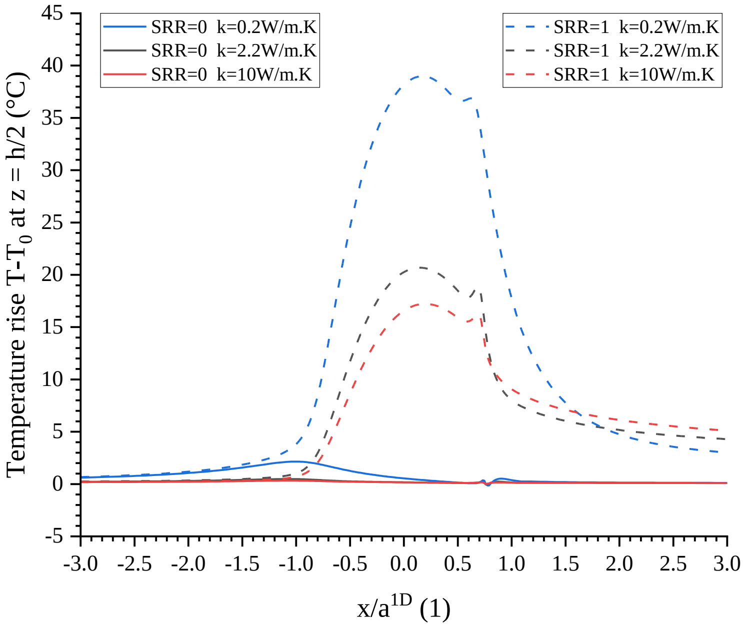

Figure 4.14: Temperature rise $T - T_0$ at $z = h/2$ along the normalized entrainment direction for $SRR = 0$ (solid lines) and $SRR = 1$ (dashed lines). For three thermal conductivities cases $k = 0.2, 2.2$, and $10\ W/m.K$.

Due to low thermal conductivity, the heat generated by the compression of the fluid in the convergent region (around $x/a^{1D} = -1$) is not evacuated to the contacting solids. Thus, for $k = 0.2\ W/m.K$, the temperature of the fluid entering the contact rises by $2.4°C$ compared to $0.5\ °C$ for the reference case (blue curves vs black curves). This higher temperature rise explains the decrease in film thickness even at $SRR = 0$. The difference in temperature rise in the inlet region persists at higher sliding (see $SRR = 1$ in Figure 4.14). Notice the extreme temperature rise in the central region ($-1 \leq x/a^{1D} \leq -1$) due to the hindering of the evacuation of the heat generated by shearing the fluid under high sliding conditions. In the case with the lowest thermal conductivity, heat does not get easily transferred in the solid surfaces from the center of the contact to outside the contact ($x/a^{1D} > 2$). Thus, the temperature of the solid surfaces outside the contact is lower for lower k and the neighboring lubricant cools down at the interface with the colder surfaces resulting in a lower lubricant temperature in the case of the lower k compared to a higher k at $x/a^{1D} > 2$.

For $\boldsymbol{SRR} > \mathbf{2}$, the minimum film thickness in the case of low k decreases sharply with increasing SRR. In contrast, in the case of high k, the minimum film thickness is similar to the uncoated case. Figure 4.15 shows the resulting temperature distribution in the lubricant inside the contact for all three thermal conductivity coating cases in addition to the case of uncoated surfaces. Also, the temperature of the lubricant near the surfaces at $x = -a^{1D}$ and $x = +a^{1D}$ are indicated.

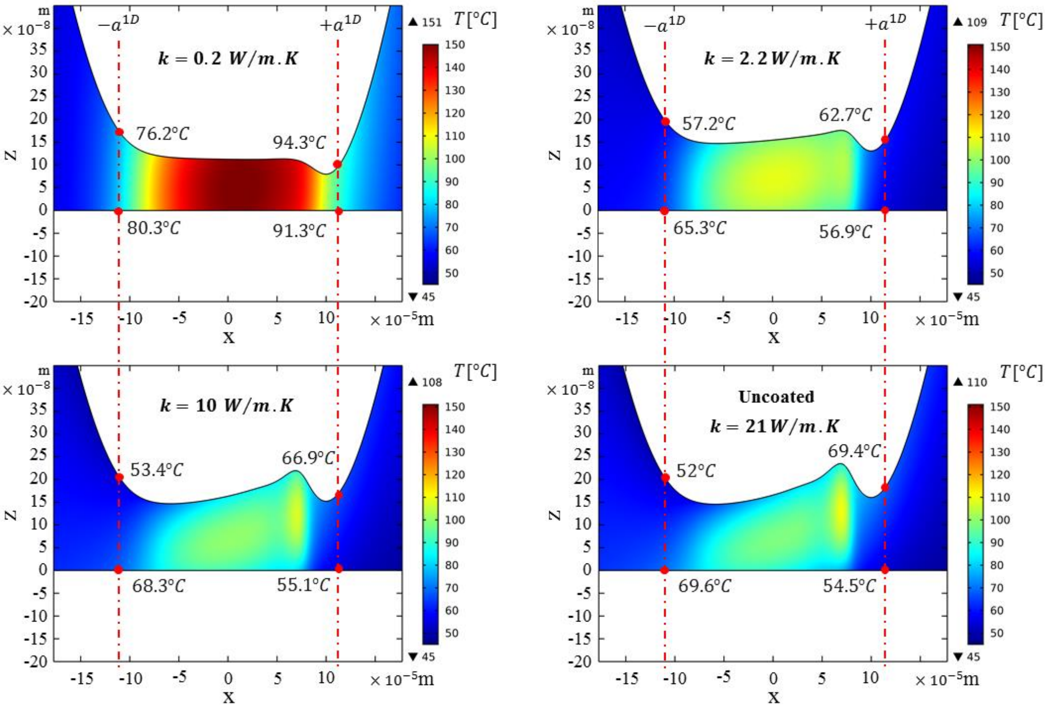

Figure 4.15: Temperature distribution in the lubricant inside the contact for three thermal conductivity cases ($k = 0.2$, 2.2 and $10\ W/m.K$) and the uncoated surfaces case at SRR=5. Temperatures of the lubricant near the surfaces at positions $x = +a^{1D}$ and $-a^{1D}$ are also shown.

The temperature distribution is more uniform across the thickness for lower k. The difference in temperature across the film thickness is much smaller for the lower thermal conductivity case compared to the higher thermal conductivity case (around $4°C$ for the former versus more than $11°C$ for the latter). In addition, the temperature of the lubricant entering the contact increases with SRR in the case of low k. Thus, the attenuation of the thermal viscosity wedge effect and the increase in the temperature of the lubricant lead to a significant decrease of h_m with SRR for $k = 0.2\ W/m.K$.

The thermal conductivity of the contacting surfaces plays a significant role in regulating the heat dissipation from the hot fluid to the colder solids and can significantly influence the temperature of the lubricant entering the contact and thus its viscosity and the resulting lubricant film thickness.

Effects on friction coefficient

Figure 4.16 shows the variation of friction coefficient with SRR for different thermal conductivities.

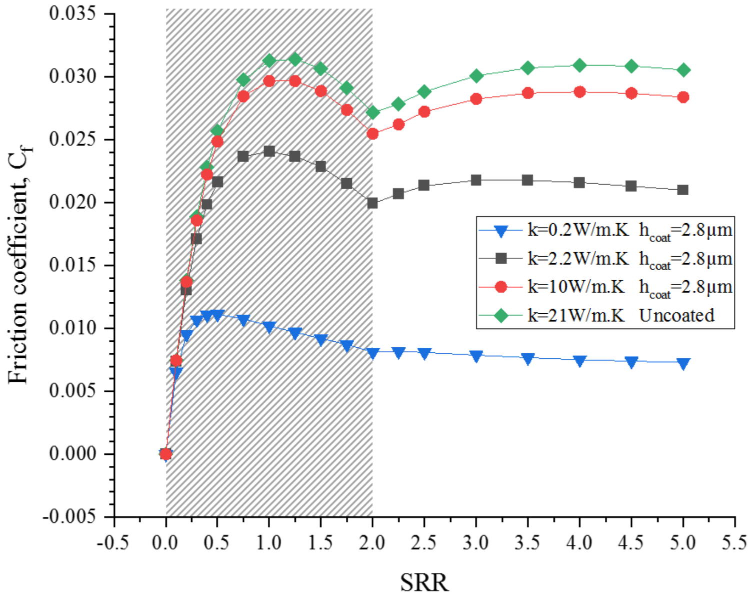

Figure 4.16: Variations of friction coefficient with SRR for cases with different thermal conductivities in addition to the uncoated case. Various conditions are represented in colors as opposed to the reference case represented in black. The gray zone indicates the range over which the friction coefficient is overestimated due to not considering the LSS.

The friction response is mostly controlled by the viscosity and shear rate of the lubricant in the central region of the contact. This response is very different for cases with different thermal conductivity. The variation of C_f with SRR for the case with the highest thermal conductivity coating is similar to the uncoated case for $SRR \leq 0.4$. Coated cases with lower thermal conductivity show a difference compared to the uncoated case at a lower SRR. Overall, for a given SRR, the friction coefficient is lower in the case with a lower k. In all cases except $k = 0.2\ W/m.K$, a local maximum is reached at $SRR > 2$ (at a different SRR for each case) after which the friction coefficient slowly decreases with increasing sliding. Overall, friction reduction due to the DLC coating discussed in section 4.2 is amplified with decreasing thermal conductivity of the coating.

4.3.2 Effects of varying the thickness of the coating

In this section, the effects of varying the thickness of the coating on the lubricant film thickness and friction coefficient are investigated. In addition to the reference case $h_{coat} = 2.8\ \mu m$, coatings of various thicknesses $h_{coat} \in \{0.2, 0.5, 1, 5, 10\}\ \mu m$ are tested. All coatings have the same thermal conductivity $k = 2.2\ W/m.k$.

Effects on lubricant film thickness

Figure 4.17 show the variation of the lubricant film thickness with SRR for cases with various coating thicknesses in addition to the uncoated case.

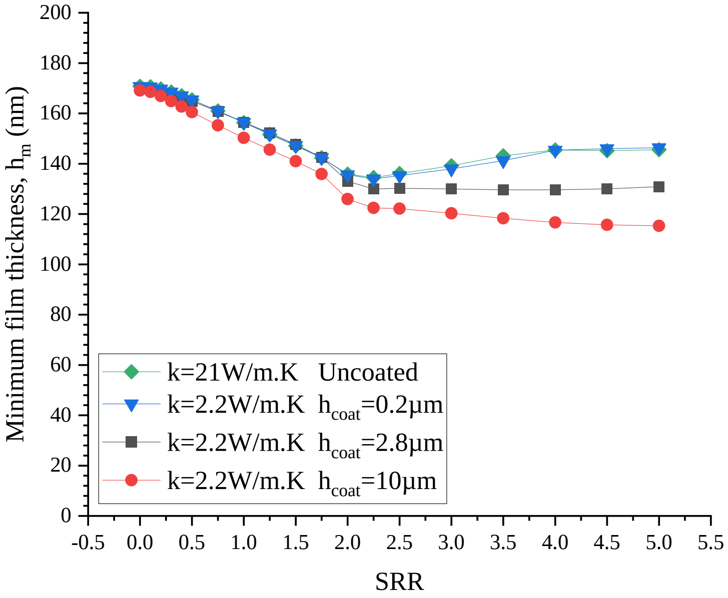

Figure 4.17: Variations of minimum film thickness with SRR for cases with different coating thicknesses in addition to the uncoated case. Various conditions are represented in colors as opposed to the reference case represented in black.

For the case with the thinner coating ($h_{coat} = 0.2\ \mu m$), the variation of film thickness is almost identical to that of the uncoated case over the whole range of SRR (0 to 5). In contrast, in the case with $h_{coat} = 10\ \mu m$, the thickness is the lowest. The thicker coating insulates the lubricant and causes its temperature in the inlet region to increase even at low SRR. The difference in h_m between cases with different coating thicknesses is very small at low SRR and increases with sliding. However, it seems to stabilize for SRR between 4 and 5 especially because, in the case of low coating thickness (or uncoated surfaces), a sort of equilibrium is reached at very high sliding between a greater viscosity wedge (which increases h_m) and a higher lubricant temperature (which decreases h_m) Figure 4.18 shows the temperature distribution inside the contact for three different coating thickness cases at $SRR = 5$.

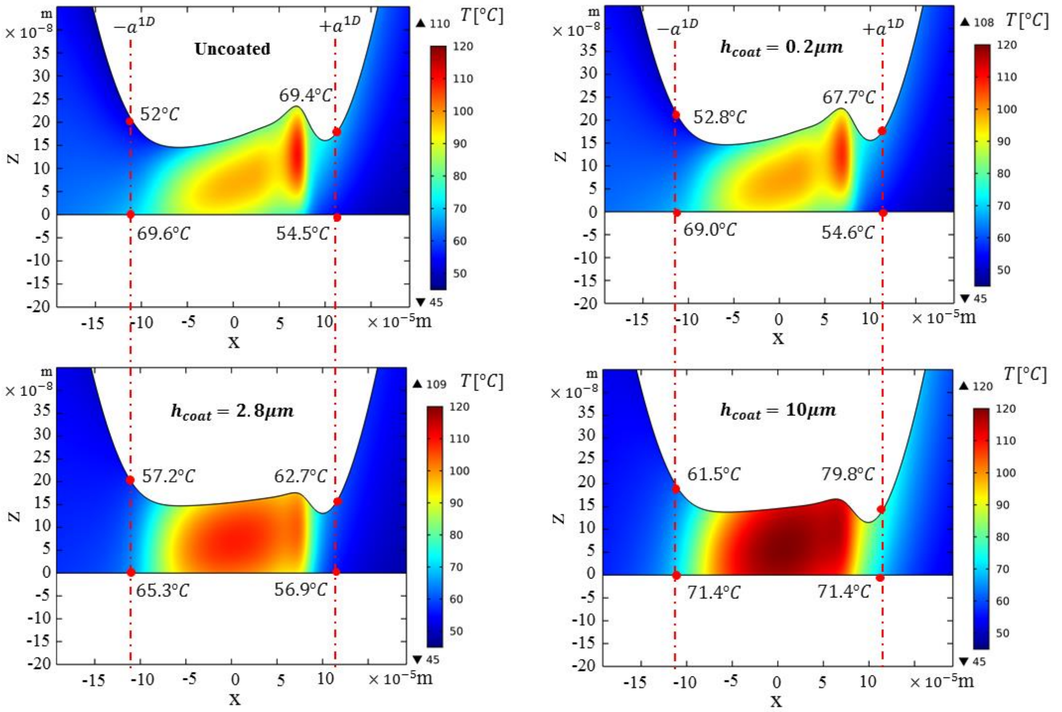

Figure 4.18: Temperature distribution in the lubricant inside the contact for three coating thickness cases $h_{coat} = 0.2, 2.8$, and $10\ \mu m$ in addition to the uncoated surfaces case at $SRR = 5$. Temperatures of the lubricant near the surfaces at positions $x = +a^{1D}$ and $x = -a^{1D}$ are shown.

Increasing the thickness of a thermally insulating coating has a similar effect as decreasing its thermal conductivity while keeping its thickness unchanged. The temperature distribution is more uniform across the lubricant's thickness in the cases $h_{coat} = 2.8\ \mu m$ and $h_{coat} = 10\ \mu m$ compared to the low coating thickness case ($h_{coat} = 0.2\ \mu m$) leading to an attenuation of the thermal viscosity wedge in the former cases under opposite sliding conditions. For high coating thickness, the minimum lubricant film thickness decreases slowly with SRR. In contrast, for low coating thickness, the thermal viscosity wedge prevails similarly to the uncoated case and the minimum film thickness increases with SRR. In addition, the lubricant enters the contact at a higher temperature in the case of $h_{coat} = 10\ \mu m$ compared to the reference case leading to a lower h_m even though the temperature gradient across the lubricant thickness is higher in the former case.

In summary, the thickness of the thermally insulating coating influence thermal equilibrium and the temperature of the lubricant entering the contact, especially in opposite sliding conditions. Thus, increasing the coating thickness can attenuate the viscosity wedge effect and increase the temperature inside the contact thus countering the increase in minimum film thickness with SRR which usually occurs in thinly-coated or uncoated contacts operating at opposite sliding.

Effects on friction coefficient

Figure 4.19 presents the variation with SRR of the friction coefficient for cases with coatings of different thicknesses in addition to the uncoated case.

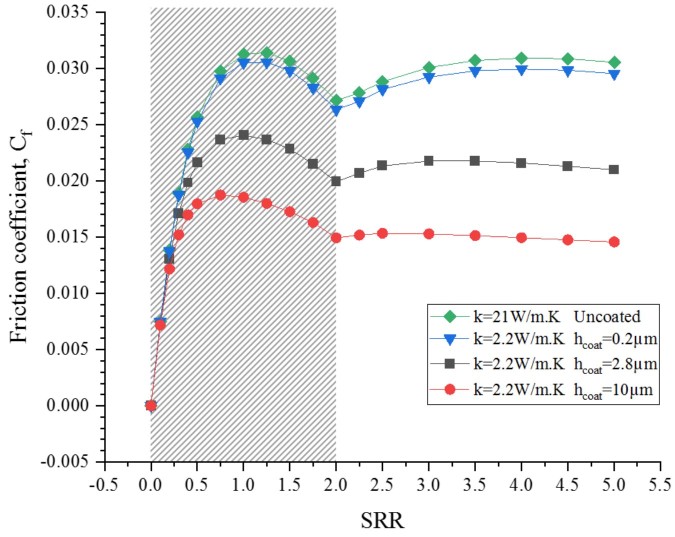

Figure 4.19: Variations of friction coefficient with SRR for cases with different coating thicknesses in addition to the uncoated case. Various conditions are represented in colors as opposed to the reference case represented in black. The gray zone indicates the range over which the friction coefficient is overestimated due to not considering the LSS.

The values of friction coefficient in the case of low coating thickness are remarkably close to those for the uncoated case over the whole range of SRR. At a given sliding condition, as the thickness of the coating increases, the friction coefficient decreases. For instance, at SRR=5, the friction coefficient decreases from 0.030 ($h_{coat} = 0.2\ \mu m$) to 0.015 ($h_{coat} = 10\ \mu m$). As mentioned earlier, friction is controlled mostly by the viscosity and shear rate of the lubricant inside the contact. These are influenced differently by the use of thicker or thinner insulating coatings. Figure 4.20 shows the variation with SRR of the average viscosity and the average shear rate inside the contact for cases with different coating thicknesses.

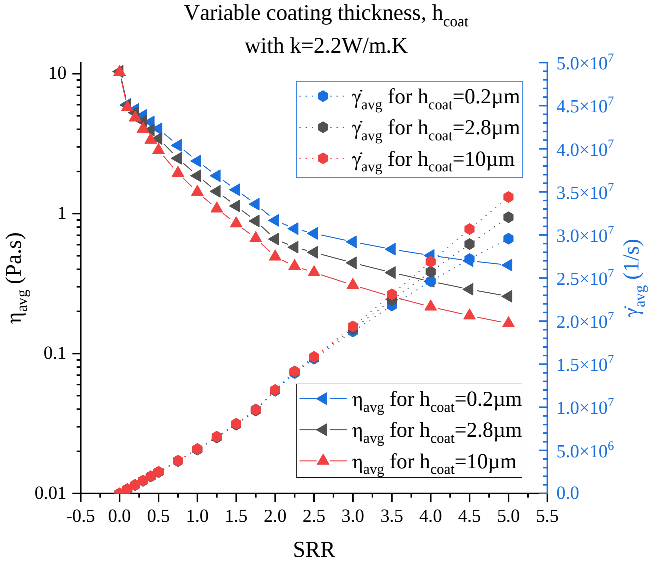

Figure 4.20: Variation with SRR of average viscosity (left axis) and average shear rate (right axis) inside the contact for various entrainment velocities. Cases with variable coating thicknesses. The averages are calculated in the contact region between $x = -a^{1D}$ and $x = +a^{1D}$

For $SRR < 2$, the average shear rate is similar for all coating thicknesses and is increasing with SRR. In contrast, the average viscosity is decreasing because of thermal and shear-thinning effects. In addition, a higher coating thickness leads to lower viscosity because the temperature of the lubricant is higher due to the entrapment of heat in the lubricant. The same trend is observed for $SRR > 2$ in terms of the difference in viscosity. However, a difference in average shear rate is observed in opposite sliding between cases with different coating thicknesses. This is due to the differences in film thickness shown previously in Figure 4.17.

To conclude, the friction response can be controlled by varying the thickness of a thermally insulating coating. A higher coating thickness hinders heat evacuation from the lubricant and lowers the friction coefficient.

4.3.3 Quantifying the influence of coating properties on film thickness and friction

In previous sections, the effects of thermal conductivity k and thickness h_{coat} of the coating were discussed separately. This section, however, quantifies the variation of friction coefficient and minimum film thickness with k and h_{coat} simultaneously.

Additional simulations are realized for various combinations of k and h_{coat}. A total of 22 combinations are simulated. These are illustrated in Figure 4.21 where different symbols correspond to different coating thicknesses.

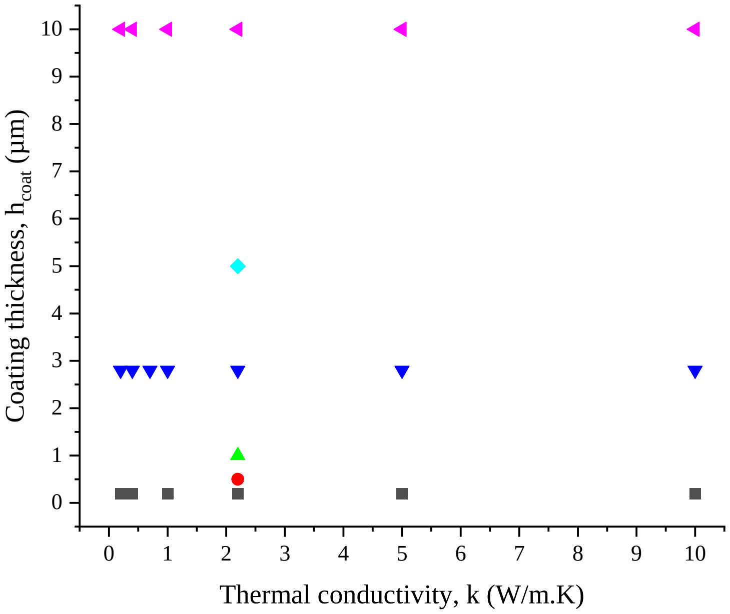

Figure 4.21: Simulation conditions defined by the thermal conductivity k and the thickness of the coating h_{coat}. A total of 22 combinations are simulated. Different symbols correspond to different coating thicknesses.

New dimensionless parameters are defined in (4.2) based on the dimensional analysis in Appendix E.

$$\bar{h}_{coat} = \frac{h_{coat}}{R}, \qquad \bar{k} = \frac{k}{C_p \rho u_e R} \tag{4.2}$$

where $R = 12.78\ mm$ is the reduced radius of curvature, $u_e = 1\ m/s$ is the entrainment velocity. In addition, $C_p = 855\ J/kg.K$ and $\rho = 2840\ kg/m^3$ are respectively the specific heat capacity and density of the coating used in all simulations. An additional dimensionless parameter $\frac{\bar{h}_{coat}}{\bar{k}} =$

$\frac{h_{coat}C_p\rho u_e}{k}$ is used to study the simultaneous effects of thermal conductivity and thickness of the coating. $\frac{\bar{h}_{coat}}{\bar{k}}$ is also employed in semi-analytical expressions of minimum lubricant film thickness and friction coefficient correction factors.

Minimum lubricant film thickness correction at high sliding

Sections 4.3.1 and 4.3.2 showed that a thermally insulating coating can significantly influence the minimum film thickness, especially at high sliding $SRR \geq 2$. This section aims to express a correction factor of the minimum lubricant film thickness in terms of coating properties (k and h_{coat}). The correction factor φ_{coat} depending on $\bar{k}$, $\bar{h}_{coat}$ and SRR is defined in (4.3).

$$\varphi_{coat} = \frac{H_m(\bar{k}, \bar{h}_{coat}, SRR)}{H_m(Uncoated, SRR)} \tag{4.3}$$

where $H_m(\bar{k}, \bar{h}_{coat}, SRR)$ is the dimensionless minimum oil film thickness for given thermal conductivity, coating thickness, and SRR whereas $H_m(Uncoated, SRR)$ is the dimensionless minimum oil film thickness in the uncoated case for the same SRR. Both are obtained by dividing h_m by R.

In general, $\varphi_{coat} \leq 1$ indicating that the coating lowers the minimum film thickness (see Figure 4.13 and Figure 4.17). The correction factor at $SRR = 2$ is denoted $\varphi_{coat,SRR=2}$. It is calculated based on numerical results at $SRR = 2$ and is plotted with respect to $\ln\left(\frac{\bar{h}_{coat}}{\bar{k}}\right)$ in Figure 4.22b whereas its natural logarithm $\ln(\varphi_{SRR=2})$ is plotted in Figure 4.22a for all the simulated configurations.

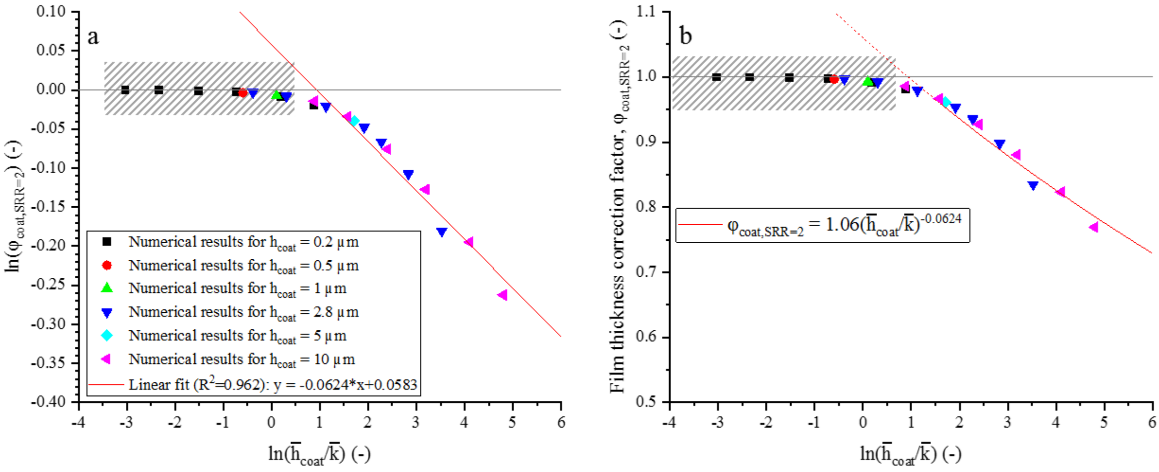

Figure 4.22: Variation of (a) $\ln(\varphi_{coat,SRR=2})$ and (b) $\varphi_{coat,SRR=2}$ with $\ln\left(\frac{\bar{h}_{coat}}{\bar{k}}\right)$. Numerical results are presented by colored symbols for each coating thickness (k is variable). The red line in (a) represents the best linear fit to numerical results excluding the points in the gray zone $\varphi_{coat,SRR=2} \geq 0.99$. The red line in (b) represents the semi-analytical expression (4.4).

The value of $\ln(\varphi_{coat,SRR=2})$ approaches zero for $\ln\left(\frac{\bar{h}_{coat}}{\bar{k}}\right) < 0.9$ whereas the variation of $\ln(\varphi_{coat,SRR=2})$, at a higher value of $\ln\left(\frac{\bar{h}_{coat}}{\bar{k}}\right)$, can be approximated to a linear decrease described by the red line shown in Figure 4.22a. The linear fit is realized using the least squares method and results in a coefficient of determination $R^2 = 0.962$. The slope and intercept of this line are used to create a semi-analytical expression relating $\varphi_{coat,SRR=2}$ to $\frac{\bar{h}_{coat}}{\bar{k}}$ in the form given in (4.4).

$$\varphi_{coat,SRR=2} = a_1 \left(\frac{\bar{h}_{coat}}{\bar{k}}\right)^{b_1} \tag{4.4}$$

where $a_1 = e^{0.0583} = 1.06$ and $b_1 = -0.0624$ are the parameters of the semi-analytical expression.

Figure 4.22b shows that at low $\frac{\bar{h}_{coat}}{\bar{k}}$ (i.e. low coating thickness and high thermal conductivity) the lubricant film thickness at $SRR = 2$ tends to 1. Thus, in this case, the coating does not affect the film thickness at $SRR = 2$. The expression (4.4) gives $\varphi_{coat,SRR=2} > 1$ for $\frac{\bar{h}_{coat}}{\bar{k}} < 2.55$ (i.e. $\ln\left(\frac{\bar{h}_{coat}}{\bar{k}}\right) < 0.935$) which is clearly not the correct behavior as illustrated by Figure 4.22b. Thus, a condition is added to expression (4.4) resulting in the following expression (4.5) which provides a correction factor that accounts for the coating properties at $SRR = 2$.

$$\varphi_{coat,SRR=2} = \begin{cases} 1, & \frac{\bar{h}_{coat}}{\bar{k}} < 2.55 \\ 1.06\left(\frac{\bar{h}_{coat}}{\bar{k}}\right)^{-0.0624}, & otherwise \end{cases} \tag{4.5}$$

Furthermore, the variation of φ_{coat} with SRR for various combinations of k and h_{coat} is plotted in Figure 4.23.

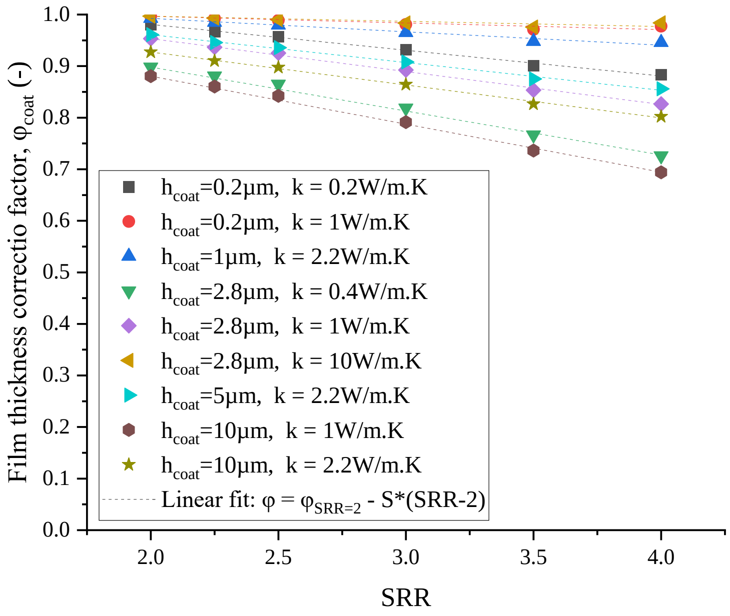

Figure 4.23: Variation of lubricant film thickness correction with SRR for various coating properties obtained numerically. The dashed lines represent the best linear fit to numerical results by a line intercepting $\varphi_{coat,SRR=2}$ for each h_{coat} and k combinations.

In the range $2 \leq SRR \leq 4$, the variation of φ_{coat} can be approximated by a line intercepting $\varphi_{coat,SRR=2}$ with a slope S (shown as dashed lines). The value of S for a given combination of k and h_{coat} is chosen such that the resulting line is the best fit for numerical results (shown as colored symbols). The least squares method is used to achieve the best fit.

The natural logarithm of S is presented in Figure 4.24a as a function of $\ln\left(\frac{\bar{h}_{coat}}{\bar{k}}\right)$ whereas S is plotted in Figure 4.24b.

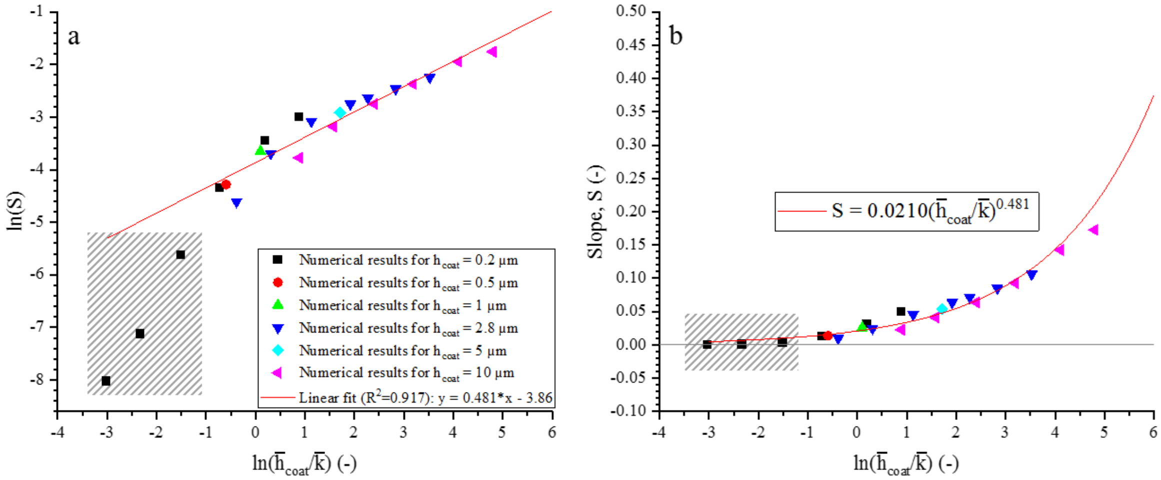

Figure 4.24: Variation of (a) $\ln(S)$ and (b) S with $\ln\left(\frac{\bar{h}_{coat}}{\bar{k}}\right)$. Numerical results are presented by colored symbols for each coating thickness (k is variable). The red line in (a) represents the best linear fit to numerical results excluding the points in the gray zone with $S \leq 0.01$. The red line in (b) represents the semi-analytical expression (4.6).

The linear fit in Figure 4.24a is realized using the least squares method and results in a coefficient of determination $R^2 = 0.917$. Note that three points (in the gray zone) are not considered for the fitting. These correspond to cases with $S \leq 0.01$ which indicate no variation of φ_{coat} with SRR.

Similar to (4.4), the semi-analytical expression of $S\left(\frac{\bar{h}_{coat}}{\bar{k}}\right)$ given in (4.6) can be deduced from the slope and intercept of the linear fit in Figure 4.24a with parameters $a_2 = 0.021$ and $b_2 = 0.481$.

$$S = a_2\left(\frac{\bar{h}_{coat}}{\bar{k}}\right)^{b_2} = 0.021\left(\frac{\bar{h}_{coat}}{\bar{k}}\right)^{0.481} \tag{4.6}$$

The semi-analytical expression is in good agreement with numerical results as shown in Figure 4.24b and can be combined with expressions (4.5) to create a semi-analytical expression (4.7) for $\varphi_{coat}(\bar{k}, \bar{h}_{coat}, SRR)$ applicable for SRR between 2 and 4.

$$\varphi_{coat} = \varphi_{coat,SRR=2} - S \times (SRR - 2)$$

$$\varphi_{caot} = \begin{cases} 1 - 0.021\left(\frac{\bar{h}_{coat}}{\bar{k}}\right)^{0.481} \times (SRR - 2), & \frac{\bar{h}_{coat}}{\bar{k}} \leq 2.55 \\ 1.06\left(\frac{\bar{h}_{coat}}{\bar{k}}\right)^{-0.0624} - 0.021\left(\frac{\bar{h}_{coat}}{\bar{k}}\right)^{0.481} \times (SRR - 2), & otherwise \end{cases} \tag{4.7}$$

Semi-analytical approach for minimum film thickness predictions

An example of the variation of dimensionless minimum film thickness H_m with SRR is given in Figure 4.25 where the operating conditions and material properties are similar to the uncoated case in section 4.2.1 except for a coating with thickness $h_{coat} = 2.8\ \mu m$ and thermal conductivity $k = 1\ W/m.K$.

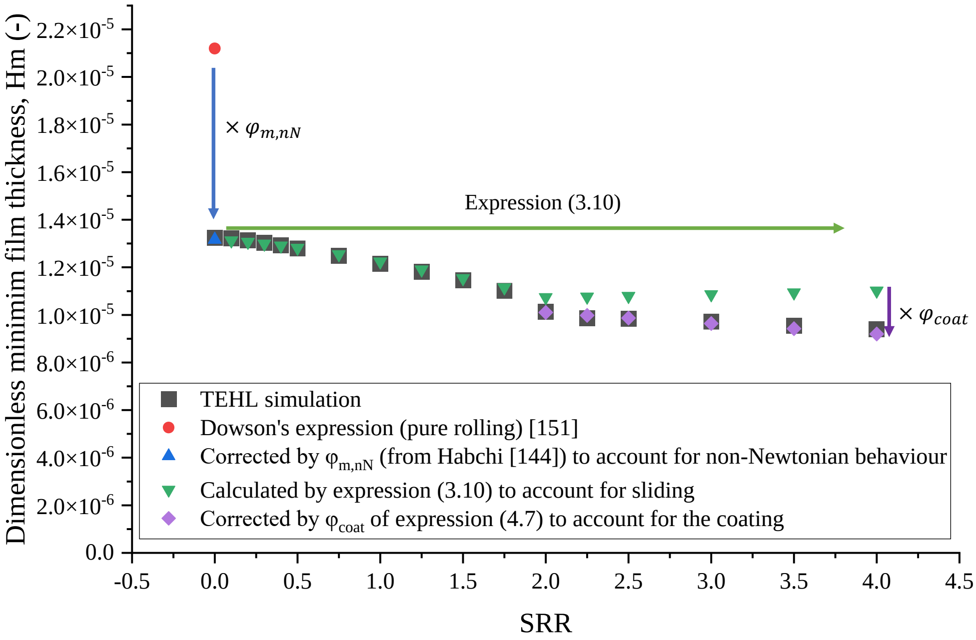

Figure 4.25: An example of the variation of dimensionless minimum film thickness H_m with SRR calculated by different methods. The coating properties correspond to $h_{coat} = 2.8\ \mu m$ and $k = 1\ W/m.K$.

The operating conditions and material properties in the uncoated case defined in section 4.2.1 result in the following dimensionless parameters:

$$U = 1.2326 \times 10^{-11}$$

$$G = 4091.5$$

$$W_{1D} = 2.9461$$

The procedure detailed in section 3.3 is applied to find the variation of the minimum film thickness with SRR in the uncoated case. First, H_m is calculated by the expression of Dowson [151] at pure rolling (red circle). Then, the correction factor from Habchi [144] is applied to account for the lubricant's non-Newtonian behavior at pure rolling (blue triangle). Next, expression (3.10) is used to account for sliding as SRR increases resulting in the variation of H_m in the uncoated case (green triangles). Finally, the correction factor φ_{coat} is applied for $2 \leq SRR \leq 4$ to account for the coating based on its properties (violet diamonds). In the example of Figure 4.25, the results of the analytical approach accounting simultaneously for non-Newtonian behavior, sliding, and coating properties are in excellent agreement with the full TEHL simulation.

The same procedure is repeated for all combinations of h_{coat} and k simulated in this section. The dimensionless minimum film thickness obtained numerically and by the semi-analytical approach are compared in Figure 4.26 to assess the validity of the latter.

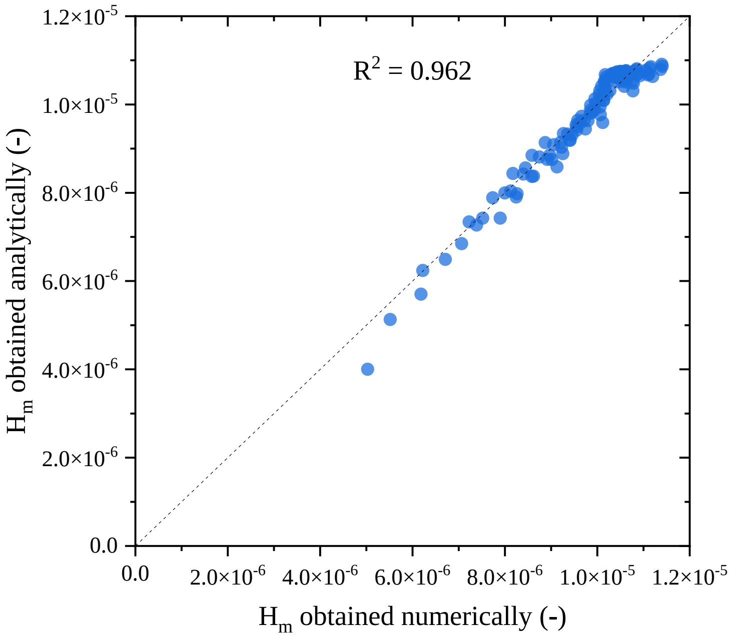

Figure 4.26: Comparison of dimensionless minimum film thickness obtained numerically by full TEHL simulation and analytically using the semi-analytical approach described in this section.

Recall that the coefficient of determination R^2 is a measure of how well a model predicts known outcomes and the closer R^2 is to 1 the more accurate the model. In the case of the semi-analytical approach versus numerical results, $R^2 = 0.962$ which is close to 1. Thus, the semi-analytical approach provides good quantitative predictions of the minimum film thickness in coated TEHL contacts at high sliding ($2 \leq SRR \leq 4$).

Friction coefficient correction at high sliding

To quantify the friction variation due to thermally insulating coatings, the friction correction factor at high sliding ψ_{coat} is defined in (4.8). It should be noted that in Figure 4.16 the friction coefficient hardly changes with varying SRR from 3 to 5. Thus, for each combination of $\bar{k}$ and $\bar{h}_{coat}$, ψ_{coat} is calculated as the mean of $\frac{C_f(\bar{k},\bar{h}_{coat},SRR)}{C_f(Uncoated,SRR)}$ over 5 values for $SRR \in [3,5]$.

$$\psi_{coat}(\bar{k},\bar{h}_{coat}) = \frac{\sum_{SRR=3}^{5}\left(\frac{C_f(\bar{k},\bar{h}_{coat},SRR)}{C_f(Uncoated,SRR)}\right)}{5} \qquad (4.8)$$

where $C_f(\bar{k},\bar{h}_{coat},SRR)$ and $C_f(Uncoated,SRR)$ are the friction coefficient at a given SRR for coated and uncoated cases respectively. In general, the friction coefficient decreases when the surfaces are coated with an insulating coating leading to $\psi_{coat} < 1$.

The variation of the friction coefficient correction factor ψ_{coat} and its natural logarithm $\ln(\psi_{coat})$ are plotted in Figure 4.27 vs $\ln\left(\frac{\bar{h}_{coat}}{\bar{k}}\right)$.

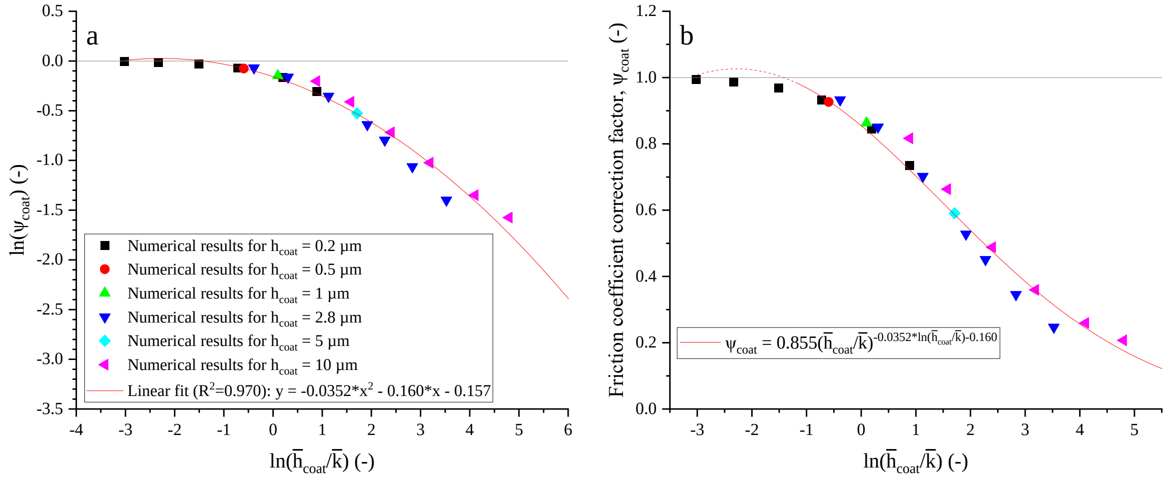

Figure 4.27: Variation of (a) $\ln(\psi_{coat})$ and (b) ψ_{coat} with $\ln\left(\frac{\bar{h}_{coat}}{\bar{k}}\right)$. Numerical results are presented by colored symbols for each coating thickness ($\bar{k}$ is variable). The red line in (a) represents the best fit of a 2nd-order polynomial to numerical results. The red line in (b) represents the semi-analytical expression (4.10).

The variation of $\ln(\psi_{coat})$ with $\ln\left(\frac{\bar{h}_{coat}}{\bar{k}}\right)$ is approximated by a 2nd-order polynomial given in (4.9) fitted to numerical results by the least squares method and resulting in a coefficient of determination $R^2 = 0.970$.

$$\ln(\psi_{coat}) = -0.0352\left[\ln\left(\frac{\bar{h}_{coat}}{\bar{k}}\right)\right]^2 - 0.160\ln\left(\frac{\bar{h}_{coat}}{\bar{k}}\right) - 0.157 \tag{4.9}$$

An expression of ψ_{coat} given in (4.10) is obtained by using the inverse function of the natural logarithm, which is the exponential function on both sides of equation (4.9), and rearranging the terms.

$$\psi_{coat} = a_3\left(\frac{\bar{h}_{coat}}{\bar{k}}\right)^{b_3\ln\left(\frac{\bar{h}_{coat}}{\bar{k}}\right)+c_3} = 0.855\left(\frac{\bar{h}_{coat}}{\bar{k}}\right)^{-0.0352\ln\left(\frac{\bar{h}_{coat}}{\bar{k}}\right)-0.160} \tag{4.10}$$

where $a_3 = e^{-0.157} = 0.855$, $b_3 = -0.0352$, and $c_3 = -0.160$ are based on the coefficients of the 2nd-order polynomial in (4.9).

Numerical results in Figure 4.27b show that for low $\frac{\bar{h}_{coat}}{\bar{k}}$ (i.e. low coating thickness and high conductivity) the correction factor approaches 1 indicating that the coating does not influence the friction coefficient at high siding. In contrast, the expression (4.10) gives $\psi_{coat} > 1$ for $-3.14 \leq \ln\left(\frac{\bar{h}_{coat}}{\bar{k}}\right) \leq -1.42$ (i.e. $0.0433 \leq \frac{\bar{h}_{coat}}{\bar{k}} \leq 0.248$) this is illustrated by the dashed part of the red curve in Figure 4.27b. Thus, a condition is applied where ψ_{coat} is set to 1 for $\frac{\bar{h}_{coat}}{\bar{k}} \leq 0.248$ resulting in a semi-analytical expression of friction coefficient correction factor of the form given in (4.11).

$$\psi_{coat} = \begin{cases} 1, & \dfrac{\bar{h}_{coat}}{\bar{k}} \leq 0.248 \\ 0.855 \left(\dfrac{\bar{h}_{coat}}{\bar{k}}\right)^{-0.0352 \ln\left(\frac{\bar{h}_{coat}}{\bar{k}}\right) - 0.160}, & otherwise \end{cases} \tag{4.11}$$

The above expression is used to calculate the variation of ψ_{coat} with the thermal conductivity of the coating for different coating thicknesses as shown in Figure 4.28 alongside numerical results.

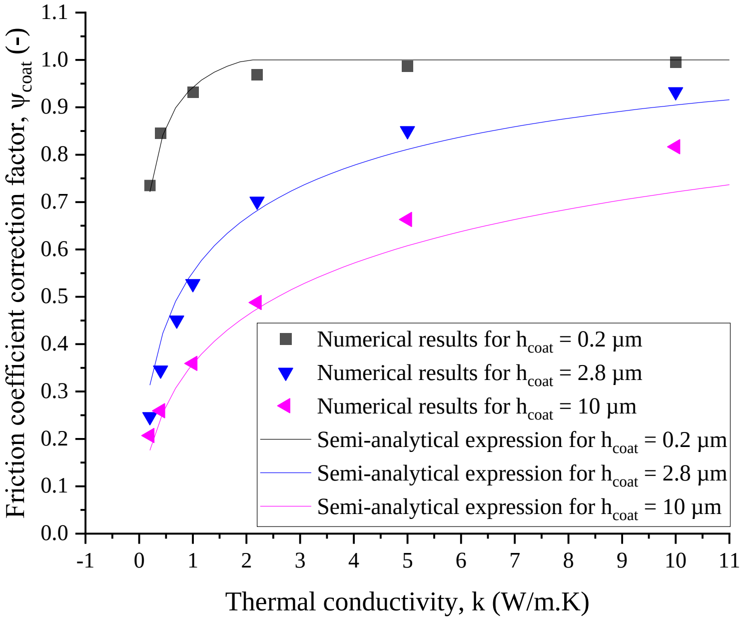

Figure 4.28: Variation of friction coefficient correction factor ψ_{coat} with the thermal conductivity of the coating for different coating thicknesses. The curves are obtained using the semi-analytical expression (4.11).

A very good agreement is obtained between numerical results and the semi-analytical expression for different combinations of coating thickness and thermal conductivity conditions. However, for high coating thickness and high conductivity the agreement is less good. Expression (4.11) provides a correction factor for predicting the friction coefficient at high sliding ($3 \leq SRR \leq 5$) when a thermally insulating coating is applied based on the known friction coefficient in the uncoated contact.

4.3.4 Conclusion

In this section, the effects of varying the thermal conductivity and the thickness of a coating on the lubricant film thickness and friction coefficient are explored using a 1D line contact TEHL numerical model.

It is found that, with low enough thermal conductivity or high coating thickness, the minimum lubricant film thickness can be affected even under rolling-sliding conditions because of the temperature rise in the inlet region due to the important thermal insulation effect. For high thermal conductivities or low coating thicknesses, the minimum film thicknesses are similar to the uncoated case over the whole range of SRR. Meanwhile, for low k and high h_{coat} the minimum film thickness decreases with increasing SRR under opposite sliding conditions and h_m is almost independent of SRR for the reference case (intermediate k and h_{coat}). These behaviors are explained by the occurrence (or not) and the intensity of the thermal viscosity wedge.

Furthermore, both the thermal conductivity and the coating thickness have a great influence on the friction response of an EHL line contact over the majority of the sliding conditions tested here. The lower thermal conductivity and the thicker coating lead to a lower friction coefficient compared to higher thermal conductivity and thinner coating.

The expressions (4.7) and (4.11) enable the mapping of minimum film thickness reduction and friction coefficient reduction at high sliding for $k \in [0.1,10]\ W/m.K$ and $h_{coat} \in [0.1,10]\ \mu m$. Figure 4.29 illustrates the combined influence of k and h_{coat} on minimum film thickness and friction coefficient for a coated contact case compared to an uncoated contact case at $SRR = 4$. The reductions are calculated as $1 - \varphi_{coat}$ and $1 - \psi_{coat}$ respectively for minimum film thickness and friction coefficient and are shown as percentages.

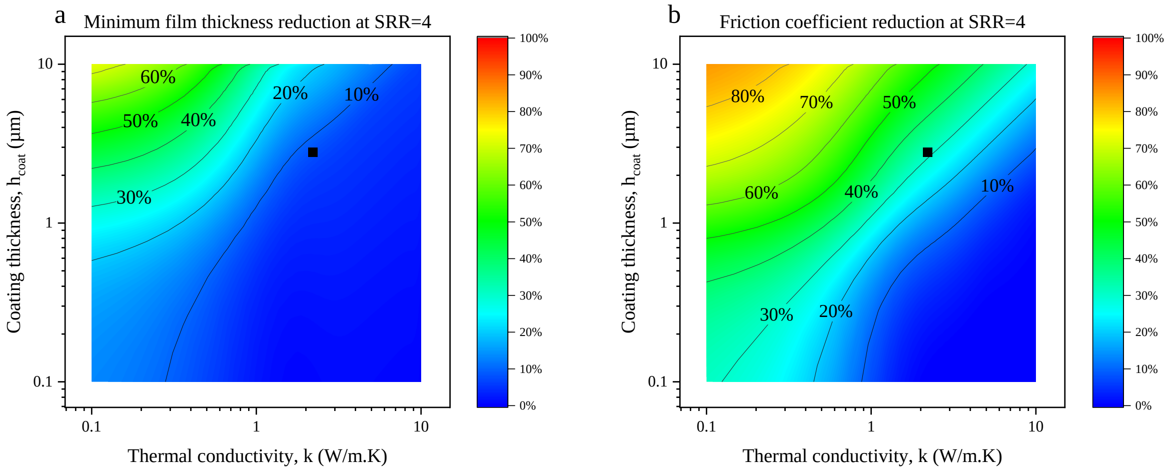

Figure 4.29: (a) Minimum film thickness reduction $1 - \varphi_{coat}$ and (b) friction coefficient reduction $1 - \psi_{coat}$ due to the use of insulating coating of thermal conductivity k and thickness h_{coat} at $SRR = 4$. Values are calculated by the semi-analytical expressions (4.7) and (4.11).

It is shown in Figure 4.29 that the film thickness and friction reductions go hand in hand at high sliding due to thermally insulating coating. The region where the minimum film thickness reduction is the most significant corresponds also to the most important friction reduction. Moreover, in the reference case (indicated by the black square in Figure 4.29) a decrease of around 30% in friction coefficient is accompanied by a decrease of around 10% in minimum film thickness.

4.4 Conclusion

This chapter presented investigations of the TEHL contact between thermally insulating surfaces for a wide range of sliding conditions. First, numerical predictions and experimental measurements of film thickness and friction coefficient from a barrel-on-disk contact were compared. Results showed the ability of the 1D numerical approach to reproduce measurements, especially at high sliding if the effect of heat accumulation in experiments is considered in the simulations. Second, the effects of using a thermally insulating coating (here, DLC coating) on lubricant film thickness and friction coefficient were revealed for a wide range of sliding conditions ($0 \leq SRR \leq 5$). When a thermally insulating coating is used, the results showed not only a reduction in friction coefficient but also in minimum film thickness. Finally, the effects of varying the coating thickness and its thermal conductivity were explored. It was revealed that both of these parameters influence friction and film thickness reduction and that they have opposite effects. The ability to control the friction reduction in a full-film lubrication regime by modifying the coating properties was demonstrated. However, the influence on the film thickness should also be considered especially at extreme sliding ($SRR \geq 2$).

The present analysis will be exploited in the next chapter where the numerical model is used to study the effects of coating the surfaces in a dynamically changing cam-follower contact.

Chapter 5: Cam-follower Contact: Impact of DLC Coatings on the Tribological Performances

DLC-coated valve-train contacts were investigated by many researchers [96,124,168]. Dobrenizki et al. [96] experimentally studied the effects of two kinds of a-C:H DLC coatings with two different lubricants on a cam-tappet test rig. They found that under the conditions tested in the test rig, the usage of DLC coatings leads to friction reduction regardless of the lubricant used. Yu et al. [168] numerically studied the effect of thermal and mechanical properties of a DLC coating in addition to its thickness on TEHL performance in cam-tappet contact. They found that a soft coating with low thermal inertia results in the lowest friction loss and that this effect is more important for thicker coatings. It should be noted that a Newtonian lubricant behavior was assumed in [168] which may lead to an overestimation of friction. More recently, Marian et al. [124] conducted a dual experimental and numerical investigation on surface modification (by DLC coating and micro-texturing) of a cam-tappet contact. DLC coating was found to decrease friction by up to 30% compared to uncoated surfaces case. Their numerical model included shear-thinning and thermal effects in addition to asperity contact to account for mixed lubrication. The asperity contact friction coefficient used in their model was estimated based on preliminary dry friction experiments.

Most of the aforementioned works focused on contact between a cam and a flat tappet. In contrast, the contact of interest in this work is between a cam and a follower with a curved pad. In this chapter, the effects of DLC coating on the performances of a cam-follower contact are studied experimentally using the Monocam test rig described in Chapter 2 and numerically using a quantitative transient TEHL approach. A wide range of rotation speeds is considered. First, surface configurations and test conditions are defined. Next, experimental and numerical results are compared. Then the effects of DLC coating on tribological performances (friction losses, and surface wear) are discussed.

5.1 Surface Configurations and Test Conditions

Three surface configurations are tested:

- Steel/Steel: this is the reference configuration where the cam and follower are uncoated. Components with short names Steel-C and Steel-F (in Table 2.7) are used in this configuration.
- DLC/DLC: in this configuration, the effect of DLC coating is revealed by comparison with the reference case. Components with short names DLC-C and DLC-F (in Table 2.7) are used in this configuration.
- Steel/DLC: this is an intermediate configuration where only the follower is DLC-coated. Components with short names Steel-C and DLC-F (in Table 2.7) are used in this configuration.

For details about the solid material properties of different components, the reader is referred to section 2.1.2. The cam-follower contact is lubricated by the same commercial engine oil used throughout this work and its properties are given in section 2.1.3.

The cam-follower test conditions listed in Table 5.1 are unchanged for all surface configurations.

Table 5.1: Cam-follower experimental conditions.

Parameter	**Unit**	**Value**
Exp. inlet temperature, T_{in}	$°C$	$25 \pm 2, 50 \pm 1, 77 \pm 1$
Cam rotation direction	−	CW, CCW
Order of speed steps	−	Ascending, descending
Camshaft rotation speed, ω	rpm	350, 590, 830, 1070, 1310, 1550, 1790, 2030

In experiments, the inlet temperature T_{in} of the lubricant is measured before entering the test box throughout the experiment and is thermally regulated at fixed temperatures of 50 ± 1°C and $77 \pm 1°C$ for intermediate and high-temperature experiments respectively. In contrast, for the low-temperature experiment, the temperature is not thermally regulated and is dictated by the room temperature at the time of the test ($T_{room} = 20 \pm 0.5°C$). Two rotation directions are tested to reveal any differences in the kinematics or the lubrication of the contact. The rotation speeds cover a wide range of conditions corresponding to engine speeds between 700 rpm and 4060 rpm typical for a 4-strokes engine in passenger cars.

In simulations, the intermediate and high temperatures are considered with the inlet temperature T_0 (set to $50°C$ and $77°C$ respectively) imposed on the lubricant entering the contact and to the bulk solids (far from the contact). The low temperature case is not simulated for two reasons. First, the rheological characterization (viscosity-shear dependency) of the lubricant is realized at the temperatures $40°C$ and $60°C$ (see section 2.1.3). At low temperature, the description of the non-Newtonian behavior by the model in (2.6) and its parameters in Table 2.4 might be inaccurate. Second, in an internal combustion engine the lubricant is rarely operating at ambient temperatures e.g. $25°C$.

Theoretically, the cam and follower are in contact for camshaft rotation angles between 100° and 260°. The variations of simulation inputs such as surface velocities, normal load, and radius of curvature over a cam rotation cycle are detailed in section 2.1.2. The equivalent radius of curvature is independent of the rotation speed and is given in Figure 2.14. In contrast, the variation of the normal load is affected by the camshaft rotation speed due to the influence of inertial forces (see Figure 2.15). Furthermore, the surface velocities u_1 and u_2 of the cam and follower respectively scale linearly with camshaft rotation speed ω. Factors $\frac{u_1}{\omega}$ and $\frac{u_2}{\omega}$ whose variations are plotted in Figure 5.1 are used to describe the variation of surface velocities.

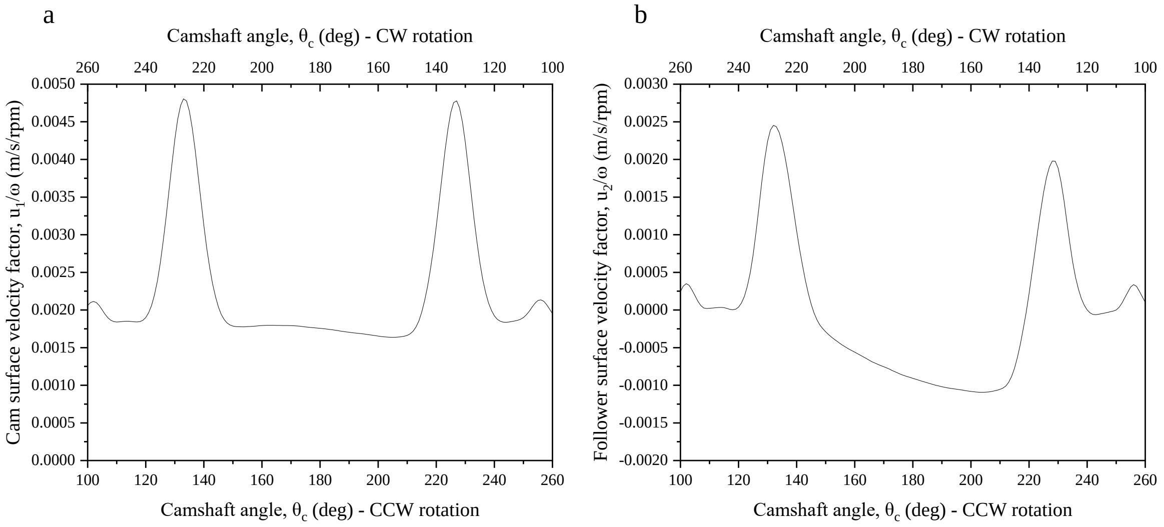

Figure 5.1: Variation of (a) cam surface velocity factor and (b) follower surface velocity factor with camshaft angle for CCW (bottom axis) and CW (top axis) rotations.

Surface velocities u_1 and u_2 are simply calculated by multiplying factors $\frac{u_1}{\omega}$ and $\frac{u_2}{\omega}$ by the camshaft rotation speed expressed in rpm for a given test.

5.2 Results and Discussion

Experimental results of the mean friction coefficient obtained from ascending and descending tests are given in Appendix F for all surface configurations and rotation directions. These revealed that experiments performed on the Monocam test rig in ascending and descending speed steps orders yield almost identical results. Thus, at each rotation speed, an average between ascending and descending results is calculated and will be used for discussions in later sections. Moreover, variations of mean friction coefficient with rotation speed from CW and CCW tests of different surface configurations are compared in Appendix F. Results show that the mean friction coefficient is lower in the CCW rotation direction compared to the CW rotation direction for all speeds. The difference is less significant at higher speeds. This suggests that, during the cycle, the CW rotation may lead to starved lubrication due to the placement of the lubrication nozzle (see Appendix F for more details). Only the case of CCW rotation is considered for the discussions in this section and for comparison with simulations of the cam-follower contact assuming fully-flooded conditions no matter the cam rotation direction.

From an experimental perspective, it should be noted that for speeds higher than $1550\,rpm$ the measurement uncertainty increases because of vibrations in the test rig. Furthermore, the sampling rate is fixed to $102.4\,kHz$ regardless of the rotation speed which reduces the temporal resolution of the measurements at high rotation speeds (fewer data points are collected during a cycle) and contributes to a degradation in the quality of the measurements.

From a numerical perspective, some assumptions (discussed later) may result in numerical predictions that do not exactly reflect reality. However, the advantage of using the numerical approach is that it gives access to a variety of variables such as the lubricant film thickness, pressure field, and temperature field during the rotation cycle when the cam and follower are in contact. These quantities are inaccessible by the experimental means employed in this work.

5.2.1 Variation of numerical h_m and C_f over time

Figure 5.2 presents the variation of (a) the minimum lubricant film thickness h_m and (b) the instantaneous friction coefficient during a cam rotation cycle between 100° and 260° (this range corresponds to the portion of the cycle where the cam and follower are in contact). These results are obtained by simulating the cam-follower contact using the transient TEHL approach.

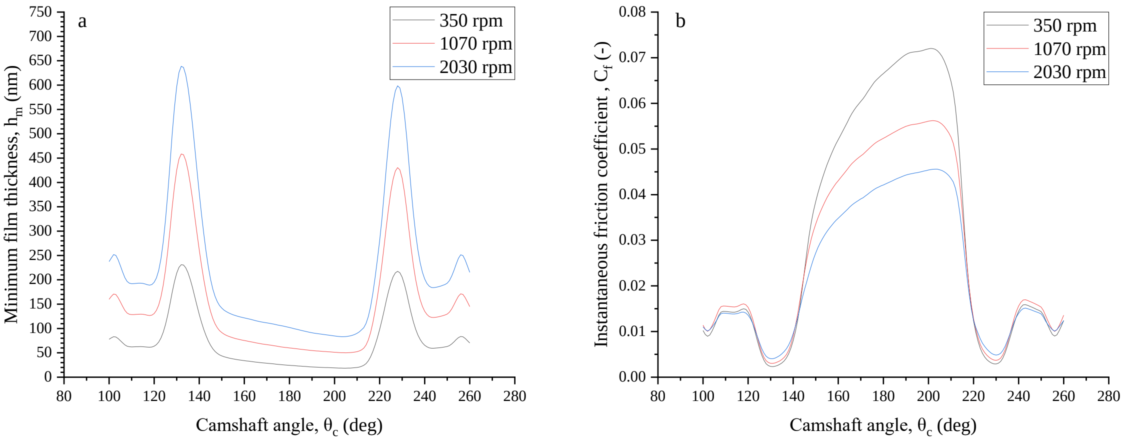

Figure 5.2: Variation of (a) minimum lubricant film thickness and (b) instantaneous friction coefficient at different camshaft rotation speeds. Results correspond to transient TEHL simulations of steel/steel configuration with CCW rotation at $T_0 = 50°\text{C}$.

On one hand, the peaks in h_m correspond to portions of the cycle where the cam-follower contact is conformal. In contrast, for angles between 146° and 219° the contact is non-conformal and operates under opposite-sliding conditions (see Figure 1.5). In this range, the minimum film thickness decreases to reach a minimum (over the whole cycle) at 204° where SRR is highest ($SRR \approx 10$). Higher camshaft rotation speed translates to higher entrainment at a given camshaft angle (SRR is unchanged). Thus, the minimum film thickness increases with camshaft rotation speed for a given camshaft angle.

On the other hand, the friction coefficient is lowest in the interval where the contact is conformal. A maximum in C_f is reached at 204° which corresponds to the highest sliding. As opposed to h_m, friction coefficient tends to decrease (under opposite sliding conditions) with increasing camshaft rotation speed. This is due to the increase in entrainment velocity and decrease in normal load. First, when $SRR > 2$, increasing the camshaft rotation speed increases the entrainment velocity and as a consequence decreases the friction coefficient for a given SRR (see diagram in Figure 3.24). Second, the normal contact load, calculated by the procedure presented in Appendix B is influenced by the dynamic forces at high rotation speeds (see Figure 2.15). The resulting variation of max Hertzian pressure in the cam-follower contact over the range $\theta_c \in [100°, 260°]$ is presented in Figure 5.3.

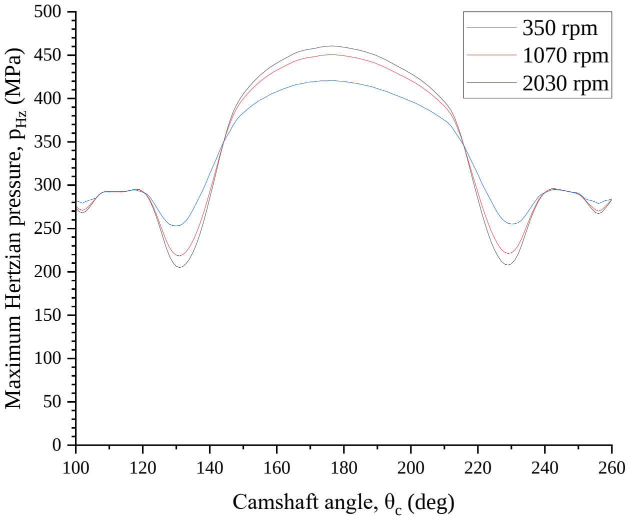

Figure 5.3: Variation of the maximum Hertzian pressure during the camshaft rotation cycle from 100° to 260° for different rotation speeds.

This figure shows that the maximum Hertzian pressure is lower for higher rotation speed during the highly-loaded portion of the cam-follower contact cycle (i.e. $146° \leq \theta_c \leq 215°$). This contributes to the decrease of friction coefficient with rotation speed (see diagram in Figure 3.15).

Next, friction measurements are compared with predictions of the transient TEHL approach.

5.2.2 Instantaneous friction coefficient

In this section, the ability of the quantitative EHL approach to predict the friction coefficient during the cycle of a cam-follower contact is assessed by comparing friction measurements and simulation results for the intermediate inlet temperature ($T_{in} = 50 \pm 1°C$ and $T_0 = 50°C$).

Figure 5.4 compares the variation of instantaneous friction coefficient with camshaft angle obtained experimentally and numerically for steel/steel and DLC/DLC configurations for the rotation speed of 350 rpm. The gray envelope attached to the experimental results refers to the variability of friction coefficient measurements calculated from 5 different cycles.

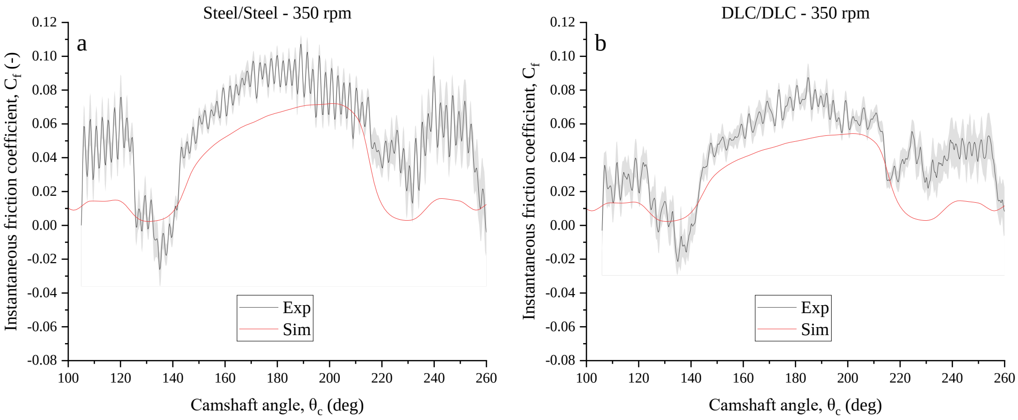

Figure 5.4: Instantaneous friction coefficient variation with camshaft angle at 350 rpm for $T_{in} = 50 \pm 1°C$ and $T_0 = 50°C$. (a) and (b) present a comparison of experimental and numerical results for steel/steel and DLC/DLC configurations respectively.

The negative values of the experimental friction coefficient observed in Figure 5.4 for $125° \leq \theta_c \leq 140°$ may be attributed to the fact that the instantaneous friction coefficient is obtained by applying the procedure described in Appendix B. This procedure is based on a simplified dynamic analysis of the cam-follower-valve mechanism. In reality, gaps between mating components and misalignments may lead to instantaneous torque measurements being lower than those predicted theoretically if a frictionless cam-follower contact is considered. This leads to a negative friction coefficient when the measured torque is converted to friction coefficient.

Numerical results follow experimental trends qualitatively except for camshaft angles between $\sim 220°$ and $\sim 230°$ where experiments show a local spike in friction coefficient while predictions keep decreasing. In reality, the follower can rebound due to the spring action toward the end of the valve closing phase and as a consequence, a spike in the normal load and then in friction coefficient may occur. In contrast, the interval $[\sim 220°, \sim 230°]$ during the cam rotation cycle corresponds to a conformal contact (see Figure 1.5) where the theoretical maximum Hertzian pressure is lowest (see Figure 5.3). Follower rebound is not considered in simulations so no spike in friction coefficient is observed.

Quantitatively, the numerical results underestimate friction for most of the rotation cycle and both surface configurations. The model assumes a full-film lubrication regardless of how small the film thickness gets and as a consequence, only the fluid friction is considered. However, in practice, mixed lubrication regime may occur at low speeds (e.g. 350 rpm) as discussed later (see section 5.2.3). In that case, asperity contact contributes to a higher friction coefficient in measurements compared to predictions.

Figure 5.5 is similar to Figure 5.4 but at the rotation speed of 1310 rpm. The vibrations in the friction coefficient obtained experimentally are higher in this case than in the low-speed case. In addition, the temporal resolution of the measurements is independent of the rotation speed. Hence, when the signals are presented in terms of camshaft angles the oscillations appear more spread-out. Even though not much information can be extracted from these friction coefficient signals, the mean friction calculated from them is used for discussions in later sections.

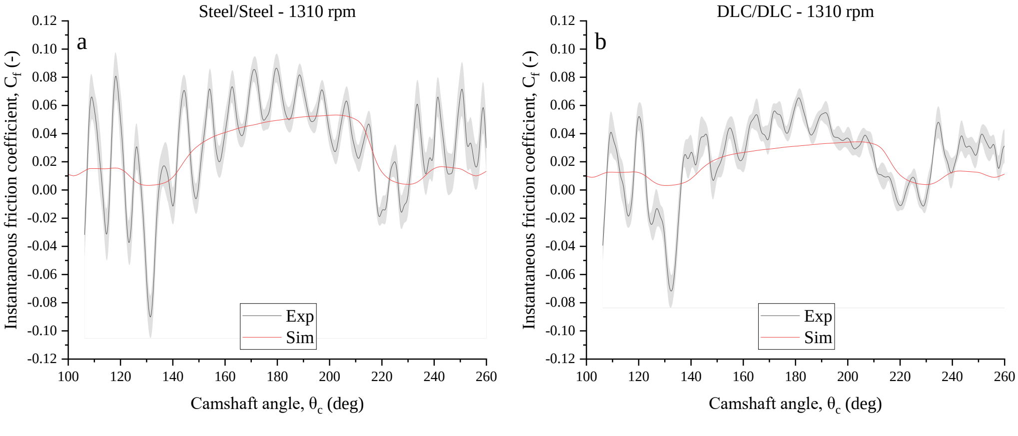

Figure 5.5: Instantaneous friction coefficient variation with camshaft angle at 1310 rpm for $T_{in} = 50 \pm 1°C$ and $T_0 = 50°C$. (a) and (b) present a comparison of experimental and numerical results for steel/steel and DLC/DLC configurations respectively.

Note that obtaining the variation of the normal load (input to TEHL transient simulations) and the variation of experimental C_f (calculated from measured torque) are both based on the dynamics of the cam-follower-valve mechanism described in Appendix B. Some assumptions are made to simplify this approach. Among those:

- rigid bodies: no elastic deformation of the cam, follower, or the valve
- no follower rebound
- no friction between the lower pad and the valve or between the follower and the pin holding it.

The simplified modeling of the cam-follower-valve mechanism may not be adapted for the high speeds tested here. This adds another layer of uncertainty (in addition to vibrations in the test rig) to the experimental results at high speeds. Accurate modeling at these conditions requires a more in-depth study of the mechanism and possibly involves multi-body and dynamic simulations. These aspects are out of the scope of the current work which concentrates on the effects of DLC coating on the performance of the cam-follower contact.

5.2.3 Mean friction coefficient

The mean friction coefficient $C_{f,mean}$ is calculated over the portion of the cam rotation cycle where there is contact between the cam and the upper pad of the follower from both experimental and numerical instantaneous friction results. In this section, experimental and numerical results are compared over a range of camshaft rotation speeds ($350\,rpm$ to $2030\,rpm$) and for different surface configurations, but first, the film thickness parameter λ is introduced. This parameter estimates the lubrication regime under which the cam-follower contact operates.

Film thickness parameter λ

At a given camshaft rotation angle, an average film thickness h_a is calculated from the profile of film thickness h obtained numerically over the contact length defined by the Hertzian half width a^{1D} (i.e. $-1 \leq x/a^{1D} \leq 1$). For example, at $\theta_c = 180°$ and for the steel/steel configuration at rotation speed 1070 rpm the film thickness profile and the average film thickness are presented respectively by black and red lines in Figure 5.6.

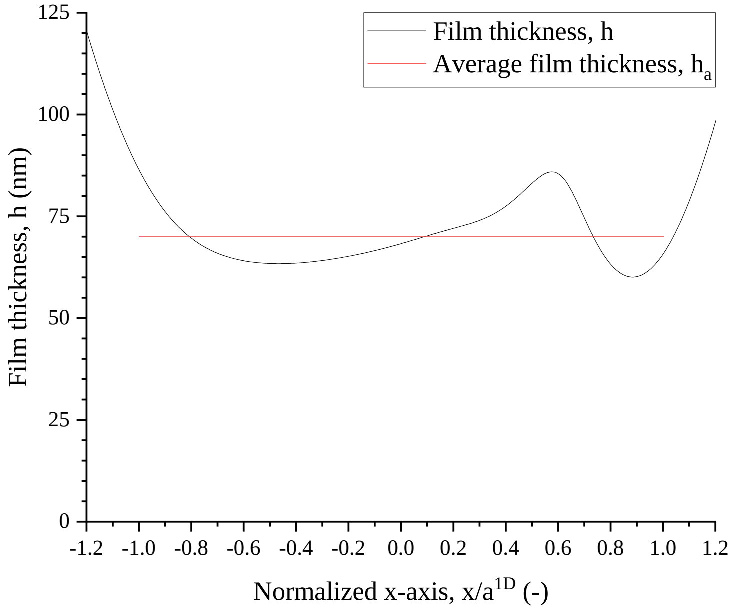

Figure 5.6: Film thickness profile and average film thickness over the contact length ($-1 \leq x/a^{1D} \leq 1$). Steel/steel configuration at 1070 rpm and $\theta_c = 180°$ for $T_0 = 50°C$.

$h_a(\theta_c)$ is calculated for each $\theta_c \in [100°, 260°]$ and a mean value over all rotation angles denoted $h_{a,mean}$ is calculated from the values of $h_a(\theta_c)$. The film thickness parameter λ is defined in (5.1) as the ratio of mean average film thickness $h_{a,mean}$ over the composite surface roughness R_q.

$$\lambda = \frac{h_{a,mean}}{R_q} \tag{5.1}$$

where $R_q = \sqrt{R_{q,1}^2 + R_{q,2}^2}$ with $R_{q,1}$ and $R_{q,2}$ the root mean squared (RMS) roughness of the surface of the cam and upper pad respectively.

The RMS roughness is measured at three different locations (opening ramp, opening flank, and nose regions) on each one of the cams, and at two locations (edge and center of the contact zone as in Figure 5.18) on each one of the followers. According to Torabi et al. [169], in a cam-follower contact during the running-in period, asperities can be flattened due to plastic deformation the surface roughness can decrease significantly. Hence, the roughness measurements are performed after the experimental campaign. Table 5.2a lists $R_{q,i}$ the RMS roughness of different components calculated by averaging measurements at different locations.

In addition, values of composite roughness calculated for different surface configurations are listed in Table 5.2b. These are used in equation (5.1) to calculate λ for a given surface configuration and a given camshaft rotation speed. Note that the composite roughness of the steel/steel configuration is significantly higher than that of the DLC/DLC because the former is less wear resistant than the latter (discussed later in section 5.2.8).

Table 5.2: (a) Root mean squared roughness $R_{q,i}$ of different components after the experimental campaign. (b) Composite roughness for different surface configurations.

a

Component i	RMS roughness, $R_{q,i}$ (nm)
Steel-C	38
DLC-C	33
Steel-F	48
DLC-F	30

b

Configuration	Composite roughness, R_q (nm)
Steel/Steel	62
DLC/DLC	45
Steel/DLC	49

Figure 5.7 represents the variation of the film thickness parameter with the camshaft rotation speed (right axis). In addition, the variations of the mean friction coefficient obtained experimentally and numerically are shown (left axis). The results corresponding to the steel/steel and DLC/DLC configurations are shown respectively in (a) and (b). A similar graph corresponding to the steel/DLC configuration is given in Appendix F.

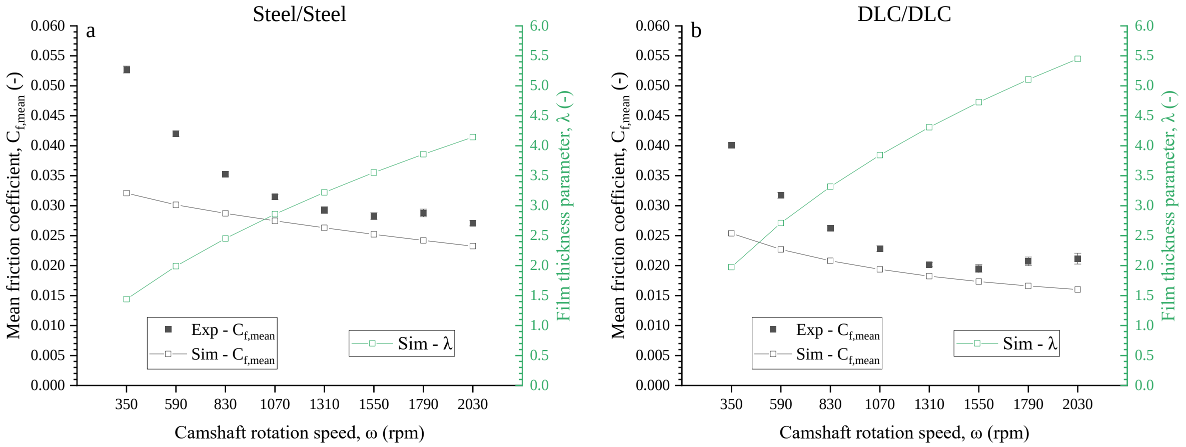

Figure 5.7: Variation with the camshaft rotation speed of the mean friction coefficient (left axis) obtained numerically and experimentally in addition to the variation of the film thickness parameter (right axis) calculated based on the mean minimum film thickness $h_{m,mean}$ from TEHL simulations and roughness measurements. Results corresponding to steel/steel and DLC/DLC configuration are respectively shown in (a) and (b). Experiments and simulations are performed at $T_{in} = 50 \pm 1°C$ and $T_0 = 50°C$ respectively.

For both surface configurations, simulations greatly underestimate the experimental mean friction coefficient at low rotation speeds. For instance, at 350 rpm the simulations predict a 39 % and 37 % lower mean friction coefficient compared to measurements for steel/steel and DLC/DLC configurations respectively. The difference between measurements and numerical predictions decreases with increasing camshaft rotation speed up to 1310 rpm where a minimum difference of about 10 % is reached for both configurations. At speeds higher than 1310 rpm, qualitative differences are observed in the variation of $C_{f,mean}$ between experiments and simulations especially for the DLC/DLC configuration. In experiments, the mean friction coefficient increases slightly with increasing rotation speed. However, it is difficult to draw conclusions from experimental results at such high rotation speeds. Furthermore, as shown in section 5.2.6, this behavior is not observed for tests at other inlet temperatures.

In the cam-follower contact studied here, as the rotation speed increases, the entrainment velocity also increases which raises the average film thickness and λ. The latter ranges between 1.4 and 4.1 for steel/steel configuration and between 2 and 5.4 for DLC/DLC configuration. The limits of each lubrication regime in terms of λ, mentioned in section 1.2, are not exact. Instead, they can be influenced by many factors. According to Zhu and Wang [170], the upper limit of the mixed lubrication regime can be as low as $\lambda = 0.6 - 1.2$ under certain conditions. In the current, cam-follower contact the lubrication regime probably ranges from mixed to EHL lubrication. The contribution of asperity contact friction decreases with increasing rotation speed and the discrepancy between numerical and experimental results decreases up to 1310 rpm.

Next, the effects of DLC coating on the tribological performance of cam-follower contact are explored.

5.2.4 Effects of DLC on film thickness

The effects of DLC coating on the film thickness are explored in Chapter 4 for a stationary line EHL contact for a wide range of SRR. Results show that at high sliding ($SRR > 2$) DLC-coated surfaces lead to a reduction in film thickness due to an attenuation of the viscosity wedge effect. In this section, the effects of DLC coating on film thickness in a cam-follower contact are investigated.

Figure 5.8 shows the temperature distribution in the deformed lubricant gap for a rotation speed of 1310 rpm at two camshaft rotation angles (150° and 180°). The subfigures on the left and right correspond to steel/steel and DLC/DLC surface configurations respectively. Operating conditions are different for different camshaft rotation angles and are given on the left of the figure. The minimum and average lubricant film thicknesses are also presented in each case.

The DLC-coated surfaces act as thermally insulating barriers leading to a higher temperature inside the contact at both rotation angles. The film thickness profiles at $\theta_c = 150°$ are barely influenced by the presence of the DLC coating. In contrast, at $\theta_c = 180°$, the sliding is more important ($SRR = 6.28$ and 2.77 respectively for 180° and 150°) and the thickness profiles are significantly affected by the DLC coating. In that case, the thermal viscosity wedge effect is attenuated due to a more uniform temperature distribution through the film thickness in the DLC/DLC configuration. The dimple zone, very prominent in the steel/steel configuration, disappears in the DLC/DLC configuration. These results are similar to the ones obtained in section 4.2.2.

The minimum film thickness decreases in the DLC/DLC configuration and a higher decrease in observed in at $\theta_c = 180°$. The film thickness correction factor φ, introduced in Chapter 4 and given by equation (4.7), is calculated for each θ_c with the corresponding operating conditions (given in Figure 5.8) and the following coating properties: $h_{coat} = 2.8\,\mu m$, $k = 2.2\,W/m.k$, $C_p = 855\,J/kg.K$, and $\rho = 2840\,kg/m^3$.

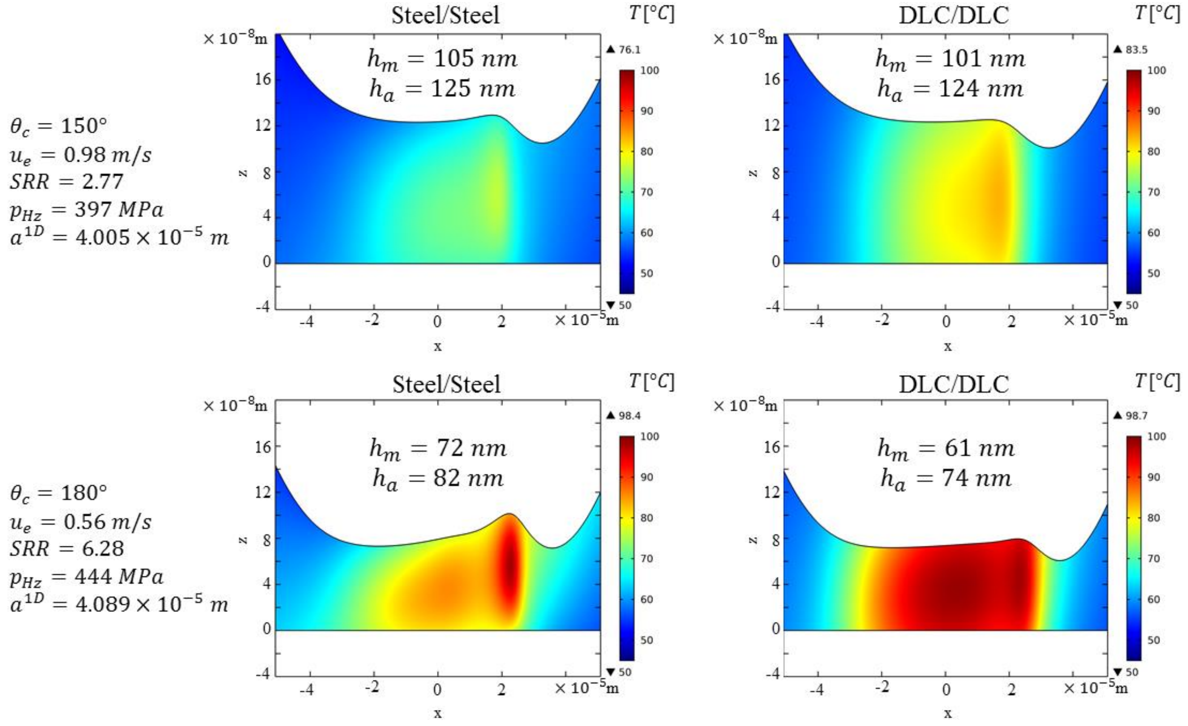

Figure 5.8: Temperature distribution in the deformed lubricant gap at two camshaft rotation angles $\theta_c = 150°$ and 180° shows respectively in the top and bottom of the figure and for two surface configurations steel/steel and DLC/DLC shown respectively on the left and right of the figure. All plots correspond to a camshaft rotation speed of 1310 rpm for $T_0 = 50°C$. Operating conditions for each rotation angle are listed on the left.

The resulting film thickness correction factors are $\varphi_{coat}(\theta_c = 150°) = 0.96$ and $\varphi_{coat}(\theta_c = 180°) = 0.88$. The ratios $\frac{h_{m,DLC/DLC}}{h_{m,Steel/Steel}}$ (analogous to correction factor) calculated based on numerical results are 0.96 and 0.85 for $\theta_c = 150°$ and 180° respectively. The semi-analytical correction factor is accurate for $\theta_c = 150°$ and slightly less accurate for $\theta_c = 180°$. This is because $SRR = 6.28$ is higher than the maximum SRR value used to fit the semi-analytical model in Chapter 4 (i.e. $SRR = 4$).

The variation of h_a with the camshaft angle is presented in Figure 5.9a for steel/steel and DLC/DLC configurations at a camshaft rotation speed of 1310 rpm. Similar to minimum film thickness, the average film thickness decreases in the DLC/DLC configuration compared to steel/steel. Thus, the mean average film thickness $h_{a,mean}$ also decreases. Even though $h_{a,mean}$ decreases slightly in the DLC/DLC configuration, the film thickness parameter λ increase because it is inversely proportional to R_q which is lower for DLC/DLC compared to steel/steel configuration (see Table 5.2b). The variation of λ with camshaft rotation speed is presented in Figure 5.9b. Results show that at any rotation speed, the DLC-coated contact operates with a higher λ. Thus, a DLC-coated contact can operate under a lubrication regime closer to the full-film regime than an uncoated contact under equal operating conditions. This contributes to the beneficial effects of using DLC-coated surfaces for friction reduction. These effects are explored in a later section.

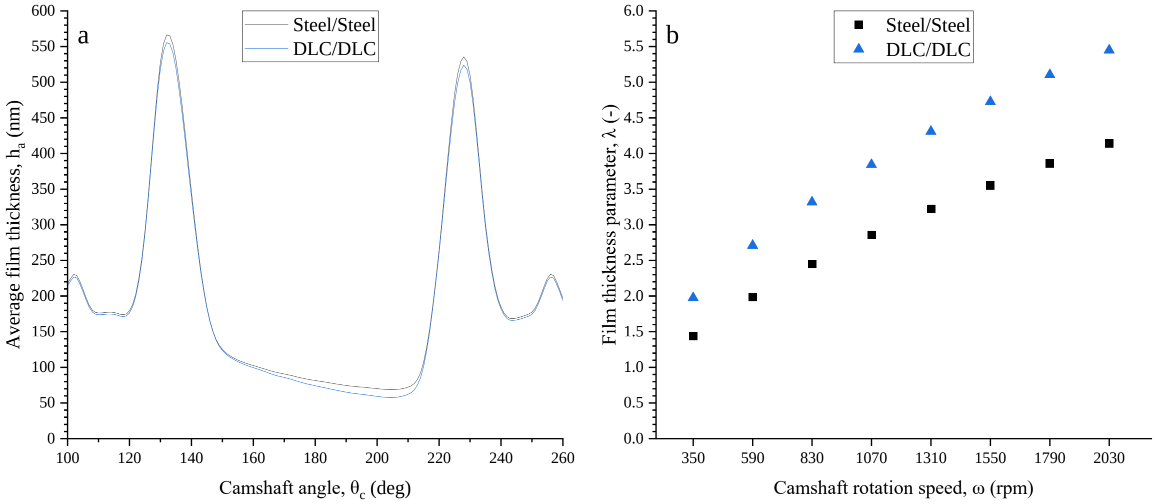

Figure 5.9: (a) Average film thickness variation with camshaft rotation angle for steel/steel and DLC/DLC configurations. The camshaft rotation speed is 1310 rpm for $T_0 = 50°C$. (b) Film thickness parameter variation with camshaft rotation speed for both steel/steel and DLC/DLC configurations.

5.2.5 Effects of DLC on heat flow in the cam-follower contact

The heat transfer in the lubricant and solids is influenced by the presence of thin film DLC coatings due to their low thermal conductivity. This section discusses the evacuation of the heat generated inside the lubricant (mainly due to shearing) by itself and through the solid/fluid interface at different operating conditions and surface configurations. The numerical results are exploited to quantify the heat transfer by calculating the power evacuated from the inside the contact in different directions. It should be mentioned that in the current cam-follower contact the width of the contact (in the y-direction) is $l = 0.012\ m$.

The heat transfer in the cam-follower contact is illustrated in Figure 5.10 where the distribution of the shear heat source Q_s in the lubricant is presented as a colored map. In addition, arrows illustrate the heat flows from the lubricant inside the contact to its surroundings. q_c, q_f, q_l, and q_r are the heat flows to the cam, the follower, the left and right of the contact respectively. On one hand, to calculate q_c and q_f, only the conductive heat flux is integrated over the lubricant/solid interfaces between $x = -a_{ref}^{1D}$ and $x = +a_{ref}^{1D}$. In this case, convective heat flux is assumed null due to the no-slip boundary condition. On the other hand, to calculate q_l and q_r only the convective heat flux is integrated over the deformed thickness at $x = -a_{ref}^{1D}$ and $x = +a_{ref}^{1D}$ respectively. In this case, heat transfer by conduction is negligible compared to convection. The results of integrating the heat fluxes are initially expressed in $[W/m]$ and should be multiplied by the cam-follower contact the width $l = 0.012\ m$ (in the y-direction) to obtain the final values of heat flows q_c, q_f, q_l, and q_r expressed in $[W]$.

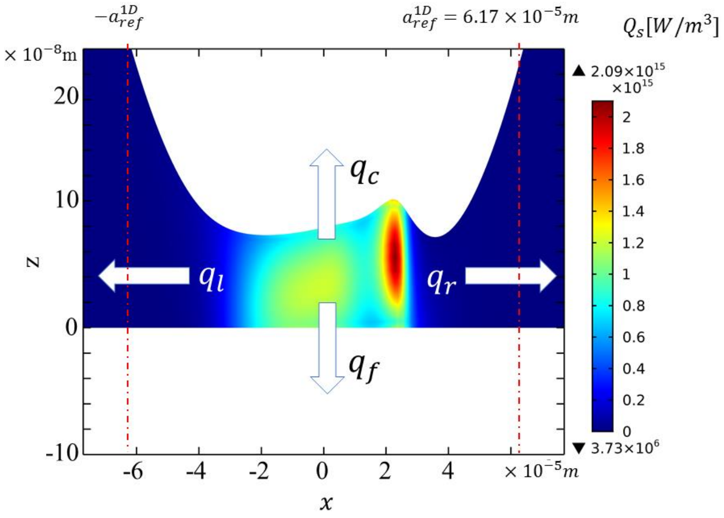

Figure 5.10: Distribution of shear heating source in the lubricant of a simulation at $T_0 = 50°C$, a steel/steel configuration, a rotation speed of 1310 rpm, and $\theta_c = 180°$. The arrows illustrate the heat flow in the system.

In the example shown in Figure 5.10 (i.e. steel/steel configuration, a rotation speed of 1310 rpm, and $\theta_c = 180°$) the values of heat flow are the following:

$$q_c = 33.26\ W \qquad q_f = 25.93\ W \qquad q_l = -0.043\ W \qquad q_r = 0.106\ W$$

The heat evacuated to the cam is higher than the one evacuated to the follower because the surface velocity of the cam is higher than that of the follower (see Figure 5.1). The majority of the heat generated in the contact flows by conduction to the solids compared to convection in the lubricant. Moreover, the negative value of q_l indicates that a small amount of heat flows into the contact from the left side (opposite direction to the arrow).

Heat flows are calculated for all camshaft rotation angles for a rotation speed of 1310 rpm and all surface configurations. Figure 5.11 show the variation of heat flows to the cam and follower respectively in (a) and (b) for different surface configurations.

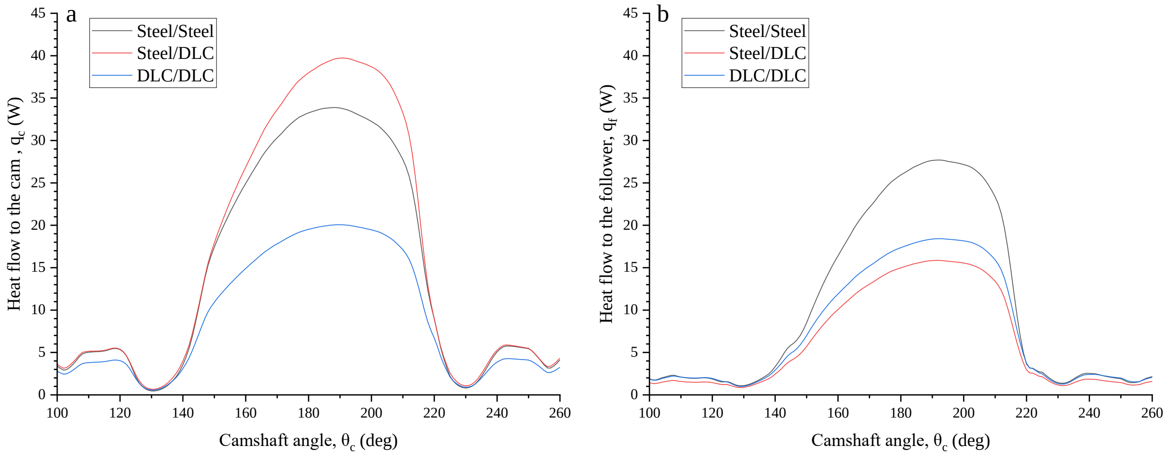

Figure 5.11: Variation of heat flows to the cam and follower respectively in (a) and (b) with camshaft rotation angle for $T_0 = 50°C$, and a rotation speed of 1310 rpm. Different colors correspond to different surface configurations.

The heat flow to solids increases under opposite sliding conditions and during the phase where the maximum Hertzian pressure is highest regardless of the surface configuration. However, the values of heat flow are different for different surface configurations. When the cam and follower are DLC-coated (i.e. DLC/DLC) the resulting heat flow to both components is lower compared to steel/steel configuration. Furthermore, an interesting mechanism is observed in Figure 5.11a for the configuration with DLC-coated follower (i.e. steel/DLC) where more heat flows to the steel cam in this configuration than in the uncoated configuration. This is because in the steel/DLC configuration heat generated in the lubricant cannot easily flow to the follower due to the thermal insulating effect of the DLC coating (q_f is lowest for steel/DLC configuration in Figure 5.11b), instead, heat is evacuated by the cam.

The sum of the quantities q_c, q_f, q_l, and q_r gives the total heat flow generated in the contact and is denoted by q_{tot}. The variation of q_{tot} with the camshaft rotation angle is presented in Figure 5.12 for different surface configurations.

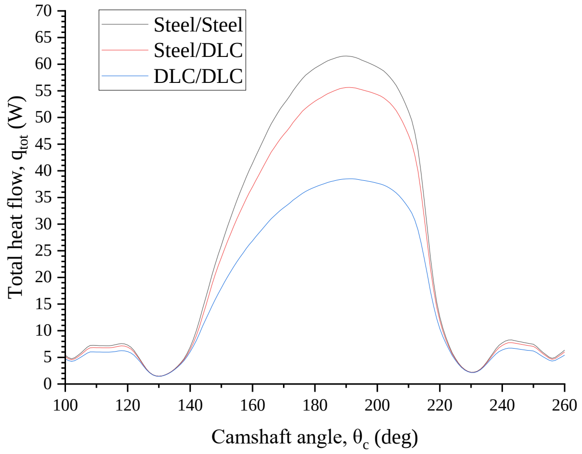

Figure 5.12: Variation of the total heat flow q_{tot} with the camshaft rotation angle for $T_0 = 50°C$, and a rotation speed of 1310 rpm. Different colors correspond to different surface configurations.

Figure 5.12 indicates that coating both the cam and the follower leads to a 37% decrease in maximum heat flow whereas coating only the follower leads to a 10% decrease compared to the uncoated steel/steel configuration.

So far, the effect of DLC-coating on heat flow is discussed for a single rotation speed (i.e. 1310 rpm). To extend the analysis to other speeds, the overall total heat flow is defined in (5.2) for each rotation speed.

$$q_{tot}^{*} = \frac{\int_{0}^{\Delta t} q_{tot}\, dt}{\Delta t} \qquad (5.2)$$

where q_{tot} is the instantaneous total heat flow assumed to be null during the cycle where there is no contact between the cam and the follower (i.e. $\theta_c < 100°$ and $\theta_c > 260°$), and Δt is the duration of one complete cycle computed for a given camshaft rotation speed as $\Delta t = \frac{60}{\omega}$ where ω is expressed in rpm. The integral in (5.2) is computed numerically using the trapezoidal rule.

Figure 5.13 variation of the overall total heat flow with the camshaft rotation speed for different surface configurations obtained by simulations at $T_0 = 50°C$.

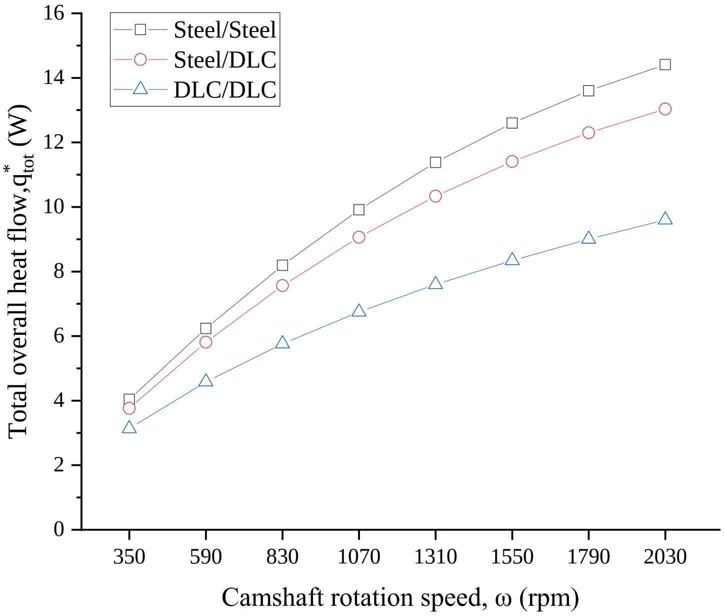

Figure 5.13: Variation of the overall total heat flow q_{tot}^{*} with the camshaft rotation speed for different surface configurations (different colors) obtained by simulations at $T_0 = 50°C$.

q_{tot}^{*} increase with increasing camshaft rotation speed. As mentioned previously, a higher camshaft rotation speed translates to higher surface velocities (see Figure 5.1). Hence, the entrainment velocity increases and leads to more shear heating (see the diagram in Figure 3.24). Also, the higher surface velocity contributes to greater heat flow from the lubricant to the bulk solids.

The DLC/DLC configuration significantly decreases the total overall heat flow compared to steel/steel due to the thermal insulation effect. The steel/DLC configuration also decreased q_{tot}^{*} but to a lesser extent. The thermal insulation effect becomes more important at higher rotation speeds. This supports the idea of using DLC coating for its thermal properties in applications the contact operates at high speeds as in motorsport for example.

Up to this point, experimental results on the Monocam test rig were not exploited in the discussion of the effect of DLC coating on the cam-follower contact. In the next section, experimental and numerical results of friction are used to reveal the role of DLC coatings over a wide range of camshaft rotation speeds.

5.2.6 Effects of DLC on mean friction coefficient

Figure 5.14 compares mean friction coefficient variation with camshaft rotation speed for different surface configurations at the intermediate temperature ($T_{in} = 50 \pm 1°C$ and $T_0 = 50°C$). Results obtained experimentally and numerically are presented in (a) and (b) respectively. In addition, results at different temperatures are discussed in Appendix G about the influence of the inlet temperature.

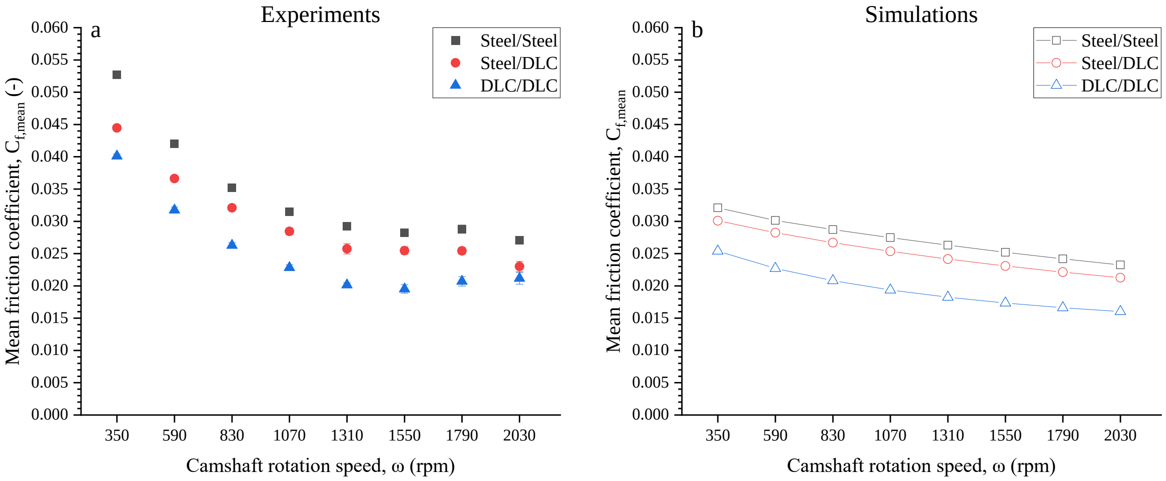

Figure 5.14: Comparison of mean friction coefficient variation with cam rotation speed for different surface configurations. Results obtained experimentally ($T_{in} = 50 \pm 1°C$) and numerically ($T_0 = 50°C$) are plotted in (a) and (b) respectively.

In experiments and simulations, for all rotation speeds, the mean friction coefficient is lowest for the DLC/DLC configuration and highest for the steel/steel configuration. The steel/DLC configuration results in intermediate friction compared to the other configurations.

The average percentage reduction in mean friction coefficient over all rotation speeds due to DLC coating is about 32 % and 27 % respectively in experiments and simulations. These values are similar to friction reduction found in Chapter 4 at high sliding when a DLC coating is applied to a cylinder-on-plane contact (30 % reduction at $SRR = 4$). Friction reduction by DLC coating is not only achieved under full film conditions (i.e. high rotation speed) due to thermal insulation but also in mixed lubrication regimes. This observation is in agreement with recent studies on DLC coating effects in cam-tappet contacts [124,171] and can be attributed mainly to three mechanisms:

- The decrease in friction due to DLC coating is, in part, caused by the DLC-coated contacts out-performing traditional uncoated steel contacts in terms of asperity (or boundary) friction. Friction coefficient measurements for different configurations were performed at HEF Groupe under a boundary lubrication regime with the same lubricant used in the current study and a similar DLC coating.

These reveal that the in a steel/steel configuration the friction coefficient is 0.12-0.13 whereas in a DLC/DLC configuration, the friction coefficient is 0.10-0.11.

- Figure 5.9b revealed that at any rotation speed, the DLC-coated contact operates with a higher λ. This is due to the lower roughness of the DLC-coated surfaces. Thus, for a given rotation speed, the DLC-coated contact operates in a regime closer to full-film lubrication than an uncoated contact.
- The two mechanisms mentioned above could not be numerically modeled in the current numerical approach because of the assumptions of smooth surfaces and full-film lubrication. In contrast, the thermal effects are considered. Hence, the decrease of the simulated mean friction coefficient in Figure 5.14b can only be attributed to the thermal insulation effect of DLC coatings. This mechanism was discussed in detail in section 4.2 of the previous chapter.

The three mechanisms mentioned here contribute to friction reduction by DLC coating. However, the influence of the third mechanism (i.e. thermal insulation) increases at high rotation speed due to the shift in lubrication toward the full-film regime. This will become clearer in section 5.2.7. Furthermore, numerical results in Figure 5.14b show that a relatively small reduction in mean friction is achieved when only the follower is coated (compared to DLC/DLC configuration). This indicates that the thermal insulation effect is not very efficient when the cam is uncoated. According to the findings in section 5.2.5, the values of total heat flow out of the contact are close for steel/steel and steel/DLC configurations.

Influence of inlet temperature on friction reduction

In this section, results of the mean friction coefficient at different inlet lubricant temperatures are explored: 25 ± 2 °C (unregulated in a room at $20 \pm 0.5^\circ C$), and $77 \pm 1^\circ C$ (regulated).

Figure 5.15 presents comparisons of the mean friction coefficient obtained experimentally from tests with different surface configurations. Results from tests at low and high inlet temperatures are shown in (a) and (b) respectively. In addition, numerical results are presented in subfigure (b) for $77^\circ C$.

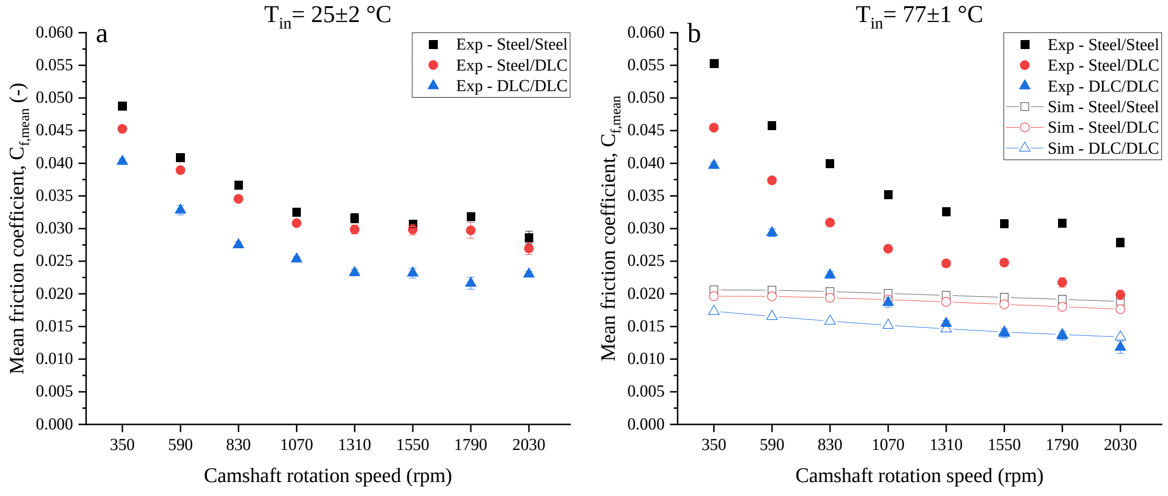

Figure 5.15: Comparison of mean friction coefficient variation with cam rotation speed for different surface configurations at (a) $T_{in} = 25 \pm 2^\circ C$ and (b) $T_{in} = 77 \pm 1^\circ C$.

Similar to the tests at $T_{in} = 50 \pm 1°C$, the DLC-coating leads to a reduction in the mean friction coefficient at a given rotation speed. The reduction is more significant at a higher lubricant inlet temperature. For instance, average percentage mean friction coefficient reductions by coating both sides of the contact are about 23% and 48% respectively for low and high lubricant inlet temperatures.

Results shown in Figure 9 of reference [171] demonstrate that the major part of friction reduction by DLC coating is due to the difference in asperity friction between uncoated surfaces and DLC-coated surfaces, while reduction due to thermal insulation is less significant. At high temperature the film thickness is greatly reduced and asperity contact increase such that the friction response is mostly controlled by the solid friction according to Lyu et al. [171]. This and the lower roughness of DLC-coated surfaces explain the observation in Figure 5.15 where friction reduction is more significant at a high temperature compared to a low temperature. In the current cam-follower contact the film thickness parameter λ is calculated based on numerical film thickness results at inlet lubricant temperature $T_0 = 77°C$ for different surface configurations. For the steel/steel configuration, λ varied between 0.8 and 2.4 for rotation speeds 350 rpm and 2030 rpm respectively. Moreover, for the DLC/DLC configuration, the range of λ was 1.1-3.2. For reference, at $T_0 = 50°C$, the ranges of λ were 1.4-4.1 and 2-5.4 for steel/steel and DLC/DLC configurations respectively. The large discrepancy in numerical predictions at high temperature highlight the limitation of the numerical approach which is not adapted for contacts operating under mixed lubrication regime.

Next, the effects of DLC coating on friction power loss are investigated.

5.2.7 Effects of DLC on friction power loss

The camshaft torque signals recorded during the tests on the Monocam test rig can be converted to instantaneous friction force following the procedure in Appendix B. For each rotation speed, the friction power loss P_f over one rotation cycle is given by (5.3).

$$P_f = \frac{W_f}{\Delta \mathrm{t}} = \frac{\int_0^{\Delta t} F_f(u_1 - u_2)\, dt}{\Delta \mathrm{t}} \tag{5.3}$$

where W_f is the friction work due to the friction force F_f acting on the sliding surfaces that is calculated from camshaft torque measurements, with $F_f = 0$ when there is no contact between the cam and the follower. u_1 and u_2 are the surface velocities of the cam and the upper pad of the follower respectively, and Δt is the duration of one complete cycle. The integral in (5.3) is computed numerically using the trapezoidal rule.

The friction work W_f calculated from experimental measurements includes contributions from fluid friction work (due to shearing of the fluid) and kinetic friction of direct asperity contact between the surfaces. In simulations, the fluid friction work is equivalent to the total heat energy dissipated from the contact to its surroundings. In other words, the overall total heat flow calculated numerically (in section 5.2.5) is a part of the friction power loss calculated experimentally. The variations of both of these quantities with the camshaft rotation speed are shown in Figure 5.16a for different surface configurations (indicated by different colors) at the inlet temperature $T_{in} = 50 \pm 1°C$ and $T_0 = 50°C$ in experiments and simulations respectively.

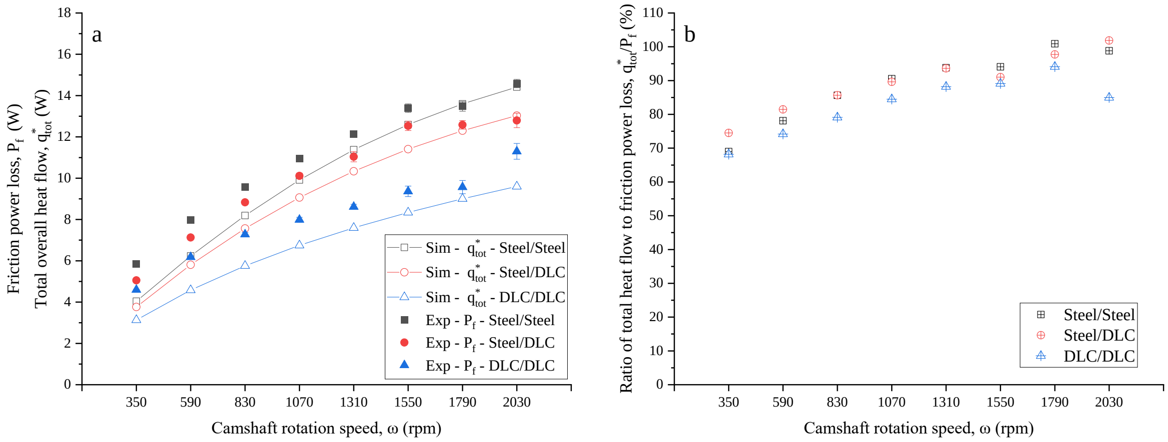

Figure 5.16: (a) Friction power loss variation with camshaft rotation speed obtained from experimental measurements (filled symbols) and variation of total overall heat flow out of the contact obtained numerically (empty symbols). (b) Variation of the ratio $\frac{q_{tot}^*}{P_f}$ with camshaft rotation speed. Results correspond to $T_{in} = 50 \pm 1°C$ and $T_0 = 50°C$. Different surface configurations are presented in different colors.

The friction power loss at a given camshaft rotation speed is reduced by the presence of a DLC-coated surface. Coating both the cam and the follower leads to a more significant decrease than coating only the follower. A similar observation is made for total heat overall heat flow obtained numerically.

The ratio of the overall heat flow over the friction power loss, $\frac{q_{tot}^*}{P_f}$, indicates how much the fluid friction obtained numerically contributes to the friction power loss obtained experimentally. The variation of this ratio with the camshaft rotation speed is plotted in Figure 5.16b for different surface configurations. Results show that for all surface configurations, the ratio $\frac{q_{tot}^*}{P_f}$ increases with increasing rotation speed. This is not surprising because as the rotation speed increases the film thickness parameter λ also increases and the lubrication shifts more toward the full-film regime.

Influence of inlet temperature on friction power loss reduction

The method used to calculate friction power loss from measurements at $T_{in} = 50 \pm 1°C$ is also used for different inlet temperatures $T_{in} = 25 \pm 2°C$ and $77 \pm 1°C$. Figure 5.17 shows the friction power loss obtained from experiments at different temperatures, for different surface configurations and three rotation speeds (350, 1310, and 2030 rpm).

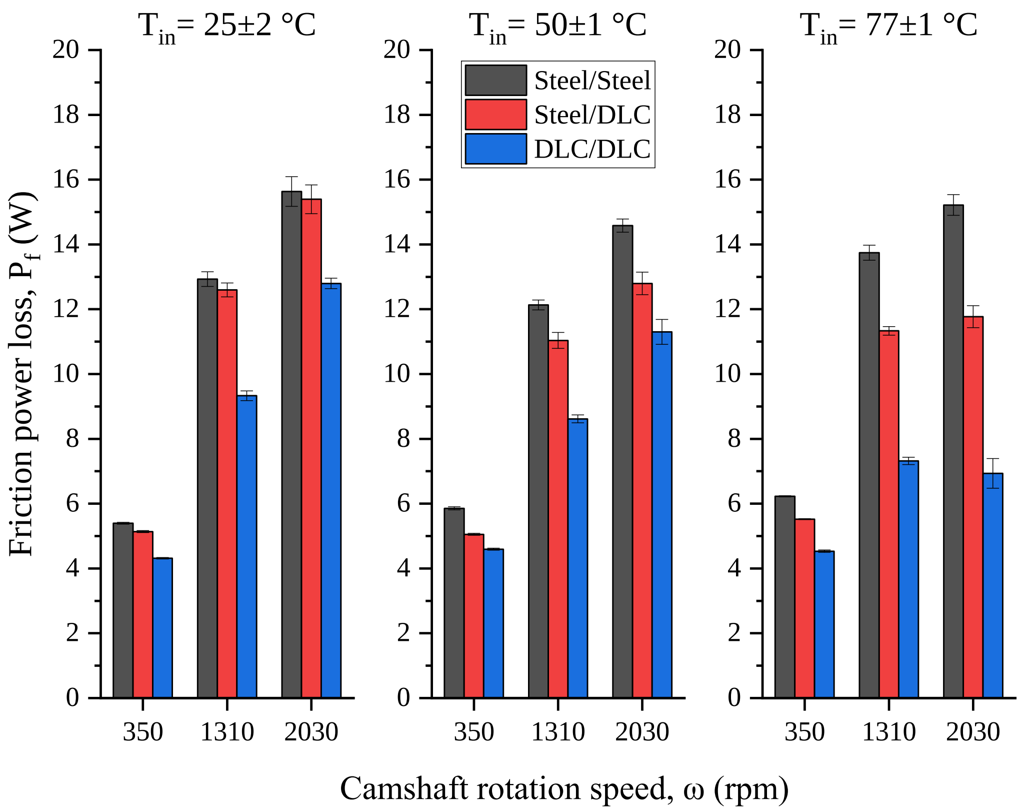

Figure 5.17: Friction power loss P_f for different surface configurations at different rotation speeds for different lubricant inlet temperatures.

In all cases, having at least one DLC-coated surface reduces friction power loss. The most advantageous use of DLC-coating is at a high inlet temperature. In contrast, at a low temperature, coating only the follower has a minor effect on friction power loss. Ranges of percentage reductions in friction power loss by DLC coating are grouped in the following Table 5.3.

Table 5.3: Percentage reductions in friction power loss for DLC-coated configurations compared to steel/steel configuration at different lubricant inlet temperatures

Inlet temperature, T_{in}	**Percentage reduction in friction power loss**	
	Steel/DLC	DLC/DLC
$25 \pm 2\,°C$	Up to 5%	18-30%
$50 \pm 1\,°C$	6-14%	22-30%
$77 \pm 1\,°C$	11-23%	27-54%

5.2.8 Effects of DLC coating on surface wear

In addition to their advantage in terms of low asperity friction and low fluid friction, the DLC coatings provide wear resistance to surfaces [96]. The state of the surface of the upper pad of the follower and the cam are examined after the experimental campaign presented in this chapter.

Figure 5.18 and Figure 5.19 group photographs of the surfaces of followers and cams respectively. Photographs are taken at positions “a” and “b” illustrated on the upper pad of the follower and the cam drawing in Figure 5.18 and Figure 5.19 respectively. Images corresponding to the uncoated and DLC-coated follower are presented on the left and right respectively. On the upper pad of the follower, position “a” corresponds to the middle of the contact zone whereas “b” corresponds to the left edge of this zone. Moreover, on the cam surface, position “a” corresponds to the nose of the cam whereas “b” corresponds to the edge of the contact zone.

On one hand, the steel surfaces of the follower and the cam suffered from abrasive wear during the experiments as shown in subfigure (a1) and (b1) of Figure 5.18 and Figure 5.19. Moreover, brown shades are visible when looking more closely at subfigure (c) of Figure 5.18. These are caused by the tribofilm resulting from chemical reactions between the steel surface and the anti-wear additives of the lubricant. In general, the films are beneficial for protecting the surfaces under severe conditions (i.e. mixed or boundary lubrication regimes). Linear grooves on the surface of the upper pad of the follower are typically caused by three-body abrasive wear due to the passage of detached solid particles between the two contacting surfaces.

In subfigures (b1) and (d) of Figure 5.18 a clear distinction is visible between the zones of the follower reached or not by the contact during the rotation cycle. The left zone of subfigure (d) is intact reflecting the initial state of the surface before the tests. In contrast, the right zone of subfigure (d) indicates that the steel surfaces underwent wear during the tests. A similar distinction is observed at the edge of the contact zone in subfigure (b1) of Figure 5.19 where wear scars are seen on the right of the contact zone boundary.

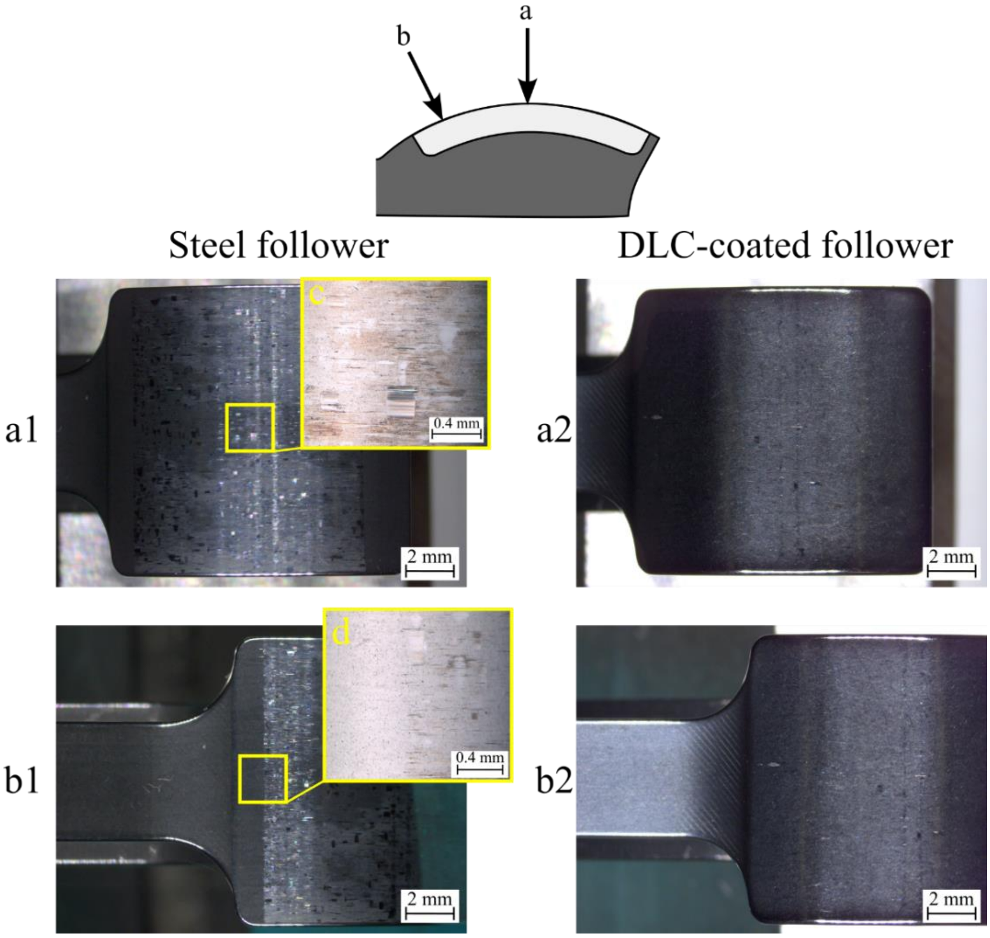

Figure 5.18: Photographs of the upper pad of the followers (uncoated steel on the left; DLC-coated on the right) after the experimental campaign. Images are taken perpendicular to the surface at positions a and b illustrated above. Zoomed in views are highlighted in yellow.

On the other hand, the DLC-coating show minor scratches and faded boundary on the left edge of the contact zone in subfigure (b2) of both Figure 5.18 and Figure 5.19.

The surface analysis provided in this section indicates that DLC-coated surfaces are more resistant to wear under the tested conditions compared to uncoated surfaces. This lowers the surface roughness after the tests. At the same time, the DLC coating attenuates the viscosity wedge under opposite sliding conditions (as demonstrated in Chapter 4 and section 5.2.4) leading to lower film thickness under a full-film lubrication regime. The reduction in surface roughness dominates the decrease in film thickness which increases the film thickness parameter λ defined in (5.1) and shift the lubrication more towards the full-film regime.

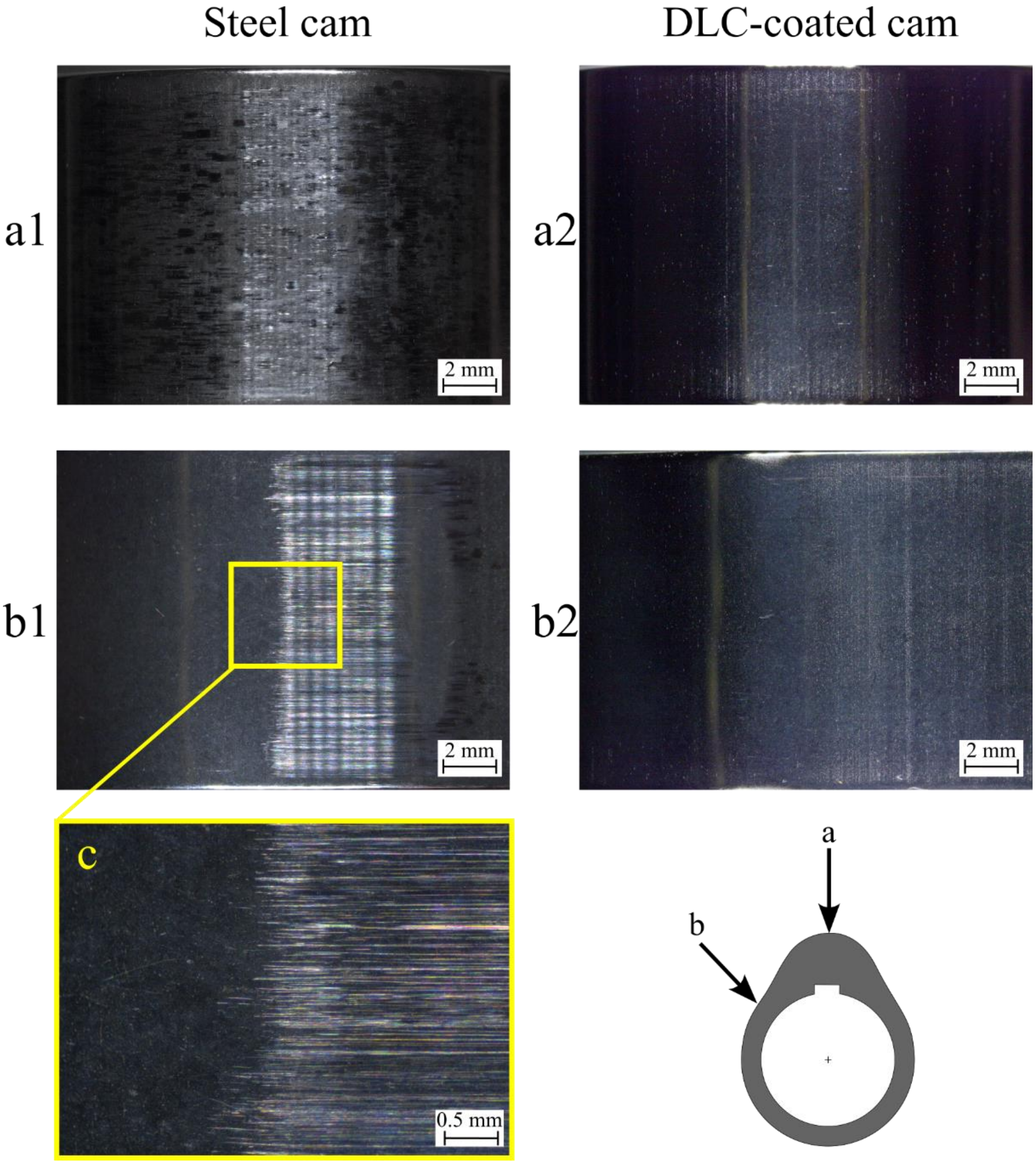

Figure 5.19: Photographs of the surface of the cam (uncoated steel on the left; DLC-coated on the right) after the experimental campaign. Images are taken perpendicular to the surface at positions a and b. One zoomed-in view is highlighted in yellow.

5.3 Conclusion

In this chapter, the effects of DLC coating on tribological performances were discussed based on experimental results from tests on the Monocam test rig and numerical results from transient TEHL simulations of cam-follower contact. Operating conditions covered a wide range of camshaft rotation speeds ($350 - 2030\,rpm$), three surface configurations (steel/steel, steel/DLC, and DLC/DLC), and different inlet lubricant temperatures ($25°C$, $50°C$, and $77°C$).

The numerical model gives access to the film thickness variation so the film thickness parameter λ is calculated based on numerical results and roughness measurements after the experiments on the Monocam test rig. The range of λ suggests that the cam follower contact operates between mixed and full-film lubrication at the intermediate temperature (i.e. $50°C$).

Results showed that the numerical approach can predict friction at $50°C$ within an acceptable error ($\sim$13% underestimation on average) at high rotation speeds ($\omega \geq 1310\,rpm$) for all surface configurations. In contrast, due to the limitation of the model that only simulates full-film lubrication regimes, the prediction error reached around 40% at the lowest rotation speed ($350\,rpm$). At low rotation speed, the friction response is mainly dictated by asperity friction rather than fluid friction. Thus, the numerical model is not adapted to this condition.

Experiments show that under a full-film or mixed lubrication regime, the DLC-coated contact performed better than the uncoated contact in terms of reduction in friction coefficient and power loss. This is due to the contribution of three mechanisms: low asperity friction of DLC, higher film thickness parameter (under equivalent conditions), and thermal insulation effect. For instance, at an inlet temperature $T_{in} = 50°C$, the reduction in friction power loss due to coatings on both surfaces ranges between 22 % and 30 % depending on the camshaft rotation speed. This reduction was amplified at a higher lubricant temperature.

Furthermore, the use of DLC coating as a wear-resistant coating is demonstrated by a comparison of surface profiles for different followers and cams used during the experimental campaign described in this chapter. The uncoated steel surfaces showed significant wear scars whereas the DLC-coating was almost intact even though they endured the same test conditions.

Chapter 6: General Conclusion

In this final chapter, a summary of the main research findings is provided, in alignment with the initial research objectives. Furthermore, the chapter will emphasize the significance and contribution of these findings to the field of tribology. It will also review the limitations of this study and provide perspectives for future research.

In internal combustion engines, reducing friction and wear of lubricated contacts increases the overall energy efficiency and lifespan of engine components. DLC coatings gained popularity in tribological applications in recent years due to their ability to reduce friction and wear. On the other hand, replacing a conductive steel surface with an insulating DLC-coated surface could significantly change the heat transfer in the lubricant film and the surfaces under high sliding applications such as the cam-follower contact.

The primary objective of this thesis is to deepen the knowledge of thermal effects occurring in EHL contacts under high sliding conditions, with a specific emphasis on investigating the role of thermally insulating DLC coatings.

The first chapter of this thesis introduces the general context of this research. Moreover, some experimental and numerical advances in the field of EHL contacts are presented in addition to an overview of thin-film DLC coatings.

The experimental and numerical approaches used throughout this study are detailed in Chapter 2. On one hand, experimentally, a barrel-on-disk tribometer is employed. It can simultaneously measure the lubricant film thickness and friction coefficient in a wide elliptical contact. In addition, a single cam-follower-valve test rig investigates the friction response of different surface configurations (uncoated and DLC-coated components) by mimicking real cam-follower contact geometry and operating conditions. On the other hand, a finite element model is used to complete and confront the experimental measurements. This includes thermal effects and accounts for coated surfaces. Moreover, the shear-thinning behavior of the commercial engine oil used in this work is considered in the numerical model and is characterized by an independent rheometer.

6.1 Main Contributions

This work brings forth several contributions to the field of EHL contacts operating under very high (opposite) sliding conditions, involving surfaces coated with thin thermally insulating films.

In the literature, the investigations of EHL contacts are usually limited to either film thickness or friction. Moreover, these quantities are seldom studied over a wide range of sliding conditions. Chapter 3, aims to simultaneously investigate film thickness and friction in a wide elliptical contact by a dual experimental-numerical approach from pure rolling to opposite sliding conditions. Findings highlight the ability of the quantitative EHL modeling approach to predict both film thickness and friction, especially when operating under opposite sliding conditions. Furthermore, the effects of varying the operating conditions are explored and a semi-analytical expression is proposed for predicting minimum film thickness in a line contact, for the first time, over a wide range of sliding conditions ($0 \leq SRR \leq 4$).

Mechanisms of friction reduction by thermally insulating coatings are already explored in previous studies, however, the effects of such coatings on film thickness under opposite sliding conditions are overlooked. Chapter 4 aims to deepen the understanding of the thermal effects of thermally insulating coating on film thickness and friction simultaneously in an EHL contact, especially at high sliding. The mechanisms of friction and film thickness reductions in coated contacts are explored. Results suggest that under opposite sliding conditions ($SRR > 2$), this reduction in friction due to the thermal insulation effect is accompanied by a decrease in the lubricant film thickness due to an attenuation of the viscosity wedge effect. Thus, when using thermally insulating coatings to reduce friction, one needs to be mindful that the film thickness can also decrease, and consequently, the lubrication regime can switch to mixed lubrication where friction may increase due to asperity contact. Which ultimately defies the reason for applying a thermally insulating coating in the first place. Moreover, the influence of coating thermal conductivity and thickness is investigated. Semi-analytical expressions of correction factors for film thickness and friction coefficient at high sliding are proposed.

Chapter 5 is an application-oriented study that focuses on the effects of DLC coatings on the tribological performances of a cam-finger follower contact. Experiments are realized on a test rig mimicking the geometry and operating conditions of real engine components. In addition, simulations were realized using a transient quantitative TEHL approach. Numerical results suggest that under most operating conditions (low to intermediate rotation speed, and intermediate to high temperature) the contact operates in the mixed lubrication regime. However, in the case of DLC-coated surfaces friction stays smaller than with steel surfaces. This phenomenon is explained by the low asperity contact friction with DLC compared to conventional steel-steel contacts. Furthermore, DLC coatings provided higher wear resistance compared to steel surfaces under the same operating conditions. The use of DLC coatings shifts the lubricated contact to the mixed lubrication regime “earlier”, but the material characteristics of DLC generate both less friction and less wear than the steel-steel contact.

6.2 Limitations

The two experimental setups used in the current study have their limitations. On one hand, the barrel-on-disk tribometer enables the simultaneous measurement of friction coefficient and lubricant film thickness with the constraint of using transparent disks required for film thickness measurements by an optical technique called Differential Colorimetric Interferometry (DCI). Thus, testing surface configurations such as DLC-coated steel disk and barrel was not possible – instead, a sapphire disk coated with a transparent DLC was used. Furthermore, the current setup lacks a precise measurement of the temperature of the lubricant entering the contact. On the other hand, the single cam-follower-valve test rig enables the direct measurement of camshaft torque. Moreover, to extract friction coefficient results, a simplified dynamic analysis of the mechanism with many assumptions is used which added a layer of uncertainty to these experimental results.

The numerical approach also has some limitations. Although the lubricant is characterized by independent rheological measurements, the description of its behavior in the numerical model still lacks consideration of the so-called “limiting shear stress” effect. Under rolling-sliding conditions ($0 \leq SRR \leq 2$), the numerical model was unable to accurately predict the friction response in highly-loaded cases.

The thermal environment of the real contact is much more complicated than the one modeled here with constant imposed temperature. Several thermal models involving different scales should be considered to capture the temperature change at the inlet of the contact under high sliding.

6.3 Perspectives for Future Research

The current work filled some of the gaps in the literature concerning friction and film thickness in thermal-EHL contacts under high sliding conditions and the thermal effect of insulating coating. However, some questions remain unanswered and constitute good starting point for future research.

- Finite element EHL models such as the one used in this study can be completed with a deep understanding and accurate description of the limiting shear stress effect. To achieve this, an out-of-contact independent rheological characterization could be coupled with molecular dynamic simulation to create rheological models able to capture the friction plateau at moderate shear, depending on pressure and temperature [150].
- Adding an asperity contact model similar to the one used by Marian et al. [124] will probably result in predictions closer to reality in the cases where mixed lubrication occurs. However, one needs to be careful in choosing the "asperity contact friction coefficient" which is influenced by operating conditions, lubricant additives, the type of contact surfaces, etc. Thus, more research is needed at the scale of asperity contacts in terms of the deformation of individual asperities and the friction at this scale where the chemical composition of the lubricant and its interaction with the surfaces cannot be overlooked.
- The semi-analytical expressions created in the current work are applicable in a limited range of operating conditions and for one specific lubricant. Hence, more comprehensive numerical studies spanning other operating conditions and lubricants are needed to create more general expressions by the same methodology developed here.
- The numerical approach used in the current work and the semi-analytical expressions could be integrated with dynamic simulations to provide a better description of the full-scale behavior of complex systems such as the cam-follower-valve mechanism. Which ultimately can accelerate the design and optimization phases of such systems.

In conclusion, this thesis has contributed to the field of tribology by addressing key gaps in the literature and advancing the understanding of various effects influencing the performance of lubricated contacts. Through experimentation and numerical simulations, significant insights have been gained into the behavior of Thermal-EHL contacts especially those operating under opposite sliding conditions and with thermally insulating coated surfaces. The findings presented here are not limited to the context under which they were developed (i.e. cam-follower contact). They can be helpful for other applications where friction and wear of lubricated contacts is a concern, e.g. future combustion engines with alternative fuels, electric cars, bearings, biomedical applications, etc.

Bibliography

[1] EU economy and society to meet climate ambitions. European Commission - European Commission n.d. http://ec.europa.eu/commission/presscorner/detail/en/IP_21_3541 (accessed January 9, 2023).

[2] Yang Z, Rutherford D. Japan 2030 fuel economy standards. International Council on Clean Transportation 2019. https://theicct.org/publication/japan-2030-fuel-economy-standards/ (accessed January 9, 2023).

[3] Environmental Protection Agency. The Safer Affordable Fuel Efficient (SAFE) Vehicles Final Rule for Model Years 2021-2026 2020. https://www.epa.gov/regulations-emissions-vehicles-and-engines/safer-affordable-fuel-efficient-safe-vehicles-final-rule (accessed January 9, 2023).

[4] Jost P. Lubrication (Tribology)–A report on the present position and industry's needs. Department of Education and Science, HM Stationary Office, London, UK 1966.

[5] Holmberg K, Erdemir A. Influence of tribology on global energy consumption, costs and emissions. Friction 2017;5:263–84. https://doi.org/10.1007/s40544-017-0183-5.

[6] Holmberg K, Andersson P, Erdemir A. Global energy consumption due to friction in passenger cars. Tribology International 2012;47:221–34. https://doi.org/10.1016/j.triboint.2011.11.022.

[7] Holmberg K, Erdemir A. The impact of tribology on energy use and CO2 emission globally and in combustion engine and electric cars. Tribology International 2019;135:389–96. https://doi.org/10.1016/j.triboint.2019.03.024.

[8] Ciechanowski B. Internal Combustion Engine 2021. https://ciechanow.ski/internal-combustion-engine/ (accessed May 11, 2023).

[9] Hayakawa S, Ogiyama K, Tate M. Development of Valvetrain for Formula One Engine 2009.

[10] Raisin J, Fillot N, Vergne P, Dureisseix D, Lacour V. Transient Thermal Elastohydrodynamic Modeling of Cam–Follower Systems: Understanding Performance. Tribology Transactions 2016;59:720–32. https://doi.org/10.1080/10402004.2015.1110865.

[11] Geoffroy B. Distribution à soupapes. Machines hydrauliques, aérodynamiques et thermiques, 1995.

[12] Stribeck R. Ball bearings for various loads. Trans ASME 1907;29:420–63.

[13] Wang Y, Wang QJ, Lin C, Shi F. Development of a Set of Stribeck Curves for Conformal Contacts of Rough Surfaces. Tribology Transactions 2006;49:526–35. https://doi.org/10.1080/10402000600846110.

[14] Gohar R, Rahnejat H. Fundamentals Of Tribology (Third Edition). World Scientific; 2018.

[15] Reynolds O. IV. On the theory of lubrication and its application to Mr. Beauchamp tower's experiments, including an experimental determination of the viscosity of olive oil. Philosophical Transactions of the Royal Society of London 1886;177:157–234. https://doi.org/10.1098/rstl.1886.0005.

[16] Kingsbury A. Experiments with an Air-Lubricated Journal. Journal of the American Society for Naval Engineers 1897;9:267–92. https://doi.org/10.1111/j.1559-3584.1897.tb05692.x.

[17] Michell A. The Lubrication of Plane Surfaces. Zeitschrift Fur Angewandete Mathematik Und Physik 1905;52:123–37.

[18] Ertel A. Hydrodynamic Lubrication Based on New Principles. Akad Nauk SSSR Prikadnaya Mathematica i Mekhanika 1939;3:41–52.

[19] Barus C. Isothermals, isopiestics and isometrics relative to viscosity. American Journal of Science 1893;s3-45:87–96. https://doi.org/10.2475/ajs.s3-45.266.87.

[20] Cameron A. Righting a 40-year-old wrong: AM Ertel—the true author of ’Grubin ehl’solution. Tribology International 1985;18:92.

[21] Grubin AN, Vinogradova IE. Investigation of the contact of machine components. Moscow: Central Scientific Research Institute for Technology and Mechanical Engineering; 1949.

[22] Dowson D, Higginson GR. A Numerical Solution to the Elasto-Hydrodynamic Problem. Journal of Mechanical Engineering Science 1959;1:6–15. https://doi.org/10.1243/JMES_JOUR_1959_001_004_02.

[23] Dowson D. ELASTO-HYDRODYNAMIC LUBRICATION: A SURVEY OF ISOTHERMAL SOLUTIONS. V o l 1962:6.

[24] Evans HP, Snidle RW. Inverse Solution of Reynolds’ Equation of Lubrication Under Point-Contact Elastohydrodynamic Conditions. Journal of Lubrication Technology 1981;103:539–46. https://doi.org/10.1115/1.3251733.

[25] Hamrock BJ, Dowson D. Isothermal Elastohydrodynamic Lubrication of Point Contacts: Part III—Fully Flooded Results. Journal of Lubrication Technology 1977;99:264–75. https://doi.org/10.1115/1.3453074.

[26] Chittenden RJ, Dowson D, Dunn JF, Taylor CM. A theoretical analysis of the isothermal elastohydrodynamic lubrication of concentrated contacts. I. Direction of lubricant entrainment coincident with the major axis of the Hertzian contact ellipse. Proc R Soc Lond A 1985;397:245–69. https://doi.org/10.1098/rspa.1985.0014.

[27] Lubrecht AA, Napel WE ten, Bosma R. Multigrid, an alternative method for calculating film thickness and pressure profiles in elastohydrodynamically lubricated line contacts. J TRIBOL-T ASME 1986;108:551–6. https://doi.org/10.1115/1.3261260.

[28] Venner CH, Napel WE ten. Multilevel solution of the elastohydrodynamically lubricated circular contact problem Part I: Theory and numerical algorithm. Wear 1992;152:351–67. https://doi.org/10.1016/0043-1648(92)90132-R.

[29] Venner CH, Napel WE ten. Multilevel solution of the elastohydrodynamically lubricated circular contact problem part 2: Smooth surface results. Wear 1992;152:369–81. https://doi.org/10.1016/0043-1648(92)90133-S.

[30] Habchi W. A full-system finite element approach to elastohydrodynamic lubrication problems : application to ultra-low-viscosity fluids. These de doctorat. Lyon, INSA, 2008.

[31] Wheeler J-D. Non-elliptical point contacts : The Torus-on-Plane conjunction. phdthesis. Université de Lyon, 2016.

[32] Raisin J, Fillot N, Dureisseix D, Vergne P, Lacour V. Characteristic times in transient thermal elastohydrodynamic line contacts. Tribology International 2015;82:472–83. https://doi.org/10.1016/j.triboint.2014.02.022.

[33] Raisin J, Fillot N, Vergne P, Dureisseix D. Numerical simulation of lubricated DLC-coated point contacts under infinite sliding conditions. Tribology International 2019;133:136–51. https://doi.org/10.1016/j.triboint.2018.12.032.

[34] Najji B, Bou-Said B, Berthe D. New Formulation for Lubrication With Non-Newtonian Fluids. J Tribol 1989;111:29–34. https://doi.org/10.1115/1.3261875.

[35] Marian M, Bartz M, Wartzack S, Rosenkranz A. Non-Dimensional Groups, Film Thickness Equations and Correction Factors for Elastohydrodynamic Lubrication: A Review. Lubricants 2020;8:95. https://doi.org/10.3390/lubricants8100095.

[36] Cameron A. The Viscosity Wedge. A S L E Transactions 1958;1:248–53. https://doi.org/10.1080/05698195808972337.

[37] Dyson A, Wilson AR. Film Thicknesses in Elastohydrodynamic Lubrication at High Slide/Roll Ratios. Proceedings of the Institution of Mechanical Engineers, Conference Proceedings 1968;183:81–97. https://doi.org/10.1243/PIME_CONF_1968_183_282_02.

[38] Yang P, Qu S, Chang Q, Guo F. On the Theory of Thermal Elastohydrodynamic Lubrication at High Slide-Roll Ratios—Line Contact Solution. Journal of Tribology 2000;123:36–41. https://doi.org/10.1115/1.1330738.

[39] Guo F, Yang P, Qu S. On the Theory of Thermal Elastohydrodynamic Lubrication at High Slide-Roll Ratios—Circular Glass-Steel Contact Solution at Opposite Sliding. Journal of Tribology 2000;123:816–21. https://doi.org/10.1115/1.1330739.

[40] Kaneta M, Nishikawa H, Kanada T, Matsuda K. Abnormal Phenomena Appearing in EHL Contacts. Journal of Tribology 1996;118:886–92. https://doi.org/10.1115/1.2831624.

[41] Guo F, Wong PL, Yang P, Yagi K. Film Formation in EHL Point Contacts under Zero Entraining Velocity Conditions. Tribology Transactions 2002;45:521–30. https://doi.org/10.1080/10402000208982583.

[42] Yagi K, Kyogoku K, Nakahara T. Relationship Between Temperature Distribution in EHL Film and Dimple Formation. Journal of Tribology 2005;127:658–65. https://doi.org/10.1115/1.1866164.

[43] Bruyere V, Fillot N, Morales-Espejel GE, Vergne P. Computational fluid dynamics and full elasticity model for sliding line thermal elastohydrodynamic contacts 2011. https://doi.org/10.1016/j.triboint.2011.04.013.

[44] Meziane B, Vergne P, Devaux N, Lafarge L, Morales-Espejel GE, Fillot N. Film thickness build-up in zero entrainment velocity wide point contacts. Tribology International 2020;141:105897. https://doi.org/10.1016/j.triboint.2019.105897.

[45] Dowson D, Taylor CM, Zhu G. A transient elastohydrodynamic lubrication analysis of a cam and follower. J Phys D: Appl Phys 1992;25:A313–20. https://doi.org/10.1088/0022-3727/25/1A/047.

[46] Messé S, Lubrecht AA. Transient elastohydrodynamic analysis of an overhead cam/tappet contact. Proceedings of the Institution of Mechanical Engineers, Part J: Journal of Engineering Tribology 2000;214:415–25. https://doi.org/10.1243/1350650001543296.

[47] Wang J, Yang P. A Numerical Analysis for TEHL of Eccentric-Tappet Pair Subjected to Transient Load. Journal of Tribology 2003;125:770–9. https://doi.org/10.1115/1.1576425.

[48] Johnson KL, Tevaarwerk JL. Shear behaviour of elastohydrodynamic oil films. Proceedings of the Royal Society of London A Mathematical and Physical Sciences 1977;356:215–36.

[49] Bair S. A Traction (Friction) Curve Is Not a Flow Curve. Lubricants 2022;10:221. https://doi.org/10.3390/lubricants10090221.

[50] Bair S. Rheology and high-pressure models for quantitative elastohydrodynamics. Proceedings of the Institution of Mechanical Engineers, Part J: Journal of Engineering Tribology 2009;223:617–28. https://doi.org/10.1243/13506501JET506.

[51] Habchi W, Bair S, Vergne P. On friction regimes in quantitative elastohydrodynamics. Tribology International 2013;58:107–17. https://doi.org/10.1016/j.triboint.2012.10.005.

[52] Björling M, Luleå tekniska universitet, Institutionen för teknikvetenskap och matematik. Friction in Elastohydrodynamic Lubrication. Luleå tekniska universitet; 2014.

[53] Albahrani SMB, Philippon D, Vergne P, Bluet JM. A review of in situ methodologies for studying elastohydrodynamic lubrication. Proceedings of the Institution of Mechanical Engineers, Part J: Journal of Engineering Tribology 2016;230:86–110. https://doi.org/10.1177/1350650115590428.

[54] Lane TB, Hughes JR. A study of the oil-film formation in gears by electrical resistance measurements. Br J Appl Phys 1952;3:315–8. https://doi.org/10.1088/0508-3443/3/10/305.

[55] Furey MJ. Metallic Contact and Friction between Sliding Surfaces. A S L E Transactions 1961;4:1–11. https://doi.org/10.1080/05698196108972414.

[56] Lewicki W. Some physical aspects of lubrication in rolling bearings and gears. University of London (Birkbeck College); 1955.

[57] Crook AW. The lubrication of rollers. Philosophical Transactions of the Royal Society of London Series A, Mathematical and Physical Sciences 1958;250:387–409.

[58] Dyson A, Wilson AR. Paper 3: Film Thicknesses in Elastohydrodynamic Lubrication by Silicone Fluids. Proceedings of the Institution of Mechanical Engineers, Conference Proceedings 1965;180:97–112. https://doi.org/10.1243/PIME_CONF_1965_180_323_02.

[59] Hamilton GM, Moore SL. First Paper: Measurement of the Oil-Film Thickness between the Piston Rings and Liner of a Small Diesel Engine. Proceedings of the Institution of Mechanical Engineers 1974;188:253–61. https://doi.org/10.1243/PIME_PROC_1974_188_028_02.

[60] Heemskerk RS, Vermeiren KN, Dolfsma H. Measurement of Lubrication Condition in Rolling Element Bearings. A S L E Transactions 1982;25:519–27. https://doi.org/10.1080/05698198208983121.

[61] Jablonka K, Glovnea R, Bongaerts J. Evaluation of EHD films by electrical capacitance. J Phys D: Appl Phys 2012;45:385301. https://doi.org/10.1088/0022-3727/45/38/385301.

[62] Cen H, Lugt PM, Morales-Espejel G. On the Film Thickness of Grease-Lubricated Contacts at Low Speeds. Tribology Transactions 2014;57:668–78. https://doi.org/10.1080/10402004.2014.897781.

[63] Cen H, Lugt PM. Film thickness in a grease lubricated ball bearing. Tribology International 2019;134:26–35. https://doi.org/10.1016/j.triboint.2019.01.032.

[64] Zhou Y, Bosman R, Lugt PM. An Experimental Study on Film Thickness in a Rolling Bearing for Fresh and Mechanically Aged Lubricating Greases. Tribology Transactions 2019;62:557–66. https://doi.org/10.1080/10402004.2018.1539202.

[65] Cen H, Bai D, Chao Y, Li Y, Li R. EHL film thickness in rolling element bearings evaluated by electrical capacitance method: a review. Tribology - Materials, Surfaces & Interfaces 2021;15:55–77. https://doi.org/10.1080/17515831.2020.1838098.

[66] Kirk MT. Hydrodynamic Lubrication of ‘Perspex.’ Nature 1962;194:965–6. https://doi.org/10.1038/194965a0.

[67] Cameron A, Gohar R, Saunders OA. Theoretical and experimental studies of the oil film in lubricated point contact. Proceedings of the Royal Society of London Series A Mathematical and Physical Sciences 1966;291:520–36. https://doi.org/10.1098/rspa.1966.0112.

[68] Foord CA, Hammann WC, Cameron A. Evaluation of Lubricants Using Optical Elastohydrodynamics. A S L E Transactions 1968;11:31–43. https://doi.org/10.1080/05698196808972206.

[69] Westlake FJ, Cameron A. Report 12: A Study of Ultra-Thin Lubricant Films Using an Optical Technique. Proceedings of the Institution of Mechanical Engineers, Conference Proceedings 1967;182:75–8. https://doi.org/10.1243/PIME_CONF_1967_182_187_02.

[70] Gustafsson L, Höglund E, Marklund O. Measuring Lubricant Film Thickness with Image Analysis. Proceedings of the Institution of Mechanical Engineers, Part J: Journal of Engineering Tribology 1994;208:199–205. https://doi.org/10.1243/PIME_PROC_1994_208_371_02.

[71] Hartl M, Křupka I, Poliščuk R, Liška M. An Automatic System for Real-Time Evaluation of EHD Film Thickness and Shape Based on the Colorimetric Interferometry. Tribology Transactions 1999;42:303–9. https://doi.org/10.1080/10402009908982221.

[72] Molimard J, Querry M, Vergne P. New tools for the experimental study of EDH and limit lubrications. In: Dowson D, Priest M, Taylor CM, Ehret P, Childs THC, Dalmaz G, et al., editors. Tribology Series, vol. 36, Elsevier; 1999, p. 717–26. https://doi.org/10.1016/S0167-8922(99)80090-X.

[73] Nakahara T, Yagi K. Influence of temperature distributions in EHL film on its thickness under high slip ratio conditions. Tribology International 2007;40:632–7. https://doi.org/10.1016/j.triboint.2005.11.020.

[74] Wheeler J-D, Molimard J, Devaux N, Philippon D, Fillot N, Vergne P, et al. A Generalized Differential Colorimetric Interferometry Method: Extension to the Film Thickness Measurement of Any Point Contact Geometry. Tribology Transactions 2018;61:648–60. https://doi.org/10.1080/10402004.2017.1386809.

[75] Dwyer-Joyce R, Drinkwater B, Donohoe C. The measurement of lubricant--film thickness using ultrasound. Proceedings of the Royal Society of London Series A: Mathematical, Physical and Engineering Sciences 2003;459:957–76.

[76] Sibley LB, Orcutt FK. Elasto-Hydrodynamic Lubrication of Rolling-Contact Surfaces. A S L E Transactions 1961;4:234–49. https://doi.org/10.1080/05698196108972435.

[77] Kannel JW, Bell JC, Allen CM. Methods for Determining Pressure Distributions in Lubricated Rolling Contact. A S L E Transactions 1965;8:250–70. https://doi.org/10.1080/05698196508972099.

[78] Cheng HS, Orcutt FK. Paper 13: A Correlation between the Theoretical and Experimental Results on the Elastohydrodynamic Lubrication of Rolling and Sliding Contacts. Proceedings of the Institution of Mechanical Engineers, Conference Proceedings 1965;180:158–68. https://doi.org/10.1243/PIME_CONF_1965_180_076_02.

[79] Orcutt FK. Experimental Study of Elastohydrodynamic Lubrication. A S L E Transactions 1965;8:381–96. https://doi.org/10.1080/05698196508972109.

[80] Hamilton GM, Moore S. Deformation and pressure in an elastohydrodynamic contact. Proc R Soc Lond A 1971;322:313–30. https://doi.org/10.1098/rspa.1971.0070.

[81] Safa MMA, Anderson JC, Leather JA. Transducers for pressure, temperature and oil film thickness measurement in bearings. Sensors and Actuators 1982;3:119–28. https://doi.org/10.1016/0250-6874(82)80013-9.

[82] Miyata S, Höhn B-R, Michaelis K, Kreil O. Experimental investigation of temperature rise in elliptical EHL contacts. Tribology International 2008;41:1074–82. https://doi.org/10.1016/j.triboint.2008.01.006.

[83] Habchi W, Vergne P. On the compressive heating/cooling mechanism in thermal elastohydrodynamic lubricated contacts. Tribology International 2015;88:143–52. https://doi.org/10.1016/j.triboint.2015.03.025.

[84] Ebner M, Ziegltrum A, Lohner T, Michaelis K, Stahl K. Measurement of EHL temperature by thin film sensors – Thermal insulation effects. Tribology International 2020;149:105515. https://doi.org/10.1016/j.triboint.2018.12.015.

[85] Gardiner DJ, Baird E, Gorvin AC, Marshall WE, Dare-Edwards MP. Raman spectra of lubricants in elastohydrodynamic entrapments. Wear 1983;91:111–4. https://doi.org/10.1016/0043-1648(83)90111-4.

[86] Jubault I, Mansot J-L, Vergne P, Lubrecht T, Molimard J. In situ pressure measurements in an elastohydrodynamically lubricated point contact using Raman microspectrometry. Comparison with numerical calculations. 2002.

[87] Jubault I, Mansot JL, Vergne P, Mazuyer D. In-situ Pressure Measurements Using Raman Microspectroscopy in a Rolling Elastohydrodynamic Contact. Journal of Tribology 2002;124:114–20. https://doi.org/10.1115/1.1401016.

[88] Jubault I, Molimard J, Lubrecht AA, Mansot JL, Vergne P. *In Situ* Pressure and Film Thickness Measurements in Rolling/Sliding Lubricated Point Contacts. Tribology Letters 2003;15:421–9. https://doi.org/10.1023/B:TRIL.0000003068.07650.2e.

[89] Turchina V, Sanborn DM, Winer WO. Temperature Measurements in Sliding Elastohydrodynamic Point Contacts. Journal of Lubrication Technology 1974;96:464–9. https://doi.org/10.1115/1.3452005.

[90] Spikes HA, Anghel V, Glovnea R. Measurement of the Rheology of Lubricant Films Within Elastohydrodynamic Contacts. Tribology Letters 2004;17:593–605. https://doi.org/10.1023/B:TRIL.0000044509.82345.16.

[91] Reddyhoff T, Spikes HA, Olver AV. Improved infrared temperature mapping of elastohydrodynamic contacts. Proceedings of the Institution of Mechanical Engineers, Part J: Journal of Engineering Tribology 2009;223:1165–77. https://doi.org/10.1243/13506501JET499.

[92] Lu J, Reddyhoff T, Dini D. 3D Measurements of Lubricant and Surface Temperatures Within an Elastohydrodynamic Contact. Tribol Lett 2017;66:7. https://doi.org/10.1007/s11249-017-0953-2.

[93] Lu J, Reddyhoff T, Dini D. A study of thermal effects in EHL rheology and friction using infrared microscopy. Tribology International 2020;146:106179. https://doi.org/10.1016/j.triboint.2020.106179.

[94] Lee P, Zhmud B. Low Friction Powertrains: Current Advances in Lubricants and Coatings. Lubricants 2021;9:74. https://doi.org/10.3390/lubricants9080074.

[95] Kano M. Super low friction of DLC applied to engine cam follower lubricated with ester-containing oil. Tribology International 2006;39:1682–5. https://doi.org/10.1016/j.triboint.2006.02.068.

[96] Dobrenizki L, Tremmel S, Wartzack S, Hoffmann DC, Brögelmann T, Bobzin K, et al. Efficiency improvement in automobile bucket tappet/camshaft contacts by DLC coatings – Influence of engine oil, temperature and camshaft speed. Surface and Coatings Technology 2016;308:360–73. https://doi.org/10.1016/j.surfcoat.2016.09.041.

[97] Angus JC, Will HA, Stanko WS. Growth of Diamond Seed Crystals by Vapor Deposition. Journal of Applied Physics 1968;39:2915–22. https://doi.org/10.1063/1.1656693.

[98] Robertson J. Diamond-like amorphous carbon. Materials Science and Engineering: R: Reports 2002;37:129–281. https://doi.org/10.1016/s0927-796x(02)00005-0.

[99] Ohtake N, Hiratsuka M, Kanda K, Akasaka H, Tsujioka M, Hirakuri K, et al. Properties and Classification of Diamond-Like Carbon Films. Materials 2021;14:315. https://doi.org/10.3390/ma14020315.

[100] Choy KL. Chemical vapour deposition of coatings. Progress in Materials Science 2003;48:57–170. https://doi.org/10.1016/S0079-6425(01)00009-3.

[101] Ernesto A. Colloidal lubrication of DLC contacts : from steady state to transient state : Application to the piston - rings - cylinder contact. phdthesis. Ecole Centrale de Lyon, 2014.

[102] Grill A. Diamond-like carbon: state of the art. Diamond and Related Materials 1999;8:428–34. https://doi.org/10.1016/S0925-9635(98)00262-3.

[103] Donnet C. Tribology of solid lubricant coatings. Condensed Matter News 1995;4:9–24.

[104] Grill A. Tribology of diamondlike carbon and related materials: an updated review. Surface and Coatings Technology 1997;94–95:507–13. https://doi.org/10.1016/S0257-8972(97)00458-1.

[105] Erdemir A, Bindal C, Pagan J, Wilbur P. Characterization of transfer layers on steel surfaces sliding against diamond-like hydrocarbon films in dry nitrogen. Surface and Coatings Technology 1995;76–77:559–63. https://doi.org/10.1016/0257-8972(95)02518-9.

[106] Tallant DR, Parmeter JE, Siegal MP, Simpson RL. The thermal stability of diamond-like carbon. Diamond and Related Materials 1995;4:191–9. https://doi.org/10.1016/0925-9635(94)00243-6.

[107] Robertson J. Properties of diamond-like carbon. Surface and Coatings Technology 1992;50:185–203. https://doi.org/10.1016/0257-8972(92)90001-Q.

[108] Morath CJ, Maris HJ, Cuomo JJ, Pappas DL, Grill A, Patel VV, et al. Picosecond optical studies of amorphous diamond and diamondlike carbon: Thermal conductivity and longitudinal sound velocity. Journal of Applied Physics 1994;76:2636–40. https://doi.org/10.1063/1.357560.

[109] Hurler W, Pietralla M, Hammerschmidt A. Determination of thermal properties of hydrogenated amorphous carbon films via mirage effect measurements. Diamond and Related Materials 1995;4:954–7. https://doi.org/10.1016/0925-9635(94)00259-2.

[110] Bullen AJ, O'Hara KE, Cahill DG, Monteiro O, von Keudell A. Thermal conductivity of amorphous carbon thin films. Journal of Applied Physics 2000;88:6317–20. https://doi.org/10.1063/1.1314301.

[111] Chen G, Hui P, Xu S. Thermal conduction in metalized tetrahedral amorphous carbon (ta±C) ®lms on silicon. Thin Solid Films 2000:5.

[112] Shamsa M, Liu WL, Balandin AA, Casiraghi C, Milne WI, Ferrari AC. Thermal conductivity of diamond-like carbon films. Appl Phys Lett 2006;89:161921. https://doi.org/10.1063/1.2362601.

[113] Arlein JL, Palaich SEM, Daly BC, Subramonium P, Antonelli GA. Optical pump-probe measurements of sound velocity and thermal conductivity of hydrogenated amorphous carbon films. Journal of Applied Physics 2008;104:033508. https://doi.org/10.1063/1.2963366.

[114] Kim JW, Yang H-S, Jun YH, Kim KC. Interfacial effect on thermal conductivity of diamond-like carbon films. J Mech Sci Technol 2010;24:1511–4. https://doi.org/10.1007/s12206-010-0416-2.

[115] Vakis AI, Yastrebov VA, Scheibert J, Nicola L, Dini D, Minfray C, et al. Modeling and simulation in tribology across scales: An overview. Tribology International 2018;125:169–99. https://doi.org/10.1016/j.triboint.2018.02.005.

[116] Grill A. Electrical and optical properties of diamond-like carbon. Thin Solid Films 1999;355–356:189–93. https://doi.org/10.1016/S0040-6090(99)00516-7.

[117] Vera J, Brulez A-C, Contraires E, Larochette M, Trannoy-Orban N, Pignon M, et al. Factors influencing microinjection molding replication quality. J Micromech Microeng 2018;28:015004. https://doi.org/10.1088/1361-6439/aa9a4e.

[118] Evans RD, Cogdell JD, Richter GA, Doll GL. Traction of Lubricated Rolling Contacts between Thin-Film Coatings and Steel. Tribology Transactions 2008;52:106–13. https://doi.org/10.1080/10402000802180144.

[119] Kalin M, Polajnar M. The Effect of Wetting and Surface Energy on the Friction and Slip in Oil-Lubricated Contacts. Tribol Lett 2013;52:185–94. https://doi.org/10.1007/s11249-013-0194-y.

[120] Björling M, Habchi W, Bair S, Larsson R, Marklund P. Friction reduction in elastohydrodynamic contacts by thin-layer thermal insulation. Tribology Letters 2014;53:477–86. https://doi.org/10.1007/s11249-013-0286-8.

[121] Habchi W. Thermal analysis of friction in coated elastohydrodynamic circular contacts. Tribology International 2016;93:530–8. https://doi.org/10.1016/j.triboint.2015.01.017.

[122] Ziegltrum A, Lohner T, Stahl K. TEHL Simulation on the Influence of Lubricants on the Frictional Losses of DLC Coated Gears. Lubricants 2018;6:17. https://doi.org/10.3390/lubricants6010017.

[123] Bobzin K, Brögelmann T, Kalscheuer C, Thiex M, Ebner M, Lohner T, et al. A contribution to the thermal effects of DLC coatings on fluid friction in EHL contacts. Lubrication Science 2018;30:285–99. https://doi.org/10.1002/ls.1421.

[124] Marian M, Weikert T, Tremmel S. On Friction Reduction by Surface Modifications in the TEHL Cam/Tappet-Contact-Experimental and Numerical Studies. Coatings 2019;9:843. https://doi.org/10.3390/coatings9120843.

[125] Hakovirta M, Vuorinen JE, He XM, Nastasi M, Schwarz RB. Heat capacity of hydrogenated diamond-like carbon films. Applied Physics Letters 2000;77:2340–2. https://doi.org/10.1063/1.1290387.

[126] Reddyhoff T, Schmidt A, Spikes H. Thermal Conductivity and Flash Temperature. Tribol Lett 2019;67:22. https://doi.org/10.1007/s11249-018-1133-8.

[127] Doki-Thonon T. Thermal effects in elastohydrodynamic spinning circular contacts. These de doctorat. Lyon, INSA, 2012.

[128] Kistler Group. Torque Evaluation Unit (Rotor) for a Torque Measuring Flange. KiTorq Rotor Datasheet 2013.

[129] Kistler Group. Torque Evaluation Unit (Stator) for a Torque Measuring Flange. KiTorq Stator Datasheet 2013.

[130] BÖHLER Edelstahl GmbH & Co KG. HOT WORK TOOL STEELS. W300 ISODISK Datasheet 2022.

[131] Bouscharain N. Etude du comportement rhéologique sous haute pression d'un lubrifiant moteur. Réalisé au LaMCoS à la demande de IREIS sous contract CO0024538; 2020.

[132] Bair SS. High Pressure Rheology for Quantitative Elastohydrodynamics. Elsevier; 2007.

[133] Mary C. Physico-chemistry, high pressure rheology and film-forming capacity of polymer-base oil solutions in EHL. phdthesis. INSA de Lyon, 2014.

[134] Bair S. Measurements of real non-Newtonian response for liquid lubricants under moderate pressures. Proceedings of the Institution of Mechanical Engineers, Part J: Journal of Engineering Tribology 2001;215:223–33. https://doi.org/10.1243/1350650011543493.

[135] Yasutomi S, Bair S, Winer WO. An Application of a Free Volume Model to Lubricant Rheology I—Dependence of Viscosity on Temperature and Pressure. Journal of Tribology 1984;106:291–302. https://doi.org/10.1115/1.3260907.

[136] Hertz H. On the contact of elastic solids. Journal Für Die Reine Und Angewandte Mathematik 1881;92:156–71.

[137] Markho PH. Highly Accurate Formulas for Rapid Calculation of the Key Geometrical Parameters of Elliptic Hertzian Contacts. Journal of Tribology 1987;109:640–7. https://doi.org/10.1115/1.3261525.

[138] Meziane B. Film thickness build-up in highly loaded lubricated contacts under Zero Entrainment Velocity condition. These de doctorat. Lyon, 2020.

[139] Habchi W, Eyheramendy D, Vergne P, Morales-Espejel G. Stabilized fully-coupled finite elements for elastohydrodynamic lubrication problems. Advances in Engineering Software 2012;46:4–18. https://doi.org/10.1016/j.advengsoft.2010.09.010.

[140] Wu SR. A penalty formulation and numerical approximation of the Reynolds-Hertz problem of elastohydrodynamic lubrication. International Journal of Engineering Science 1986;24:1001–13. https://doi.org/10.1016/0020-7225(86)90032-7.

[141] COMSOL. COMSOL Multiphysics 5.5 Documentation 2019. https://doc.comsol.com/5.5/docserver/#!/com.comsol.help.comsol/helpdesk/helpdesk.html (accessed January 18, 2023).

[142] Amine G, Fillot N, Philippon D, Devaux N, Dufils J, Macron E. Dual experimental-numerical study of oil film thickness and friction in a wide elliptical TEHL contact: From pure rolling to opposite sliding. Tribology International 2023;184:108466. https://doi.org/10.1016/j.triboint.2023.108466.

[143] Chittenden RJ, Dowson D, Taylor CM. Elastohydrodynamic Film Thickness in Concentrated Contacts: Part 2: Correlation of Experimental Results with Elastohydrodynamic Theory. Proceedings of the Institution of Mechanical Engineers, Part C: Journal of Mechanical Engineering Science 1986;200:219–26. https://doi.org/10.1243/PIME_PROC_1986_200_117_02.

[144] Habchi W, Bair S, Qureshi F, Covitch M. A Film Thickness Correction Formula for Double-Newtonian Shear-Thinning in Rolling EHL Circular Contacts. Tribol Lett 2013;50:59–66. https://doi.org/10.1007/s11249-012-0078-6.

[145] Nijenbanning G, Venner CH, Moes H. Film thickness in elastohydrodynamically lubricated elliptic contacts. Wear 1994;176:217–29. https://doi.org/10.1016/0043-1648(94)90150-3.

[146] He L, Dan G, Tom R, Hugh S, JianBin L. SCIENCE CHINA Influence of thermal effects on elastohydrodynamic (EHD) lubrication behavior at high speeds. Sci China Tech Sci 2015;58:551–8. https://doi.org/10.1007/s11431-014-5564-7.

[147] Kumar P, Khonsari MM. Combined Effects of Shear Thinning and Viscous Heating on EHL Characteristics of Rolling/Sliding Line Contacts. Journal of Tribology 2008;130. https://doi.org/10.1115/1.2959111.

[148] Martinie L, Vergne P. Lubrication at Extreme Conditions: A Discussion About the Limiting Shear Stress Concept. Tribol Lett 2016;63:21. https://doi.org/10.1007/s11249-016-0709-4.

[149] Ndiaye S-N, Martinie L, Philippon D, Devaux N, Vergne P. A Quantitative Friction-Based Approach of the Limiting Shear Stress Pressure and Temperature Dependence. Tribol Lett 2017;65:149. https://doi.org/10.1007/s11249-017-0929-2.

[150] Xu R, Martinie L, Vergne P, Joly L, Fillot N. An Approach for Quantitative EHD Friction Prediction Based on Rheological Experiments and Molecular Dynamics Simulations. Tribol Lett 2023;71:69. https://doi.org/10.1007/s11249-023-01740-5.

[151] Dowson D. Paper 10: Elastohydrodynamics. Proceedings of the Institution of Mechanical Engineers, Conference Proceedings 1967;182:151–67. https://doi.org/10.1243/PIME_CONF_1967_182_014_02.

[152] Dowson D, Higginson GR. The Effect of Material Properties on the Lubrication of Elastic Rollers. Journal of Mechanical Engineering Science 1960;2:188–94. https://doi.org/10.1243/JMES_JOUR_1960_002_028_02.

[153] Moes H. Discussion on a Paper by D. Dowson. Proc Inst Mech Engrs 1965:244–5.

[154] Dowson D, Toyoda S. A Central Film Thickness Formula for Elastohydrodynamic Line Contacts. Proc 5th Leeds-Lyon Symp, 1978 1978;60.

[155] Greenwood JA, Kauzlarich JJ. Inlet Shear Heating in Elastohydrodynamic Lubrication. Journal of Lubrication Technology 1973;95:417–23. https://doi.org/10.1115/1.3451844.

[156] Murch LE, Wilson WRD. A Thermal Elastohydrodynamic Inlet Zone Analysis. Journal of Lubrication Technology 1975;97:212–6. https://doi.org/10.1115/1.3452559.

[157] Jackson A. A Simple Method for Determining Thermal EHL Correction Factors for Rolling Element Bearings and Gears. A S L E Transactions 1981;24:159–63. https://doi.org/10.1080/05698198108983008.

[158] Wilson WRD, Sheu S. Effect of Inlet Shear Heating Due to Sliding on Elastohydrodynamic Film Thickness. Journal of Lubrication Technology 1983;105:187–8. https://doi.org/10.1115/1.3254563.

[159] Pandey RK, Ghosh MK. Thermal effects on film thickness and traction in rolling/sliding EHL line contacts—an accurate inlet zone analysis. Wear 1996;192:118–27. https://doi.org/10.1016/0043-1648(95)06778-7.

[160] Bair S, Khonsari M. An EHD Inlet Zone Analysis Incorporating the Second Newtonian. Journal of Tribology 1996;118:341–3. https://doi.org/10.1115/1.2831306.

[161] Bair S, Vergne P, Marchetti M. The Effect of Shear-Thinning on Film Thickness for Space Lubricants. Tribology Transactions 2002;45:330–3. https://doi.org/10.1080/10402000208982557.

[162] Bair S. Shear thinning correction for rolling/sliding elastohydrodynamic film thickness. Proceedings of the Institution of Mechanical Engineers, Part J: Journal of Engineering Tribology 2005;219:69–74. https://doi.org/10.1243/135065005X9709.

[163] Jang JY, Khonsari MM, Bair S. Correction Factor Formula to Predict the Central and Minimum Film Thickness for Shear-Thinning Fluids in EHL. Journal of Tribology 2008;130. https://doi.org/10.1115/1.2842249.

[164] Bird RB, Armstrong RC, Hassager O. Dynamics of polymeric liquids. Vol. 1, 2nd Ed. : Fluid mechanics 1987.

[165] Habchi W. A numerical model for the solution of thermal elastohydrodynamic lubrication in coated circular contacts. Tribology International 2014;73:57–68. https://doi.org/10.1016/j.triboint.2014.01.002.

[166] Björling M, Isaksson P, Marklund P, Larsson R. The Influence of DLC Coating on EHL Friction Coefficient. Tribol Lett 2012;47:285–94. https://doi.org/10.1007/s11249-012-9987-7.

[167] Habchi W. Influence of thermo-mechanical properties of coatings on friction in elastohydrodynamic lubricated contacts. Tribology International 2015;90:113–22. https://doi.org/10.1016/j.triboint.2015.04.020.

[168] Yu C, Meng X, Xie Y. Numerical simulation of the effects of coating on thermal elastohydrodynamic lubrication in cam/tappet contact. Proceedings of the Institution of Mechanical Engineers, Part J: Journal of Engineering Tribology 2017;231:221–39. https://doi.org/10.1177/1350650116652046.

[169] Torabi A, Akbarzadeh S, Salimpour M, Khonsari MM. On the running-in behavior of cam-follower mechanism. Tribology International 2018;118:301–13. https://doi.org/10.1016/j.triboint.2017.09.034.

[170] Zhu D, Wang Q. On the ratio range of mixed lubrication. Proceedings of the Institution of Mechanical Engineers, Part J: Journal of Engineering Tribology 2012;226:1010–22. https://doi.org/10.1177/1350650112461867.

[171] Lyu B, Meng X, Zhang R, Cui Y. A Comprehensive Numerical Study on Friction Reduction and Wear Resistance by Surface Coating on Cam/Tappet Pairs under Different Conditions. Coatings 2020;10:485. https://doi.org/10.3390/coatings10050485.

[172] Buckingham E. On Physically Similar Systems; Illustrations of the Use of Dimensional Equations. Phys Rev 1914;4:345–76. https://doi.org/10.1103/PhysRev.4.345.

Appendix A: Optical Measurements Calibration for DLC-coated Glass Disk

The usual calibration phase before any experiment on JEROTRIB involving non-circular contacts consists of saving, in the form of monochromatic and colored pictures, 8 to 10 interference patterns generated by a lightly-loaded static contact (barrel and disk stationery) at random locations around the disk and the barrel. Then the procedure described in [74] is applied to each pair of pictures and one triplet of calibration curves (one curve for each one of red, green, and blue colors) is calculated representing the variation of the intensity of each color with respect to the gap between the surfaces. Figure A.1 presents an example, taken from [74], of a triplet of calibration curves in the range $0 < h < 800\ nm$, where h is the lubricant gap thickness. Similar triplets of calibration curves are calculated at different locations around the disk and a single representative triplet is chosen to be used in the analysis of interference images from a dynamic (disk and barrel moving) fully-loaded contact. The accuracy of film thickness measurements is directly influenced by how representative the chosen triplet is of the set of all triplets of calibration curves.

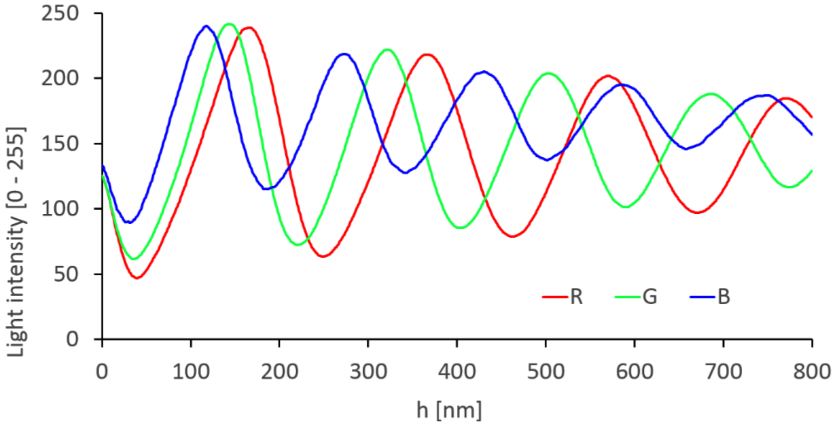

Figure A.1: An example of a triplet of calibration curves in the range $0 < h < 800\ nm$, where h is the lubricant gap thickness. Taken from [74].

The N-BK7 glass disk was coated by a thin coating (under 100nm) of semi-reflective a-C:H DLC coating. During the calibration phase, a large discrepancy was noticed between the calibration curves calculated from images taken at different locations on the disk. A single representative triplet could not be found indicating that the transmissivity of the coated glass disk is not uniform all around the disk. Different optical paths lead to different calibration curves at different locations on the disk. As a consequence, using a single triplet to calculate the film thickness during the tests resulted in a measurement uncertainty of around $\pm 50\ nm$.

To overcome this limitation, calibration curves were created at 15 different angular positions of the disk shown in Figure A.2.

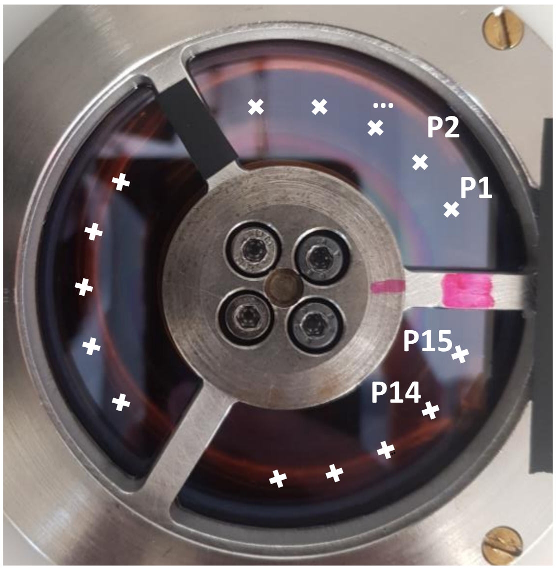

Figure A.2: Angular positions on Glass-DLC-D at which calibration curves are created

During the image analysis phase, a dedicated MATLAB® analysis program associates each interference image to an angular position and automatically uses the calibration curve created at the nearest position to calculate the lubricant film thickness. In this manner, the thickness measurement uncertainty decreases from $\pm 50\ nm$ to less than $\pm 6\ nm$.

Appendix B: Dynamics of Cam-follower-valve Mechanism

The study of the dynamics of the cam-follower-valve mechanism is needed for two purposes:

- To calculate the normal load, w_N, at the cam-follower contact point which is an input to the transient TEHL simulations of Chapter 5. In this case, the friction coefficient, C_f, is assumed to be equal to zero.
- To calculate the variation of normal and friction forces in addition to friction coefficient based on measurements of cam torque from the Monocam test rig.

Figure B.1a shows the cam-follower-valve mechanism during the counterclockwise rotation of the cam.

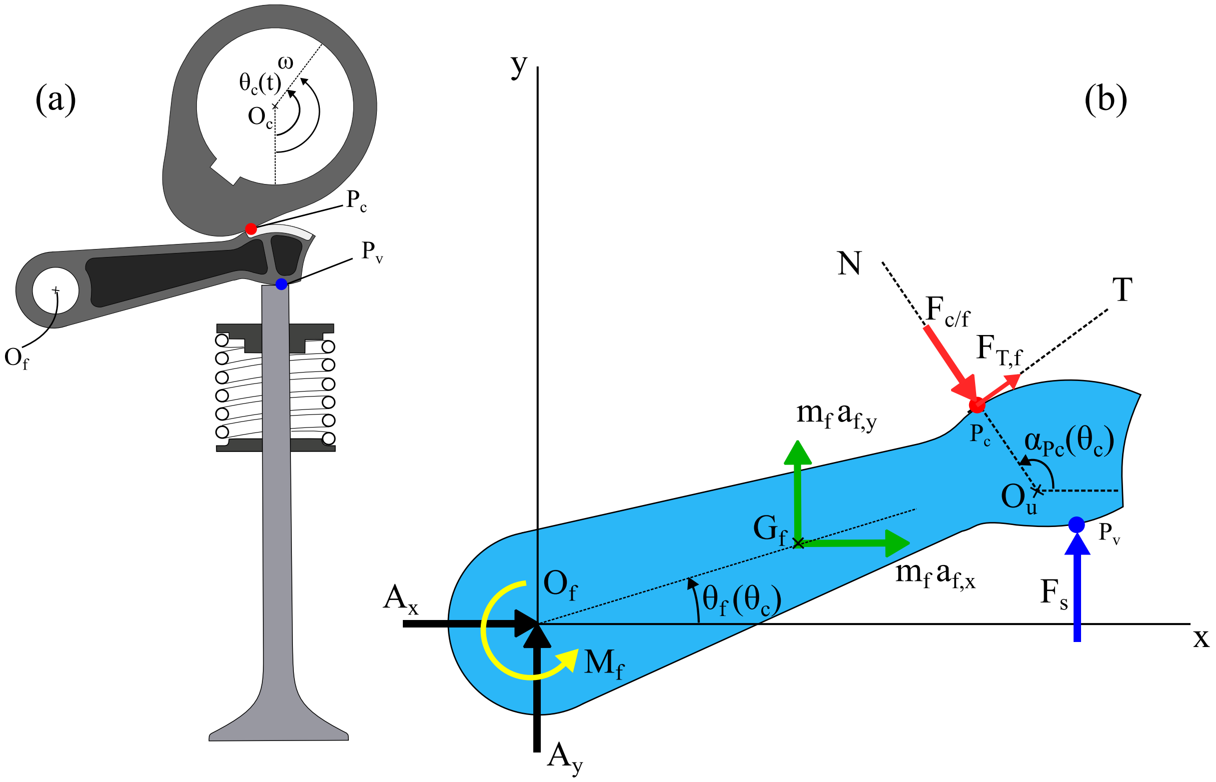

Figure B.1: (a) cam-follower-valve mechanism during the rotation of the cam and (b) the free-body diagram of the follower with a Cartesian frame of reference centered at O_f.

Point P_c is the contact point between the upper pad of the follower and the cam while P_v is the contact point between the lower pad and the valve. The Cartesian coordinates of these points can be calculated with respect to a frame centered at O_f (the center of rotation of the follower) by using the equations in [11]. The coordinates of points P_c and P_v are a function of the rotation angle of the cam called θ_c which itself is a function of time and the constant angular speed ω of the cam expressed in rad/s as in (B.1).

$$\theta_c = \omega t \tag{B.1}$$

The mass of the follower is $m_f = 0.0192\ kg$ and the mass of the valve and half of the mass of the spring are grouped in the mass $m_v = 0.0521\ kg$. The shape of the follower is approximated to a cylinder to simplify the calculation of its moment of inertia, I_{z,O_f}, around the z-axis (pointing outwards from the page) passing by O_f given by the following equation (B.2).

$$I_{z,O_f} = \frac{m_f(3R_f^2 + H_f^2)}{12} \tag{B.2}$$

where, $R_f = 0.0045\,m$ and $H_f = 0.0392\,m$ are the radius of the cylinder and its height respectively.

Moreover, the coordinates of the center of gravity, G_f, of the cylinder can be calculated based on the angular position θ_f which itself is a function of θ_c.

At a given instant t, a free-body diagram of the follower can be drawn as in Figure B.1b. The following forces act on the follower:

- A_x and A_y: reaction forces at the location of the pin O_f in x and y directions respectively. These forces are unknown and should be calculated.
- F_s: Force acting vertically on the lower follower pad which includes the compressed spring force and the effect of the acceleration of the mass m_v (valve + ½ spring). F_s is given by (B.3).

$$F_s = Kl_v + m_v\omega^2\frac{d^2l_v}{d\theta_c^2} \tag{B.3}$$

The first term of (B.3) is the force of a spring with stiffness K which is displaced a distance equal to the valve lift l_v. Note that a lift profile describes the variation of l_v with θ_c. The second term is dynamic force due to the acceleration of the mass m_v. The acceleration of the valve can be expressed as in (B.4). By applying the chain rule and replacing $\frac{d\theta_c}{dt}$ by ω in one ends up with the form given in (B.4).

$$\frac{d^2l_v}{dt^2} = \frac{d}{dt}\left(\frac{dl_v}{dt}\right) = \frac{d}{dt}\left(\frac{dl_v}{d\theta_c}\times\frac{d\theta_c}{dt}\right) = \omega\frac{d}{dt}\left(\frac{dl_v}{d\theta_c}\right) = \omega\frac{d}{d\theta_c}\left(\frac{dl_v}{d\theta_c}\right)\times\frac{d\theta_c}{dt} = \omega^2\frac{d^2l_v}{d\theta_c^2} \tag{B.4}$$

The term $\frac{d^2l_v}{d\theta_c^2}$ can be calculated by numerically deriving the lift profile $l_v(\theta_c)$ twice with respect to θ_c.

- $m_f a_{f,x}$ and $m_f a_{f,y}$: The dynamic forces due to the acceleration of the follower in the x and y direction respectively. These are applied to the center of gravity of the follower G_f. The accelerations can be calculated by numerically deriving the coordinates of G_f twice with respect to time using the chain rule and replacing $\frac{d\theta_c}{dt}$ by ω similarly to (B.4). Note that the gravitational force is neglected compared to the other forces involved in the cam-follower-valve mechanism.
- $F_{c/f}$ is the force normal to the upper pad. This force is unknown and should be calculated. The direction N is given by the angle $\alpha_{P_c}(\theta_c)$ formed between the segment joining the center of the upper pad O_u to the point P_c and the horizontal. The coordinates of O_u and P_c are function of θ_c thus the angle $\alpha_{P_c}(\theta_c)$ is given by equation (B.5)

$$\alpha_{P_c}(\theta_c) = arccos\left(\frac{x_{P_c} - x_{O_u}}{r_u}\right) \tag{B.5}$$

where, x_{M_c} and x_{O_u} are the x-coordinates of M_c and O_u respectively, and r_u is the radius of the upper pad.

- $F_{T,f}$ is the force in the tangential direction, T, perpendicular to the normal direction N. This force represents the friction force applied to the follower. Its direction depends on the rotation direction of the cam. Hence, F_T can be expressed as a function of the normal force, the friction coefficient C_f and the cam rotation direction as given in (B.6).

$$F_{T,f} = sign(\omega) C_f F_{c/f} \tag{B.6}$$

with $sign(\omega)$ equals 1 if the cam rotates in the counterclockwise direction and -1 if the cam rotates in the clockwise direction.

In addition to the forces, the torque M_f of the follower of inertia I_{z,O_f} and rotating around O_f is given by (B.7). Here the chain rule is used with $\omega = \frac{d\theta_c}{dt}$ to replace $\frac{d^2\theta_f}{dt^2}$ by $\omega^2 \cdot \frac{d^2\theta_f}{d\theta_c^2}$.

$$M_f = I_{z,O_f} \cdot \ddot{\theta}_f = I_{z,O_f} \cdot \frac{d^2\theta_f}{dt^2} = I_{z,O_f} \cdot \omega^2 \cdot \frac{d^2\theta_f}{d\theta_c^2} \tag{B.7}$$

Note that the friction between the follower and the pin at O_f is neglected.

At a given time t, the external forces and torques applied on the follower are in equilibrium. Meaning that the sum of external forces in the x direction, the sum of forces in the y direction, and the sum of torques around the point P_c are all equal to 0.

$$\sum F_{ext,x} = 0 \tag{B.8}$$

$$\sum F_{ext,y} = 0 \tag{B.9}$$

$$\sum M_{ext,P_c} = 0 \tag{B.10}$$

Equation (B.8) becomes:

$$A_x + m_f a_{f,x} - F_{c/f} \cos(\alpha_{P_c}) + F_{T,f} \cos\left(\alpha_{P_c} - \frac{\pi}{2}\right) = 0$$

$$A_x + m_f a_{f,x} - F_{c/f} \cos(\alpha_{P_c}) + sign(\omega) C_f F_{c/f} \cos\left(\alpha_{P_c} - \frac{\pi}{2}\right) = 0$$

$$A_x + F_{c/f} \left[-\cos(\alpha_{P_c}) + sign(\omega)\, C_f \cos\left(\alpha_{P_c} - \frac{\pi}{2}\right)\right] = -m_f a_{f,x} \tag{B.11}$$

Equation (B.9) becomes:

$$A_y + m_f a_{f,y} - F_{c/f} \sin(\alpha_{P_c}) + F_{T,f} \sin\left(\alpha_{P_c} - \frac{\pi}{2}\right) + F_s = 0$$

$$A_y + m_f a_{f,y} - F_{c/f} \sin(\alpha_{P_c}) + sign(\omega) C_f F_{c/f} \sin\left(\alpha_{P_c} - \frac{\pi}{2}\right) + F_s = 0$$

$$A_y + F_{c/f} \left[-\sin(\alpha_{P_c}) + sign(\omega) C_f \sin\left(\alpha_{P_c} - \frac{\pi}{2}\right)\right] = -F_s - m_f a_{f,y} \tag{B.12}$$

Equation (B.10) becomes:

$$y_{P_c} A_x + \left(y_{P_c} - y_{G_f}\right) m_f a_{f,x} - x_{P_c} A_y - \left(x_{P_c} - x_{G_f}\right) m_f a_{f,y} + \left(x_{P_v} - x_{P_c}\right) F_s + M_f = 0$$

$$y_{P_c} A_x - x_{P_c} A_y = \left(x_{P_c} - x_{G_f}\right) m_f a_{f,y} - \left(y_{P_c} - y_{G_f}\right) m_f a_{f,x} - \left(x_{P_v} - x_{P_c}\right) F_s - M_f \tag{B.13}$$

On one hand, if the goal is to calculate the normal load in the cam-follower contact then C_f is set to 0. Thus, the system of linear equations (B.11), (B.12), and (B.13) can simply be solved to calculate the three unknowns A_x, A_y, and $F_{c/f}$.

The normal load in the cam-follower contact is calculated by dividing the normal force $F_{c/f}$ by the width of the cam-follower contact $l_{c/f}$ (in the z-direction) as in (B.14).

$$w_N = \frac{F_{c/f}}{l_{c/f}} \tag{B.14}$$

The same procedure is repeated for all instants where there is contact between the cam and the follower. Hence, the evolution of the normal load with the camshaft rotation angle is obtained and can be used as input to the transient TEHL simulations of the cam-follower contact.

On the other hand, if the goal is to calculate the variation of experimental C_f. The equations (B.8) and (B.9) are written in the forms (B.15) and (B.16) respectively.

$$\begin{gathered} A_x + m_f a_{f,x} - F_{c/f}\cos(\alpha_{P_c}) + F_{T,f}\cos\left(\alpha_{P_c} - \frac{\pi}{2}\right) = 0 \\ A_x - F_{c/f}\cos(\alpha_{P_c}) + F_{T,f}\cos\left(\alpha_{P_c} - \frac{\pi}{2}\right) = -m_f a_{f,x} \end{gathered} \tag{B.15}$$

$$\begin{gathered} A_y + m_f a_{f,y} - F_{c/f}\sin(\alpha_{P_c}) + F_{T,f}\sin\left(\alpha_{P_c} - \frac{\pi}{2}\right) + F_s = 0 \\ A_y - F_{c/f}\sin(\alpha_{P_c}) + F_{T,f}\sin\left(\alpha_{P_c} - \frac{\pi}{2}\right) = -F_s - m_f a_{f,y} \end{gathered} \tag{B.16}$$

Equation (B.13) stays unchanged. However, an additional equation should be used to solve for the 4 unknowns A_x, A_y, $F_{c/f}$ and $F_{T,f}$. The fourth equation is based on the free body diagram of the cam drawn in Figure B.2 for at a given instant t.

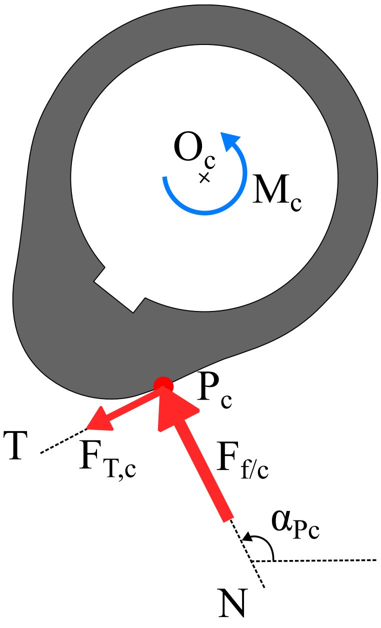

Figure B.2: Free-body diagram of the cam at an instant t for CCW rotation direction.

Here, $F_{f/c}$ is the force normal to the cam at P_c that is equal and opposite to $F_{c/f}$ (acting on the follower). Also, $F_{T,c}$ is the force tangent to the cam at P_c representing the friction force applied to the cam which is equal and opposite to $F_{T,f}$ the tangential force acting on the follower. M_c is the cam toque measured experimentally in the Monocam test rig. To satisfy the equilibrium, the sum of external torques around the cam center O_c is equal to zero as given by (B.17).

$$\sum M_{ext,O_c} = 0 \tag{B.17}$$

By developing (B.17) and rearranging its terms, the equation (B.18) is obtained.

$$\kappa_1 F_{f/c} + \kappa_2 F_{T,c} = sign(\omega) M_c \tag{B.18}$$

with

$$\kappa_1 = \left(x_{O_c} - x_{P_c}\right)\sin\left(\alpha_{P_c}\right) - \left(y_{O_c} - y_{P_c}\right)\cos\left(\alpha_{P_c}\right)$$

$$\kappa_2 = -\left(x_{O_c} - x_{P_c}\right)\ \sin\left(\alpha_{P_c} - \frac{\pi}{2}\right) + \left(y_{O_c} - y_{P_c}\right)\cos\left(\alpha_{P_c} - \frac{\pi}{2}\right)$$

Note that $sign(\omega)$ is introduced to account for the CW rotation case where the direction of cam torque is inverted.

$F_{f/c}$ and $F_{T,c}$ are replaced respectively with $F_{c/f}$ and $F_{T,f}$ to obtain the 4th equation (B.19) needed to solve for the four unknowns A_x, A_y, $F_{c/f}$, and $F_{T,f}$.

$$\kappa_1 F_{c/f} + \kappa_2 F_{T,f} = sign(\omega) M_c \tag{B.19}$$

The solution of the system of equations (B.13), (B.15), (B.16), and (B.19) results in $F_{c/f}$ the contact normal force and $F_{T,f}$ the contact friction force. Thus, the friction coefficient is calculated as $C_f = \frac{F_{T,f}}{F_{c/f}}$.

The same procedure is repeated for all instants where there is contact between the cam and the follower. Hence, the variation of the friction coefficient with the camshaft rotation angle is obtained and can be compared to numerical results.

Appendix C: 2D Wide Elliptical Contact Versus Equivalent 1D Line Contact

Nijenbanning et al. [145] suggested that if an elliptical contact is wide enough (i.e. ellipticity parameter $D < 0.1$) it can be modeled by an equivalent 1D line contact. Maximum Hertzian pressure and half-width in the line contact should be equal respectively to the maximum Hertzian pressure and the minor axis length of the elliptical contact. By satisfying these conditions, one can calculate the equivalent load and equivalent radius for the 1D contact based on those of the 2D contact as in equations (3.1) and (3.2).

The 1D line contact model used in Chapter 3 is compared to a corresponding 2D elliptical model. The Reynold domain length in the entrainment direction is the same in both models and is equal to 10 (symmetrical around the center). Also, the width of the Reynolds domain in the 2D case is equal to 10 . The operating conditions are the following: $T_0 = 45°C, p_{Hz} = 504\ MPa, and\ u_e = 1\ m/s$. SRR is varied from 0 to 4. It should be noted that the 2D model required a very fine mesh (maximum dimensionless mech size equal to 0.9) in the subsurface of the deformable solid to reach mesh independence.

Figure C.1a shows the variation of minimum film thickness on the central line and central film thickness calculated by the 1D and 2D models.

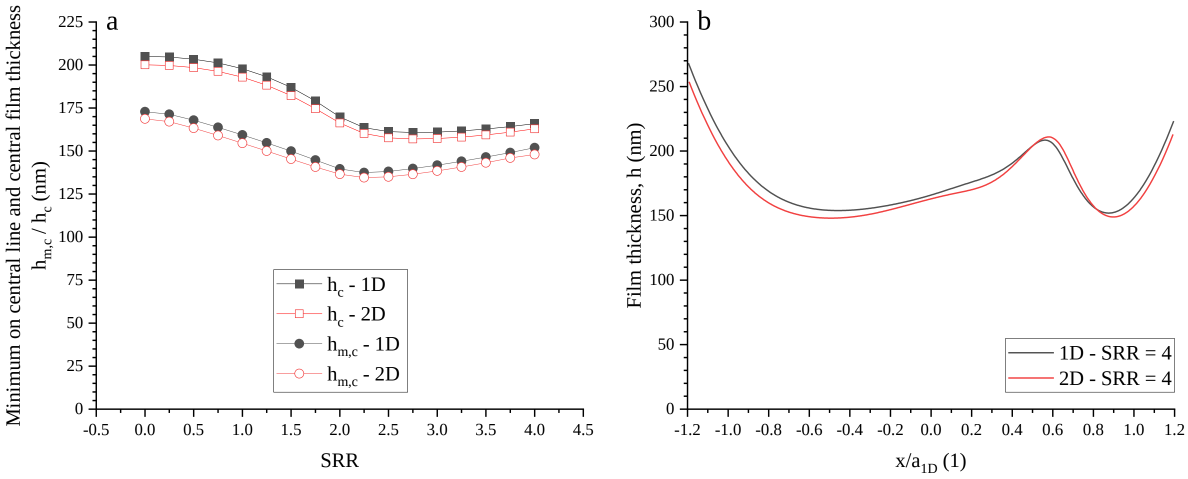

Figure C.1: (a) Variation with SRR of minimum on the central line and central film thickness. (b) Thickness profiles along the entrainment direction for $SRR = 4$. Results obtained by the 1D line contact model are presented in black while those obtained by the 2D elliptical contact model are presented in red. $T_0 = 45°C, u_e = 1\ m/s$, and $p_{Hz} = 504\ MPa$.

Notice that the thickness calculated by the 2D model is lower than that calculated by the 1D model for all sliding conditions. The average percentage difference in $h_{m,c}$ is 2.6 % corresponding to 3.8 nm in absolute difference and the average percentage difference in h_c is 2.3 % corresponding to 4.1 nm in absolute difference. These differences are of the same order as the uncertainty of the experimental measurements in this work. Also, the trends in the variation of $h_{m,c}$ and h_c with SRR are identical for both 1D and 2D simulations. These results show that the equivalence established by Nijenbanning et al. [145] is not only applicable for pure rolling contacts under isothermal and Newtonian behavior but also at extreme sliding where thermal and shear-thinning effects are significant under the chosen operating conditions. Furthermore, the thickness profiles along the entrainment direction calculated by the 1D and 2D models and shown in Figure C.1b are very similar over the entire contact region.

Figure C.2 represents the variation of the friction coefficient with SRR for the 1D and 2D models.

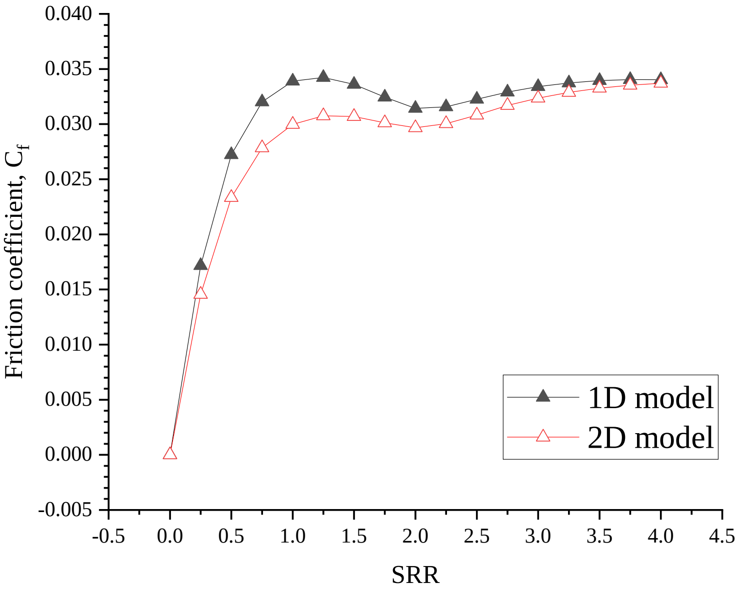

Figure C.2: Variation with SRR of friction coefficient calculated by the 1D line contact model (in black) and the 2D elliptical contact model (in red). $T_0 = 45°C, u_e = 1\ m/s$, and $p_{Hz} = 504\ MPa$.

The friction coefficient calculated by the 2D model is higher than that calculated by the 1D model for all SRR conditions. The difference at $SRR \geq\ 2$ averages around 3.3% in percentage difference corresponding to 0.001 in absolute difference. However, a more significant difference (13 % on average) in friction coefficient between 1D and 2D models exists for $SRR < 2$. In contrast with h_c and $h_{m,c}$ which are defined on the central line along the entrainment direction, the friction coefficient is calculated by integrating the shear rate over the whole elliptical contact domain in the case of the 2D model. Due to the geometry of the contacting surfaces in 2D elliptical contact, the pressure decreases in the vicinity of the central line as soon as one starts to move in the lateral direction (i.e. in the y-direction perpendicular to the entrainment). However, by extending the 1D line contact in the y-direction a constant pressure is obtained along the y-direction and is equal to that at the central line (i.e. $y = 0$). The high pressure in the 1D case increases the viscosity of the lubricant and as a consequence, the average friction force calculated in the 1D contact also increases. For this reason, the friction coefficient calculated by an equivalent 1D line contact overestimates that calculated by the 2D elliptical contact in Figure C.2. The difference in C_f between the 1D and 2D models decreases with increasing sliding and it almost vanishes at $SRR = 4$. As sliding increases, the temperature inside the contact also increases. By the same logic applied before, if one extends the 1D line contact into the y-direction a constant temperature in the y-direction is obtained. At high sliding, the higher pressure (normally leading to higher viscosity) in the extended 1D contact is compensated by a higher temperature which lowers the viscosity of the lubricant and the friction force. One ends up with a friction coefficient closer to that found by the 2D model with increasing sliding.

All in all, the qualitative trends are well reproduced by the 1D model. In addition, the maximum quantitative difference appears the range of $SRR \in [0.5,1.75]$, where accurately modeling the rheological behavior of lubricants is still very challenging (see section 3.1.4).

An important thing to consider is the size of the computational problem that needs to be solved. On one hand, the 1D model has 19,331 degrees of freedom combining EHL, non-Newtonian and thermal behaviors. On the other hand, the 2D model has about 783,263 degrees of freedom. To simulate all sliding conditions for the reference case it takes around 21 minutes for the 1D model (on a 4-core Intel i7 machine) compared to 31.5 hours for the 2D model (on an 8-core Intel Xeon machine). Thus, from a practical point of view, the use of the 1D line contact is much more advantageous than the 2D elliptical model.

The 1D model is used for the numerical parametric study and comparison with experimental measurements while keeping in mind the potential loss of accuracy, especially in terms of friction coefficient, due to the conversion from a 2D wide elliptical contact model to a 1D line contact model. In terms of film thickness parameters, the 1D equivalent model can be used with confidence over all the tested conditions.

Appendix D: Estimation of Minimum and Central Film Thickness

The estimation shown in this appendix applies to the pure rolling condition and requires rheological characterization of the lubricant that enables the description of viscosity variation by a Carreau-like law.

Starting with operating conditions, geometry, and fluid properties, one can define classical dimensionless parameters [152]:

$$U = \frac{\mu_0\, u_e}{E' R_x^{2D}} \qquad G = \alpha^* E' \qquad W_{2D} = \frac{w_{2D}}{E' (R_x^{2D})^2} \qquad H_c = \frac{h_c}{R_x^{2D}} \qquad H_m = \frac{h_m}{R_x^{2D}}$$

where μ_0 and α^* are respectively the viscosity and the viscosity-pressure coefficient at atmospheric pressure at a given temperature corresponding to that of the test. Their values are given in Table 2.5 for various temperatures. E' is the reduced Young's modulus given by equation (2.9) and R_x^{2D} is the reduced radius of curvature given by equation (2.23). H_c and H_m are respectively the dimensionless central and minimum film thickness parameters.

Chittenden et al. [143] derived analytical expressions to calculate central and minimum film thickness in the dimensionless form:

$$H_{c,Chittenden} = 4.31\, U^{0.68}\, G^{0.49}\, W_{2D}^{-0.073} \left(1 - e^{-1.23\left(\frac{R_y^{2D}}{R_x^{2D}}\right)^{2/3}} \right)$$

$$H_{m,Chittenden} = 3.68\, U^{0.68}\, G^{0.49}\, W_{2D}^{-0.073} \left(1 - e^{-0.67\left(\frac{R_y^{2D}}{R_x^{2D}}\right)^{2/3}} \right)$$

The above expressions are limited to EHL contact where non-Newtonian effects can be neglected. Correction factors must be applied to make use of Chittenden expressions to estimate film thickness for a non-Newtonian lubricant.

Furthermore, Habchi et al. [144] derived an expression for a non-Newtonian correction factor. Note that the expression presented here is the form given in [35].

$$\varphi_{m,nN} = R_{CY}^{0.893} + [\, 1 - R_{CY}^{0.893}\,] \cdot (1 + 1.543\, \Gamma)^{n_{CY}-1}$$

$$\varphi_{c,nN} = R_{CY}^{0.7469} + [1 - R_{CY}^{0.7469}]. (1 + 1.678\, \Gamma)^{n_{CY}-1}$$

Where R_{CY} and n_{CY} are parameters of the Carreau-Yasuda model. Both of these parameters are obtained by the rheological characterization of the fluid (see section 2.1.3). Γ is the Weissenberg number [164] defined based on the Newtonian central thickness following the expression:

$$\Gamma = \frac{\mu_0\, u_e}{H_{c,Chittenden}\; R_x^{2D} G_{cy}}$$

Finally, the Chittenden estimations corrected for non-Newtonian behavior by the factor of Habchi are calculated as follows:

$$H_{m,non-Newtonian} = \varphi_{m,nN} \times H_{m,Chittenden}, \qquad H_{c,non-Newtonian} = \varphi_{c,nN} \times H_{c,Chittenden}$$

Appendix E: Dimensional Analysis of Coated EHL Contacts

The Buckingham Π theorem [172] is used to determine the relationship between physical variables influencing the coated EHL contact behavior and express them in terms of dimensionless groups. The theorem states that if a physical problem involves n variables, which can be expressed in terms of m fundamental dimensions (such as length, time, mass, temperature, etc.), then the problem can be reduced to $(n - m)$ dimensionless groups (or Π-terms). The Buckingham Π theorem consists of 5 steps.

Step 1: All the variables ($n = 13$) involved in coated EHL contact are listed in Table E.1 alongside their SI units and dimensions expressed in terms of fundamental dimensions ($m = 4$) of length, mass, time and temperature respectively denoted L, M, T, and Θ.

Table E.1: List of variables involved in the coated EHL contact problem with their units and dimensions.

Variable	**SI unit**	**Dimension**
Entrainment velocity, u_e	m/s	$\mathrm{LT^{-1}}$
Sliding velocity, u_s	m/s	$\mathrm{LT^{-1}}$
Normal load, w_{1D}	N/m	$\mathrm{MT^{-2}}$
Reduced Young's modulus, R	m	L
Reduced radius of curvature, E'	Pa	$\mathrm{L^{-1}MT^{-2}}$
Lubricant viscosity, η	$Pa.s$	$\mathrm{L^{-1}MT^{-1}}$
Pressure-viscosity coefficient, α	$1/Pa$	$\mathrm{LM^{-1}T^{2}}$
Minimum lubricant film thickness, h_m	m	L
Central lubricant film thickness h_c	m	L
Thermal conductivity of the coating, k	$W/m.K$	$\mathrm{LMT^{-3}\Theta^{-1}}$
Specific heat capacity of the coating, Cp	$J/kg.K$	$\mathrm{L^{2}T^{-2}\Theta^{-1}}$
Density of the coating, ρ	kg/m^3	$\mathrm{L^{-3}M}$
Coating thickness, h_{coat}	m	L

Step 2: $m = 4$ repeating variables are chosen because 4 fundamental dimensions appear in the derived dimensions of the variables. Note that there are certain criteria for choosing repeating variables:

- None of the repeating variables can be dimensionless
- No two repeating variables can have the same overall dimension

In the current case, the selected repeating variables are u_e, R, η, and k. These will appear in all Π-terms.

Step 3: the number of the remaining variables is $n - m = 9$. Choosing one of these variables, for example considering w_{1D}, the theorem states that a dimensionless group Π exists such that:

$$\Pi = u_e^a R^b \eta^c k^d w_{1D}^e \rightarrow [\Pi] = [u_e]^a [R]^b [\eta]^c [k]^d [w_{1D}]^e \qquad \text{(E.1)}$$

where the "[x]" denotes the dimensions on the variable x and "a" through "e" are exponents that need to be calculated. Replacing each variable in (E.1) with its corresponding dimension gives (E.2).

$$[\mathrm{L}^0\mathrm{M}^0\mathrm{T}^0\Theta^0\ ] = [\mathrm{LT}^{-1}]^a[\mathrm{L}]^b[\mathrm{L}^{-1}\mathrm{MT}^{-1}]^c[\mathrm{LMT}^{-3}\Theta^{-1}]^d[\mathrm{MT}^{-2}]^e \tag{E.2}$$

An equation relating the exponents is written for each fundamental dimension as follows:

$$\begin{aligned} &\text{L:} && a+b-c+d=0 \\ &\text{M:} && c+d+e=0 \\ &\text{T:} && -a-c-3d-2e=0 \\ &\Theta\text{:} && -d=0 \end{aligned} \tag{E.3}$$

Given the four equations with 5 variables in (E.3), all exponents can be expressed in terms of the exponent "e". Resulting in $a=-e, b=0, c=-e$, and $d=0$. Thus, the Π-term is given by (E.4) where the exponent can be dropped since Π is dimensionless.

$$\Pi = u_e^{-e}R^0\eta^{-e}k^0w_{1D}^e = \left(\frac{w_{1D}}{u_e\eta}\right)^e = \frac{w_{1D}}{u_e\eta} \tag{E.4}$$

Step 4: the calculation realized in step 3 is repeated for all the remaining variables resulting in 8 additional Π-terms.

Step 5: Additional dimensionless groups can be formed as functions of other Π-terms. The 9 principal Π-terms are listed in Table E.2 whereas the derived terms useful in the context of coated EHL contact are listed in Table E.3.

Table E.2: Principal dimensionless groups.

Variable	Π-term	Expression
u_s	Π_1	$\frac{u_s}{u_e}$
w_{1D}	Π_2	$\frac{w_{1D}}{u_e\eta}$
E'	Π_3	$\frac{u_e\eta}{RE'}$
α	Π_4	$\frac{u_e\eta\alpha}{R}$
h_m	Π_5	$\frac{h_m}{R}$
h_c	Π_6	$\frac{h_c}{R}$
Cp	Π_7	$\frac{\eta Cp}{k}$
ρ	Π_8	$\frac{u_eR\rho}{\eta}$
h_{coat}	Π_9	$\frac{h_{coat}}{R}$

Table E.3: Derived dimensionless groups.

Combined Π-terms	Π-term	Expression
$\Pi_2 \times \Pi_3$	Π_{10}	$\frac{w_{1D}}{RE'}$
$\Pi_4 \div \Pi_3$	Π_{11}	$E'\alpha$
$\frac{1}{\Pi_7 \times \Pi_8}$	Π_{12}	$\frac{k}{\rho Cpu_e R}$

It should be noted that some of the dimensionless groups ($\Pi_3, \Pi_5, \Pi_6, \Pi_{10}$, and Π_{11}) are the same as those defined by [152] to be used in classical film thickness estimation expressions. Moreover, Π_1 corresponds to the definition of SRR in the current work. Π_9 and Π_{12} are related to the properties of the coating and are used in Chapter 4 to quantify the effects of varying the thermal conductivity and thickness of the coating applied to a line EHL contact.

Appendix F: Experimental Results Related to the Cam-Follower Contact

F.1 Effect of speed steps order

In experiments, speed steps are tested in ascending and descending orders to ensure measurement repeatability. Figure F.1 shows the variation of mean friction coefficient with camshaft rotation speed obtained during ascending and descending speed steps tests at $50 \pm 1°C$ for all surface configurations and rotation directions.

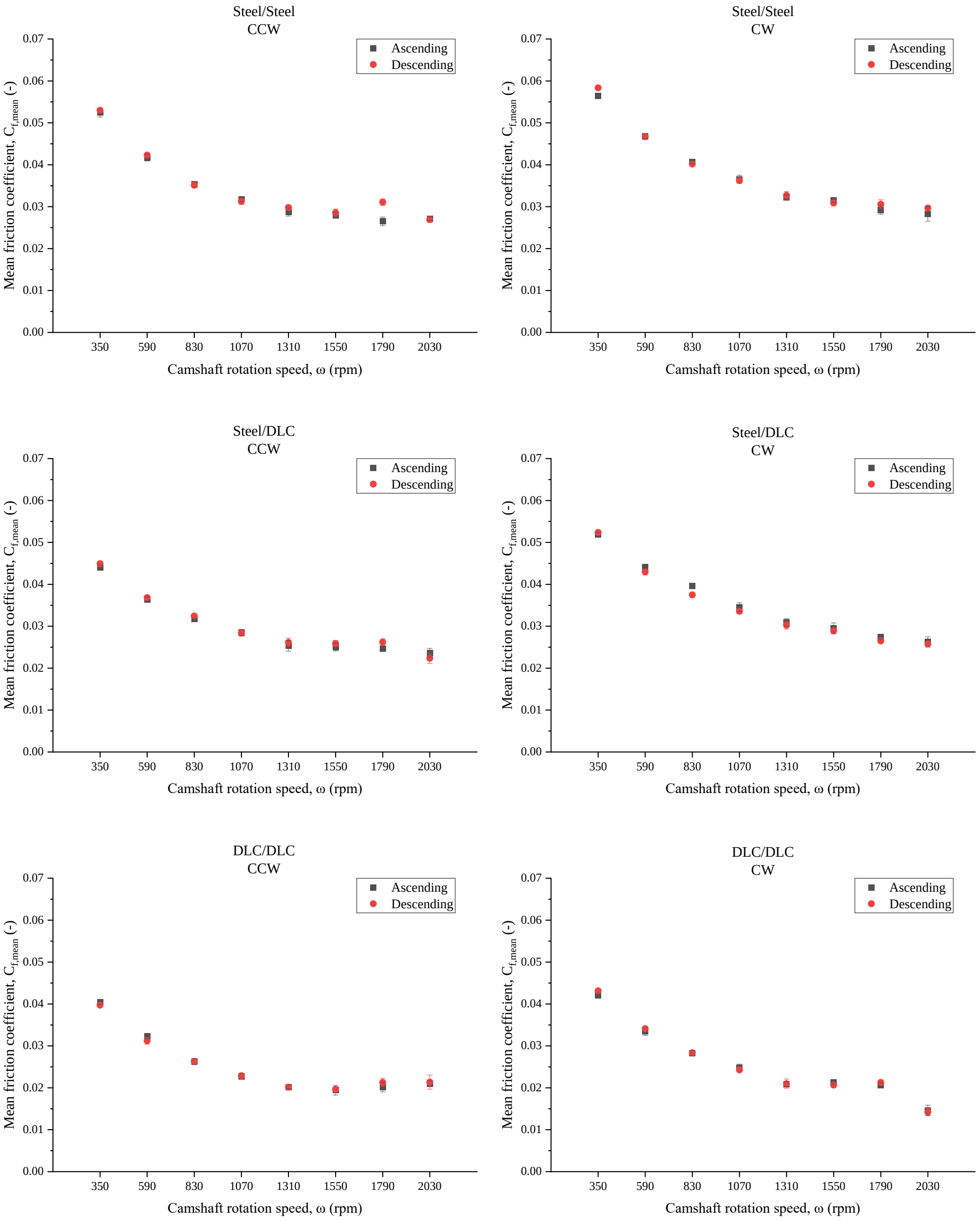

Figure F.1: Variation of mean friction coefficient with camshaft rotation speed: comparison of results obtained from ascending and descending speed steps tests. Different surface configurations and rotation directions for $T_{in} = 50 \pm 1°C$ are shown.

Results from ascending and descending speed steps tests are very close for most camshaft rotation speeds which indicates that the measurements are repeatable.

F.2 Effect of rotation direction

Variations of mean friction coefficient with rotation speed from CW and CCW tests for the reference configuration (steel/steel) at 50°C are presented in Figure F.2.

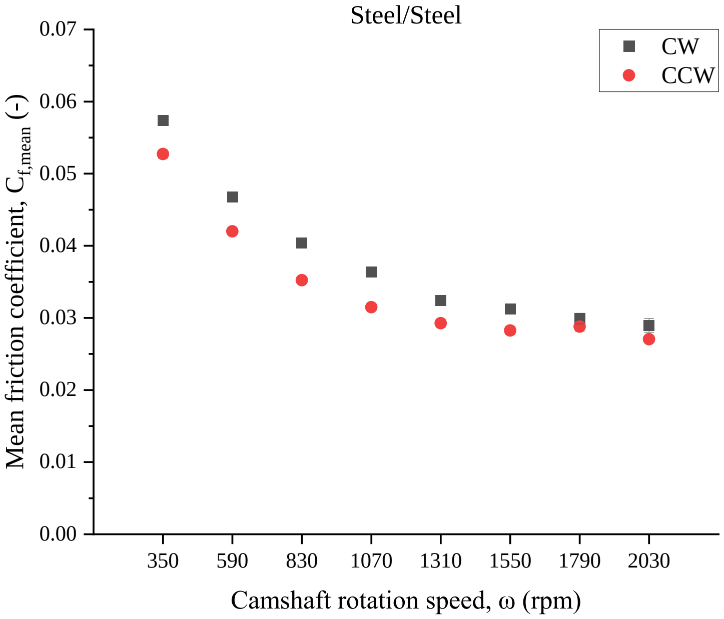

Figure F.2: Variation of mean friction coefficient with camshaft rotation speed: comparison of results obtained from CW and CCW tests for steel/steel configuration at $50°C$.

The mean friction coefficient is lower in the CCW rotation direction compared to the CW rotation direction for all speeds. The difference is less significant at higher speeds. Similar results are observed for other surface configurations presented in Figure F.3.

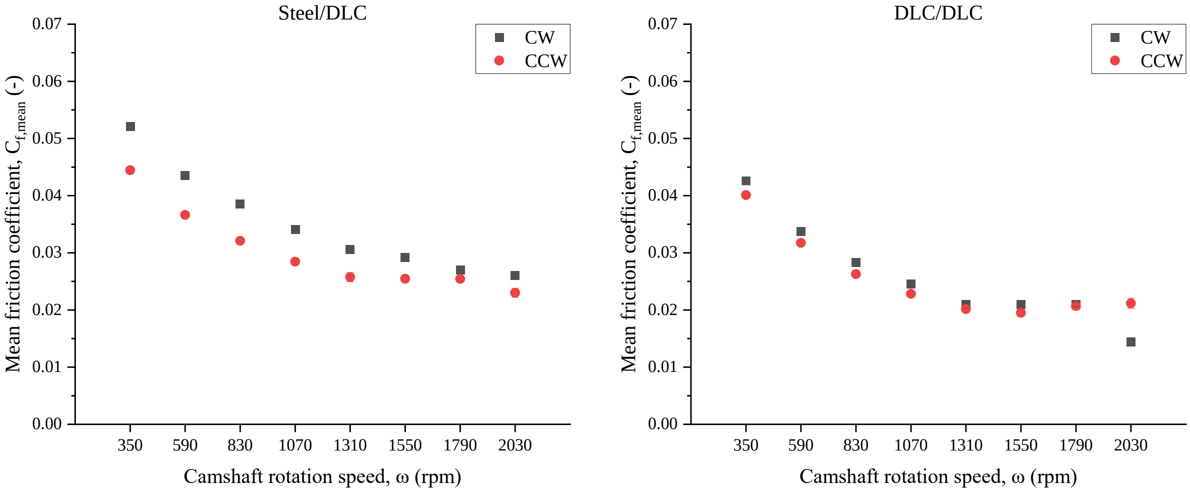

Figure F.3: Variation of mean friction coefficient with camshaft rotation speed: comparison of results obtained from CW and CCW tests for steel/DLC and DLC/DLC configurations.

Recall that the lubrication of the cam-follower contact is provided via a nozzle in the follower. Counterclockwise rotation is suspected to be more favorable for the entrainment of the lubricant into the contact as illustrated in Figure F.4.

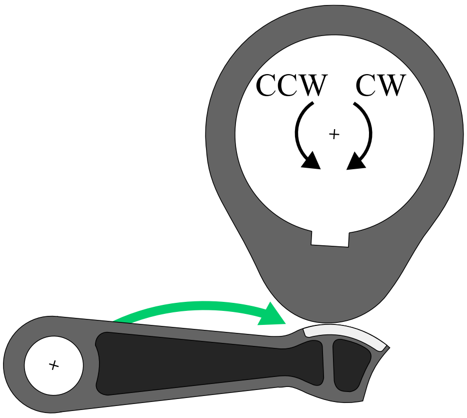

Figure F.4: Cam-follower mechanism lubricated via a nozzle in the follower.

For instance, at the lowest rotation speed (i.e. 350 rpm) the variation of friction coefficient is plotted in Figure F.5a for both CW and CCW rotation directions. Also, the curvilinear position of the contact point on the upper pad with respect to the initial position P_0 is plotted in Figure F.5b. A difference is observed in the magnitude of friction coefficient in the nose region where $SRR > 2$ (i.e. $146° \leq \theta_c \leq 219°$, see Figure 1.5).

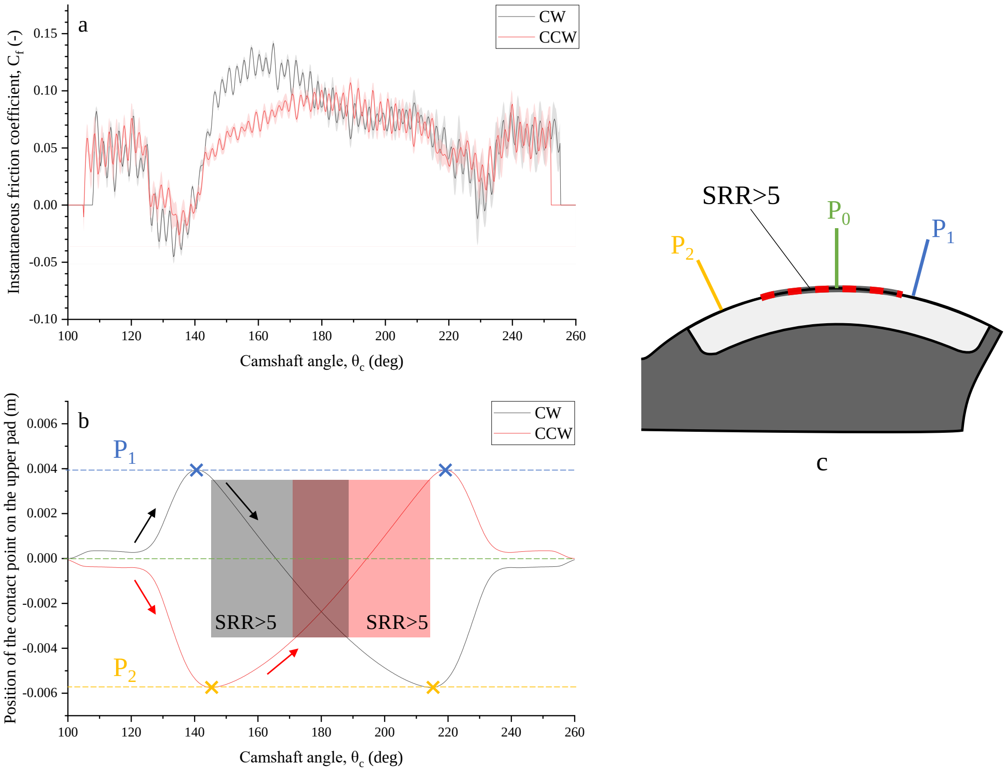

Figure F.5: Variation of (a) instantaneous friction coefficient and (b) position of the contact point on the upper pad with camshaft rotation angle for CW and CCW. (c) Illustration of the locations of extreme points P1 and P2 on the upper pad of the follower, in addition, the point P0 where the contact begins and ends. Results correspond to steel/steel configuration at $T_{in} = 50 \pm 1°C$ with camshaft rotation speed of 350 rpm.

Point P$_1$ corresponds to the furthest location from the lubrication nozzle on the upper pad, reached during the cycle. On one hand, in the case of CW rotation, the point of contact moves first from P$_0$ to P$_1$ and then travels from P$_1$ to P$_2$ passing by the zone of extreme sliding with $SRR > 5$ (highlighted in gray in Figure F.5b). The cam surface is lubricated by the lubricant nozzle just after leaving the contact. During the rotation of the cam, the oil might detach from its surface leading to starved lubrication when re-entering the contact. Starved lubrication leads to an increase in friction coefficient. On the other hand, in the case of CCW rotation, the point of contact first moves towards P$_2$ then from P$_2$ towards P$_1$ passing by the red zone in Figure F.5b. However, in this case, the cam surface is lubricated by the nozzle just before it the contact. This ensures better lubrication and lower friction compared to the CW rotation case. This can explain the difference in mean friction coefficient between CW and CCW rotation, as observed in Figure F.5. Only the case of CCW rotation is considered for the discussion in Chapter 5 and for comparison with simulations that are always under fully-flooded conditions no matter the rotation direction.

F.3 Experimental and numerical results in steel/DLC configuration

In section 5.2.3 experimental and numerical results were compared for steel/steel and DLC/DLC configurations. Figure F.6 completes the comparison for steel/DLC configuration. Similar to the results discussed in Chapter 5, the numerical approach predicts mean friction with good accuracy for high rotation speeds where asperity friction is minimized. In contrast, for low rotation speeds predictions significantly underestimate friction because the numerical model assumes full-film lubrication which is not the case in reality at low speeds (λ less than 2).

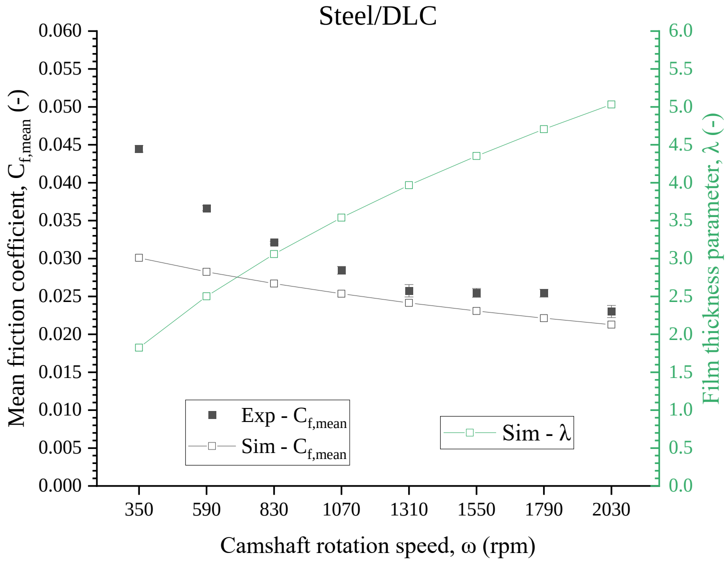

Figure F.6: Variation with the camshaft rotation speed of the mean friction coefficient (left axis) obtained numerically and experimentally in addition to the variation of the film thickness parameter (right axis) calculated based on the mean minimum film thickness $h_{a,mean}$ from TEHL simulations. Results correspond to steel/DLC configuration.

Publications

The research presented in this document has resulted so far in one peer-reviewed article and was presented at an international conference.

Article:

Amine G, Fillot N, Philippon D, Devaux N, Dufils J, Macron E. *Dual experimental-numerical study of oil film thickness and friction in a wide elliptical TEHL contact: From pure rolling to opposite sliding*. Tribology International 2023;184:108466.

Presentation:

Amine G, Fillot N, Philippon D, Devaux N, Dufils J, Macron E. *Thermal effects of DLC coating on EHL performance: From pure rolling to opposite sliding*. 7th World Tribology Congress (July 2022-Lyon, France).

FOLIO ADMINISTRATIF

THESE DE L'INSA LYON, MEMBRE DE L'UNIVERSITE DE LYON

NOM : AMINE DATE de SOUTENANCE : 28/08/2023

Prénoms : Georges

TITRE : High sliding EHL contacts: thermal effects of DLC coatings

NATURE : Doctorat Numéro d'ordre : 2023ISAL0049

Ecole doctorale : Mécanique, Énergétique, Génie civil, Acoustique (MEGA)

Spécialité : Génie Mécanique

RESUME :

Cette thèse explore l'influence des revêtements Diamond-Like Carbon (DLC) sur à la fois le frottement et l'épaisseur du film dans les contacts thermo-élastohydrodynamiques (TEHL) pour une large gamme de conditions de glissement. Des études précédentes ont principalement examiné la réduction du frottement due aux revêtements DLC sous des conditions de roulement-glissement et ont trouvé une influence négligeable sur l'épaisseur du film. Cependant, les surfaces thermiquement isolantes sont suspectées de réduire l'effet bénéfique du « viscosity wedge » à haut cisaillement. Cette thèse étudie une large gamme de conditions de glissement, telles que le glissement opposé trouvé dans divers composants mécaniques tels que le contact came-linguet. Une double approche expérimentale et numérique est utilisée. D'une part, des expériences sont menées sur un tribomètre tonneau-sur-disque et sur un banc d'essai came-linguet-poussoir. D'autre part, une approche EHL quantitative est proposée sur la base d'une caractérisation rhéologique indépendante d'un lubrifiant commercial et réalisée à l'aide d'un solveur éléments finis. Les résultats démontrent la capacité du modèle numérique à reproduire à la fois les mesures de frottement et d'épaisseur du film, en particulier dans des conditions de glissement opposé. Sur une large gamme de conditions de fonctionnement examinées dans cette étude, le modèle numérique montre que l'utilisation des revêtements DLC conduit non seulement à une diminution du frottement (d'environ 30 % dans certains cas), mais également à une diminution de l'épaisseur de film (jusqu'à 10 %). De plus, les résultats numériques et expérimentaux indiquent tous deux que l'application d'un revêtement DLC au contact came-linguet est bénéfique en termes de réduction du frottement. En outre, cette étude vise à quantifier la diminution de l'épaisseur du film lors du glissement à haute vitesse, ce qui est essentiel pour anticiper le risque de contact entre aspérités.

MOTS-CLÉS : Lubrification TEHL, Fort glissement, Effet thermique, Revêtement DLC, Cam-linguet.

Laboratoire (s) de recherche : LAMCOS

Directeur de thèse : FILLOT, Nicolas

Président de jury :

Composition du jury : LARSSON, Roland; HABCHI, Wassim; MINFRAY, Clotilde; FILLOT, Nicolas